THE UNIVERSITY OF CHICAGO

COHERENT NONEQUILIBRIUM MANY-BODY DYNAMICS IN DRIVEN BOSE CONDENSATES

A DISSERTATION SUBMITTED TO
THE FACULTY OF THE DIVISION OF THE PHYSICAL SCIENCES
IN CANDIDACY FOR THE DEGREE OF
DOCTOR OF PHILOSOPHY

DEPARTMENT OF PHYSICS

BY
LEI FENG

CHICAGO, ILLINOIS
JUNE 2019

To my loving family

TABLE OF CONTENTS

LIST OF FIGURES

ACKNOWLEDGMENTS

Firstly, I would like to sincerely thank my advisor, Professor Cheng Chin, for his generous support and wise guidance during my Ph. D. study. None of the works in this thesis could be possible without him. Cheng is a great scientist who has great knowledge and everlasting enthusiasm over a large spectrum physics and a great advisor encouraging independent and critical thinking. He takes every chance to bring valuable opportunities for his student to further advance their career in science. I would always be thankful for the wonderful research experience in the Chin lab.

I would also like to acknowledge my great teammates in the Cesium lab. First of all, I particularly appreciate the great friendship with Dr. Logan W. Clark who is not only extremely smart but also has an incredibly generous and charming personality. During my early novice years in Cesium lab, he patiently guided me through all the mists and offered invaluable spiritual support. We not only collaborated on mysterious experiments on studying quantum phase transitions and Bose fireworks but also shared the great moments in our life. I am very much honored to witness the lovely marriage of Logan and Marianne who is also a great friend and an excellent *Doctor*. I also have the privilege to enjoy the delicious cookies from Logan's mom, Ms. Clark. He is such a charming person and great physicist and I am so proud to have him as a good friend. Meanwhile, Zhengdong and Kevin joined the Cesium lab and bring in fresh enthusiasm. Zhendong is very quick learner and very hard-working in the experiments. Kevin is remarkably good in theory and often thinks out of the box, which I often learn from him. They two makes a great team and bring a bright future to Cesium lab. I am also grateful to Chen-Lung, Xibo, and Harry. Their hard works laid the very foundation for all the cool experiments in Cesium lab. They often offer great advice whenever we need help with troubleshooting.

I would also like to thank all the great postdocs in Chin lab. My first project building an RSC lattice laser is kindly supervised by Dr. Eric Hazlett. Later after I joined Li-Cs lab, Dr. Colin Parker trained me everything about cooling and trapping of cold atoms. I really

value the experiences fixing Bitter coils and replacing the ovens. After Colin left, Dr. Brian Desalvo joined the Li-Cs lab and really brought the experiment to a new level and I really enjoyed the time we overlapped. After I moved to Cesium lab, Dr. Anita Gaj joined Logan and me and brought great knowledge and insight to the team. Later Dr. Jiazhong Hu joined the Cesium lab and brought fresh concepts from quantum optics to our matter-wave system. Enthusiastic Dr. Mickey McDonald often offers help whenever I have physics or technical questions.

I am also grateful to other members in the Chin lab. Thanks to Jacob Johansen, who patiently taught me Efimov physics during my time in Li-Cs. Thanks to Gustaf Downs for his friendship and inspiration during his time in Quantum Matter Synthesizer lab. Thanks to Krutik Patel for his great advice on writing and Jonathan Trisnadi for inspirational discussions on physics.

I would also like to thank Professor Kathryn Levin and her postdocs Brian W. Anderson and Fu Han. Professor Kathryn Levin has been a very supportive member of my thesis committee and offered me guidance not only on collaborated researches but also on a future career in science. I have collaborated with Brian and Han on various simulation projects and their perspectives on physics are always valuable to me.

I am very grateful to Professors Jonathan Simon and Henry Frisch, my thesis committee members, for their valuable advice over the time and their hard work reviewing my thesis.

Thank you to JFI staffs Maria Jimenez, Eileen Sheu, and John Phillips for their support and their hard work enables a great research environment. Thank you also to the members of the University of Chicago Physics Department, particularly Amy Schulz and Professor David Reid, for establishing a pleasant and stimulating environment for my graduate studies. I am grateful for the fellowship support that I have received from the Chicago Materials Research Science and Engineering Center (MRSEC).

I am deeply grateful for the constant support and understanding from my loving family. Thank you to my wife Jie Hou for your patient and persistent support throughout my

graduate studies.

ABSTRACT

The understanding of quantum many-body physics is the key to develop new quantum technologies including novel quantum materials, high-precision sensors, and quantum computers. However, understanding the general quantum many-body physics is extremely difficult, particularly when such systems are driven far from an equilibrium state. Ultracold atoms, a clean, fully controllable, and coherent quantum many-body systems can provide useful insights into the fundamental properties of quantum matter. This thesis discusses experiments on studying nonequilibrium dynamics in driven ultracold bosonic atoms with fantastic static and dynamical controls of the inter-particle interactions through Feshbach resonances and external trapping potentials using optical lattices and digital micromirror device (DMD).

With this versatile apparatus, we first study the critical dynamics across a quantum phase transition in shaken optical lattices. Across a ferromagnetic transition where the $\mathbb{Z}_2$ inversion symmetry is broken, we are interested in how the system evolves toward the new ground states generally with a different symmetry. Utilizing the phase imprinting technique with DMD, we show that the macroscopic coherence is maintained across the phase transition, the system undergoes a coherent population transfer of particles toward lower energy states and quantum fluctuations determine the domain structure but do not destroy the macroscopic coherence.

We then present the complex correlations rising from the matter-wave version of a high-harmonic generation with oscillating interaction. This high-harmonic generation of matterwave is a result of stimulated secondary collisions. The stimulated primary collisions, two condensate atoms collide absorbing one energy quantum from the oscillating field, give rise to the first observation of Bose fireworks. The scattered atoms from the primary collisions can further collide with each other or the ground-state atoms from the condensate and such secondary collisions promote atoms to higher momentum modes. Moreover, we show the density-wave dynamics prior to the jets emission within the condensate with oscillating interactions and explain the asymmetry in the jets emission pattern based on near-field in-

terference. Besides, we further demonstrate the spatial and temporal phase coherence of the emitted jets using matter-wave interference and connect our matter-wave jets emission to the famous Unruh radiation in relativistic physics.

CHAPTER 1

INTRODUCTION

My specific journey of exploring quantum physics starts with ^{87}Rb atoms at room temperature. I investigated the single-particle quantum coherence in a three-level Λ system with electromagnetically-induced transparency (EIT)[38, 39, 72]. Although we had more than 10^{23} atoms in a glass vapor cell, they do not really sense the existence of each other since the thermal de Broglie wavelength of a single atom is more than five orders of magnitude smaller than inter-particle separation at room temperature. At this limit, having more atoms simply means a large signal irrespective of whether they are bosons or fermions. This makes it a great system for us to learn all the interesting properties of a single atom, the basic constituents of matter in our universe.

At extremely low temperature when the thermal de Broglie wavelength of a single atom is comparable with the inter-particle separation, the system enters the realm of quantum many-body physics when quantum statistics start to matter. For bosons, the many-body system transitions to a new phase of matter, called Bose-Einstein condensates (BECs) [3, 28, 86]. BECs exhibits quantum mechanical wave behaviors such as matter-wave interference since the system can stay in a superposition of different momentum states. BECs with weak interaction also manifest superfluidity and flows around obstacles without friction. Meanwhile, atoms in the BEC can still behave like particles and inter-particle collisions create interesting excitations. 'More is different', as suggested by P. W. Anderson [4], at such a macroscopical level entirely new fundamental laws of physics are required to correctly describe the many-body system although we understand everything about its constituents. Developing a fundamental understanding of many-body behavior is an important and challenging goal in modern physics.

Quantum many-body problems such as that with BECs are fundamentally difficult to solve. The resources required to specify a general quantum many-body quantum systems depend exponentially on the number of particles in the system, namely on the number of

degrees of freedom. Although statistical mechanics provides powerful tools to describe the complex and interacting many-body system in equilibrium, understanding the dynamics when a quantum many-body system is brought far away from equilibrium remains challenging.

This thesis focuses on the nonequilibrium dynamics of the weakly interacting ultracold atoms with periodic driving. Recent researches suggest that such a driven quantum system can exhibit interesting behaviors as rich as their static counterparts. Novel nonequilibrium phases of matter, such as time crystals [109, 21], that are normally forbidden in equilibrium can be realized in a periodically driven system. Typically we expect a driven quantum system to absorb energy from its driving field and eventually heats up to an infinite temperature state. Surprisingly the quantum coherence persists for a long period of time in such a periodically driven system irrespective to the heating effect from driving. This quantum coherent dynamics is the focus of the experimental studies presented in this thesis.

We explore the nonequilibrium physics in BECs with two different driving techniques: the coherent critical dynamics across a quantum phase transition in shaken optical lattices and the collective emission of matter-wave jets with oscillating interactions between particles. This thesis is organized as follows: In Ch. 2, we describe the important features of the experimental apparatus that we use to produce ultracold atoms. Most importantly the improvement of the systems and driving techniques that is essential to the studies in this thesis. In Ch. 3 we present an overview of the Floquet theory in shaken optical lattices and two-mode squeezing in matter-wave jet emission. In Ch. 4, we present the coherent inflationary dynamics when BECs are driven across a $\mathbb{Z}_2$ quantum phase transition. Here the system evolves toward the new ground states with macroscopic coherence extending beyond the domain size that seeded by the quantum fluctuations. In Ch. 5, we present the high-harmonic generation of matter-wave jets that results from the stimulated secondary collisions. Here we have developed a new pattern recognition algorithm to comprehensively show the correlations between emitted matter-wave jets. In Ch. 6, we show the density-

wave dynamics prior to the formation of matter-wave jets within the BECs and provide an intuitive explanation to the asymmetry of jets emission observed in the near-field limit. In Ch. 7, we demonstrate spatial and temporal phase coherence of the emitted matter-wave jets. Meanwhile, we show that the two-mode squeezing process during the matter-wave emission can be used to simulate Rindler frame transformation and hence connect the Bose fireworks to the famous Unruh radiation in relativistic physics. At last in Ch. 8, we discuss many interesting future directions in studying coherent nonequilibrium dynamics with preliminary results in our experiment.

CHAPTER 2

SYSTEM

The apparatus, which creates ultracold cesium atoms, is an extremely robust and versatile system. The cooling lasers and science chamber are set up on two separate stable optical tables and all of the lasers are delivered to atoms via optical fibers. This isolation between the two systems brings great convenience to daily operation and maintenance. We produce ultracold atoms in one, two, or three dimensions with different setups of optical dipole traps. We detect the atomic gas with a high-resolution imaging system based on resonant absorption of light by atoms. We are also able to project arbitrary, dynamical potentials onto the atoms using a digital micromirror device (DMD). Besides, we can actively correct the potentials based on absorption images, creating trapping potentials such as a homogeneous box. Most importantly, we can control the interaction between atoms using the magnetic field or optical field through the Feshbach resonances. A lot of these great features are inherited from the previous generations of outstanding colleagues and the details are comprehensively discussed in their theses [56, 111, 46, 22]. In this chapter, we summarize the important features of the system and some of the technical improvements we implemented.

2.1 General setup for cooling and trapping of BEC

Our experiments start with laser cooling and trapping of ^{133}Cs atoms. We first heat the oven with cesium atoms to 60°C creating a large flux of atoms into the Zeeman slower. The atoms are later decelerated by a counter-propagating laser in a spatially varying magnetic field. We then trap the atoms in a Magneto-Optical Trap (MOT). Following MOT, we perform brief durations of compressed MOT and molasses cooling. Afterward, we load atoms into a three-dimensional optical lattice to perform degenerate Raman Sideband Cooling (dRSC) and obtain roughly 6,000,000∼8,000,000 atoms at ∼3 μK. We further switch to a cigar-shaped elliptical dipole trap and evaporatively cool our atoms to a Bose-Einstein condensate of

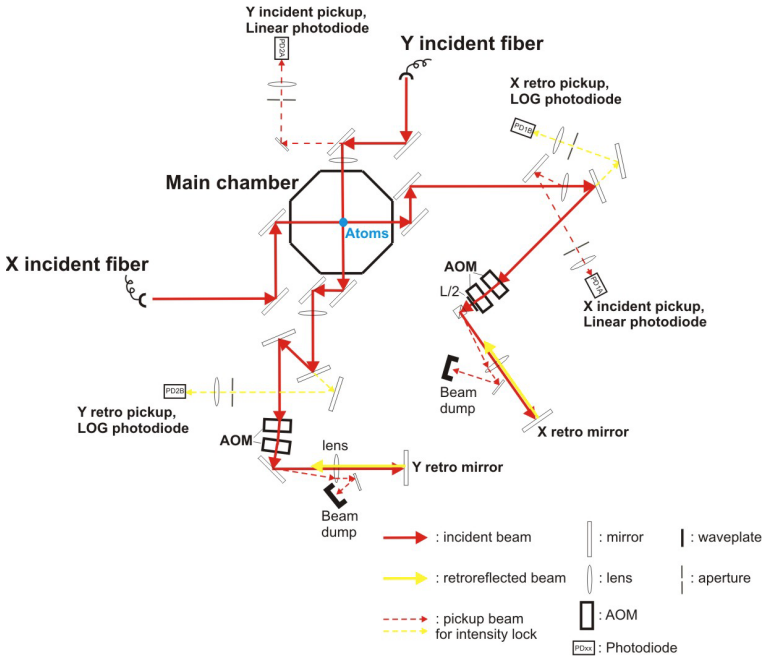

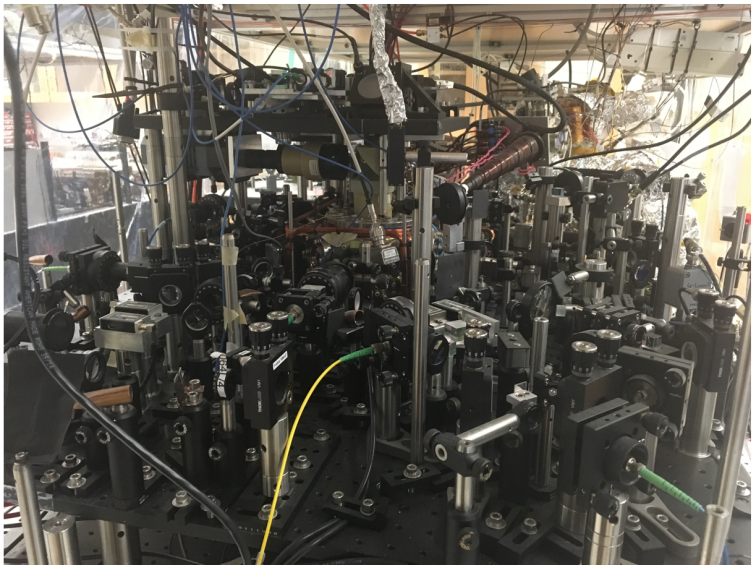

Figure 2.1: **Overview of the apparatus.** Top: A top-down view of the arrangement of the dipole trap beams, the retro-reflections for forming horizontal optical lattices. This figure is regenerated from Ref. [111]. Bottom: A side view of the experimental apparatus.

.

typically 30,000∼120,000 atoms at ∼10 nK [56, 111, 46, 22]. After the evaporative cooling, we transfer the atoms into different trapping potentials depending on the type of experiments, such as optical lattices in Ch. 4 and box potential in Ch. 5.

The cigar-shaped dipole trap is formed by three intense 1064 nm laser beams from a Mephisto Mopa laser, which we recently upgrade its output power to 25 W. The laser beam, propagating along the x-axis (y-axis), has a round-shaped beam profile and provide dipole trap for atoms along the y-axis (x-axis) and we call it XDT (YDT) beam. XDT and YDT beams together form a cross dipole trap and play an important role in loading atoms from the dRSC stage for later evaporation. A third laser beam (ZDT) propagating at 45° angle has an elliptical intensity profile and primary vertical confinement in the z-axis. This ZDT beam is more tightly focused and provides strong horizontal trapping in the xy-plane as well.Combing XDT, YDT and ZDT beams, we make a cigar-shaped trap with typical trapping frequency of $(\omega_x, \omega_y, \omega_z) = 2\pi\times(12,30,70)$ Hz, making the profile of the BEC highly elliptical.

We make optical lattices by retro-reflating the XDT and YDT beams. Each of the retro-reflected laser beams is controlled by a pair of acoustic-optical modulators (AOM) driven by radio frequency (RF) wave. The AOMs are set up in a way that retro-reflected beams are maximally suppressed when the RF wave is turned off. By tuning the power of the RF wave, we adjust the power of the retro-reflected beams. The retro-reflected beams interfere with the original dipole trap beams to form optical lattices with lattice spacing $d = 532$ nm. The corresponding lattice momentum is $q_L = \hbar k_L$ with wavenumber $k_L = \pi/d$. In the rest of the thesis, we use q_L and k_L interchangeable to refer to momentum in our system since their difference is only the Planck constant $\hbar$. We also defined a recoil energy $E_R = \hbar^2 k_L^2/2m$ as the kinetic energy that atoms gain when they scatter lattice photon.

We can shake the lattice by modulating the phase of the RF wave to the second AMO sinusoidally as $\theta(t) = \theta_0 \sin(\omega_m t)$ with ω_m the modulation frequency and θ_0 the modulation amplitude. The jth order diffracted beam from the AOM is phase shifted accordingly by $j(ft + \theta(t))$ with respect to the 0'th order beam from a single pass, where f is the carrier

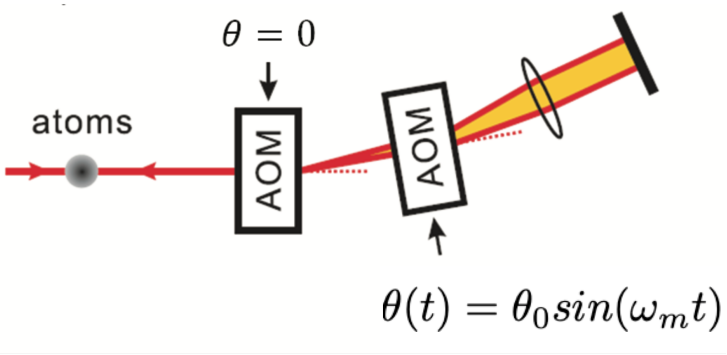

Figure 2.2: **Setup of acoustic-optical modulators (AOMs) to form optical lattices.** Optical lattices along both the $x-$ and $y-$axis can be formed by retroflecting the the corresponding dipole trap beam with lattice period $d = 532$ nm. The depth and phase of the optical lattice can be controlled using the AOMs. We use the -1 diffraction order of one AOM and +1 order of the other so that there is not frequency shift between the dipole trap beam and its retroflection. Lattice shaking can be achieved by modulating the phase of the RF wave with $\theta(t) = \theta_0 \sin(\omega_m t)$ with ω_m the modulation frequency and θ_0 the modulation amplitude. The figure is regenerated from Ref. [24].

.

frequency of RF wave. In our setup, the retroreflected beam passes the first AOM twice as -1 order and the second AOM twice as +1 order. The two AOMs are driven by the RF waves from the same source and we only perform phase modulation on the second AOM. As a result, the phase of the retro-reflected beam is shifted by $\phi(t) = 2(ft + \theta(t) - ft) = 2\theta(t)$. The lattice is correspondingly displaced by $\Delta x(t) = \frac{s}{2}\sin(\omega_m t)$ with shaking amplitude $s = 2\frac{\theta_0}{\pi}d$.

In this thesis, we normally transfer our atoms to the dipole traps with much tighter confinement in the vertical direction while small but symmetric confinement in the horizontal direction to form a more circular sample. This dipole trap is realized by taking advantage of the vertical lattice beams. Here two beams, split vertically from the same 1064 nm laser, interfere with each other at an angle of 16° producing an optical lattice with a spacing of $\sim$3.8 μm along the z-axis. The horizontal trapping from this lattice is negligible. We load all of our atoms from the cigar-shaped trap to a single site of the lattice by carefully tuning the power of the ZDT beam and magnetic field gradient during the transfer. Finally, the ZDT beam is fully turned off and the vertical confinement is only given by the lattice

with a typical trapping frequency of $\omega_z = 200$ Hz and a depth of $h\times 500$ Hz. If we wish to further compress the trap to get an effective two-dimensional gas, the vertical trapping can be further increased to a maximum of $\omega_z = 2$ kHz, far beyond the typical chemical potential or temperature of the gas [56, 111, 46].

2.2 Control of the interaction

The interaction between ultracold atoms is normally through s-wave scattering, characterized by the scattering length a. If we only focus on low energy and long wavelength physics, the interaction between atoms can be approximated by the Fermi pseudo-potential,

$$V(\mathbf{r}) = g\delta(\mathbf{r}), \tag{2.1}$$

with $\delta(\mathbf{r})$ the Dirac delta function. The interaction strength g can be parametrized using s-wave scattering length a, which is given by

$$g = \frac{4\pi\hbar^2 a}{m}. \tag{2.2}$$

For positive scattering length $a > 0$, the interaction is repulsive. For negtiave scattering length $a < 0$, the interaction is attractive.

In ultracold atoms, this scattering length can be tuned using the Feshbach resonance [20]. Near Feshbach resonance, the scattering length can be easily adjusted to any desired value by simply changing the magnetic field. This resonance happens at the magnetic field B_0 when a two-atom bound state in a closed scattering channel approaches the state of free atoms in an open channel. The scattering length as a function of the magnetic field B has the form of

$$a(B) = a_{bg}\left(1 - \frac{\Delta}{B - B_0}\right) \tag{2.3}$$

with a_{bg} the background scattering length far from the resonance and Δ the width of the res-

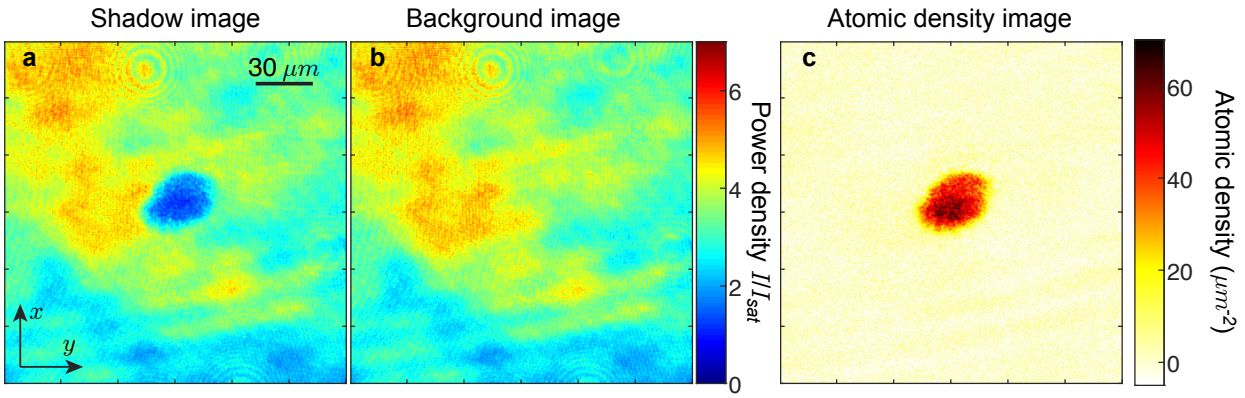

Figure 2.3: **Saturated *in situ* absorption imaging. a** The shadow image of atoms taken after 20 μs exposure to the imaging laser beam.**a** The background image is taken without atoms after 20 μs exposure to the imaging laser beam. **C** The column density image of atoms extracted from the combined optical density image.

.

onance. In our experiment, we frequently make use of the Feshbach resonance at $B_0 = 11.7$ G with the width $\Delta = 28.7$ G and the background scattering length $a_{bg} = 1720a_0$. Here a_0 is the Bohr radius.

2.3 Imaging of atoms

2.3.1 in situ imaging

In our experiment, the scattered light is collected to the CCD camera by an objective lens. In the primary vertical direction, we have a high-resolution objective with a large numerical aperture NA = 0.5, which locates less than one inch from the atoms. The magnification is 21.5 in the vertical imaging setup and 1 pixel in the camera corresponds to 0.606 μm in the atom plane. Here we can achieve a typical aberration limited resolution of 1.4 μm. In the auxiliary horizontal direction, the objective is approximately 10 inches away from the atoms. The magnification is only 1.2 and the resolution is 10.8 μm limited by the CCP pixel size. We typically image our atoms in the vertical direction and only uses the horizontal for diagnostic purposes.

Strong saturation absorption imaging is the base of all imaging techniques in our experiment. Here cesium atoms are illuminated with a laser beam resonant to the transition from $F = 4$ to $F' = 5$ with the intensity much larger than the saturation intensity, $I \gg I_{sat}$. This intense imaging beam is pulsed on for a short period of 20 μs to make an observation of the instantaneous status of the atomic gas. The CCD camera captures the spatial intensity distribution of the laser in the image plane. With the atoms, we have a shadow image with an intensity distribution of $I_{out}(\mathbf{r})$. Here we define $\mathbf{r} = (x, y)$ in the image plane. Without the atoms, we get the original distribution of the imaging beam $I_{in}(\mathbf{r})$. Based on Beer-Lambert law, the measured atomic density distribution is given by

$$n_{meas}(\mathbf{r}) = \frac{1}{\sigma_0}\left[\frac{I_{in}(\mathbf{r}) - I_{out}(\mathbf{r})}{I_{sat}} - \ln(\frac{I_{out}(\mathbf{r})}{I_{in}(\mathbf{r})})\right], \tag{2.4}$$

with σ_0 the resonance scattering cross section (Fig. 2.3). This measured atomic density is a result of the real atomic density distribution convoluted with the resolution of the imaging system. The resolution of the imaging systems is characterized by points spread function $P(\mathbf{r})$ [56, 46]. The measured atomic density is given by

$$n_{meas}(\mathbf{r}) = \int d\mathbf{r}' n(\mathbf{r}') P(\mathbf{r} - \mathbf{r}'), \tag{2.5}$$

where $n(\mathbf{r})$ is the real atomic density distribution. If the point spread function is simply a Delta function, the measured density is the real atomic density. With finite but spatially narrow point spread function, the measured density is still a good approximation to the atomic density.

In our experiment, we characterize the point spread function by measuring the modulation transfer function (MTF) $M(k) = |\tilde{P}(k)|$ with $\tilde{P}(k)$ the Fourier transform of the point spread function [56]. This MTF can be calculated from the measurement of the density fluctuation

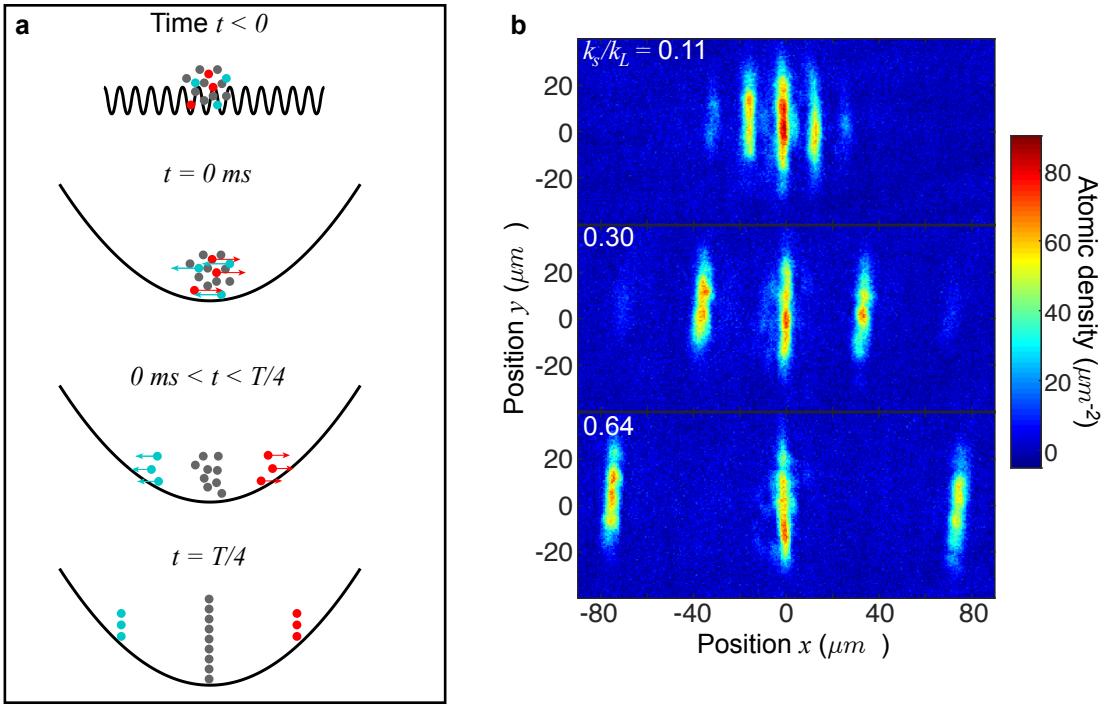

Figure 2.4: **Time-of-flight imaging with focusing.** **a** Atoms with different initial momentum $\pm k_s$ focus on different positions in the trap after a quarter of the trapping period. **b** Example images after time the time-of-flight with the focus in a harmonic trap along the x-axis after momentum seeding. We pulse on an optical lattice with lattice momentum k_s, which is projected from a DMD device. This pulse partially transfers the condensates to $\pm nk_s$ momentum states with integer n = 0,1,2... These images provide a calibration to the imaging.

power spectrum of a thermal gas, which is given by

$$M^2(k) = \frac{|\langle \delta n_{meas}(k) \rangle|^2}{NS(k)}, \tag{2.6}$$

where N is the total number of atoms and $S(k)$ is the structure factor. For hot enough thermal gas, the structure factor can be safely approximated to $S(k) = 1$. As a result, the MTF is simply given by the power spectrum, $M(k) = \sqrt{\frac{|\langle \delta n_{meas}(k) \rangle|^2}{N}}$.

2.3.2 Time-of-flight imaging with focus

Beside detecting atomic density in real space, we can also measure atomic distribution in momentum space after a time-of-flight (TOF). By releasing the atoms into free space, the atomic density distribution in momentum space can be measured after a long time-of-flight. In our experiment, we perform the TOF imaging with an additional focus to further improve momentum space resolution with a harmonic trap [97]. The principle of this method is intuitively illustrated in Fig. 2.4. Consider atoms with momentum q are suddenly released to the center of a harmonic trap in x-axis. The atoms oscillate in the harmonic trap with its position relative to the trap center $x(t) = \frac{q}{m\omega}\sin(\omega_x t)$. After a quarter of the trapping period $T = \frac{2\pi}{\omega_x}$, the initial momentum q relates to the position of the atoms by $q = m\omega x(T/4)$. Therefore, atoms with different initial momentum focus on different positions in the trap as shown in Fig. 2.5. More intuitively, we can regard this harmonic trap to atoms as a lens to a beam of light in Fourier optics. Like a lens, the harmonic trap transforms real space wavefunction to the momentum space.

To implement this imaging technique, we first reduce the scattering length to zero by switching the magnetic field right before time-of-flight to avoid atom collisions. At the same time, we increase the magnetic field gradient to properly levitated the atoms into our imaging plane while we turn off the dipole traps. During time-of-flight, all the dipole traps are turned off except the focusing trap along the x-axis (XDT beam). By carefully tuning the intensity of the dipole beam, we are able to focus the atoms in the same momentum state into a sharp peak after a quarter of the trapping period of 60 ms. The calibration of the imaging technique is shown in Fig. 2.5. We first pulse on an optical lattice with lattice momentum k_s before TOF, which is projected from a DMD device. This pulse partially transfers the condensates to $\pm nk_s$ momentum states with integer $n = 0,1,2...$ After the TOF, we extract the position of every visible momentum peak and obtain a mapping between momentum to position. With this technique, we achieve a resolution in the momentum space to $\delta k = 0.08\ k_L$, only limited by the anharmonicity of our trap. Based on the same principle, we can

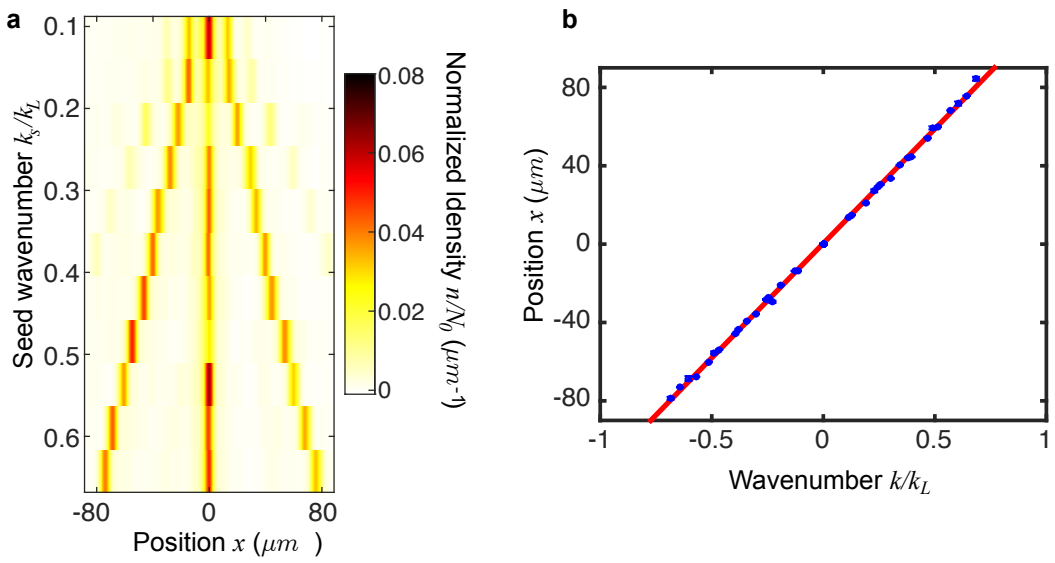

Figure 2.5: **Calibration of momentum in time-of-flight imaging. a** Integrated density distribution of momentum-seeded condensates after the time-of-flight with focus, $n(x) = \int dyn(x, y)$ with different seed momentum k_s. **b** The position of the density peaks as a function of their corresponding momentum. Blue dots indicate experimental data and red solid line is a linear fit the the data.

also turn on the harmonic trap along the y-axis at the same time to perform a time-of-flight in a two-dimensional harmonic trap. This two-dimensional imaging technique is utilized in Ch. 5 and Ch. 7.

2.3.3 Domain reconstruction imaging in shaken lattice

Imaging techniques described in Sec. 2.3.1 and 2.3.2 are generally applicable to both the shaken lattice experiments and the experiments with oscillating interaction. The domain reconstruction imaging in this section is a special case that can be only applied in shaken lattice when the system form domains in the effective ferromagnetic phase (see Ch. 3). The pseudo-spin up (down) domains in our experiments correspond to positive (negative) quasi-momentum states. The purpose of domain reconstruction is to obtain the spatial quasi-momentum distribution after a very short TOF. The previous study shows that atomic density distributions among the Bragg peaks after a short TOF can be used to reconstruct

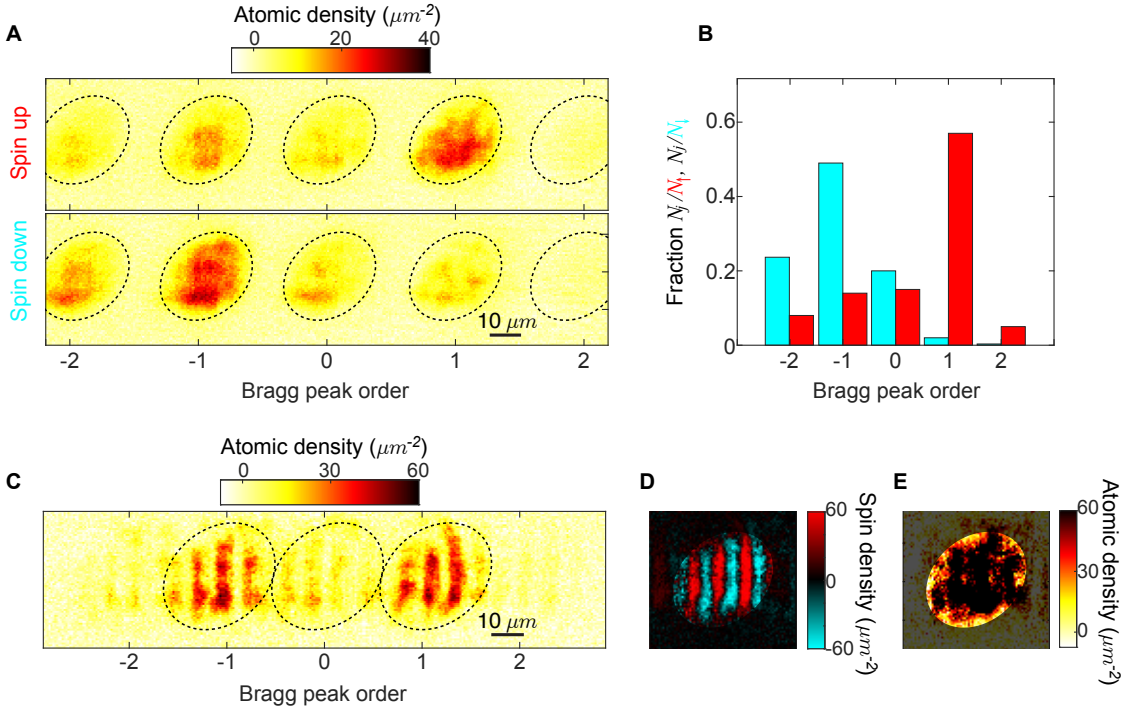

Figure 2.6: **Domain reconstruction imaging.** To detect different the pseudo-spin states in a shaken optical lattice in a ferromagnetic phase, we rapidly increase the shaking amplitude over 0.5 ms before a TOF with a duration of 3 ms. The images shown here correspond to the lattice depth $V = 8.9\ E_R$, the shaking frequency $\omega_m = 8.0$ kHz and amplitude $s = 25$ nm right before amplification. **a** Sample TOF images showing occupation of each Bragg peak with all of the atoms in pseudo-spin up (top) or down (bottom). For these images, we use a longer TOF lasting 5 ms to clearly distinguish each Bragg peaks and use extracted fractional occupation as a calibration. Here each spin predominantly occupies a different Bragg peak. **b** We show the fraction of atom number N_j/N_t in each Bragg peak for the spin up (red) and down (cyan), with N_j the atoms number in the jth Bragg peak and N_t the total atom number. **c** A example image of the density distribution after 3 ms TOF with amplification for condensate in the ferromagnetic phase. The ellipses mark the two dominant Bragg peaks. textbfd The reconstructed domain image based on the fractions in panel **b**. **e** The reconstructed overall atomic density image.

the pseudo-spin domain structure after a short TOF [46]. However, the distortion during the expansion of the gas limits the resolution of fine domains.

A significant improvement is achieved by adding an additional amplification stage [22]. During this amplification, the shaking amplitude is rapidly increased by as much as a factor of 15 over 0.5 ms. By carefully choosing the final shaking amplitude and timing based on the shaking amplitude right before the amplification, this fast ramp excites the atoms to the second excited energy band without changing their quasi-momentums. After a brief TOF, atoms with positive (negative) quasi-momentum mostly appear in the +1(-1) Bragg peak, making it much easier to spatially distinguish the negative and positive momentum atoms.

To apply this imaging technique, we first bias all the atoms to the same pseudo-spin (finite quasi-momentum state) and take TOF images of condensates (Fig. 2.6**a**). We use these images to calibrate the projection of each pseudo-spin state onto Bragg peaks (Fig. 2.6**b**). Therefore, we can reconstruct the domain image based on this calibration for a condensate with arbitrary domains (Fig. 2.6**c** and **d**).

2.4 Fixing fringes in dipole trap

During the effective ferromagnetic quantum phase transition, we identified two types of systematic noises that biasing the domain formation. These two technical noise cause an offset of the initial velocity of the condensate leading to an artificial symmetry breaking. As a result, the most of the atoms become complete pseudo-spin up or down instead of forming domains as we drive the system across the critical point at a finite speed. The most dominant source is the fringes in the YDT beam path. In our experiment, the YDT beam is delivered to our system via an optical fiber. The beam propagates forward and passes the atoms. It is then retroreflected and interferes with the forward-propagating beam forming the optical lattices. The issue is that the retroreflected beam is reflected by the fiber tip once more and interferes with the forward-propagating beam at a small angle producing fringes with a large spacing of 37 μm. These fringes drift due to thermal effects and offset of the initial velocity

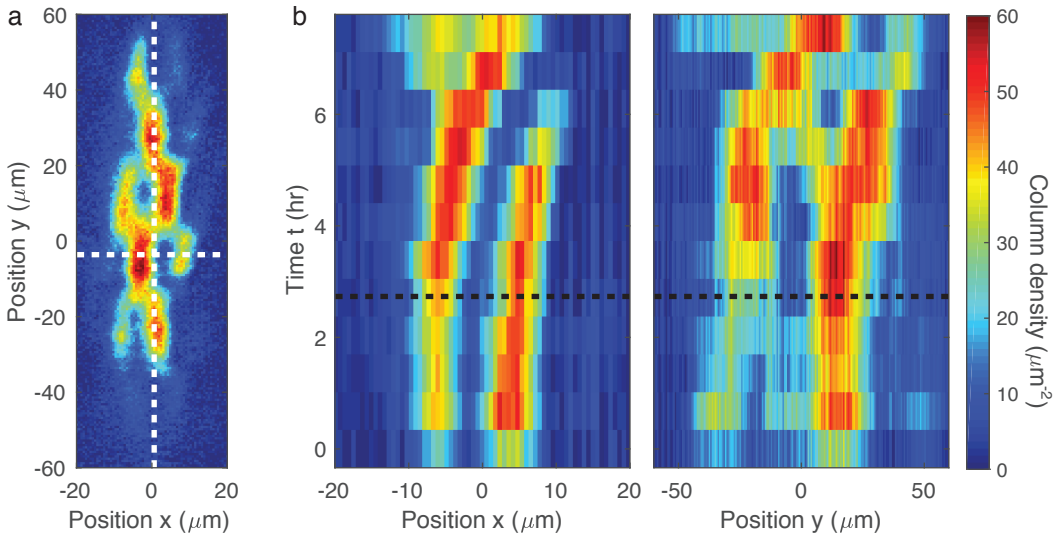

Figure 2.7: **Moving fringes from XDT beam.** **a** Condensate atoms trapped in the XDT trap shows fringes in the beam path based Thomas-Fermi approximation. Here the vertical lattice trap is also turn on giving a very thin sample along the vertical direction. The scattering length between atoms are tuned to $41a_0$. The white dashed lines indicates cuts shown in panel **b**. **b** Motion of the fringes can be seen from the horizontal (left) and vertical (right) cut of the image in **a** due to thermal drift. The black dashed lines indicate the moment when the main field coil is switched on, which is the major heating source in our system. The fringes are initially stationary but quickly drift as soon as we turn on the coils.

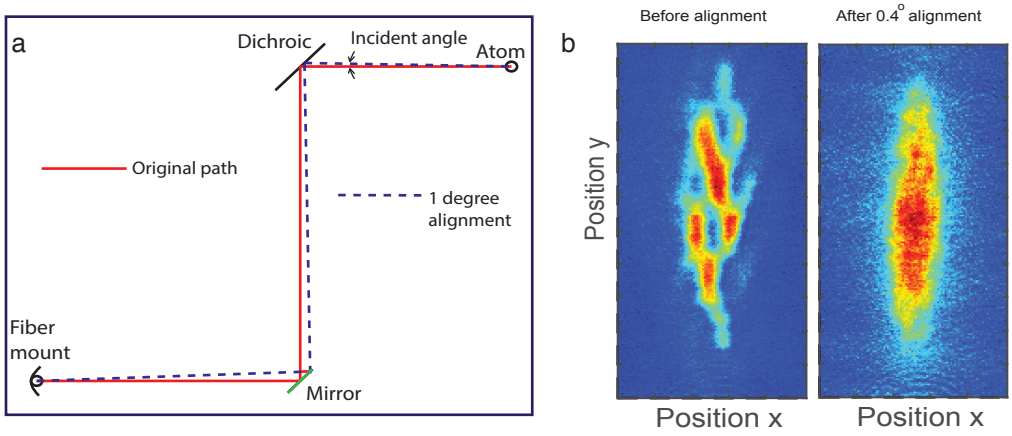

Figure 2.8: **Eliminating fringes from XDT beam: Part I. a** Our setup only allows us to adjust the incident angle of the XDT beam by less than 1°. We change both the fiber mount and a mirror together to change the incident angle while keeping the atoms at the same location on the camera.**b** After 0.4° adjustment of the incident angle, the fringes are greatly reduced. The scattering length is set to be $41a_0$.

of the condensate. This scenario is thoroughly addressed in Ref. [22].

Another minor source of the noise is the fringes in the XDT beam path. In this beam path, we install an optical isolator at the fiber output to eliminate any reflection due to the fiber tip. However, we still get the checkerboard-like fringes with large spacing drifts as the system warms up after running the main magnetic field coil (our magnetic field coils are not subjected to water cooling and is the major heating source). These fringes are detected by loading atoms only to the XDT trap and changing the scattering length to a small positive value based on Thomas-Fermi approximation, $n(\mathbf{r}) = \sqrt{\frac{\mu - V(\mathbf{r})}{g}}$. As a result, the local density corrugation captures the weak trapping potential from the fringes. We later find that these fringes result from the interference between the main beam and the weak reflections from the window of the science chamber.

The XDT beam is initially aligned near perpendicular the surface of the window. As a result, window reflections can easily overlap the main beam and interfere. To eliminate the fringes, we thus need to tilt the incident angle of the XDT beam. However, we still would like to keep the atoms at the same location. To do so, we adjust the fiber mount and the

mirror together to change the incident angle while keeping the atoms at the same location on the camera (see Fig. 2.8). After 0.4° adjustment of the incident angle, the fringes are greatly reduced at $40a_0$.

To improve the sensitivity and perform further improvement, we reduce the scattering length to even lower value of $17a_0$. We see much weaker features showing the remnants of the fringes. Fourier transformation of the atom images is shown in Fig. 2.9, where we can clearly see two peaks (peak 1 and 2) indicating two sets of fringes roughly along the diagonal and off-diagonal directions (Although the images show four peaks, only two of them contains non-redundant information due to inversion symmetry of the Fourier transform). Peak 2 reduces as we continue to increasing the incident angle. Peak 1 reduces at the beginning but increases as we further increase the incident angle. This observation suggests that the diagonal and the off-diagonal fringes are due to reflections from different surfaces. At last, we choose the incident angle at which the overall fringes are minimized.

2.5 Aberration in DMD projection

In Chin Lab, we use a digital micromirror device (DMD) to project arbitrary repulsive potential to our atoms (see Fig. 2.10). The DMD is an array of micromirrors and each micromirror can be controlled by a computer to orient at either of the "on-state" angle or "off-state" angle, which are separated by 24°. We shine a blue-detuned 788 nm laser beam on the DMD and the on-state mirrors direct the light to the atoms while the off-state mirrors reflect light into a beam dump. The specific DMD we use is DLP3000 with 608×684 pixels with each pixel a square mirror of $7.6\mu m$. This device also supports the dynamical switch of the programmed pattern up to a speed of 4 kHz. We work in the image plane and the pattern on DMD is projected to the atoms through the high-resolution imaging system with an overall demagnification factor of 36 so that pixel length $7.6\mu m$ on DMD corresponds to a length of $0.21\mu m$ on atoms.

One application of the DMD in our experiment is to project dynamical optical lattices and

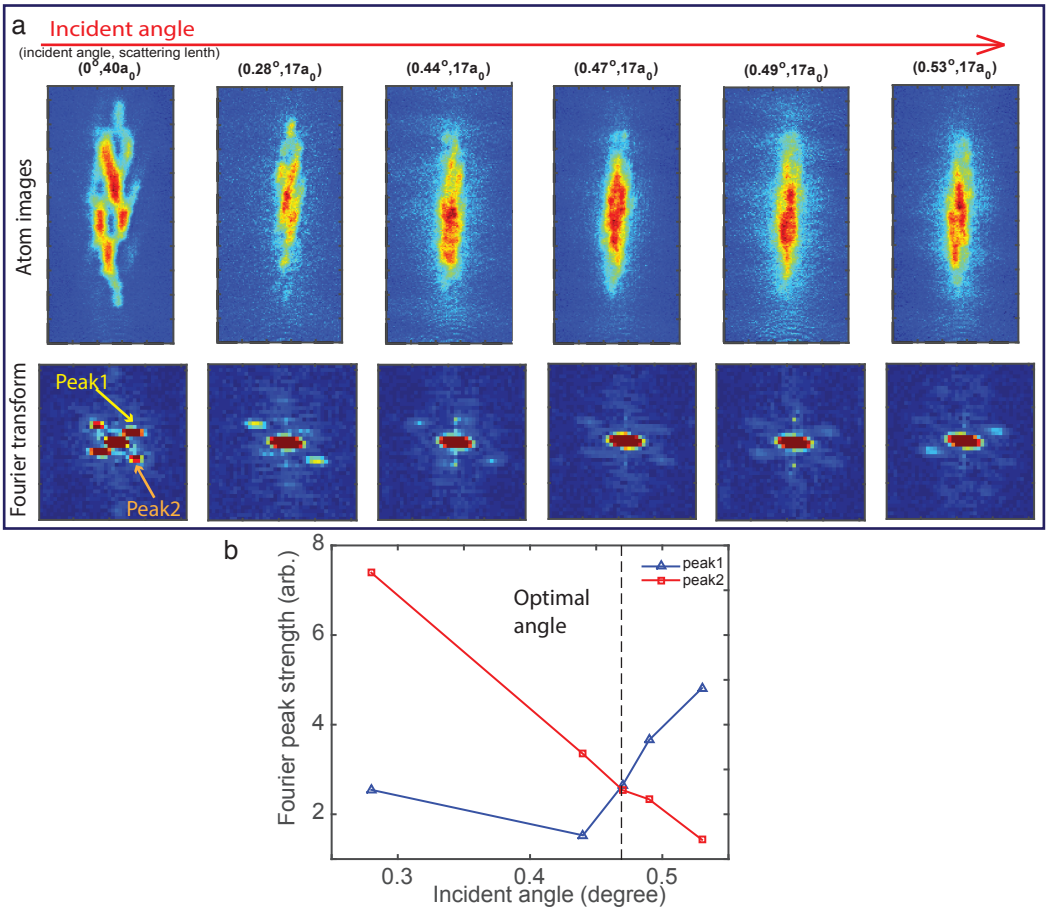

Figure 2.9: **Eliminating fringes from XDT beam: Part II.** By reducing the scattering length to a lower value of $17a_0$, we improve our sensitivity to detect much weaker remnants of the fringes. **a** By performing Fourier transformation of the atomic density image (top), we see two sets of fringes indicated by peak 1 and 2 in Fourier amplitudes (bottom). **b** The different dependance of the peak value on incident angle suggests that the two sets of fringes are likely caused by reflections from different surface. We finally pick an optimal angle at $0.47°$.

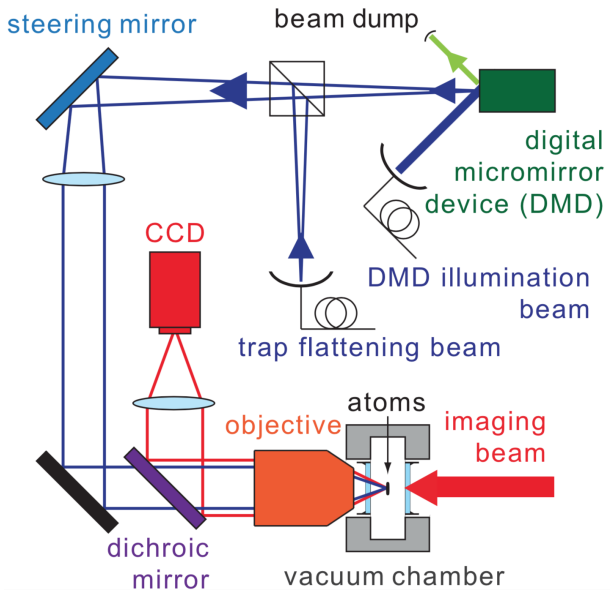

Figure 2.10: **Setup of digital micromirror device (DMD).** A schematic of the DMD integrated in the vertical high-resolution imaging path in our apparatus. The figure is regenerated from Ref. [24].

.

perform Bragg spectroscopy [46]. Another application is to form arbitrary dipole traps with fine details for the atoms. Precise control of such optical potential can be achieved using feedback from images of atoms. The trapping potential can be inferred from the atomic density of Bose condensates. This information is further transferred to the computer control of the DMD. Therefore the projected DMD pattern can be further improved. However, the precision of the control is limited by the aberration of the projection.

We can characterize the aberrations by measuring the phase shift profile $\Theta(\mathbf{k})$ for different projection wavenumber $\mathbf{k}$ in the atom plane. Ideally, within the resolution of an imaging system, the phase shift is uniform for any transverse wavenumber $\mathbf{k}$. However, any tiny misalignment and imperfections cause wavenumber dependent phase shift. In our experiment, we can characterize this phase shift by projecting static optical lattices to atoms. A programmed lattice on DMD scatters light into different orders, $\mathbf{k}_0$ and $\mathbf{k}_0 \pm \mathbf{k}$. By blocking the $\mathbf{k}_0 \pm \mathbf{k}$ order, the projected lattice at atom plane reflects the phase shift between the $\mathbf{k}_0 \mp \mathbf{k}$ order and $\mathbf{k}_0$ (see Fig. 2.11**a**). This projected lattice potential is thus reflected in the

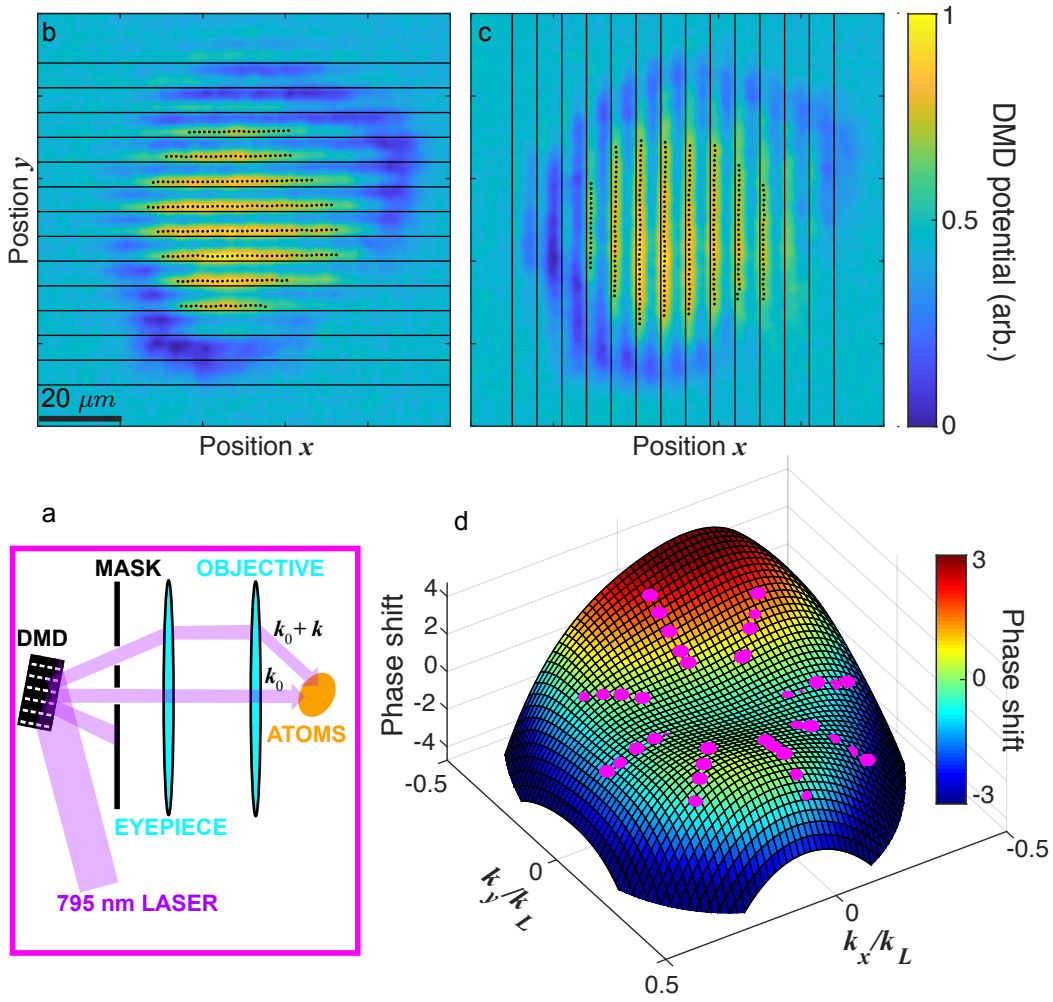

Figure 2.11: **Aberration in DMD projection.** **a** Illustration of the setup for measuring phase shift between the zeroth order then +1 order of the diffracted beam from the programed lattice on DMD with wavenumber **k**. **b** and **c** are examples of the projected lattice potential along y- and x-axis in atom plane. The solid lines mark the position of the lattice without aberrations and the dots mark the position of the projected lattice. **d** The extracted phase shift $\Theta(\mathbf{k})$.

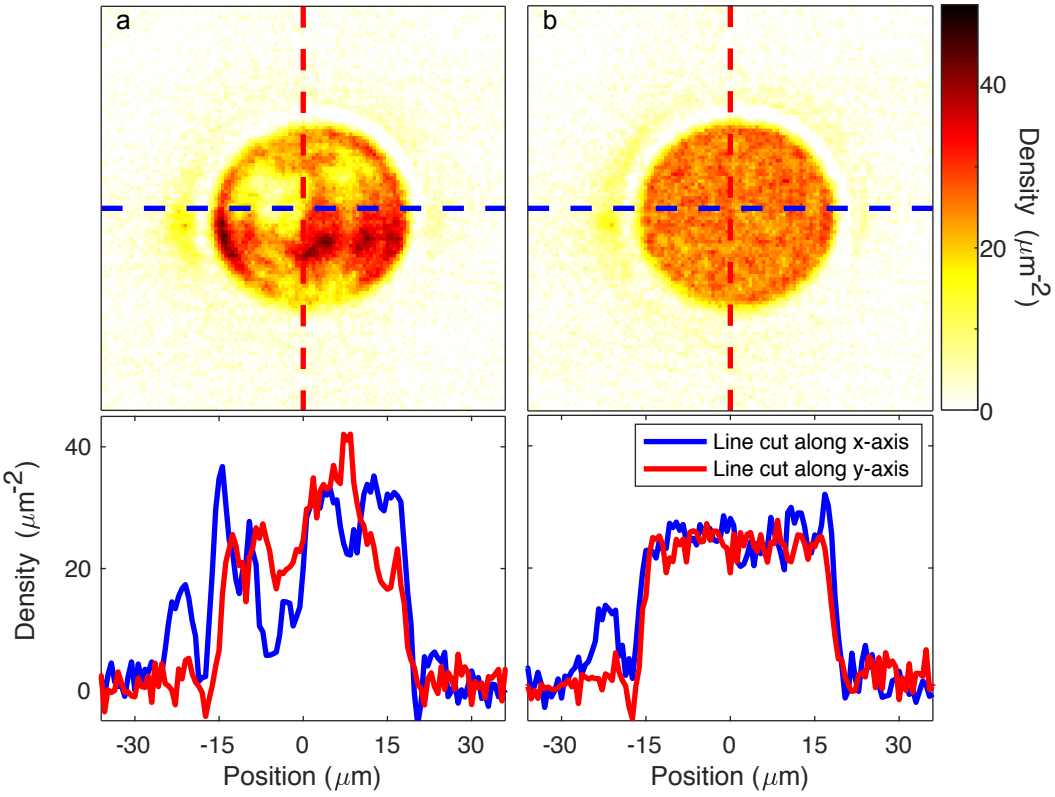

Figure 2.12: **BEC with flat density profile.** The BEC is initially prepared in XDT, YDT and ZDT cross dipole traps. **a** Density profile of BEC when a round-box trap with the initial guess for compensating the harmonic potential. **b** Density profile of BEC after iterations of correction on the DMD potential based on feedback from atomic density. The radius of the round-box trap is 11.7 μm. The total number of atoms trapped in the box is approximately 25,000. The scattering length between atoms is set to $40a_0$. The top panels show the two-dimensional density profile and the bottom panels show the line cuts along the corresponding colored dashed lines.

density profile of the condensates. Taking a differential measurement (measure the difference between the density profile of condensates with and without the projected lattice), we can cleanly extract the phase shift (see Fig. 2.11**b** and **c** for examples). In all the measurement the center position of the programmed lattice pattern is the same and thus the phase of the zeroth order beam $\mathbf{k}_0$ is fixed. Therefore we can comprehensively obtain the aberration of the projection (see Fig. 2.11**d**). The best approach to fix this issue is to use adaptive optics to compensate for the phase shift. Currently, we attempt to phase shift the programmed pattern on DMD to remove the effect from aberrations instead.

Without the phase shift information and the corresponding compensation of the DMD, the feedback control over optical potential always gives fine fringes along the direction with maximal phase aberration. As we implement the phase compensation on DMD by phase shifting the corresponding Fourier modes by $-\Theta(\mathbf{k})$, we can thus achieve very precise control. One example is shown in Fig. 2.12, where we use DMD to project a potential to cancel the horizontal harmonic trap producing a flat density profile for BEC. From the spatial fluctuation of the density profile, we can estimate the standard deviation of the potential fluctuation to be approximately 0.2 nK.

CHAPTER 3

DRIVEN BOSE-EINSTEIN CONDENSATES

Ultracold atom is a well-known great platform to perform the quantum simulation. In order to simulate different physics, careful engineering is required. Floquet engineering is a widely implemented technique in ultracold atoms to shape the original Hamiltonian to that as designed by periodically driving the system. In this chapter, we present two methods in our system to coherently drive the Bose condensates as to modify the behavior of atoms at both the single-particle level and interacting many-body level. Particularly, by shaking the optical lattices, we can create novel single-particle dispersion from the hybridization of various bands in the original static lattice; by modulating inter-particle interactions, we can enable inelastic collisions which are normally forbidden due to energy conservation. In the following sections, we give an introduction to both of the driving methods and review the interesting physics that have been investigated before the experiments in this thesis in our system.

3.1 Shaken optical lattice

3.1.1 Optical lattices and band structure

Optical lattices can be created by interfering laser beams. For simplicity, we first consider the one-dimensional case where the optical lattices are generated by interfering with two counter-propagating laser beams. These two laser beams thus form a standing wave with the intensity of light varies in space as $I(x) = I_0 \cos^2(k_L x)$, where wavenumber k_L is given by $k_L = 2\pi/\lambda$ with λ the wavelength of the laser beam and I_0 the intensity of the laser beam. Based on a two-level model, this standing wave traps atoms to its node or anti-node depending on whether the laser frequency is blue or red detuned. We thus obtain a periodic

tapping potential given by

$$V(x) = \frac{3\pi c^2}{2\omega_0^3}\frac{\Gamma}{\delta}I(x), \tag{3.1}$$

where c is the speed of light, ω_0 is the resonant transition frequency, Γ is the linewidth of the transition, and δ is the laser detuning from the resonant transition frequency.

The Hamiltonian of a single quantum particle with mass m moving in such a one-dimensional periodic potential that oriented along the x-axis is given by

$$H_0(x) = -\frac{\hbar^2}{2m}\frac{d^2}{dx^2} + \frac{V_0}{2}\cos(2k_L x), \tag{3.2}$$

By introducing the dimensionless energy $u_k = E_k/E_R$, the lattice depth $v = V_0/E_R$, with recoil energy $E_R = \frac{\hbar^2 k_L^2}{2m}$, and the dimensionless coordinate $z = k_L x$, we rewrite the eigenvalue equation as

$$\left(\frac{d^2}{dz^2} + \varepsilon_\kappa - \frac{v}{2}\cos(2z)\right)\varphi(z) = 0 \tag{3.3}$$

with $\varphi(z) = \psi(z/k_L)/\sqrt{k_L}$.

Note that the equation above is the standard form of Mathieu equation and its famous stability chart gives the band structure. Specifically, the stable solution of the form $e^{i\kappa z}u_\kappa(z)$ with characteristic value ε_κ is just the Bloch waves with wavenumber $k = \kappa k_L$, which can be written as

$$\psi_k(x) = e^{ikx}u_k(x), \tag{3.4}$$

where the function $u_k(x)$ inherits the periodicity of the lattice potential $u_k(x) = u_k(x + d)$ with $d = \pi/k_L$ the lattice constant. When we restrain the wavenumber within the first Brillouin zone, the energy bands are simply given by $E_k^{(n)} = \varepsilon_{-|\kappa|-n}E_R$ for even integer n and $E_k^{(n)} = \varepsilon_{|\kappa|-(n+1)}E_R$ for odd n, with $\kappa = k/k_L \in [-1, 1]$. And the corresponding eigenstate wavefunction has the form of $\psi_k^{(n)}(x) = e^{ikx}u_k^{(n)}(x)$.

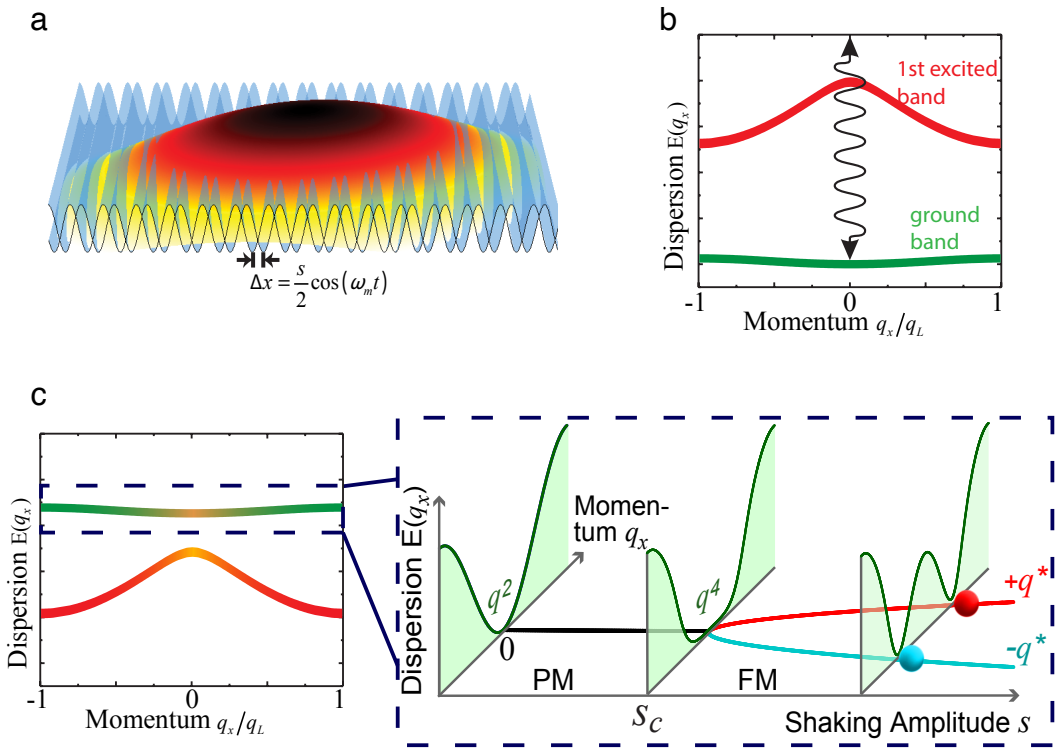

Figure 3.1: **One-dimensional lattice shaking and band structure. a** Lattice shaking by periodically translating lattice back and forth with a shaking amplitude s and shaking frequency ω_m. **b** We choose a near-resonant shaking frequency that is slightly blue detuned from the bandgap at zero momentum. **c** Such choice of shaking parameters allows a significant mix of the excited band to the ground band in which the condensates are initially prepared. The ground band starts with the single minimum at zero momentum at $s = 0$ nm and flattens as we increase the shaking amplitude. After a critical value s_c the single minimum bifurcate into two minimums at finite momentum $\pm q^*$ with $q^* \sim \sqrt{s - s_c}$.

3.1.2 Shaken lattice

We shake the lattice by translating the whole optical lattices back and forth as shown in Fig. 3.1. This periodic translation is implemented by sinusoidally modulating the phase of the RF wave driving the acoustic modulator, shown in Fig. 2.2. Therefore the Hamiltonian is periodic not only in space but also in time, which can be written as

$$H(x,t) = -\frac{\hbar^2}{2m}\frac{d^2}{dx^2} + \frac{V_0}{2}\cos\left(2k_L\left[x + \Delta x(t)\right]\right), \tag{3.5}$$

where the time-dependent displacement $\Delta x(t) = \frac{s}{2}\cos(\omega_m t)$ corresponds to the lattice shaking with the amplitude s at the frequency ω_m. Since the Hamiltonian is time-dependent, we can not simply diagonalize it to obtain the band structure and the eigenstates. Here the eigenstates at time t_1 is not necessary the eigenstates at time t_2. However, it is possible to absorb the time-dependence into the eigenstates themselves and obtain a time-independent effective Hamiltonian using Floquet states.

Before diving into a comprehensive description based on Floquet theory, we first develop an intuitive two-level model. We choose a shaking frequency that is slightly blue-detuned from the band gap between the ground band and the first excited band that is shown in Fig. 3.1**b**. The lattice shaking primarily couples the ground band to the excited state in a perturbation regime where the shaking the shaking amplitude is much smaller than the lattice period, $k_L s \ll 1$. By expanding the shaking lattice potential to the first order, we separate the Hamiltonian of the system and have $H = H_0 + H'$, where the time-dependent perturbation is given by $H' = -\frac{k_L s V_0}{2}\sin(2k_L x)\sin(\omega_m t)$.

In a deep lattice the Bloch waves look very similar to harmonic oscillator states on each lattice site and we can safely approximate the coupling matrix as $\langle\psi_e(k)|H'(t)|\psi_g(k)\rangle \approx -W\sin(\omega_m t)$ with the coupling strength $W = -\frac{k_L s V_0}{\sqrt{2}}\left(\frac{E_R}{V_0}\right)^{1/4}$ independent of wavenumber

k. We thus write the approximate form of the full Hamiltonian as

$$H_{TL} = \begin{bmatrix} E_k^{(1)} & -W\sin(\omega_m t) \\ -W\sin(\omega_m t) & E_k^{(2)} \end{bmatrix}. \tag{3.6}$$

For a two-level model with sinusoidal coupling, we can easlily bring the system into a rotating frame with the transformation $|\tilde{\psi}_g(k)\rangle = |\psi_g(k)\rangle$ and $|\tilde{\psi}_e(k)\rangle = e^{-i\omega_m t}|\psi_e(k)\rangle$. We further ignore the fast rotating terms at frequency $2\omega_m$. As a result, we obtain a time-independent Hamiltonian

$$H_{RWA} = \begin{bmatrix} E_k^{(1)} & W/2 \\ W/2 & E_k^{(2)} - \hbar\omega_m \end{bmatrix}. \tag{3.7}$$

By diagonalizing the Hamiltonian, we the energy of the hybridized bands given by

$$\varepsilon_k^{\pm} = E_k^{(1)} + \frac{\hbar\delta_k \pm \sqrt{\hbar^2\delta_k^2 + W^2}}{2}, \tag{3.8}$$

with the detuning $\delta_k = (E_k^{(2)} - E_1^{(1)})/\hbar - \omega_m$. The corresponding eigenstates are time-dependent in the lab frame,

$$|\psi_{\pm}(k,t)\rangle = \frac{1}{\sqrt{2W'(W' \mp \hbar\delta_k)}}\left(-\frac{\hbar\delta_k \mp W'}{W}|\psi_g(k)\rangle + e^{i\omega_m t}|\psi_e(k)\rangle\right), \tag{3.9}$$

with $W' = \sqrt{\hbar^2\delta_k^2 + W^2}$. It is interesting to note that such eigenstates are actually time periodic, $|\psi_{\pm}(k,t)\rangle = |\psi_{\pm}(k, t + \frac{2\pi}{\omega_m})\rangle$. The time evolution of an arbitrary state is given by $|\psi(k,t)\rangle = a_+ e^{i\varepsilon_k^+ t}|\psi_+(k,t)\rangle + a_- e^{i\varepsilon_k^- t}|\psi_-(k,t)\rangle$ with coefficients $a_{\pm}$ time-independent. In Sec. 3.1.3 we shall see that such states $e^{i\varepsilon_k^{\pm} t}|\psi_{\pm}(k,t)\rangle$ are just examples of the Floquet steady states.

In our experiment, we always prepare our atoms in the zero-momentum state in the ground band of the static lattice. In the perturbation regime desrcibed above, we expect the atoms to stay in the ground band even after the hybridization from lattice shaking. The

effective ground band, which is now ε_k^+ has higher energy because of blue-detuned shaking, results from the interplay between the momentum-dependent detuning δ_k and the normal single-well structure of the unperturbed ground band. Close to the center of the band at $k = 0$, the detuning is small and level repulsion cause the energy to shift up; away from the center, the detuning increases quickly and the band is barely perturbed. This level repulsion also depends on the shaking amplitude. As the shaking amplitude increases, the center of the band starts to flatten but the band still has a single minimum at $k = 0$. Beyond a threshold value s_c, the level repulsion is strong enough to cause the bifurcation of the lone minimum at $k = 0$ into two at finite momentum $\pm k^*$, shown in Fig. 3.1**c**.

3.1.3 Floquet theory

This two-level model already captures the essence of the double-well band due to lattice shaking with large amplitude. However, to comprehensively obtain the effective band structure, we thus resort to the Floquet theory which takes all the unperturbed bands into account. In a system with time-independent Hamiltonian, we can simply diagonalize Hamiltonian to obtain the eigenstates and each of the eigenstates evolves in time with a simple phase winding given by the corresponding eigenvalue. But this simple method no longer works for a time-dependent Hamiltonian. However, in a special case where the Hamiltonian is time-periodic $H(t) = H(t + T)$, we might be able to find some states which also return to itself up to a complex phase after a single Floquet period T. Particularly when we are only interested in stroboscopic dynamics in intervals of the period T, these time-periodic states just look like ordinary eigenstates. Such examples are presented in Sec. 3.1.2 in which we introduced the two-level toy model.

Floquet theory gives a comprehensive calculation of such states that can form a complete basis [53, 33]. As we mentioned above, such steady states should return to itself after a Floquet period T with some extra phase winding. Therefore these states must be the eigenstates of the time evolution operator $U(T, 0)$, and satisfy $U(T, 0)|n\rangle = e^{-i\varepsilon^{(n)}T/\hbar}|n\rangle$

in the Schrödinger picture. This equation gives a set of the eigenvalues $\{e^{-i\varepsilon^{(n)}T/\hbar}\}$ and the corresponding set of eigenstates $\{|n\rangle\}$. We can rewrite the time evolution operator for single period as $U(T,0) = e^{-\frac{i}{\hbar}H_{eff}T}$, where H_{eff} is Hermitian, possessing real eigenvalues. This suggestive form implies $e^{-\frac{i}{\hbar}H_{eff}t}|n\rangle = e^{-i\varepsilon^{(n)}t}|n\rangle$ and we can treat H_{eff} as a effective Hamiltonian that describes the slow (compared with $2\pi/T$) dynamics with Floquet bands given by $\varepsilon^{(n)}$. We further introduce an extra unitary kicking operator $P(t)$ to capture the fast dynamics, which is also periodic $P(t) = P(t+T)$. Combing the slow and fast evolutions, we obtain the complete time evolution operator at an arbitrary time as $U(t,0) = P(t)e^{-\frac{i}{\hbar}H_{eff}t}$. Applying $U(t,0)$ to a initial state $|\psi(0)\rangle = \sum_n a_n|n\rangle$ with a_n time-independent constant, we get

$$\begin{aligned} |\psi(t)\rangle &= U(t,0)|\psi(0)\rangle \\ &= \sum_n a_n P(t)e^{-\frac{i}{\hbar}H_{eff}t}|n\rangle \\ &= \sum_n a_n e^{-\frac{i}{\hbar}\varepsilon^{(n)}t}|u^{(n)}(t)\rangle, \end{aligned} \tag{3.10}$$

with the Floquet function defined as $|u^{(n)}(t)\rangle \equiv P(t)|n\rangle$. Note that such Floquet functions are periodic in time, $|u^{(n)}(t+T)\rangle = |u^{(n)}(t)\rangle$, which is temporal analogue of the Bloch functions in space. Therefore the Floquet states are given by $\{e^{-\frac{i}{\hbar}\varepsilon^{(n)}t}|u^{(n)}(t)\rangle\}$. If we only plan to look at the slow dynamics of the system, we can simply isolate such slow evolution by doing a transformation $|\tilde{\psi}(t)\rangle = P^{-1}(t)|\psi(t)\rangle$. As a result, we have

$$i\hbar\frac{d}{dt}|\tilde{\psi}(t)\rangle = H_{eff}|\tilde{\psi}(t)\rangle. \tag{3.11}$$

To calculate the Floquet bands numerically, we diagonalize the single-period time evolution operator $U(T,0)$. We first solve the eigenvalue problem for the time-averaged Hamiltonian $H_{av} = \langle H(t)\rangle$ and obtain the bands given by eigenvalues $\{E_k^{(n)}\}$ and the corresponding Bloch waves $\{|\varphi_k^{(n)}\rangle\}$. Then we write the full Hamiltonian of the system in this basis.

The Hamiltonian can be separated into two terms, $H(t) = H_{av} + H'(t)$ with H' being the time-dependent part. To calculate the time-evolution operator $U_k(T)$ for different quasi-momentum states, we use the Lie-Trotter product formula $e^{A+B} = \lim_{N\to\infty}(e^{A/N}e^{B/N})^N$ where A and B are two not necessarily commuting operators. We can divide any time interval t into N segments with $\Delta t = t/N$ and obtain the time evolution operator

$$\begin{aligned} U_k(t) &= e^{-\frac{i}{\hbar}\int_0^t H(t')dt'} \\ &\approx \prod_{j=1}^{N}\left(e^{-\frac{i}{\hbar}H_{av}\Delta t}e^{-\frac{i}{\hbar}H'(j\Delta t)\Delta t}\right) \\ &\approx \prod_{j=1}^{N} e^{-\frac{i}{\hbar}H_{av}\Delta t}\left(1-\frac{i}{\hbar}H'(j\Delta t)\Delta t\right). \end{aligned} \tag{3.12}$$

In the last step, we used the first order approximation of the time evolution for $H'(t)$. We then solve diagonalize the single period time evolution operator $U(T,0)$ to obtain the quasi-energy bands. Compared with the two-level model, the Floquet theory significantly improves the accuracy of the calculated quasi-energy bands.

3.1.4 Quantum phase transition

So far we have only discussed the effect of lattice shaking on a single atom. Lattice shaking can dramatically change the single particle dispersion. Particularly when we shake the lattice beyond a critical amplitude, the single minimum of the ground band dispersion even bifurcates into two. The interesting question is how the bosons would react to such a change of dispersion. When we start with a condensate at the $k = 0$ state in the ground band $|\varphi_0^{(1)}\rangle$, non-interacting atoms stay at the $k = 0$ Floquet state $e^{-\frac{i}{\hbar}\varepsilon^{(1)}t}|u_k^{(1)}(t)\rangle$. This is guaranteed when we choose proper shaking parameters to stay away from avoided crossings, where atoms can be excited to other excited bands. As a result, nothing interesting happens even in the case with the double-well dispersion beyond the critical shaking amplitude.

It is the interaction between particles that introduces interesting dynamics by exciting

pairs of atoms into finite momentum states within the ground band (Ch. 4). Particularly for repulsively interacting bosons, we would naturally expect these bosons to condense to the state with minimal energy. At the single-particle level, there are numerous minimal energy states beyond the critical shaking amplitude. Such states include the finite momentum states at $\pm k^*$ and the superpositions of them. However, the interaction between atoms will break the degeneracy of these single-particle minimal energy states. This breaking of the degeneracy can be demonstrated with a toy model where we use the plane waves as an approximation of the Floquet function in an infinitely large one-dimensional system. In this model, we parametrize these single-particle ground state wavefunction as

$$\Psi_G = \sqrt{n_0}(\epsilon_+ e^{ik^*x} + \epsilon_- e^{-ik^*x}) \tag{3.13}$$

with n_0 the average density and $|\epsilon_+|^2 + |\epsilon_-|^2 = 1$. For bosons with positive interaction strength $g > 0$ the interaction energy per particle is given by [20],

$$\begin{aligned} E_{int} &= \frac{g}{2}\int dx \Psi_G^*(x)\Psi_G^*(x)\Psi_G(x)\Psi_G(x) / \int dx \Psi_G^*(x)\Psi_G(x) \\ &= \frac{gn_0}{2}\left(1 + 2|\epsilon_+|^2|\epsilon_-|^2\right). \end{aligned} \tag{3.14}$$

The minimal interaction energy is obtained if $(|\epsilon_+|^2, |\epsilon_-|^2) = (1, 0)$ or $(0, 1)$. This indicates that interaction spontaneously breaks the symmetry such that the atoms only occupy either of the $\pm k^*$ states as the absolute many-body ground state. Such spontaneous symmetry breaking makes the double-well side an effective ferromagnetic phase. We can treat the Bose condensate as a pseudo-spin system in which spin-up (-down) corresponds to finite momentum states k^* $(-k^*)$. Just like a regular ferromagnet whose energy is minimized when all spins aligned into the same direction, the condensate minimizes its energy if all atoms occupy the same quasi-momentum state. Such continuous phase transition was the first experimentally investigated in a one-dimensional lattice in Chin Lab in 2013 [85].

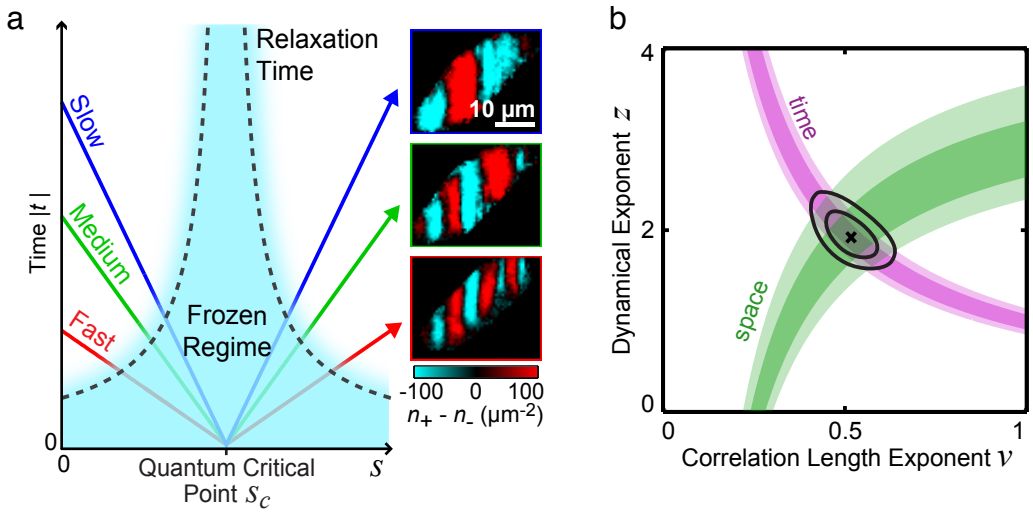

Figure 3.2: **Kibble-Zurek mechanism** textbfa When the condensate is taken across the critical point, the evolution becomes diabatic in the frozen regime (cyan) if the remaining time for the system to reach the critical point becomes less than the relaxation time. Because the relaxation time diverges near the critical point, faster ramps cause freezing farther from the critical point, limiting the system to smaller domains. Sample domain images are shown for slow, medium, and fast ramps. **b** Constrain of the critical exponents extracted from the temporal unfreezing dynamics (magenta) and spatial measurement of the domain size and correlation length (green). The cross marks the best values of $z = 1.9(2)$ and $\nu = 0.52(5)$ with contours of 68% and 95% fitting confidence. Theoretical prediction based on mean-field theory gives $z = 2$ and $\nu = 0.5$. Both of the figures appear in Ref. [24].

3.1.5 Kibble-Zurek scaling of domain formation

Previously we only focuses on the static properties of the phase transition such as the many-body ground states at the ferromagnetic side. In a realistic experiment, we always dynamically drive the system across the quantum critical point with a ramp of the shaking amplitude. Such a dynamical ramp is often non-adiabatic, which means that the system can not go to the many-body ground states at the end of the ramp. Instead, the system tends to form domains just as a regular ferromagnet. We observe that both the time for the formation of the domains and the size of the domains after crossing the critical point clearly depend on how fast we go across the phase transition. We understand that such critical dynamics are fully captured by the Kibble-Zurek mechanism [24], an universal principle that governs all critical phenomena near a continuous phase transition across various systems in condensed

matter, cosmology and beyond.

Kibble-Zurek mechanism, which is first discussed by T. Kibble in cosmology [64] and later extended to condensed matter by W. Zurek [113], provides an intuitive picture of quantum critical dynamics as shown in Fig. 3.2. In the Kibble-Zurek picture, when the remaining time for the system to reach the critical point becomes shorter than the relaxation time, the dynamics becomes effectively frozen. According to Landau theory of second order phase transitions, both the correlation length and relaxation time of the system diverge near the critical point. As are a result, the suspension of the dynamics is inevitable when the system is driven across the critical point at a finite speed due to such divergence of the relaxation time. The dynamics eventually unfreezes after a delay t_{KZ} once passing the critical point and the system can effectively react to the ramp because the relaxation time becomes shorter than the elapsed time after the system passes the critical point. When system unfreezes, topological defects (domain walls) start to form with a typical separation of d_{KZ}, proportional to the equilibrium correlation length. Kibble and Zurek predict an important universal power-law scaling of both the formation time of the defects t_{KZ} and the size of domains d_{KZ} on the ramp rate $\dot{s}$,

$$t_{KZ} \propto \dot{s}^{-\frac{z\nu}{1+z\nu}}, \tag{3.15}$$

$$d_{KZ} \propto \dot{s}^{-\frac{\nu}{1+z\nu}}, \tag{3.16}$$

with z and ν the dynamical and correlation length exponents in equilibrium given by the universality class of the phase transition.

We can test this universal scaling symmetry near the effective quantum phase transition in our system [24]. Here we adiabatically load Bose condensates into a one-dimensional optical lattice and linearly ramp up the lattice shaking amplitude at ramp rate $\dot{s}$. The unfreezing dynamics is investigated by monitoring the quasi-momentum fluctuation at various times during the ramp. Thus we test the temporal scaling of unfreezing time with the linear

ramp rate. After the system unfreezes, we image the domain structure of pseudo-spins. We extract both the average size of the domain and the correlation length to test the spatial scaling symmetry. By combining the scaling exponents from both the temporal and spatial measurements, we obtain the critical exponents $z = 1.9(2)$ and $\nu = 0.52(5)$. Prediction based on mean-field theory gives $z = 2$ and $\nu = 0.5$, which agrees very well with our experiment.

Although the Kibble-Zurek picture gives universal scaling predictions across various systems, it provides little information on the details of the microscopic dynamics in a particular system. During a quantum phase transition, a many-body system, originally prepared in the ground state with macroscopic coherence, is suddenly transferred to a metastable state after passing the critical point. How does the system evolve toward the new ground states with a different symmetry? A complete understanding of the processes that underlie the quantum critical dynamics is one of the focuses of this thesis and the detailed study is presented in Ch. 4.

3.2 Oscillating interaction

We can test this universal scaling symmetry near the effective quantum phase transition in our system [24]. Here we adiabatically load Bose condensates into a one-dimensional optical lattice and linearly ramp up the lattice shaking amplitude at ramp rate $\dot{s}$. The unfreezing dynamics is investigated by monitoring the quasi-momentum fluctuation at various times during the ramp. Thus we test the temporal scaling of unfreezing time with the linear ramp rate. After the system unfreezes, we image the domain structure of pseudo-spins. We extract both the average size of the domain and the correlation length to test the spatial scaling symmetry. By combining the scaling exponents from both the temporal and spatial measurements, we obtain the critical exponents $z = 1.9(2)$ and $\nu = 0.52(5)$. Prediction based on mean-field theory gives $z = 2$ and $\nu = 0.5$, which agrees very well with our experiment.

Although the Kibble-Zurek picture gives universal scaling predictions across various systems, it provides little information on the details of the microscopic dynamics in a particular

system. During a quantum phase transition, a many-body system, originally prepared in the ground state with macroscopic coherence, is suddenly transferred to a metastable state after passing the critical point. How does the system evolve toward the new ground states generally with a different symmetry? A complete understanding of the processes that underlie the quantum critical dynamics remains evasive. The answer to this question is one of the focuses of this thesis and the detailed study is presented in Ch. 4.

Ultracold atomic gases provide a powerful platform. It not only allows precise and versatile controls on single particles but also enables controls over pair-wise interactions. This controllability over inter-particle interaction empowers us to investigate scattering in quantum many-body systems. In this section, we explore an interesting phenomenon, which we call it "Bose fireworks", induced by periodically modulated interactions between atoms. This interesting observation turns out to be a surprise for us as we originally try to engineer density-dependent tunneling in shaken optical lattices with modulated interaction [23]. After modulating the scattering length between atoms for some time, on the order of few milliseconds, atoms are suddenly ejected out of the condensates. Such drastic emission of atoms is first observed in a harmonic trap and it does not really look like fireworks. When we later switch to a cylindrically symmetric disk-shaped trap to only study the effect from the modulated interaction, the beautiful emission patterns like fireworks are clear to us for the first time. In this section, we shall discuss the key elements of the Bose fireworks in Ref. [25] and the knowledge of these key points are essential to understanding the physics in Ch. 5, 6, and 7.

3.2.1 Condensates with oscillating interaction in disk-shaped trap

In Cs lab, we start with cigar-shaped condensates in a cross dipole trap made of three beams of a high-power 1064 nm laser. To make the sample like a thin disk, we first carefully turn off this cross dipole trap and transfer atoms into a vertical optical lattice trap with a spacing of 4 μm. The timing and trap depth is carefully tuned during the process so that all the

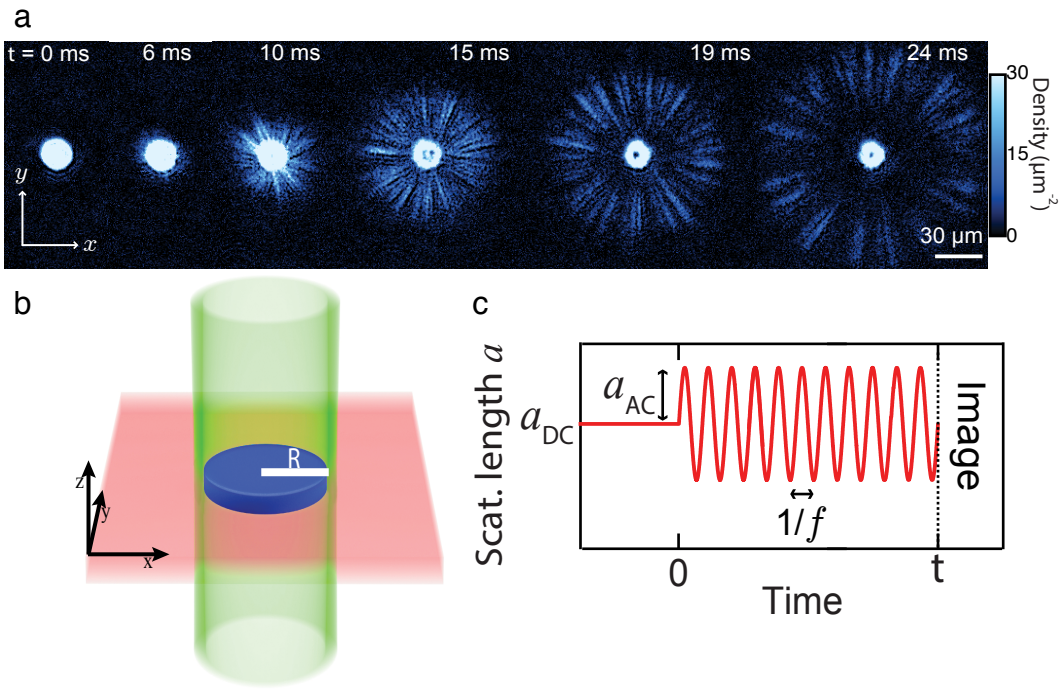

Figure 3.3: **Bose fireworks in driven condensates a** Emission of matter-wave jets after modulating the scattering length for various times τ. Each image corresponds to a single, independent experimental realization. **b** Disk-shaped trap of radius R made of a repulsive cylindrical shell (green) and an attractive sheet (red).**c** The scattering length is modulated as $a(t) = a_{dc} + a_{ac}\sin(\omega t)$ with $\omega = 2\pi f$ for a time τ before imaging. Here modulation frequency $f = 3.5$ kHz, DC offset $a_{dc} = 5a_0$ and AC amplitude $a_{ac} = 60a0$. All the figures are modified version of that in Ref. [25].

atoms are transferred into a single layer of the vertical lattice trap, which locates close to the focus of the high-resolution objective. Meanwhile, a ring-shaped barrier is first created with a large radius of 30 μm using the DMD with a 780 nm laser and slowly shrinks down to the desired size by switching preloaded patterns. At last, we have Bose condensates in a disk-shaped trap with the typical horizontal barrier height of $h\times$150 Hz and the vertical harmonic trapping frequency of $2\pi\times$210 Hz and the depth of $h\times$500 Hz.

After preparing the condensates in this trap, we modulate the magnetic field around 17.22 G, close to the zero-crossing near the Feshbach resonance, at frequency f. This modulation causes the pair-wise s-wave scattering length a to oscillate with the amplitude a_{ac}. Here we also need a small positive average scattering length a_{dc} to avoid the collapse of BEC. Meanwhile, we want this offset as small as possible to reduce heating from elastic collisions. As a result during the compression of the horizontal ring-shaped barrier, we slowly ramp the magnetic field to continuously change the scattering length from $40a_0$ to $5a_0$, in terms of the Bohr radius a_0. For typical experiments, we apply the modulation amplitude of a_{ac} much larger than the offset a_{dc} so that the interaction between atoms alternates between repulsion and attraction. After modulating the interaction for $\sim$10 ms, the jets emerge and fly out radially from the condensates in the horizontal plane. The emission pattern appears to be random from shot to shot in the experiment but every jet looks to have the same angular width and often emerges in company with a partner moving the opposite direction.

3.2.2 Stimulated inelastic collision

By monitoring the speed of these emitted jets after they leave the condensates, we can precisely measure the kinetic energy of the atoms inside the jets. We find that the kinetic energy of each atom in the jets equals to half of the quantum of the modulation field $hf/2$. This implies that these emitted atoms are created from pair-wise inelastic collisions within the condensates. Two atoms with zero momentum absorb the energy quantum of hf from the modulation field and scatter into opposite directions with exactly the same amount of mo-

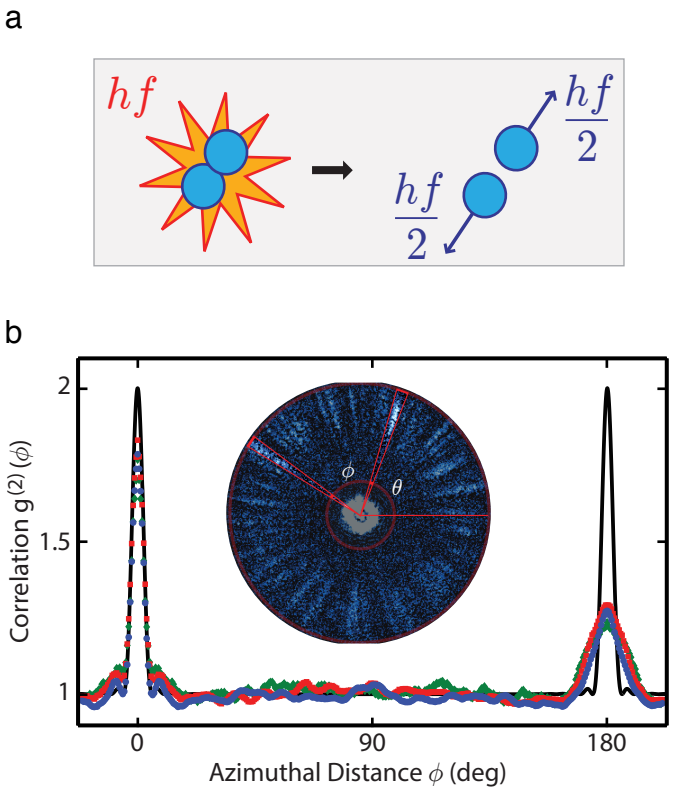

Figure 3.4: **Inelastic collision and correlation function. a** Illustration the microscopic process leading to jets: two atoms collide, absorb one energy quantum from the oscillating field and are ejected in opposite directions. **b** Azimuthal density-density correlations of jets emitted from condensates driven at $f = 1.9$ kHz and $a_{ac} = 60a_0$ for modulation durations of $\tau = 4.4$ ms (green diamonds), 5.6 ms (red squares) and 8.0 ms (blue circles). The correlation function is remarkably consistent throughout the amplification process, even when the number of atoms in jets grows by an order of magnitude as we increase the modulation duration. The solid curve shows the theoretical correlation function. All the figures are modified version of that in Ref. [25].

mentum $\hbar k_f = \sqrt{hf/m}$ to conserve both energy and momentum, shown in Fig. 3.4**a**. Such collisions are normally suppressed in unperturbed condensates since they do not conserve energy.

However, with only spontaneous inelastic collisions, we should expect the modulation of interaction to only generate a diffuse, spherical shell of atoms propagating out of the condensate. The fact that emission only prefers the horizontal plane and the inhomogeneous jets structure suggest a collective collision process happening throughout condensate. In this collective process, excited atoms generated from a previous inelastic collision stimulate further scattering to populate atoms into the same momentum modes. This process accelerates as more atoms populates the same mode and finally atoms emit our in a particular direction and manifest as jets. As a result, angular directions which initially has more spontaneously atoms will end up to have stronger jets.

This runaway process is only possible when the excited atoms can stimulate further collisions while leaving the condensates. Given a modulation frequency f, the speed of the excited atoms is $v = \sqrt{hf/m}$. Their escaping rate can be approximated as $\Gamma = \alpha v/R$ with α a dimensionless constant. While the scattering rate inside the condensates, at which atoms can stimulate further collisions, is given by $\gamma = 2hn_0a_{ac}/m$ with n_0 the density of the condensates. Escaping and scattering compete so that the runaway stimulation can only occur if the collision happens faster than the escape of atoms, $\gamma > \Gamma$. Based on this intuitive understanding, we can obtain the threshold condition,

$$\frac{n_0 a_{ac} R}{\sqrt{f}} \geq \frac{\alpha}{2}\sqrt{\frac{m}{h}}, \tag{3.17}$$

where the left side contains parameters that can be controlled experimentally while the right side is just a constant. This intuitive treatment of the threshold behavior offers excellent guidance to further experiments presented in the following chapters.

3.2.3 Width of jets and asymmetry in correlation function

To further test this pair-wise inelastic scattering of atoms, we can calculate the angular correlation function suggest a correlation

$$g^{(2)}(\phi) = \frac{\langle n(\theta)[n(\theta+\phi) - \delta(\phi)]\rangle}{\langle n(\theta)\rangle\langle n(\theta+\phi)\rangle}, \tag{3.18}$$

where $n(\phi)$ is the angular density of atoms emitted at an angle of θ, see inset of Fig. 3.4, $\delta(\phi)$ is the Dirac delta function and the angle brackets indicate averaging over angle θ first and then over ensembles of many images. We observe two peaks in this measured correlation function. Peak at $\phi = 0^\circ$ results from stimulated collisions due to bosonic statistics leading to bunching of excited atoms in the same momentum mode. Peak at $\phi = 180^\circ$ results from the pair-wise scattering process discussed above and backward and forward jets mutually stimulate to conserve total momentum.

One important piece of information we can get from the correlation function is the angular width of the jets from the peak at $\phi = 0^\circ$. It turns out to be limited by the Heisenberg uncertainty principle. Given a finite size of the condensates with radius R, the uncertainty of the momentum is given by $\Delta p \propto \frac{\hbar}{R}$. This momentum uncertainty reflects in the angular direction as $\Delta\theta = \frac{\Delta p}{p} \propto \frac{1}{k_f R}$. In our experiments, we find that the angular width follows

$$\Delta\theta \approx \frac{1.63}{k_f R}. \tag{3.19}$$

Another interesting piece of this correlation function is the much lower peak value at $\phi = 180^\circ$. Conservation of momentum in pair-wise scattering in principle guarantees that each jet is accompanied by a counter-propagating partner, which gives $g^{(2)}(0^\circ) = g^{(2)}(180^\circ)$. This asymmetry attracts attention not only from condensed matter physics [108] and but also from high energy physics [7]. In Ch. 6, we will address such asymmetry in detail. In short, this asymmetry is caused by the near-field interference between jets. In the far-felid

observation where the jet structure can faithfully reflect the momentum space distribution, the symmetry recovers.

CHAPTER 4

COHERENT INFLATIONARY DYNAMICS IN DRIVEN CONDENSATES

Quantum phase transitions, transitions between many-body ground states, are of extensive interest in research ranging from condensed matter physics to cosmology [91, 79, 65, 104]. Key features of the phase transitions include a stage with rapidly growing new order, called inflation in cosmology [45], followed by the formation of topological defects [64, 113, 29]. How inflation is initiated and evolves into topological defects remains a hot debate topic. Ultracold atomic gas offers a pristine and tunable platform to investigate quantum critical dynamics [87, 13, 32]. In particular, critical behaviors have been studied in normal Bose gas to superfluid phase transition [68, 81], Bose-glass to condensate transition [75], and Dicke phase transitions [10, 66]. Remarkable studies on the dynamics crossing a ferromagnetic phase transition [92, 9], miscible to immiscible phase transition [83], and polar to the broken-axisymmetry phase transition [6] have been done in spinor condensates.

In this chapter we discuss the observation of coherent inflationary dynamics across a quantum critical point in a paramagnetic to ferromagnetic phase transition in driven Bose-Einstein condensates. During such a quantum phase transition, a many-body system, originally prepared in the ground state with macroscopic coherence, is suddenly transferred to a metastable state after passing the critical point [91, 64, 32]. An example shown in Fig. 4.1 is a ferromagnetic transition where the Z_2 inversion symmetry is broken. How does the system evolve toward the new ground states generally with a different symmetry? One can hypothesize two possible scenarios: 1. Fluctuations break the system into locally coherent segments which evolve toward the new ground states independently. After relaxation, the system forms domains with local coherence [79, 32]. 2. Maintaining the macroscopic coherence, the system undergoes a coherent population transfer of particles toward lower energy states. Here fluctuations determine the domain structure but do not destroy the macroscopic

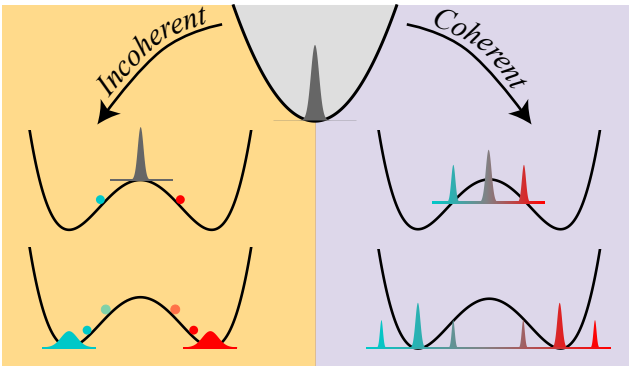

Figure 4.1: **Paradigms of dynamics crossing a ferromagnetic quantum critical point.** Two scenarios describing the quantum phase transition: (Left) In the incoherent picture, the system is broken into locally coherent segments by fluctuations. Each segment evolves independently toward a new ground state. Particles eventually rethermalize at the energy minima to form domains. (Right) In the coherent scenario, the system evolves toward the new ground states with macroscopic coherence extending beyond the domain size.

coherence.While both scenarios support rapid evolution toward new ground states, the key differences are the time and length scales of the coherence in the dynamical process.

In our system, the inflation manifests in the exponential growth of density waves and populations in well-resolved momentum states. After the inflation stage, extended coherent dynamics is evident in both real and momentum space. We present an intuitive description of the quantum critical dynamics in our system and demonstrate the essential role of phase fluctuations in the formation of topological defects.

4.1 Experimental setup

We utilize three-dimensional Bose-Einstein condensates of 30,000 cesium atoms confined in an optical dipole trap. The trap is tightly confined in the gravity direction with a trapping frequency of $2\pi\times226$ Hz. Trapping frequencies in the two in-plane directions are $2\pi\times6$ and $2\pi\times9$ Hz. The s-wave scattering length is 50 a_0, where a_0 is the Bohr radius. We adiabatically load the BEC into a one-dimensional optical lattice with a depth of 8.9 E_R and period $d = 532$ nm, where $E_R = h\times$ 1.3 kHz is the recoil energy.

Our experiment is based on such cesium Bose-Einstein condensates loaded into a one-

dimensional phase-modulated optical lattice [85]. The modulation translates the lattice periodically with displacement $\Delta x = \frac{s}{2}\sin\omega t$, where s is the shaking amplitude and ω is the shaking frequency. The shaking frequency is fixed to $\omega = 2\pi\times 8$ kHz, which is $2\pi\times 0.87$ kHz above the gap at zero-momentum between the ground and the first excited Bloch band in the lattice. Shaking hybridizes the ground and excited Bloch bands and results in an effective dispersion ε_q for the condensate [85], where the lowest energy state at quasi-momentum $q = 0$ bifurcates into two ground states at $+q^*$ and $-q^*$ (named pseudo-spin up and down), when s exceeds a critical value s_c. When the system is driven across the critical point in finite time, domains of pseudo-spins form in accordance with universal Kibble-Zurek scaling [24] and excitations within a domain display a roton dispersion [47], however, a complete understanding of the processes that underlie the quantum critical dynamics remains evasive.

To reveal the nature of the quantum phase transition, we exploit three schemes to analyze the critical dynamics of the condensate: 1. *in situ* imaging to record the atomic density profile, 2. time-of-flight with a focusing technique [97] to probe the momentum space distribution n_q, and 3. pseudo-spin reconstruction to reveal domain structure [24].

4.2 Dynamics in slow ramp experiment

There are various ways to drive the system across the critical point. In this experiment, we linearly ramp up the shaking amplitude s across the critical value at a constant speed. Here the slow ramp is still fast compared to an adiabatic ramp where the system always stays in the many-body ground state, therefore we still expect to see formation of magnetic domains as the system goes across the critical point. Here the linear ramp starts at $s = 0$ nm with ramp rate $\dot{s} = 0.64$ nm/ms. Given the lattice depth and shaking frequency mentioned above, the critical shaking amplitude $s_c = 13.1$ nm.

We observe two key features indicating coherent evolution. First, from *in situ* images, the density wave emerges about 20 ms after passing the critical point. Quantified with the density structure factor S_q [58], the density wave shows an almost fixed wavenumber. Second, from

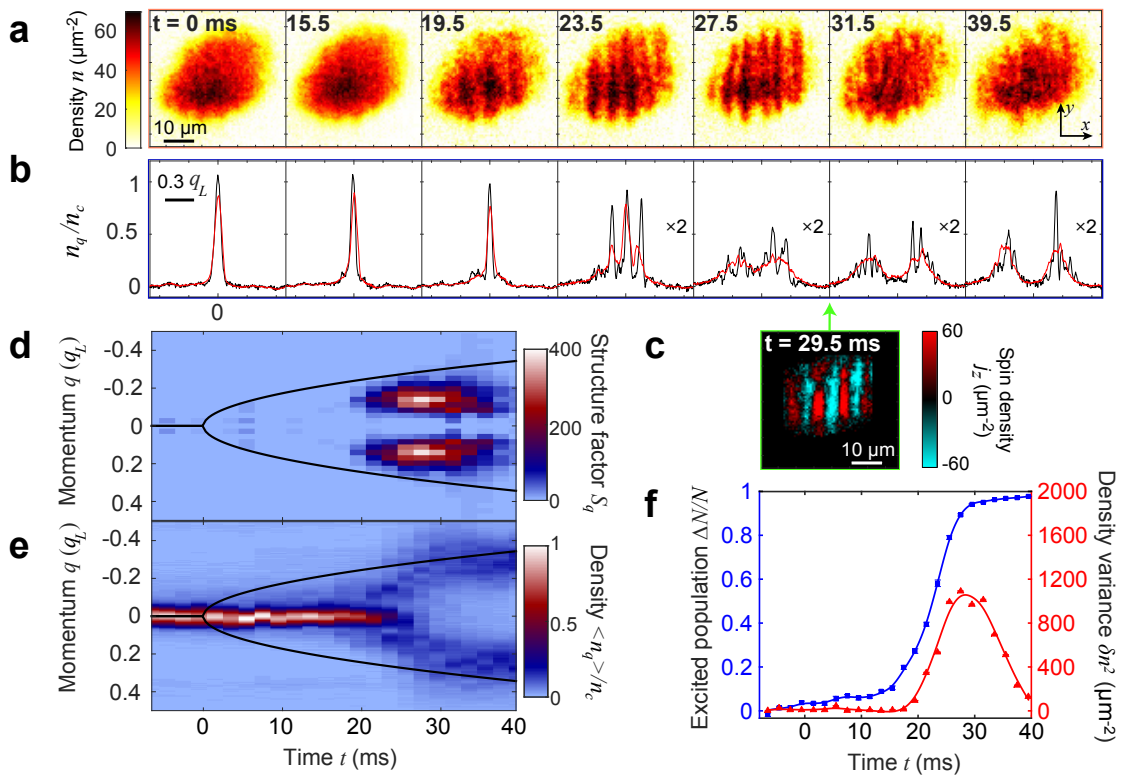

Figure 4.2: **Development of density waves and momentum space population across the quantum critical point.** Density waves and sharp peaks in momentum space emerge when we linearly ramp up the shaking amplitude s with a ramp rate $\dot{s} = 0.64$ nm/ms across the critical point $s_c = 13.1$ nm at time $t = 0$. **a,** Single shot *in situ* images of the condensate. **b,** Momentum distribution n_q from time-of-flight measurement(black). Here n_c is the averaged peak density in the momentum space of unshaken condensates. Averaging over repeated experiments gives two broad peaks centered around $q = 0$ (red). **c,** Domain structure from reconstruction [24], where $j_z = n_{q^*} - n_{-q^*}$ is the spin density. **d,** The density structure factor $S_q = \langle \Delta n_q^2 \rangle / N$, extracted from the Fourier transform of the density fluctuation $\Delta n(x) = n(x) - \langle n(x) \rangle$ integrated along y axis. Here N is the total atom number and $\langle . \rangle$ indicates an average over repeated measurements. Peaks appear at $\pm q_d = \pm 0.14\ q_L$ with $q_L = \pi\hbar/d$ being the lattice momentum and d being the lattice period. **e,** The averaged population distribution $\langle n_q \rangle$ in momentum space. Solid black curves in both **d** and **e** show the instantaneous, theoretical ground state momenta $\pm q^*$. **f,** Fractional population excited out of $q = 0$ state (blue square) and the density variance δn^2 from integrating the structure factor S_q. Solid lines are guides to the eye. The error bars indicate 1σ standard error.

time-of-flight images, the atomic population forms sharp side peaks in individual samples; over repeated measurements the side peaks average to broader features. These observations suggest that atoms occupy a coherent superposition of well-defined momentum states and the density wave emerges from their interference. Though the density wave diminishes after 30 ms, the persistent narrow momentum peaks in atomic population n_q suggest a long-lasting coherence. In addition, the period of the density waves approximately matches twice the averaged domain size. Both features will be further discussed in later section 4.4.

A more comprehensive analysis of the density wave and the population distribution in momentum space suggests that the system evolution can be separated into two stages: inflation and relaxation. To see this, we evaluate the density variance $\delta n^2 = \int dq S_q$ from *in situ* images as well as the total population in finite momentum states $\Delta N = \sum_{q>0} N_q$ from time-of-flight measurements, where N_q is the total atom number in the $\pm q$ states. For short times after the phase transition, both quantities show a characteristic exponential-like growth; we name this period the inflation stage, see Fig. 4.2**f**. After inflation, all atoms relax toward non-zero momentum states at $q = \pm q^*$ while the density wave diminishes. In the following section 4.4, we investigate the two stages, inflation and relaxation, separately.

4.3 Theory of inflation

Here we start with the many-body Hamlitonian in the second quantization form [86],

$$H = \sum_q \varepsilon_q \hat{a}_q^\dagger \hat{a}_q + \frac{U_0}{2V} \sum_{q,q',p} \hat{a}_{q+p}^\dagger \hat{a}_{q'-p}^\dagger \hat{a}_q \hat{a}_{q'}, \tag{4.1}$$

where ε_q is the single atom dispersion, U_0 is the two-body interaction energy, V is the volume of the system and $\hat{a}_{\pm q}^\dagger$ and $\hat{a}_{\pm q}$ are bosonic creation and annihilation operators of an atom with momentum $\pm q$. Shaking of the optical lattice dramatically change the single particle

dispersion and in the ferromagnetic phase it is given by

$$\varepsilon_q = \epsilon \left[\left(\frac{q}{q^*} \right)^2 - 1 \right]^2 - \epsilon, \tag{4.2}$$

where ϵ is the kinetic energy barrier hight. Thus the dispersion is in a double-well shape in momentum space and has two minima at $q = \pm q^*$ sparated by the kinetic energy barrier (Fig. S2**b**) [85, 24].

4.3.1 Hamiltonian of inflaton and solution

Under Bogoliubov approximaton, we introduce a new quasi-particle field, inflaton, to rewrite the Hamiltonian of Bose-Einstein condensates. At the beginning of the phase transition, we assume that the $q = 0$ state is macroscopically occupied. Thus the condensate consists of N atoms and has a chemical potential $\mu = U_0 N/V$. The many-body Hamiltonian Eq.(4.1) reduces to

$$H = \frac{1}{2} N\mu + \sum_{q>0} (\mu + \varepsilon_q)(\hat{a}_q^\dagger \hat{a}_q + \hat{a}_{-q}^\dagger \hat{a}_{-q}) + \sum_{q>0} \mu(\hat{a}_q^\dagger \hat{a}_{-q}^\dagger + \hat{a}_q \hat{a}_{-q}). \tag{4.3}$$

Conventional Bogoliubov transformation to diagonalize the Hamiltonian using bosonic operators fails in our case because of $\varepsilon_q < 0$. Instead, we adopt a different approach by introducing the following transformation

$$\hat{\imath}_{\pm q} \;\; = \;\; u_q \hat{a}_{\pm q} + \nu_q \hat{a}_{\mp q}^\dagger, \tag{4.4}$$

where $\hat{\imath}_{\pm q}^\dagger$ and $\hat{\imath}_{\pm q}$ are the creation and anihilation operators of an inflaton with momentum

$\pm q$ and the coefficients $u_q, \nu_q > 0$ for $\varepsilon_q < 0$ satisfy

$$u_q^2 = \frac{1}{2}(\frac{\mu}{\hbar\lambda_q} + 1) \tag{4.5}$$

$$\nu_q^2 = \frac{1}{2}(\frac{\mu}{\hbar\lambda_q} - 1) \tag{4.6}$$

$$\hbar\lambda_q = \sqrt{-\varepsilon_q(2\mu + \varepsilon_q)}. \tag{4.7}$$

The inflaton field operators obey bosonic commutation relations: $[\hat{\imath}_q, \hat{\imath}_{q'}] = [\hat{\imath}_q^\dagger, \hat{\imath}_{q'}^\dagger] = 0$ and $[\hat{\imath}_q, \hat{\imath}_{q'}^\dagger] = \delta_{qq'}$.

As a result, the Hamiltonian reduces to

$$H = \sum_{q>0} \hbar\lambda_q(\hat{\imath}_q^\dagger \hat{\imath}_{-q}^\dagger + \hat{\imath}_q \hat{\imath}_{-q}) + \frac{1}{2}N\mu - \sum_{q>0}(\mu + \varepsilon_q). \tag{4.8}$$

Beside the two constant terms, the Hamiltonian shows that inflatons are created and annihilated in pairs with opposite momentum. Here the inflation dispersion λ_q is related to the growth rate of the inflatons (Fig. 4.3**a**).

To show the exponential growth, we look at the dynamics of the inflaton in the Heisenberg picture, which yields

$$\partial_t \hat{\imath}_{\pm q}(t) = \frac{i}{\hbar}[H, \hat{\imath}_{\pm q}(t)] = -i\lambda_q \hat{\imath}_{\mp q}^\dagger(t) \tag{4.9}$$

$$\partial_t \hat{\imath}_{\pm q}^\dagger(t) = \frac{i}{\hbar}[H, \hat{\imath}_{\pm q}^\dagger(t)] = i\lambda_q \hat{\imath}_{\mp q}(t). \tag{4.10}$$

The solutions of the above equations are

$$\hat{\imath}_{\pm q}(t) = \hat{\imath}_{\pm q}(0)\cosh\lambda_q t - \hat{\imath}^\dagger(0)_{\mp q} i\sinh\lambda_q t \tag{4.11}$$

$$\hat{\imath}_{\pm q}^\dagger(t) = \hat{\imath}_{\pm q}^\dagger(0)\cosh\lambda_q t + \hat{\imath}_{\mp q}(0) i\sinh\lambda_q t. \tag{4.12}$$

Based on these solutions, the inflaton population $m_{\pm q}(t) \equiv < \hat{\imath}_{\pm q}^\dagger(t)\hat{\imath}_{\pm q}(t) >$ evolves accord-

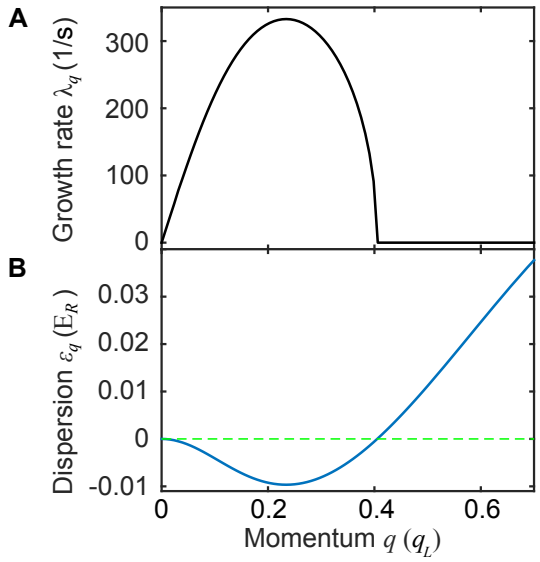

Figure 4.3: **Inflaton growth rate and single particle dispersion**. Here the shaking amplitude $s = 25$ nm with atoms in an 8.9 E_R lattice. The chemical potential $\mu = h\times150$ Hz. We shows the inflaton growth rate λ_q (**a**) and the single particle dispersion ε_q (**b**). The green dashed line (in **b**) indicates the zero-crossing of ε_q.

ing to

$$m_{\pm q}(t) = m_{\pm q}(0)\cosh^2\lambda_q t + m_{\mp q}(0)\sinh^2\lambda_q t + \sinh^2\lambda_q t, \tag{4.13}$$

where the first two terms on the right-hand-side correspond to Bose stimulation and the last term originates from spontaneous emission of inflatons.

We further simplify the results by defining the total inflaton population in $\pm q$ modes $M_k = m_q + m_{-q}$ and have

$$M_q(t) + 1 = [M_q(0) + 1]\cosh 2\lambda_q t. \tag{4.14}$$

From this result we see that the inflaton population, including the contribution from spontaneous emission, grows exponentially with a rate of $2\lambda_q$.

4.3.2 Experimental observables

The exponential growth of inflaton fields is reflected in the momentum population in the time-of-flight measurements, and the structure factor of the density wave. First of all, we define the population in momentum state $\pm q$ as $N_q = \langle \hat{a}_q^\dagger \hat{a}_q \rangle + \langle \hat{a}_{-q}^\dagger \hat{a}_{-q} \rangle$. To calculate the atom population from inflatons, we use the inverse inflaton transformation $\hat{a}_{\pm q} = u_q \hat{\iota}_{\pm q} - \nu_q \hat{\iota}_{\mp k}^\dagger$. We thus rewrite the atom population as

$$N_q + 1 = \frac{\mu}{\hbar \lambda_q} \left(M_q + 1 \right) - \frac{\mu + \varepsilon_q}{\hbar \lambda_q} \left(\langle \hat{\iota}_q \hat{\iota}_{-q} + \hat{\iota}_q^\dagger \hat{\iota}_{-q}^\dagger \rangle \right). \tag{4.15}$$

Since $\hat{\iota}_q \hat{\iota}_{-q} + \hat{\iota}_q^\dagger \hat{\iota}_{-q}^\dagger$ commutes with the Hamiltonian and does not vary with time, the number of atoms in an inflaton is given by $\partial N_q / \partial M_q = \mu / \hbar \lambda_q$.

Secondly, the structure factor, defined as the Fourier transform of the density-density correlation function [69], can be expressed in terms of the correlations in the momentum space as

$$S_q = \frac{1}{N} \sum_{p,p'} \langle \hat{a}_{p+q}^\dagger \hat{a}_p \hat{a}_{p'-q}^\dagger \hat{a}_{p'} \rangle. \tag{4.16}$$

For small number of excitations $\langle \hat{a}_q^\dagger \hat{a}_q \rangle \ll \langle \hat{a}_0^\dagger \hat{a}_0 \rangle \approx N$ and $\varepsilon_q < 0$, one can rewrite S_q as

$$S_q = \frac{-\varepsilon_q}{\hbar \lambda_q} \left(M_q + 1 + \langle \hat{\iota}_q \hat{\iota}_{-q} + \hat{\iota}_q^\dagger \hat{\iota}_{-q}^\dagger \rangle \right). \tag{4.17}$$

Based on Eqs.(4.15) and (4.17), we futher determine the time evolution of the observables. In the beginning of the phase transition, we assume that there is no net source of correlated inflatons in a regular Bose-Einstein condensate

$$\langle \hat{\iota}_q \hat{\iota}_{-q} \rangle = \langle \hat{\iota}_q^\dagger \hat{\iota}_{-q}^\dagger \rangle = 0. \tag{4.18}$$

As a result, the initial value of inflaton population at $t = 0$ is

$$M_q(0) + 1 = \frac{\hbar\lambda_q}{\mu}[N_q(0) + 1]. \tag{4.19}$$

Finally, we obtain the time evolution of $N_q(t)$ and $S_q(t)$,

$$N_q(t) + 1 = [N_q(0) + 1]\cosh(2\lambda_q t) \tag{4.20}$$

$$S_q(t) = \frac{-\varepsilon_q}{\mu}[N_q(0) + 1]\cosh(2\lambda_q t). \tag{4.21}$$

This result explains the similar exponential-like growth of both observable in Fig. 4.2**f**. This is because that shortly after passing the quantum critical point, the $q = 0$ state remains microscopically occupied, which justifies the Bogoliubov approximation.

4.4 Inflation and relaxation in fast quench experiment

To further test the inflation theory, we perform quench experiments by suddenly driving the system across the critical point, and measure the growth rate of the population in different momentum modes. Right before the quench, we seed a small initial population in the desired momentum states $\pm q'$ by imprinting a sinusoidal phase pattern on the condensate $\delta\phi \sin(q'x/\hbar)$. Here $\delta\phi$ is the seed amplitude and the wavenumber $q'/\hbar$ is externally controlled.

We imprint the phase pattern across the condensate using a digital micromirror device (DMD) with a 795 nm laser, see Fig. 4.4. To ensure a sinusoidal modulation, we set a grating pattern on the DMD with twice of the desired period $2\pi\hbar/q'$ and only let the ± 1 orders from the diffraction pass in the Fourier plane. The diffracted beams interfere on the atoms, giving a clean sinusoidally varying potential. The imprinting pulse lasts for 20 to 40 μs, which is very short compared to the condensate and lattice time scale.Right after the seeding pulse, the wavefunction of the condensates can be written as

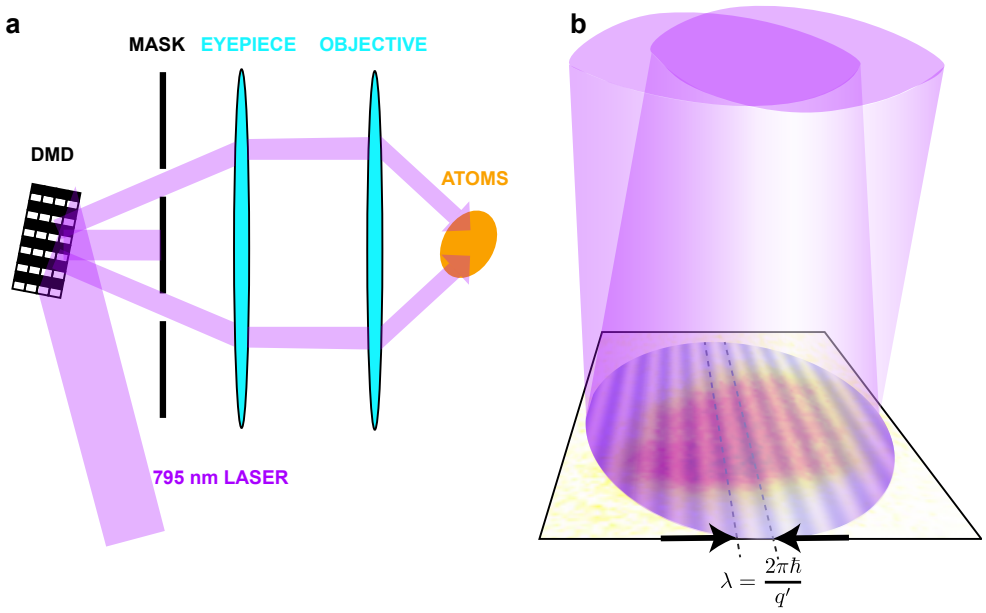

Figure 4.4: **Phase imprinting using digital micromirror device** A grating pattern is programmed to the digital micromirror device. The diffracted beams from a 795 nm laser are selectively blocked for creating clean sinusoidal lattices in the presence of aberrations. The beam-selection mask is placed in a Fourier plane along the optical path of the DMD projection which only allows the two desired diffraction orders to transmit. The presence of aberrations only cause a phase shift between the two diffracted beams, which affects the position of the resulting lattice but not its depth or spacing.

$\psi = \psi_0 e^{i\delta\phi \sin(q'x/\hbar)}$, where ψ_0 is a constant, q' is the seeding momentum, $\delta\phi$ is the seeding amplitude and normally $\delta\phi < 1$. Thus we transfer a small fraction of the atomic population to the $\pm q'$ states. This is easy to see if we expand the wavefunction using the Bessel functions, $\psi = \psi_0 \left[J_0(\delta\phi) - J_1(\delta\phi) e^{-iq'x/\hbar} - J_{-1}(\delta\phi) e^{iq'x/\hbar} + ... \right]$.

After seeding, the condensate quickly grows two side peaks at the seeding momentum $\pm q'$ (Fig. 4.5**a**). To extract the growth rate, we monitor the population in the momentum states. To obtain the atom population $N_{q'}$ in the momentum states $\pm q'$, we integrate the populations in the momentum states within the intervals $[q' - \delta q, q' + \delta q]$ and $[-q' - \delta q, -q' + \delta q]$. The population grows exponentially in the beginning but reaches a maximum at a later time when the population in the $k = 0$ state is depleted (Fig. 4.5**b**). We fit the fast growing interval, where $N_{q'}/N \leq 0.3$, right after the quench according to Eq. (4.20) and compare the growth rate to the prediction (Fig. 4.5**c**). Our measured growth rates qualitatively agree with the Bogoliubov result. We find quantitative agreement with our numerical simulation based on the Gross-Piteavskii equation which incorporates the depletion of the condensate. In particular, we confirm that only modes $|q| \leq 0.4\ q_L$ with kinetic energy $\varepsilon_q < 0$ exponentially grow and the fastest growth appears at momentum $q \approx \pm q^*$. Here $q_L = \pi\hbar/d$ is the lattice momentum with d being the lattice period.

Remarkably, in the absence of seeding, the sample spontaneously grows momentum peaks near $\pm q^*$ with a growth rate very close to that seeded at a similar momentum (Fig. 4.5**c** and the inset). For unseeded samples, many momentum modes can in principle be populated by quantum or thermal fluctuations and then amplified by inflation. The dominance of the modes near $\pm q^*$ can be understood since they have the highest growth rate and become dominant during inflation.

Following the inflation stage, the condensates display persistent coherent dynamics in both time-of-flight and *in situ* measurements (Fig. 4.6). After the rapid growth of the population at seeded momentum $\pm q'$, the system generates higher order harmonics at $\pm 2q', \pm 3q'...$, and the atomic populations are coherently transferred between these momentum states. The

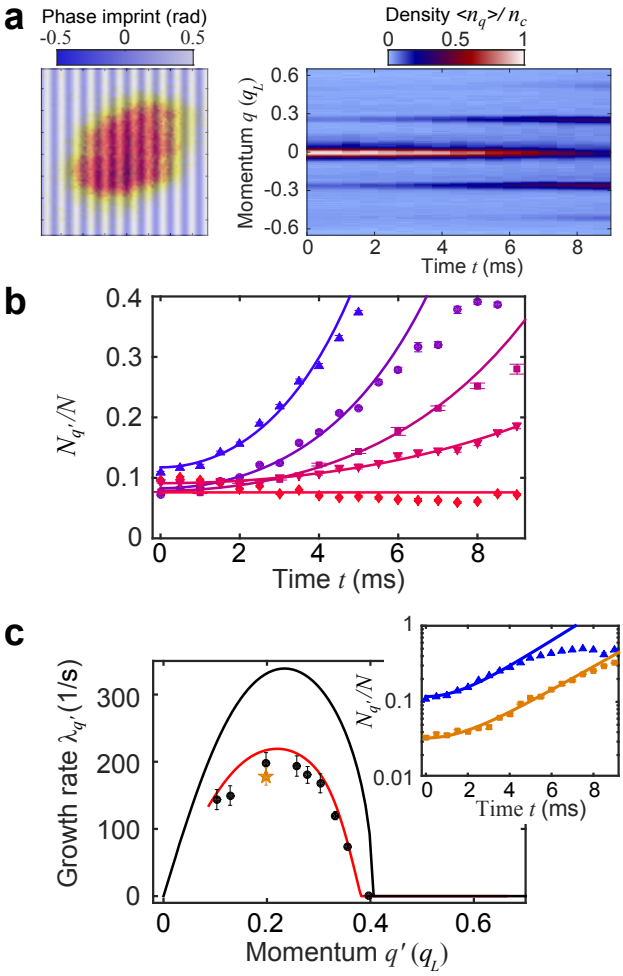

Figure 4.5: **Growth of excitations during the inflation phase.** We quench the seeded condensates from shaking amplitude $s_c = 13.1$ nm to $s = 25$ nm, where the new ground states are at $\pm q^* = \pm 0.24\ q_L$. **a,** At $t = 0$, we quickly imprint a phase modulation in 20 μs on the condensate with a seeding momentum $q' = 0.26\ q_L$ (left). Subsequent time of flight measurements reveal two side peaks emerging at $\pm q'$ (right). **b,** the fractional population in both side peaks $N_{q'}/N$ evolves for different seeding momentum: $q' = 0.19$ (triangle), 0.30 (circle), 0.33 (square), 0.36 (inverted triangle) and 0.40 q_L (diamond), from blue to red. Solid lines are fits using Eq. (4.20) to extract the growth rate $\lambda_{q'}$. **c,** The growth rates for seeded (black) and unseeded experiments (orange star) are compared with Bogoliubov theory (black line)and numerical simulation (red line). Inset compares the growth for seeded experiment with $q' = 0.19\ q_L$ (blue) and the unseeded quench experiment (orange). The error bars indicate 1σ standard error.

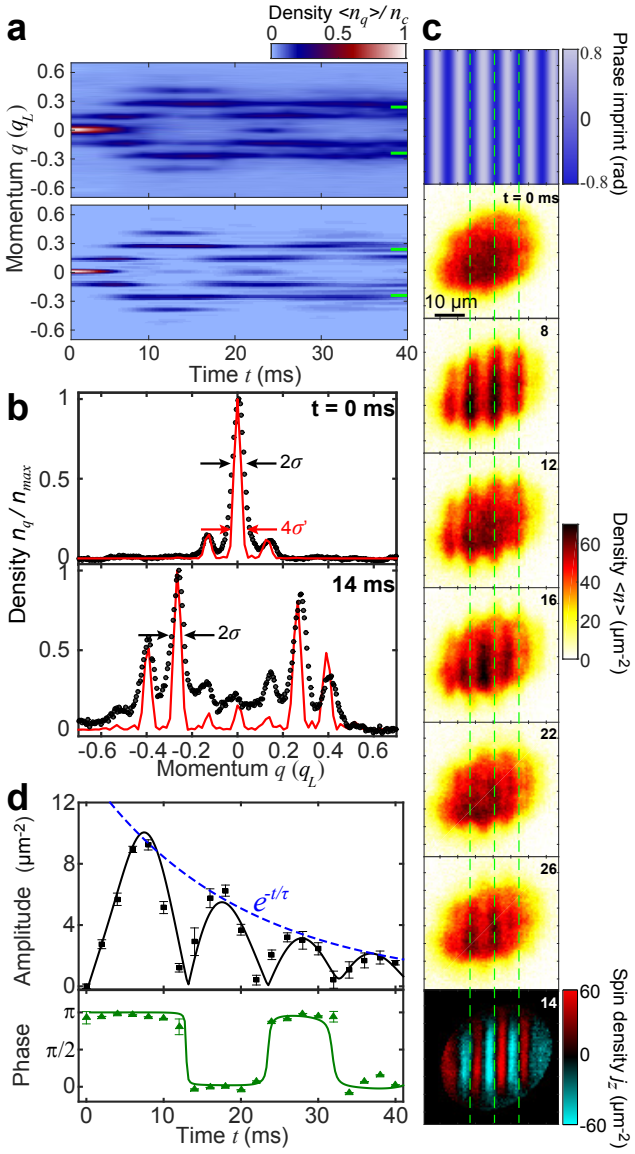

Figure 4.6: **Coherent quantum critical dynamics.** The condensates are seeded at momentum $q' = 0.13\ q_L$ and quenched from shaking amplitude $s_c = 13.1$ nm to $s = 25\ nm$. **a,** Coherent oscillations in momentum space (top: experiment, bottom: numerical calculation). The green solid lines indicate the position of $\pm q^*$. **b,** Line cuts of the experimental data at $t = 0$ and 14 ms (black dot). The solid red lines are from numerical calculations. The experimental peaks in both cuts show similar root-mean-square radius of $\sigma = 0.026\ q_L$ and $0.028\ q_L$ from Gaussian fits. The numerical calculation shows $\sigma' = 0.015\ q_L$, determined by the sample size. **c,** Oscillation of the density wave and the domain structure at $t = 14\ ms$. Both density waves and domains appear aligned with the seed pattern (green dashed line). **d,** Amplitude (black square) and phase (green triangle) of the density wave are compared with the numerical calculation (solid lines). A settling time $\tau = 20$ ms is extracted from the decay of the envelope function (blue dashed line). The error bars indicate 1σ standard error.

emergence of higher harmonics is due to nonlinear mixing of the matter waves and can be well described based on our numerical model. An example at $t = 14$ ms shows multiple side peaks that conform to the simulation. Intriguingly, the individual momentum peaks are as narrow as the zero momentum peak of the original condensate; the widths are only limited by the detection resolution.

A narrow momentum peak indicates long coherence length based on uncertainty principle. Here we extract a lower bound of the coherence length based on uncertainty principle in Fig. 4.6**b**. Given the mean square width of the atom population peaks in momentum space σ, the coherence length of the system is then $l_\phi \propto h/\sigma$. In our simulation (see Sec. 4.5), based on fully coherent condensates with coherence length equals to the system diameter of 30 μm, the mean square width σ' is almost half of that in the corresponding experiments. This indicates that the coherence length is $l_\phi > 15$ μm in the experiment, which is approximately 3 times larger than the domain size of 4 μm and is half of the system size, 30 μm in the direction of shaking.

Together with the dynamics in momentum space, density waves in seeded samples also display coherent oscillations in quench experiments (Fig. 4.6**c**). The density wave appears aligned to the imprinted pattern, and its phase displays multiple alternations (Fig. 4.6**d**) which are synchronized with oscillations of the population in momentum space. The contrast of the density wave oscillates and slowly decays with a time constant of $\tau = 20$ ms. Both the alternation and the decay are in good agreement with our simulation. Finally, we find that domains are fully formed as early as $t = 14$ ms, and remain constant afterward. Importantly, the domain structure is deterministic in the seeded experiments, and the domain walls line up with the density wave yielding a domain size half the period of the density wave.

The observed coherent dynamics can be understood based on a simple physical picture. Phase imprinting across the condensate locally breaks the inversion symmetry by inserting a current $j = \frac{\hbar}{m}\phi'(x)$, where $\phi(x)$ is the phase of the condensate wavefunction. Within one period of the imprinted phase pattern, the sign of the local momentum flips twice, resulting

in two neighboring domains with opposite momenta. After the momentum kick, atoms in neighboring domains can flow toward or away from each other determined by the group velocity $v_g(x) = d\varepsilon_q/dq$, leading to the observed density peaks and troughs. Since density waves cost energy in a BEC with repulsive interactions, the atom flow reverses after half an oscillation period, yielding the phase alternation of the density wave.

The decisive role of phase imprinting in the real and momentum space dynamics and domain structure indicates the importance of phase fluctuations in quantum critical dynamics. Together with the emergence of density waves and atomic occupation in well-resolved momentum states, we present strong evidence supporting the coherent scenario of the quantum phase transition in our system. Furthermore, the phase imprinting technique can find new applications to engineering desired structure of domain walls, which will enable future study on the dynamics and interactions of topological defects.

4.5 GPE simulation of inflation

The coherent dynamics can be well captured by Gross-Pitaevskii theory when we approximate quantum fluctuation using random noise. Here we perform a numerical simulation is based on the Gross-Pitaevskii equation with an effective model in a one-dimensional lattice. In this model, space is discretized into lattice sites and kinetic motion is replaced by hopping between neighboring sites. We define $\psi_j(t)$ the value of the condensate wavefunction of site j at time t and the evolution is given by

$$i\gamma\hbar\frac{\partial}{\partial t}\psi_j(t) = -\sum_{n=1}^{n_T} t_k[\psi_{j-n}(t) + \psi_{j+n}(t)] + \left[\frac{1}{2}m\omega^2(jd)^2 + g|\psi_j(t)|^2 - \mu\right]\psi_j(t) \quad (4.22)$$

.

Here t_n is the tunneling energy between two lattice sites spatially separated by n sites, m is the atomic mass of Cs, ω is the harmonic trapping frequency, g is the coupling constant, μ is the chemical potential , d is the lattice period and n_T is the truncation number that

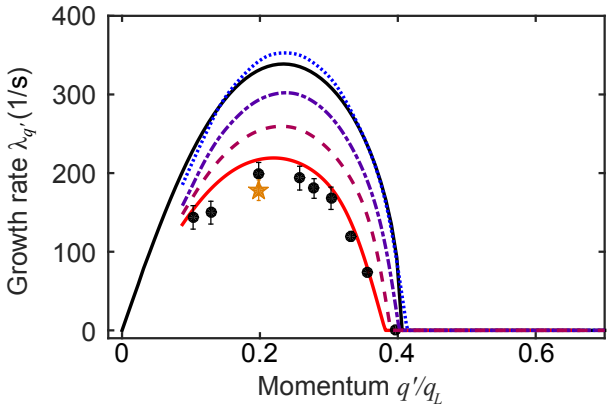

Figure 4.7: **Simulation of inflaton growth rate.** Here we show the measured growth rate $\lambda_{q'}$ from seeded (black dot) as well as the unseeded quench experiment (orange star). Black solid line is the prediction from Bogoliubov theory with effective chemical potential $\mu = h\times 125$ Hz. Lines in color from blue to red show the results from simulation with the seed amplitude $\delta\phi$: 0.1 (dot), 0.3 (dash-dot), 0.5 (dash) and 0.7 (red solid) . In the simulation, the trapping frequency $\omega = 2\pi\times$ 12 Hz, chemical potential $\mu = h\times 150$ Hz, lattice depth is 8.9 E_R and shaking amplitude $s = 25$ nm, which are based on the corresponding experiment.

shall be discussed later. γ is a parameter that controls the evolution in either imaginary time ($\gamma = i$) or real time ($\gamma = 1$). Particularly in imaginary time, evolution of the equation gives the ground state wavefunction of the system. In our simulation of inflation, we keep a small imaginary part by setting $\gamma = \cos\varphi + i\sin\varphi$ with $\varphi = 0.015$, which accounts for the dissipation in our system.

Tunneling energy t_n is determined from the Bloch band structure. In our experiment, all the atoms dominantly occupy the ground band even with lattice shaking. The tunneling energy is then the inverse Fourier transform of the ground band dispersion $t_n = \sum_q e^{-inq/\hbar}\varepsilon_q$. In a non-shaken lattice, the nearest-neighbor tunneling t_1 is the only significant term and sufficient to capture most of the physics. However, in a shaken lattice, where the ground band dispersion is significantly modified, higher order tunneling become significant as well. In our simulation, we found that $n_T = 3$ is a good truncation number and t_n with $n > 3$ are negligible.

We perform the simulation for our seeded quench experiment as follows. We first evolve equation in imaginary time to reach the ground state wavefunction in a non-shaken lattice.

To implement the seed, we multiply this ground state wavefunction by a spatially-varying phase factor $e^{i\delta\theta(j)}$ with $\delta\theta(j) = \delta\phi \sin(\frac{q'}{\hbar} jd)$ as the initial wavefunction for the next step, where $\delta\phi$ is the seed amplitude and q' is the seed momentum. To simulate the quench, we now evolve the initial wavefunction with a new set of tunneling energies in a shaken lattice. Later all the observables are extracted from the wavefunction in the same way as we did in our data anlaysis.

Simulations with respect to different seed amplitudes explain the discrepancy between experiment and Bogoliubov theory visible in Fig. 4.5**c** from the main text. Here we show the inflaton growth rate $\lambda_{q'}$ from our simulation in Fig. 4.7. For comparison, we also include the experimental data as well as the prediction from Bogoliubov theory. First, for small initial population depletion from the $q = 0$ state where $\delta\phi \leq 0.1$, the results from simulation agree well with that from Bogoliubov theory. However, further increase of $\delta\phi$ quickly drives the system out of the perturbative regime. As a result, the growth rate $\lambda_{q'}$ decreases as the seed amplitude $\delta\phi$ increases. The measured growth rates concur with the simulation with seed amplitude $\delta\phi = 0.7$, which is estimated to be 0.6(0.1) in experiments from the initial population depletion of the $q = 0$ state.

4.6 Kibble-Zurek scaling of the coherent dynamics

These coherent inflationary dynamics happen when the system the system is driven across a quantum phase transition. We know such dynamics should follow the Kibble-Zurek scaling that we demonstrated in the previous section by studying the formation of spin domains. We expect these density wave dynamics should scale in the same way as the domains and be compatible with the universality hypothesis, according to which the collective dynamics across a critical point are invariant in the space and time coordinates that scale with the Kibble-Zurek power law.

This scaling can be clearly see from the normalized contrast C_n of the density wave when the system is driven across the phase transition with constant speed by linearly ramping up

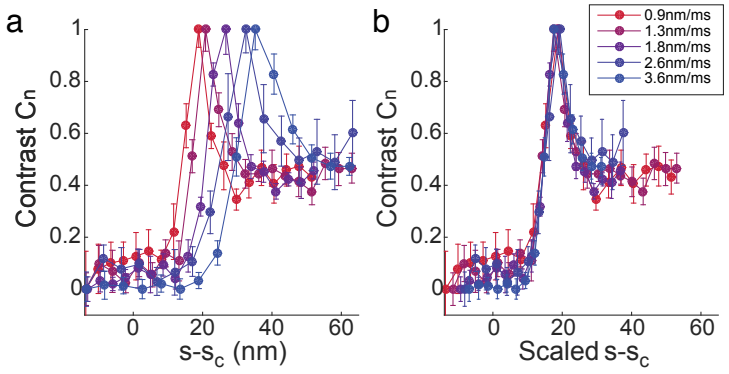

Figure 4.8: **Kibble-Zurek scaling of inflationary dynamics.** **a** shows the normalized contrast C_n as a function of shaking amplitude $s - s_c$. For slower(faster) ramp, the dynamics of the system unfreezes at smaller(larger) value of shaking amplitude. **b** shows the normalized contrast C_n as a function of rescaled shaking amplitude according to Kibble-Zurek scaling. Here the shaking amplitude of the ramps are rescaled to that of the slowest ramp with $\dot{s} = 0.9$ nm/ms based on $s - s_c \sim \dot{s}^{-0.5}$.

the shaking amplitude. Here we define the contrast $C = \int \Delta n(x, y) dxdy$, namely the total power of the density modulation, where $\Delta n(x, y) = n(x, y) - \bar{n}(x, y)$ is the column density fluctuation around its mean $\bar{n}(x, y)$ that is averaged from shot to shot. This contrast is then normalized to $C_n = (C - C_{min})/(C_{max} - C_{min})$, where C_{min} (C_{max}) is the minimum (maximum) value of the contrast during a linear ramp.

Figure 4.8**a** shows the normalized contrast C_n as a function of shaking amplitude $s - s_c$ for different linear ramps. According to the Kibble-Zurek mechanism, the system unfreezes at time scale of $t_{KZ} \sim \dot{s}^{-a}$ with $a = z\nu/(1 + z\nu) = 0.5$ in our system. If we now convert time t to shaking amplitude by $s - s_c = \dot{s}t$, we should have that the unfreezing shaking amplitude $s_{KZ} - s_c \sim \dot{s}^{1-a}$. Thus for slower(faster) ramp, the dynamics of the system unfreezes at smaller(larger) value of shaking amplitude. Once we rescale the shaking amplitude for different linear ramps to that of the ramp with $\dot{s} = 0.9$ nm/ms accordingly, the time evolution of the normalized contrast perfect collapse into a same form, see Fig. 4.8**b**. This nice collapse presents another test of the scaling law and the universal hypothesis.

4.7 Density-density correlation

We notice that the inflation Hamiltonian present a pair-generatio process, where a pair of inflaton with momentum $\pm q$ are generated simultaneously. This process resembles that from two-mode squeezing in quantum optics [106]. Here we evaluate the density-density correlations which we have not shown before. We will first theoretically calculate the correlation function based on the inflaton Hamiltonian. We then shall show the density-density correlations function from our 1D numerical simulation. At last, we extract the correlations from our data in a unseeded quench experiment to show the experimental evidence of the density-density correlation.

4.7.1 Theory based on two-mode squeezing

We start by considering the inflation Hamiltonian only for a single pair of momentum modes, which is simply given by

$$H = \hbar\lambda(\iota_q^\dagger \iota_{-q}^\dagger + \iota_q \iota_{-q}). \tag{4.23}$$

This Hamiltonian has the same form of a two-mode squeezing Hamiltonian similar to that in the "Bose Fireworks". The quantum state of the system generated from vacuum in the interaction picture can then be written as following.

$$|\psi\rangle_{q,-q} = \frac{1}{\cosh\gamma} \sum_{n=0}^{\infty} (-i\tanh\gamma)^n |n,n\rangle, \tag{4.24}$$

where $\gamma = \lambda t$. We are interested in calculating the expectation value of various observables.

We can first do a simple check to make sure that this calculation is consistent with that in Sec. 4.3. Here we want to see if we can obtain the same time evolution for atom number

excitation in Eq. (4.20). Let's first look at the inflaton number operator $m_{\pm q} = \iota^\dagger_{\pm q}\iota_{\pm q}$,

$$\langle m_{\pm q}\rangle = \langle \iota^\dagger_{\pm q}\iota_{\pm q}\rangle = \frac{1}{\cosh^2\gamma}\sum_{n=0}^{\infty}(\tanh^2\gamma)^n n \tag{4.25}$$

$$= \sinh^2\gamma \equiv \langle n\rangle, \tag{4.26}$$

where we can think of a probability density distribution function of

$$P(n) \equiv \frac{1}{\cosh^2\gamma}\sum_{n=0}^{\infty}(\tanh^2\gamma)^n \tag{4.27}$$

with variable n and $\langle n\rangle$ the mean value of the variable n. This greatly simplifies the calculation in the following. The interference operators $\iota^\dagger_{\pm q}\iota^\dagger_{\mp q} = (\iota_{\pm q}\iota_{\mp q})^\dagger$ and

$$\langle \iota_{\pm q}\iota_{\mp q}\rangle = \frac{-i\tanh\gamma}{\cosh^2\gamma}\sum_{n=0}^{\inf}(\tanh^2\gamma)^n(n+1) \tag{4.28}$$

$$= -i\tanh\gamma\langle n+1\rangle \tag{4.29}$$

which is imaginary. Based on the Bogoliubov transformation, the excited atomic population is given by

$$\begin{aligned}\langle n_{\pm q}\rangle = \langle a^\dagger_{\pm q}a_{\pm q}\rangle &= \langle (u\iota^\dagger_{\pm q} - \nu\iota_{\mp q})(u\iota_{\pm q} - \nu\iota^\dagger_{\mp q})\rangle \\ &= u^2\langle \iota^\dagger_{\pm q}\iota_{\pm q}\rangle + \nu^2\langle \iota_{\mp q}\iota^\dagger_{\mp q}\rangle - u\nu\underbrace{\langle \iota^\dagger_{\pm q}\iota^\dagger_{\mp q} + \iota_{\pm q}\iota_{\mp q}\rangle}_{=0} \\ &= (u^2+\nu^2)\langle n\rangle + \nu^2. \end{aligned} \tag{4.30}$$

Therefore the relation between atomic population and the inflaton population is given by $\langle a^\dagger_q a_q + a^\dagger_{-q}a_{-q} + 1\rangle = \frac{\mu}{\hbar\lambda}\langle \iota^\dagger_q\iota_q + \iota^\dagger_{-q}\iota_{-q} + 1\rangle$, which is the same results in Eq. (4.20).

We are interested in the relation between the density-density correlations in atom basis and inflaton basis. The density-density correlation between atoms in $\pm q$ states is given by

$\langle n_q n_{-q}\rangle = \langle a_q^\dagger a_q a_{-q}^\dagger a_{-q}\rangle$, where

$$
\begin{aligned}
a_q^\dagger a_q a_{-q}^\dagger a_{-q} = & \underbrace{(u^2\iota_q^\dagger\iota_q + \nu^2\iota_{-q}\iota_{-q}^\dagger)(u^2\iota_{-q}^\dagger\iota_{-q} + \nu^2\iota_q\iota_q^\dagger)}_{F_1} \\
& + \underbrace{u^2\nu^2(\iota_q^\dagger\iota_{-q}^\dagger + \iota_q\iota_{-q})^2}_{F_2} \\
& - \underbrace{u\nu[(\iota_q^\dagger\iota_{-q}^\dagger + \iota_q\iota_{-q})(u^2\iota_{-q}^\dagger\iota_{-q} + \nu^2\iota_q\iota_q^\dagger) + (u^2\iota_q^\dagger\iota_q + \nu^2\iota_{-q}\iota_{-q}^\dagger)(\iota_q^\dagger\iota_{-q}^\dagger + \iota_q\iota_{-q})]}_{F_3}.
\end{aligned}
$$

Here we have used the inverse transformation $\iota_{\pm q} = ua_{\pm q} + \nu a_{\mp q}^\dagger$. We have divided this quantity into three parts F_1, F_2 and F_3 and we shall deal with each of them separately in the following. Regarding the first term F_1, we have

$$
\begin{aligned}
\langle F_1\rangle &= \langle(u^2\iota_q^\dagger\iota_q + \nu^2\iota_{-q}\iota_{-q}^\dagger)(u^2\iota_{-q}^\dagger\iota_{-q} + \nu^2\iota_q\iota_q^\dagger)\rangle \\
&= u^4\langle n^2\rangle + \nu^4\langle(1+n)^2\rangle + 2u^2\nu^2\langle n(n+1)\rangle \\
&= \langle(u^2 n + \nu^2(n+1))^2\rangle \\
&\approx (u^2+\nu^2)^2\langle n^2\rangle|_{n\gg 1}.
\end{aligned} \tag{4.31}
$$

Regarding the second term F_2, we have

$$
\begin{aligned}
\langle F_2\rangle &= \langle u^2\nu^2(\iota_q^\dagger\iota_{-q}^\dagger + \iota_q\iota_{-q})^2\rangle \\
&= 2u\nu^2(\langle(n+1)^2\rangle + \langle n^2\rangle - 2\tanh^2\gamma\langle(n+1)(n+2)\rangle) \\
&\approx 0|_{n\gg 1\&\gamma\gg 1}.
\end{aligned} \tag{4.32}
$$

Last for the third term F_3, we have

$$\begin{aligned}\langle F_3\rangle &= u\nu\langle(\iota_q^\dagger\iota_{-q}^\dagger+\iota_q\iota_{-q})(u^2\iota_{-q}^\dagger\iota_{-q}+\nu^2\iota_q\iota_q^\dagger)+(u^2\iota_q^\dagger\iota_q+\nu^2\iota_{-q}\iota_{-q}^\dagger)(\iota_q^\dagger\iota_{-q}^\dagger+\iota_q\iota_{-q})\rangle\\ &= u\nu\langle(\iota_q^\dagger\iota_{-q}^\dagger+\iota_q\iota_{-q})(u^2\iota_{-q}^\dagger\iota_{-q}+\nu^2\iota_q\iota_q^\dagger)+(u^2\iota_q\iota_q^\dagger+\nu^2\iota_{-q}^\dagger\iota_{-q})(\iota_q^\dagger\iota_{-q}^\dagger+\iota_q\iota_{-q})\rangle\\ &- u\nu(u^2-\nu^2)\underbrace{\langle\iota_q^\dagger\iota_{-q}^\dagger+\iota_q\iota_{-q}\rangle}_{=0}.\end{aligned}$$

We can again divide this term into several parts as follows,

$$\begin{aligned}A &= \langle\iota_q^\dagger\iota_{-q}^\dagger\iota_{-q}^\dagger\iota_{-q}\rangle = \langle\iota_{-q}^\dagger\iota_{-q}\iota_q\iota_{-q}\rangle^\dagger\\ B &= \langle\iota_q\iota_{-q}\iota_{-q}^\dagger\iota_{-q}\rangle = \langle\iota_{-q}^\dagger\iota_{-q}\iota_q^\dagger\iota_{-q}^\dagger\rangle^\dagger\\ C &= \langle\iota_q^\dagger\iota_{-q}^\dagger\iota_q\iota_q^\dagger\rangle = \langle\iota_q\iota_q^\dagger\iota_q\iota_{-q}\rangle^\dagger\\ D &= \langle\iota_q\iota_{-q}\iota_q\iota_q^\dagger\rangle = \langle\iota_q\iota_q^\dagger\iota_q^\dagger\iota_{-q}^\dagger\rangle^\dagger.\end{aligned}$$

It's easy to test that A, B, C and D are pure imaginary, for example

$$\begin{aligned}\langle\iota_q^\dagger\iota_{-q}^\dagger\iota_{-q}^\dagger\iota_{-q}\rangle &= \frac{i\tanh\gamma}{\cosh^2\gamma}\sum_{n=0}^{\inf}(\tanh^2\gamma)^n n(n+1)\\ &= i\tanh\gamma\langle n(n+1)\rangle.\end{aligned}$$

As a result, we can easily find that

$$\begin{aligned}\langle F_3\rangle &= u\nu[u^2(A+B)+\nu^2(C+D)+u^2(A+B)^*+\nu^2(C+D)^*]\\ &= 0\end{aligned}\tag{4.33}$$

. Finally we can see that under the approximation that $n \gg 1$ and $\gamma \gg 1$, combining the results from Eq. (4.31,4.32, 4.33) we shall have the overall density-density correlation

$$\langle n_q n_{-q}\rangle = \langle a_q^\dagger a_q a_{-q}^\dagger a_{-q}\rangle \approx (u^2+\nu^2)^2\langle n^2\rangle$$
$$= (u^2+\nu^2)^2\langle m_q m_{-q}\rangle, \tag{4.34}$$

and the correlation between density fluctuations

$$\langle \delta n_q \delta n_{-q}\rangle = \langle a_q^\dagger a_q a_{-q}^\dagger a_{-q}\rangle - \langle a_q^\dagger a_q\rangle\langle a_{-q}^\dagger a_{-q}\rangle \approx (u^2+\nu^2)^2[\langle \iota_q^\dagger \iota_q \iota_{-q}^\dagger \iota_{-q}\rangle - \langle \iota_q^\dagger \iota_q\rangle\langle \iota_{-q}^\dagger \iota_{-q}\rangle]$$
$$- 2\nu^2(u^2+\nu^2)\langle n\rangle - \nu^4$$
$$\approx (u^2+\nu^2)^2[\langle m_q m_{-q}\rangle - \langle m_q\rangle\langle m_{-q}\rangle]$$
$$\tag{4.35}$$

Following the same spirit, we can also obtain the density-density correlations $\langle \tilde{n}_q \tilde{n}_q\rangle = \langle a_q^\dagger a_q a_q^\dagger a_q\rangle$ at limit $\langle m\rangle \gg 1$. Here we obtain

$$\langle n_q n_q\rangle = \langle a_q^\dagger a_q a_q^\dagger a_q\rangle \approx (u^2+\nu^2)^2\langle n^2\rangle \tag{4.36}$$
$$= (u^2+\nu^2)^2\langle m_q m_{-q}\rangle$$

, and

$$\langle \delta\tilde{n}_q \delta\tilde{n}_q\rangle = \langle a_q^\dagger a_q a_q^\dagger a_q\rangle - \langle a_q^\dagger a_q\rangle\langle a_q^\dagger a_q\rangle \approx (u^2+\nu^2)^2[\langle \iota_q^\dagger \iota_q \iota_{-q}^\dagger \iota_{-q}\rangle - \langle \iota_q^\dagger \iota_q\rangle\langle \iota_{-q}^\dagger \iota_{-q}\rangle]$$
$$- 2\nu^2(u^2+\nu^2)\langle n\rangle - \nu^4$$
$$\approx (u^2+\nu^2)^2[\langle m_q m_{-q}\rangle - \langle m_q\rangle\langle m_{-q}\rangle] \tag{4.37}$$

.

This result indicates a simple relation between the atom density-density correlations and inflaton density-density correlation. More interestingly, it shows that the detectable $\langle n_q n_q\rangle = \langle n_q n_{-q}\rangle \propto \langle m_q m_{-q}\rangle$ and $\langle \delta n_q \delta n_q\rangle = \langle \delta n_q \delta n_{-q}\rangle \propto \langle \delta m_q \delta m_{-q}\rangle$, meaning the cor-

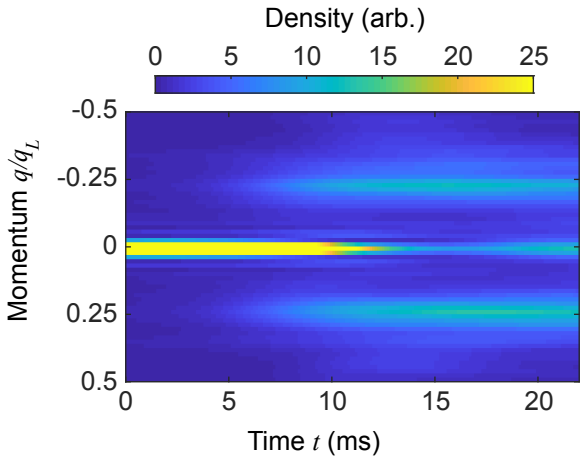

Figure 4.9: **Time evolution of atomic population in 1D GPE simulation.** Here the shaking amplitude is suddenly turn on from $s = 0$ nm to $s = 25$ nm at time $t = 0$. The minima of the single particle dispersion locate at $\pm q^* = \pm 0.24 q_L$.

relation from pair-production should reflected in all the four quadrants in $q - q'$ plane during the inflation stage when the inflation Hamiltonian still holds. When the condensate become largely depleted, the story should be different.

4.7.2 Numerical simulation on quench experiment

Based on our previous 1D numerical simulation in Sec. 4.5, we can first see if we get such correlation between $\pm q$ during the inflation stage. Here we use parameters to numerically calculate the evolution after a sudden quench of shaking amplitude from $s = 0$ nm to $s = 25$ nm at $t = 0$ ms. According to Floquet theory, the minima of the dispersion appear at $\pm q^* = \pm 0.24 q_L$ at $s = 25$ nm. Figure 4.9 shows the time evolution of the density distribution $\langle n_q \rangle$ in momentum space, where atomic population evolves into the new lower energy states.

We can further evaluate the density-density correlation between different momentum modes $\langle n_q n_{q'} \rangle$, shown in Fig. 4.10. At early time, the center spot at $(q, q') = (0, 0)$ is simply from the condensate itself while the horizontal and vertical lines are from the random seed as well as the condensate. As atoms evolve to new energy minima, strong correlations start

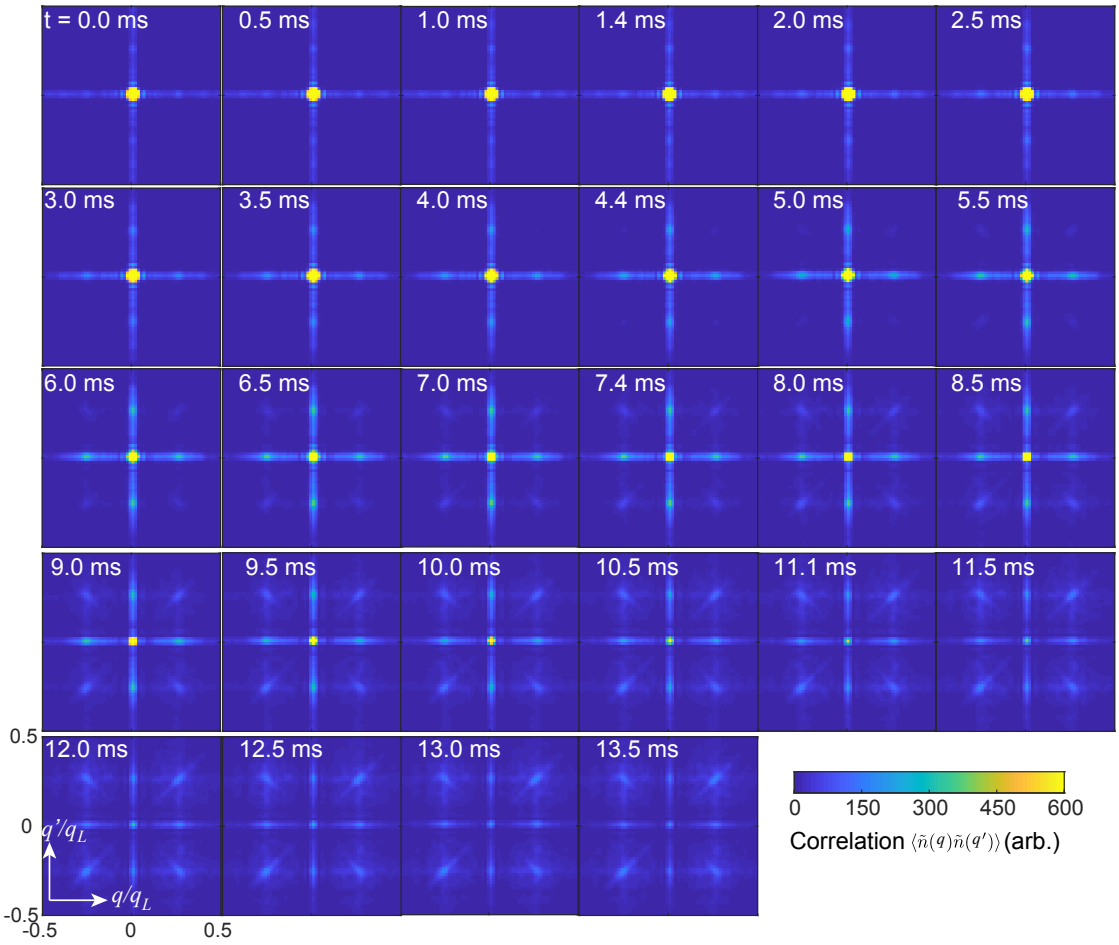

Figure 4.10: **Density-density correlation of atomic population in 1D GPE simulation.** The density-density correlation between different momentum modes $\langle n_q n_{q'} \rangle$ shows qualitative agreement with the theory, where the correlation in the diagonal and off-diagonal direction are approximately the same.

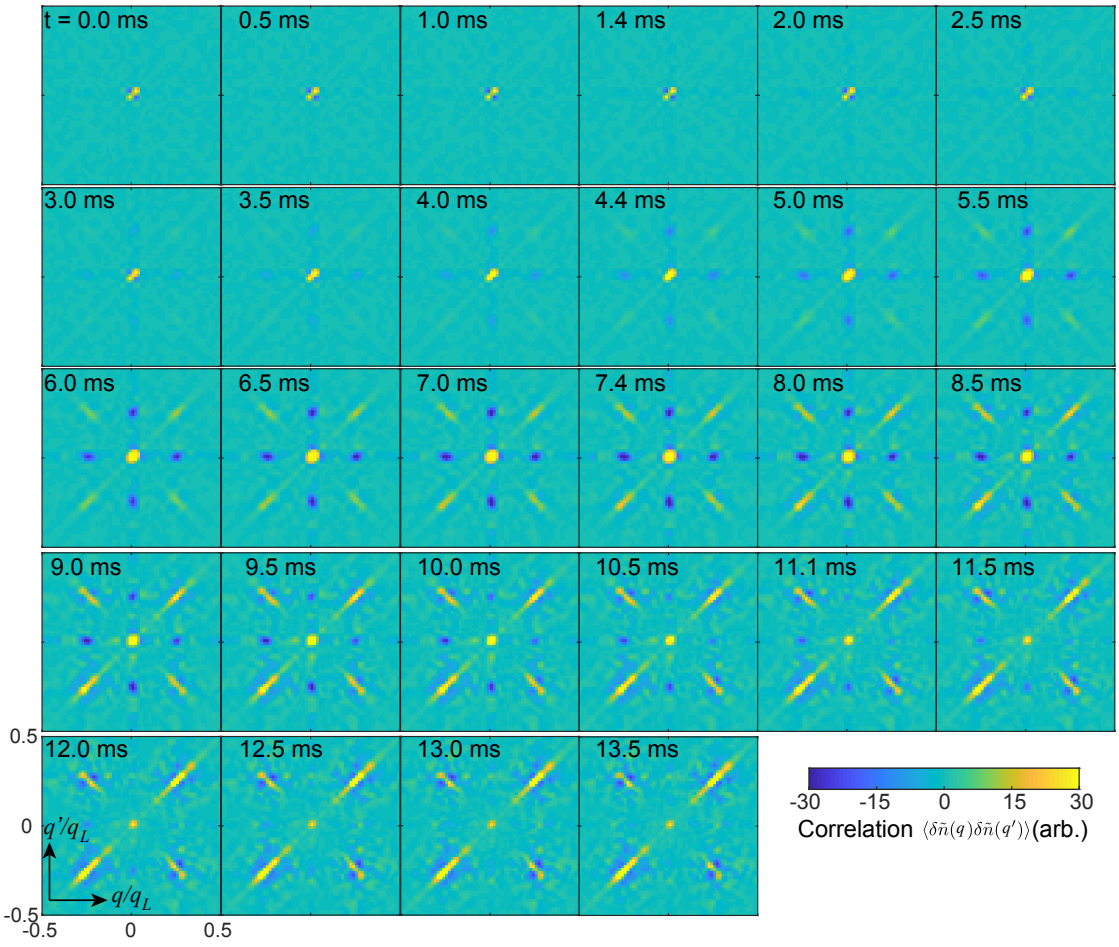

Figure 4.11: **Correlation of atomic density fluctuation in 1D GPE simulation.** The correlation between density fluctuations of different momentum modes $\langle\delta\tilde{n}_q\delta\tilde{n}_{q'}\rangle$ shows clearer indication of pair production in the off-diagonal direction.

to appear along the diagonal and off-diagonal directions. This comes from the simultaneous generation of the inflaton pairs. At the same time, the center spots decays due to depletion of the condensate.

A more interesting quantity to look at is the correlation between density fluctuations, $\langle\delta\tilde{n}_q\delta\tilde{n}_{q'}\rangle$, shown in Fig. 4.11. The clear positive correlations rising along the off-diagonal direction clearly indicate simultaneous generation of inflaton pairs while depleting the condensate. This depletion shows up as negative correlations along horizontal and vertical directions. The positive correlation along the off-diagonal direction later decays during the

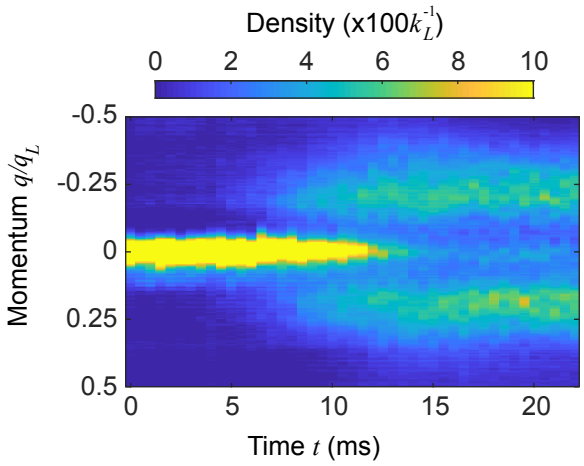

Figure 4.12: **Time evolution of atomic population in unseeded quench experiment.** Here the shaking amplitude is suddenly turn on from $s = 0$ nm to $s = 25$ nm at time $t = 0$. The minima of the single particle dispersion locate at $\pm q = \pm 0.24 q_L$. The momentum

relaxation and become negative eventually indicating hopping from $\pm q^*$ to $\mp q^*$ (which is not clearly shown here but it will become obvious at a later time).

4.7.3 Correlation in unseeded quench experiment

Beside the simulation, We have also performed experiments where no seed is applied. The final shaking amplitude is set to $s = 25$ nm. Figure 4.12 shows the density distribution $\langle \tilde{n}_q \rangle$ in momentum space from a focused time-of-flight measurement. Here $t = 0$ ms is the time when we quench on shaking. The experiments show very similar results as that in the numerical simulation except that the momentum modes seems to be much broader. The broadening comes from two effects: the resolution in momentum space after focused time-of-flight and the fluctuation of the trapping potential.

The fluctuation of the trapping potential can be seen from the fact that the excitation spectrum drifts up and down after focused time flight (see Fig. 4.13). This fluctuation likely comes from the instability of the harmonic trap or drifting fringes from interference between stray light. The amount of shift is on the order of $0.05 q_L$, 15% of q^*, which is

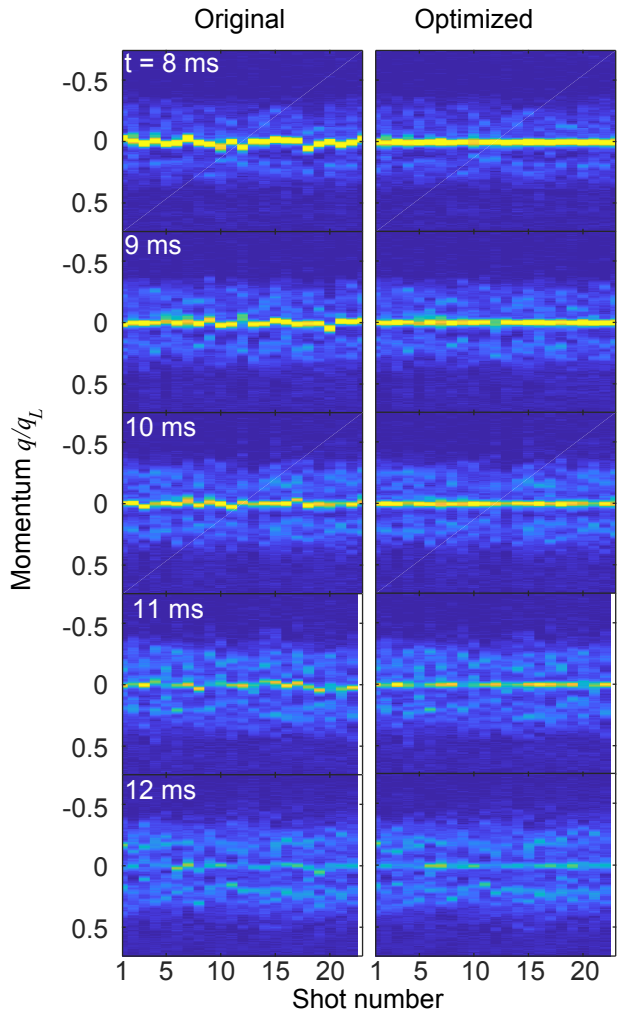

Figure 4.13: **Fluctuation and optimization in atomic population in unseeded quench experiment.** Left: the fluctuation of atomic distribution in momentum space from shot to shot. Right: the aligned atomic distribution in momentum space based on the location of the center peak from BEC.

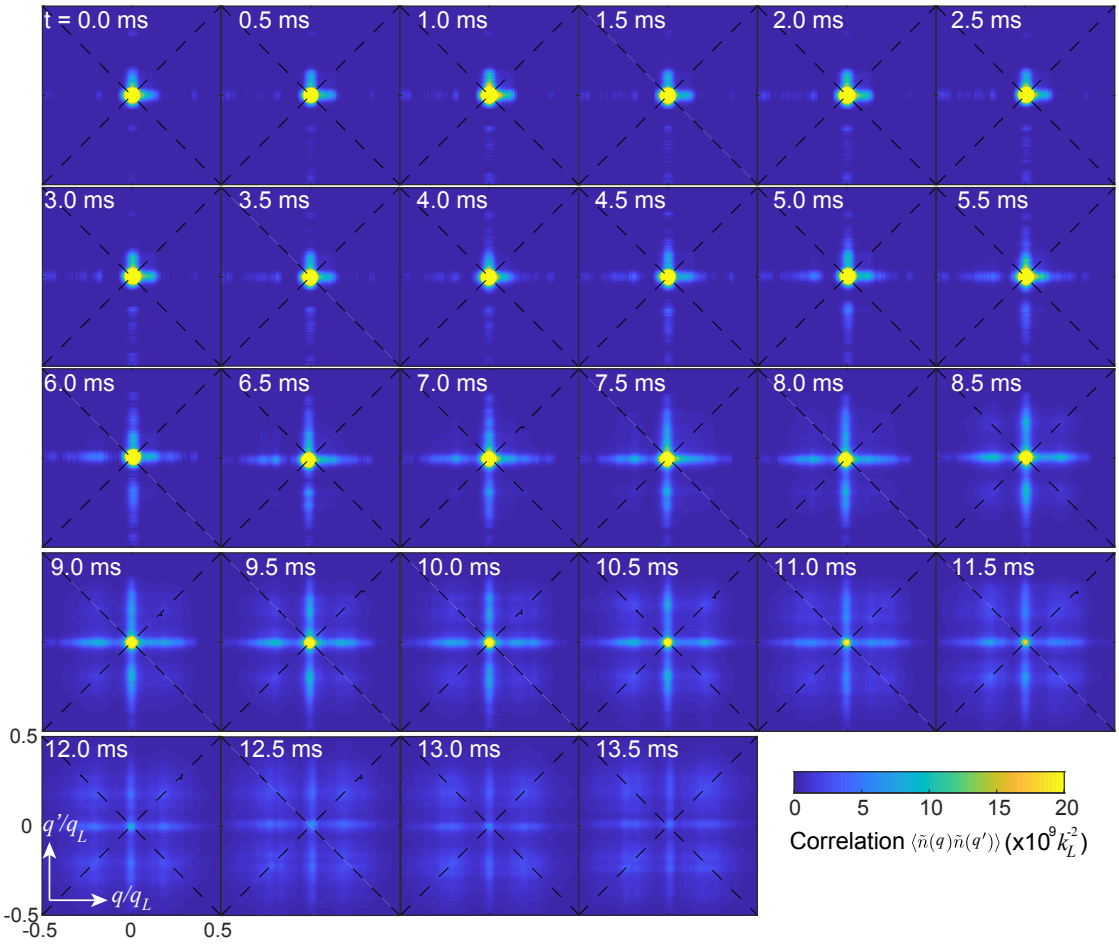

Figure 4.14: **Density-density correlation of atomic population from unseeded quench experiment.**

very significant. Therefore these fluctuations can totally smear out any correlation between density fluctuations. To overcome this issue, we tried to align the density distribution in momentum space from different iterations of experiment based on the center peak at $q = 0$. Unfortunately, this technique does not work for the relaxation stage at later time when the condensate would be completely depleted.

After the center alignment, we then calculate the density-density correlation as we did earlier in the numerical simulation. Figure 4.14 shows the density-density correlation between different momentum modes, $\langle \tilde{n}_q \tilde{n}_{q'} \rangle$, where alignment largely improved the signal.

We then proceed to look at the correlations between density fluctuations between different

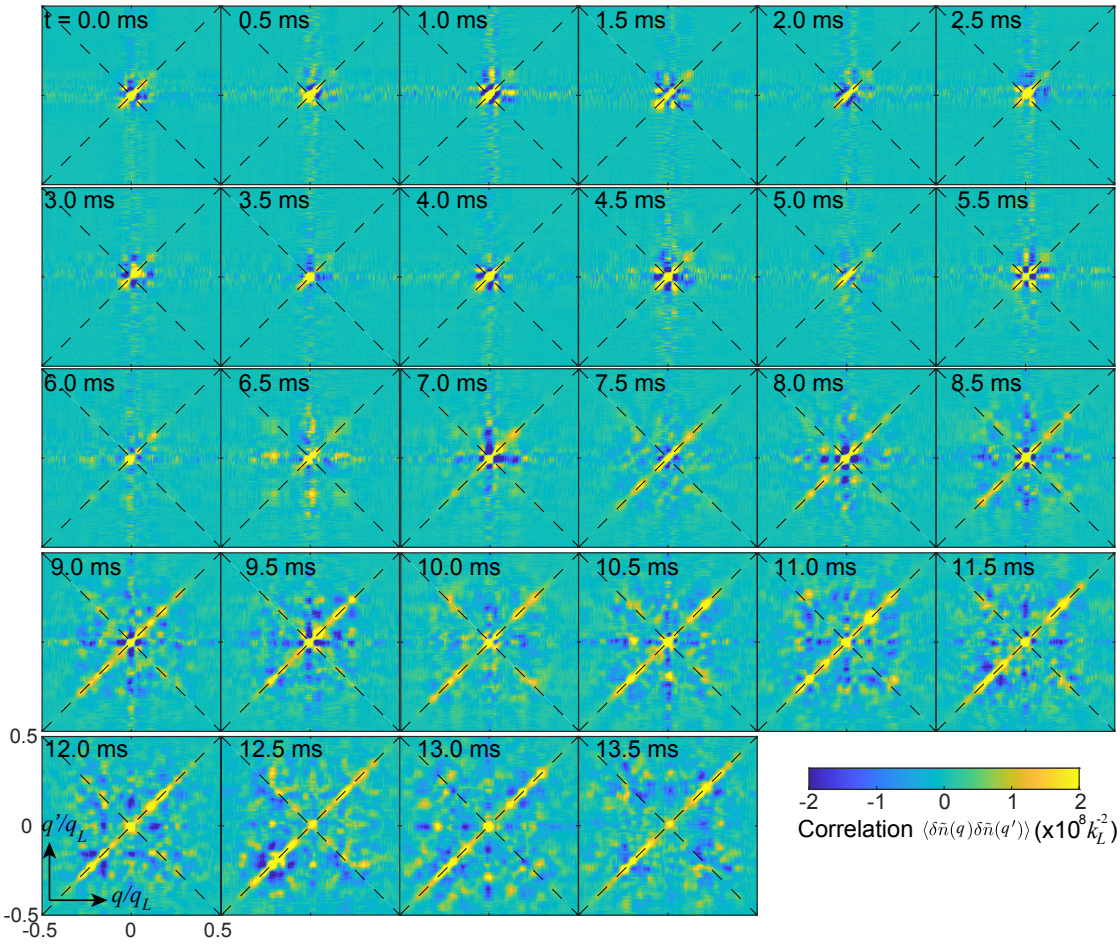

Figure 4.15: **Correlation of atomic density fluctuation from unseeded quench experiment.**

momentum modes, $\langle \delta\tilde{n}_q \delta\tilde{n}_{q'} \rangle$, see Fig. 4.15. This time similar correlations shows up in our experiment as well. We can now see the clear positive correlation rising along the off-diagonal direction, which indicate simultaneous generation of inflaton pairs. We can even see that this positive correlation along the off-diagonal direction later decays when condensate is significantly depleted at later time.

CHAPTER 5

HIGH-HARMONIC GENERATION OF MATTER-WAVE JETS

High harmonic generation is an elegant phenomenon in nonlinear optics in which photon populations are transferred to specific excited modes; it enables modern applications such as X-ray sources [19], attosecond spectroscopy [51, 31] and frequency combs [61, 42]. The generation of high harmonics relies on strong coherent driving the nonlinearity of the coupling between photons and particles [15].

In atom optics, the matter-wave analog of optics, naturally inherits nonlinearity stems from atomic interactions [90, 26]. The matter-wave versions of lasers [76, 1, 14, 48], superradiance [59, 78, 94], four-wave mixing [30, 102], Faraday instability [98, 34] and spin-squeezing [43, 88], have made manifest the quantum coherence of matter waves. In particular, a sufficiently strong photon-atom scattering can generate high harmonics of matter waves in superradiant BECs [59, 94]. Moreover, related experiments on splitting and interfering a condensate [5, 49] have demonstrated and characterized high-order correlations [44, 27, 96], akin to homodyne detection with lasers. Beyond analogies to quantum optics, the manipulation of coherent matter waves can also offer a unique platform to simulate large-scale [57, 99, 36] and high-energy physics [7].

We demonstrate high harmonic generation of matter waves by strongly modulating the interactions between atoms in a Bose condensate. We have seen that matter waves emerging from the driven condensates form jet-like emission (Bose fireworks) due to inelastic collisions between atoms [25, 108]. Above a threshold in the driving amplitude, a quantized spectrum of the matter-wave manifests due to bosonic stimulation, whose temporal evolution suggests a hierarchy of the atomic emission process. By applying a pattern recognition algorithm [40, 80] (see Sec. 5.4), we identify intriguing second- and higher-order correlations of emitted atoms that are not obvious from individual experiments.

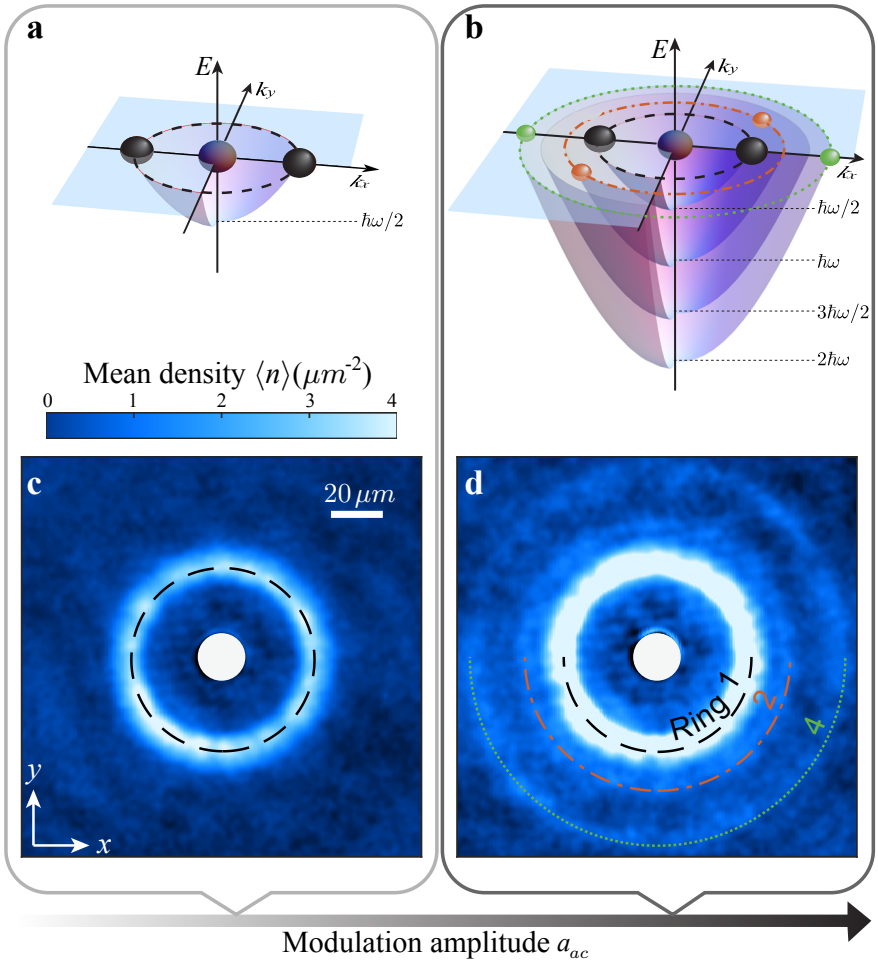

Figure 5.1: **The first and high harmonic generation of matter-wave jets in driven condensates.** **a** and **b** show the dispersion relation between energy E and momentum $\hbar\mathbf{k} = \hbar\left(k_x, k_y\right)$ in the dressed-state picture. **c** shows the average *in situ* image of emitted atoms at a small modulation amplitude $a_{ac} = 25\ a_0$. The emission pattern displays a single ring (highlighted by the black dashed circle) indicating the generation of matter-wave jets with momentum k_f. **d** shows two more rings (orange and green circles) in the average image at a larger modulation amplitude $a_{ac} = 45\ a_0$. Atoms in these three rings have quantized kinetic energy of $\hbar\omega/2$, $\hbar\omega$, and $2\hbar\omega$ respectively. The *in situ* images are taken at 21 ms after the beginning of the modulation.

5.1 Experimental setup

The experiment starts with Bose-Einstein condensates of 6×10^4 cesium atoms loaded into a uniform disk-shaped trap with a radius of 7 μm, a barrier height of $h\times$300 Hz in the horizontal direction and harmonic trapping frequency of 220 Hz in the vertical direction [25], where $h = 2\pi\hbar$ is the Planck constant. The interaction between atoms, characterized by the s-wave scattering length a, can be tuned near a Feshbach resonance by varying the magnetic field [20].

After the preparation, we oscillate the scattering length as $a(t) = a_{dc} + a_{ac}\sin(\omega t)$ for a short period of time τ= 5 ms with a small DC value $a_{dc} = 3\ a_0$ and a tunable amplitude a_{ac} at frequency $\omega = 2\pi \times 2$ kHz. Here a_0 is the Bohr radius. We then perform either *in situ* imaging or time-of-flight measurement on the sample. At a modulation amplitude $a_{ac} = 25\ a_0$ we see the emission of matter-wave jets with each atom emitted at kinetic energy of $\hbar\omega/2$, as evidenced by the velocity with which they leave the sample [25].The angles of the emitted jets vary randomly from shot to shot, resulting in a single isotropic ring of atoms after averaging images over many trials (Fig. 5.1**c**). At a larger amplitude $a_{ac} = 45\ a_0$ multiple rings form, labeled as ring 1, ring 2 and ring 4 (Fig. 5.1**d**). Atoms in each ring have quantized kinetic energy of $E_j = j\hbar\omega/2 = j\hbar^2k_f^2/2m$ with $j = 1$, 2, and 4, where $k_f = \sqrt{m\omega/\hbar}$ is the characteristic wave number of the jets and m is the atomic mass.

5.2 Five wave-mixing

To describe atoms with oscillating scattering length, we derive the Hamiltonian of the system. We start with the general form of the Hamiltonian

$$H = \int d^3\mathbf{r}\Psi^\dagger(\mathbf{r},t)\frac{p^2}{2m}\Psi(\mathbf{r},t) + \frac{g(t)}{2}\int d^3\mathbf{r}\Psi^\dagger(\mathbf{r},t)\Psi^\dagger(\mathbf{r},t)\Psi(\mathbf{r},t)\Psi(\mathbf{r},t) + \frac{1}{\mu_0}\int d^3\mathbf{r}|B(\mathbf{r},t)|^2 \tag{5.1}$$

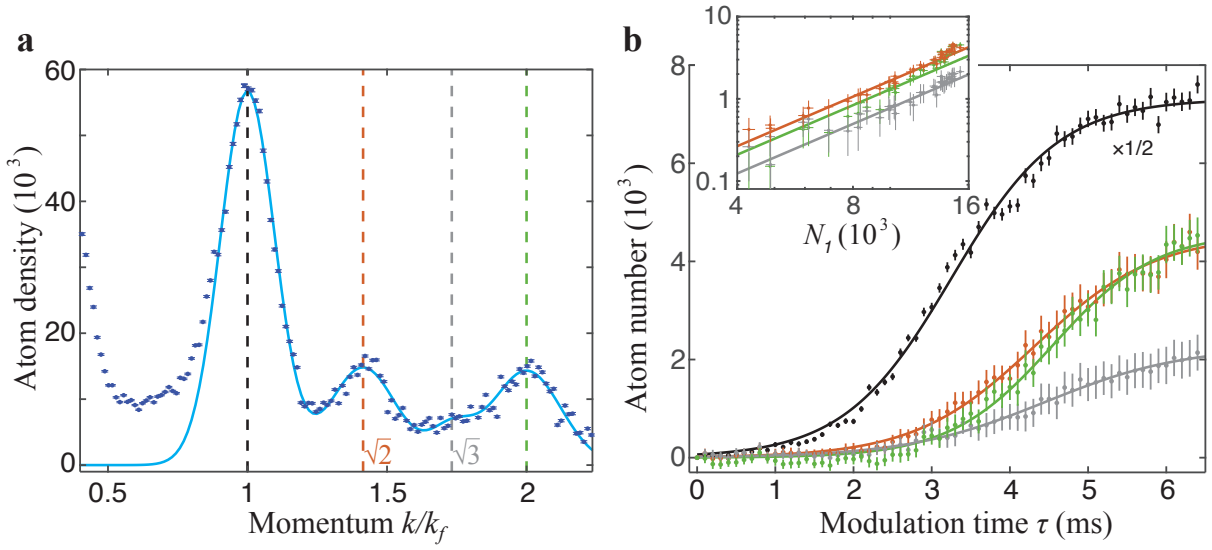

Figure 5.2: **The atomic population growth in multiple rings. a** A snapshot of the population distribution in momentum space measured by the focused-TOF imaging $\tau = 6$ ms after the modulation starts. The cyan curve is a fit to the experimental data for $k/k_f > 0.85$ using a combination of 4 Gaussians. The vertical dashed lines indicate centers of the Gaussians, fixed at $k/k_f = 1$ (black), $\sqrt{2}$ (orange), $\sqrt{3}$ (gray), and 2 (green), respectively. **b** Extracted atom number in each ring as a function of modulation time τ. The atom number in ring 1 (black) is scaled by a factor of 1/2. Populations in ring 2 (orange), 3 (gray), and 4 (green) start growing after ring 1 is significantly populated. Inset: atom number in ring 2, 3 and 4 as a function of atom number in ring 1 on a log-log scale. The solid lines are the power-law fits to the data with the exponent fixed to 2. The error bars represent one standard error.

, where $g(t) = 4\pi\hbar^2 a(t)/m$ is the interaction constant, scattering length $a(t) = a_{dc} + a_{ac}\sin(\omega t)$ is from magnetic field modulation $B(\mathbf{r}, t) = B_{ac}\sin(\omega t)$ with B_{ac} the modulation amplitude, and μ_0 is the vacuum permeability. By applying the Fourier transformation

$$\Psi(\mathbf{r}, t) = \frac{1}{\sqrt{V}} \sum_k e^{i\mathbf{kr}} a_{\mathbf{k}} \tag{5.2}$$

, where V is the volume of the condensate, we obtain the Hamiltonian in momentum space

$$H = \sum_{\mathbf{k}} \epsilon_k a^\dagger_{\mathbf{k}} a_{\mathbf{k}} + \frac{g(t)}{2V} \sum_{\mathbf{k}_1, \mathbf{k}_2, \Delta\mathbf{k}} a^\dagger_{\mathbf{k}_1 + \Delta\mathbf{k}} a^\dagger_{\mathbf{k}_2 - \Delta\mathbf{k}} a_{\mathbf{k}_1} a_{\mathbf{k}_2} + \frac{1}{\mu_0} \int d^3\mathbf{r} |B(\mathbf{r}, t)|^2 \tag{5.3}$$

.

When modulating the scattering length using magnetic field within a linear region near a Feshbach resonance, the change of scattering length is proportional to the change of magnetic field $\delta a = \eta \delta B$ with η a constant. As we introduce the quantization of the magnetic field,

$$B = i\sqrt{\frac{\hbar\omega\mu_0}{2V}}(b - b^\dagger) \tag{5.4}$$

with b ($b^\dagger$) the creation (annihilation) operator for a RF photon, the Hamiltonian can be rewritten as

$$H = \sum_{\mathbf{k}} \epsilon_k a^\dagger_{\mathbf{k}} a_{\mathbf{k}} + \hbar\omega b^\dagger b + \sum_{\mathbf{k_1}, \mathbf{k_2}, \Delta\mathbf{k}} \left(A a^\dagger_{\mathbf{k_1} + \Delta\mathbf{k}} a^\dagger_{\mathbf{k_2} - \Delta\mathbf{k}} a_{\mathbf{k_1}} a_{\mathbf{k_2}} b + h.c. \right), \tag{5.5}$$

with coupling constant A defined by

$$A = i\frac{\pi\hbar^2\eta}{mV}\sqrt{\frac{2\hbar\omega\mu_0}{V}}. \tag{5.6}$$

Notice that we neglect the momentum carried by the RF photon, which is eleven orders of magnitude smaller than $\hbar k_f$ in our experiments. The resonant terms that satisfy energy

conservation,

$$\epsilon_{\mathbf{k_1}+\Delta\mathbf{k}} + \epsilon_{\mathbf{k_2}-\Delta\mathbf{k}} = \epsilon_{\mathbf{k_1}} + \epsilon_{\mathbf{k_2}} \pm \hbar\omega, \tag{5.7}$$

describe the dominant collision processes.

The Hamiltonian describes a five-wave mixing process where, by absorbing or emitting one photon, an atom pair increases or decreases its total kinetic energy by an energy quantum $\hbar\omega$.This five-wave mixing process distinguishes our system from that in twin beam generation experiments [17, 60, 97]. In these twin beam generation experiments, atoms are first pumped to an excited state. The excited atoms then scatter and decay into pairs of emitted atoms. Since the pumping is a single atom process and is not phase correlated with the emission of atom pairs, the systems are better described by the four-wave mixing. In contrast, the phase of the driving field is directly imprinted to the phases of the scattering atoms in our system and therefore it is better described by the five-wave mixing process although the momentum transfer by the photon is negligible.

Based merely on the conservation of energy and momentum, the five-wave mixing can produce atoms in a continuous spectrum of energy states. However, given bosonic stimulation, we expect a quantized energy spectrum of the emitted atoms. Here starting with the condensate, the collisions first excite atoms to ring 1. As the population in ring 1 builds up, atoms can be further promoted to higher momentum modes through the matter-wave mixing of the condensate and the atoms in ring 1. Because of bosonic stimulation, such process is dominated by scattering involving three macroscopically occupied modes and the fourth unoccupied mode with higher energy. Therefore a hierarchy of stimulated collisions is expected. From energy conservation Eq. (5.7), atoms in the fourth mode acquire discrete energies $E_j = j\hbar\omega/2$ with $j = 2, 3, 4, ...$, analogous to the photon spectra from high harmonic generation.

5.3 Hierarchy of stimulated collisions

We further inspect the evolution of atomic population in each ring using time-of-flight imaging [36]. Figure 5.2**a** shows an example of the momentum distribution after modulating the scattering length for $\tau = 5$ ms. Beside the distinct peaks at $|\mathbf{k}| = k_f$, $\sqrt{2}k_f$ and $2k_f$, which are apparent from *in situ* images (Fig. 5.1), we also detect a much weaker peak at $|\mathbf{k}| = \sqrt{3}k_f$ (ring 3). We fit the density distribution using a combination of four Gaussians with fixed central positions and widths. These central positions and widths are extracted from the data after a long-time strong modulation, where different rings are maximally populated by stimulated emission in order to achieve the best accuracy. During this process, the centers and widths of the four Gaussians are fitting parameters as well.

Populations in all four rings initially show a fast exponential growth and then gradually saturate afterward (Fig. 5.2**b**). The population growth of rings 2, 3 and 4 are delayed with respect to that of ring 1. Furthermore, we observe that the populations in higher-order rings are proportional to the square of the population in ring 1, $N_j \propto N_1^2$ with $j = 2$, 3 and 4 (Fig. 5.2**b** inset). Because the population grows exponentially, this relation is equivalent to $\dot{N}_j \propto N_1^2$, which suggests that the production of atoms in the these rings involves two modes in ring 1. This observation is in agreement with a perturbative model in Sec. 5.5. We thus consider these processes as secondary collisions, which occur after ring 1 is populated by primary collisions. To gather more information about these secondary collisions, we look into the detailed structure of the emission pattern using a pattern recognition algorithm.

5.4 Pattern recognition

Beyond the population growth, emissions from secondary collisions display a wealth of intriguing angular structures (Fig. 5.3**a**) that are not obvious from the average image. To investigate these structures, we employ a pattern-recognition algorithm based on unsupervised machine learning, which does not require labeled training data. This ensures no human

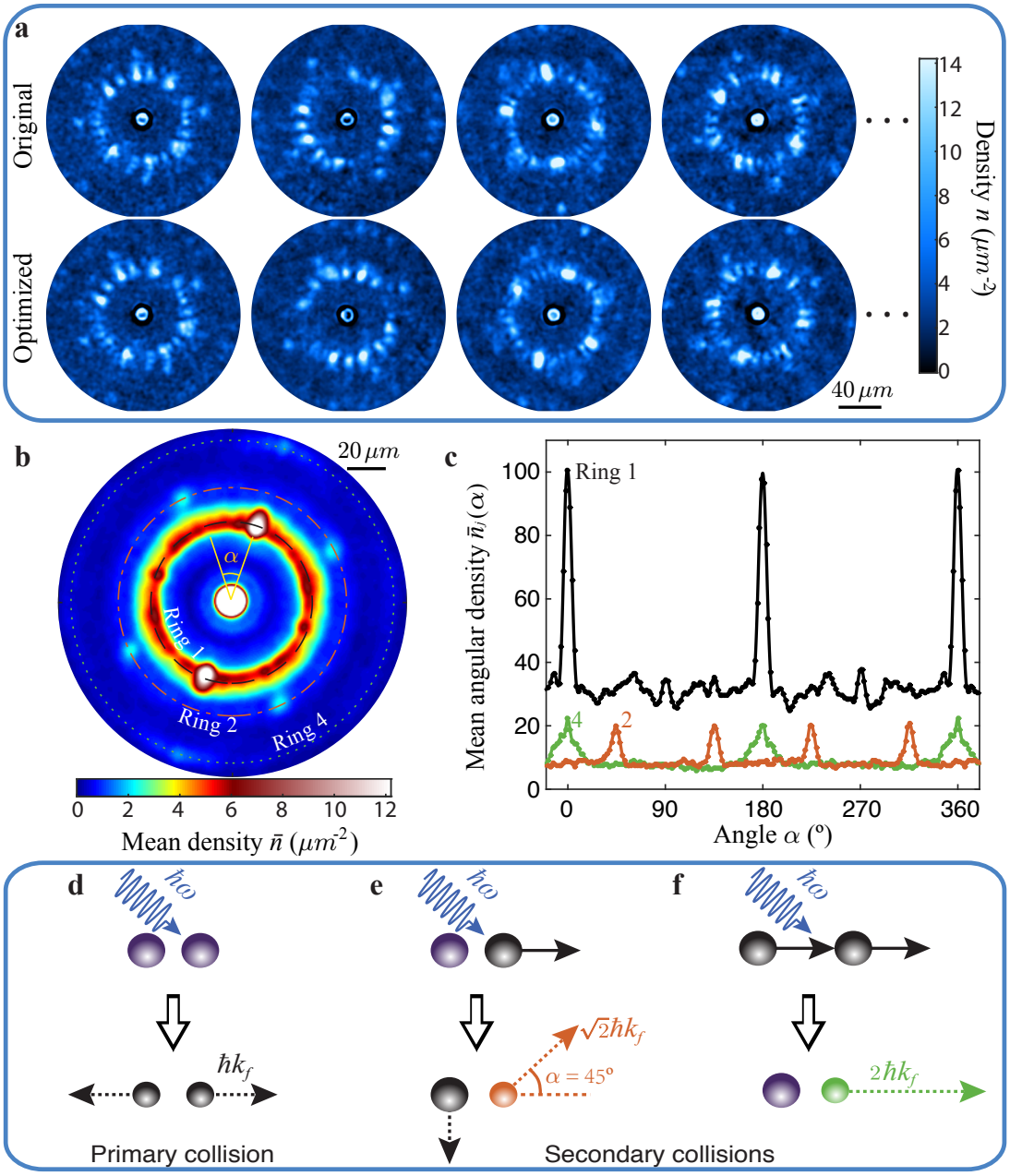

Figure 5.3: **Pattern recognition and microscopic interpretation. a** Examples from a dataset of 209 raw images (top). The bottom row shows the corresponding rotated images that maximize the angular variance of the mean image. **b** The average of all 209 images after individual rotations, showing the resulting pattern Φ. Besides the bright center spot corresponding to the remnant condensate, ten more distinct spots emerge in an angular-uniform background: four in ring 1 at $\alpha = 0°$, 90°, 180° and 270°; four in ring 2 at $\alpha = 45°$, 135°, 225° and 315°; and two in ring 4 at $\alpha = 0°$ and 180°. **c** Angular density distributions in ring 1, 2 and 4 extracted from the pattern; the ten bright spots from **b** show up as peaks in the distributions. **d-f** Illustration the microscopic processes that are responsible for the peaks. The purple balls indicate atoms in the condensate. The black, orange and green balls represent atoms in ring 1, 2 and 4 with momentum of k_f, $\sqrt{2}k_f$, and $2k_f$, respectively.

bias to the final recognized common pattern. To identify the key features from the images, the algorithm minimizes a loss function that favors the common pattern by adjusting the orientation of each individual image.

5.4.1 Pattern recognition algorithm

To explain the implementation, we can consider each image a combination of several common patterns that are randomly rotated and contribute to the image with different weights. This randomness results isotropic rings in the average image. To make the pattern stand out, we align the strongest component while the rest average to a smooth background. This alignment can be achieved by maximizing the angular variance of the average image after rotation. Thus we can define the loss function as the negative of the angular variance.

We can simplify the calculation of the angular variance by incorporating the rotation symmetry of our system. Since the emitted atoms that contain essential information of the pattern form quantized rings, each image I_i can be faithfully represented by the angular density of rings $\{n_1^{(i)}(\theta), n_2^{(i)}(\theta), n_4^{(i)}(\theta)\}$. Here the angular density of each ring is given by the integral over the radial direction $n_j^{(i)}(\theta) = \int_{R_j-\sigma}^{R_j+\sigma} n^{(i)}(r,\theta)dr$, with R_j the center of the ring and σ the $1/e$ width of the ring, which is 7 μm in this experiment. Note that we exclude ring 3 due to its low signal level. We then apply a rotation to each individual image with an angle θ_i, thus the angular density becomes $\{n_1^{(i)}(\theta+\theta_i), n_2^{(i)}(\theta+\theta_i), n_4^{(i)}(\theta+\theta_i)\}$. The random rotation angle θ_1 for the first image is fixed during the following optimization process, which breaks the rotational symmetry and orient the recognized pattern. According to our definition, the loss function $L(\{\theta_i\})$ is given by

$$L(\{\theta_i\}) = \sum_j^{\{1,2,4\}} L_j(\{\theta_i\}), \tag{5.8}$$

, where

$$L_j(\{\theta_i\}) = -\frac{1}{2\pi}\int d\theta \left[\frac{1}{M}\sum_{i=1}^{M} n_j^{(i)}(\theta+\theta_i) - \bar{n}_j\right]^2 \tag{5.9}$$

with

$$\bar{n}_j = \frac{1}{M}\sum_{i=1}^{M}\frac{1}{2\pi}\int d\theta n_j^{(i)}(\theta+\theta_i) \tag{5.10}$$

and $M = 209$ is the number of images in our dataset. It is easy to see that $\bar{n}_j$ is a constant independent of $\{\theta_i\}$. We use a derivative-free search algorithm to find local minima of the loss function $L(\{\theta_i\})$. All the local minima yield similar and robust emission patterns shown in Fig. 5.3**c**.

5.4.2 Results

This robust and intriguing pattern Φ in the jet emission contains multiple distinct spots at non-zero momenta on top of angularly uniform rings 1, 2 and 4(Fig. 5.3**b**). These spots arise from a characteristic arrangement of jets which repeatedly appears across many images. Since the condensate has rotational symmetry, instances of this arrangement are randomly oriented in each trial, but the strongest instance in each image is identified and aligned by our algorithm. To better characterize these features, we extract the mean angular density $\bar{n}_j(\alpha)$ for each ring with α the relative angle to the brightest spot in ring 1 (Fig. 5.3**c**). In this way, we convert the pattern into a series of angular density plots with a flat background and clear peaks representing the spots. This flat background arises from averaging the weaker jets, whose orientations are uncorrelated with the pattern Φ. Since we observe no discernible features from ring 3, in the following we focus on those from rings 1, 2, and 4.

Beside the results shown in Fig. 5.3, we also find similar but different patterns when defining the loss function only based on single ring j. The pattern obtained based on ring 1 is very similar to that shown in Fig. 5.3**C** (Fig.5.4**a**). These patterns obtained based on ring 2 or ring 4 show much brighter spots in the associated rings. These pattern contain

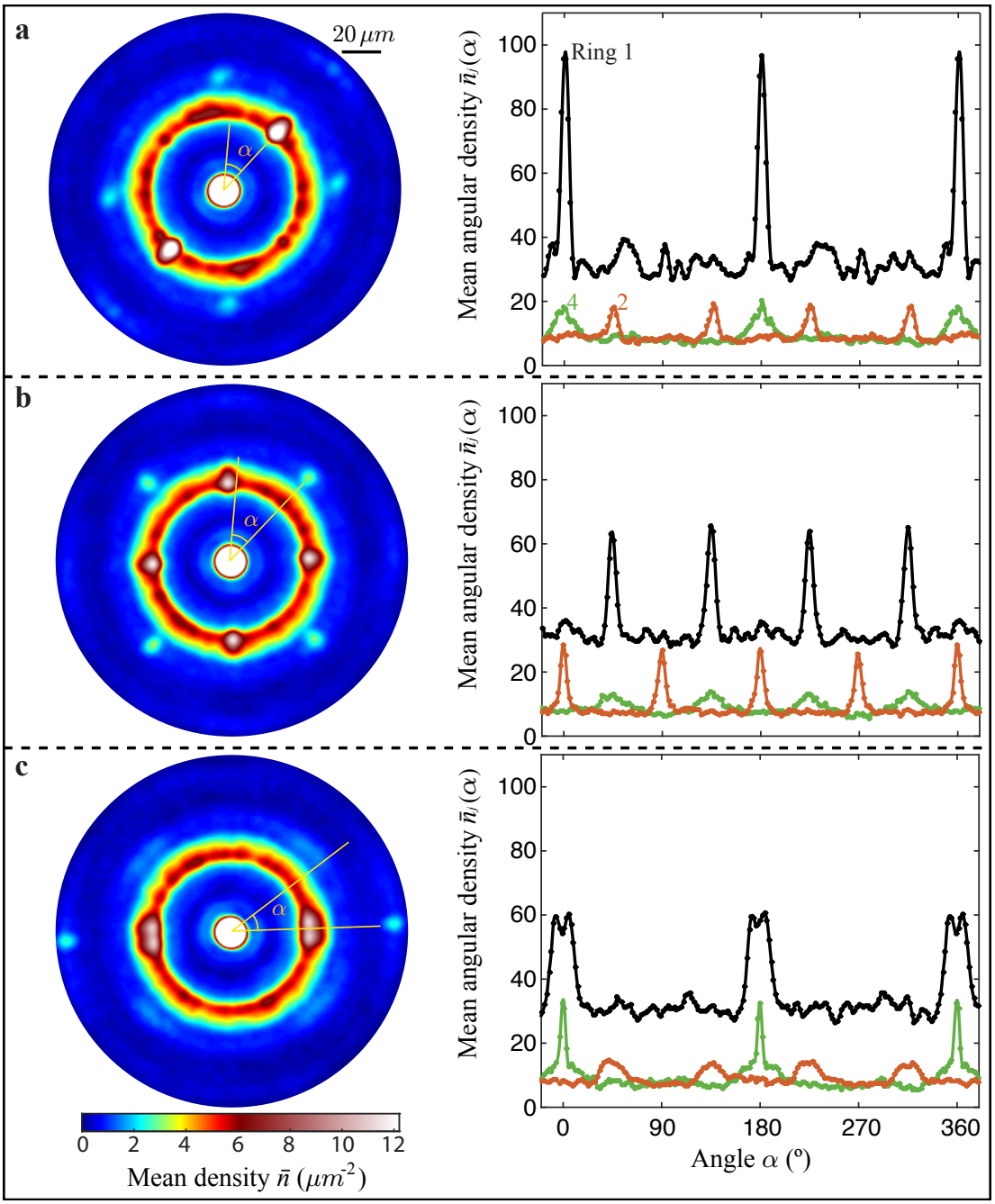

Figure 5.4: **Pattern recognition based on individual rings.** Left column: the pattern that show up in average image after application of pattern recognition algoritm respectively to ring 1 **a**, ring 2 **b** and ring 4 **c**. Right column: the corresponding avearge angular density regarding to each ring in the pattern image, where angle α is defined relative to the brightest spot in ring 1, ring 2 and ring 4 respectively.

information about density-density correlations, which are addressed in detail in Sec. 5.6. In particular, the angular density $\bar{n}_2$ in Fig.5.4**b** ($\bar{n}_4$ in Fig.5.4**c**) is analogous to the auto-correlations $g_{22}^{(2)}$ ($g_{44}^{(2)}$). Additionally, the angular densities $\bar{n}_1$ and $\bar{n}_4$ ($\bar{n}_1$ and $\bar{n}_2$) reflect the cross-correlations $g_{12}^{(2)}$ and $g_{24}^{(2)}$ ($g_{14}^{(2)}$ and $g_{24}^{(2)}$).

Excluding the uniform background, we find that the concurrence of multiple spots in the pattern Φ points to particular scattering processes populating the corresponding momentum modes. As the first example, two strong peaks in ring 1 ($\alpha = 0^\circ$ and 180°) come from primary collisions of two condensate atoms, which absorb one energy quantum and are scattered into opposite directions with momentum $\pm\hbar k_f$, shown in Fig. 5.3**d**.

Following the primary collisions, which are equally likely to emit back-to-back pairs of jets in any direction, strongly stimulated secondary collisions occur that preferentially emit jets in particular directions relative to the primary jets. Although there are many secondary collision processes that satisfy energy and momentum conservation, a small number of them involving three macroscopically occupied modes dominates over others. This is a result of Bosonic stimulation, which enhances the rate of scattering processes involving highly occupied modes. The appearance of discrete secondary jets is analogous to optical parametric amplification in a non-linear medium.

These dominant secondary collisions induce eight additional peaks in total among the three rings in the pattern. The four peaks in ring 2 (at $\alpha = 45^\circ$, 135°, 225° and 315°) and two peaks in ring 1 (at $\alpha = 90^\circ$ and 270°) arise from the collisions between an atom from ring 1 and another atom from the condensate. One example of such collisions is illustrated in Fig. 5.3**e**, where a pair of atoms populate two specific modes at $\alpha = 45^\circ$ in ring 2 and at $\alpha = 270^\circ$ in ring 1 by absorbing one photon. This collision process is highly stimulated because it involves three atoms from modes which are already macroscopically occupied; one atom comes from the condensate and two atoms come from jets produced in primary collisions. Another highly stimulated secondary collision process, shown in Fig. 5.3**f**, can explain the origin of the two peaks in ring 4. Here two co-propagating atoms from ring

1 collide; one atom is promoted to ring 4 and the other returns to the condensate. For a detailed comparison of these processes to other possible secondary collisions (see Sec. 5.5).

5.5 Perturbation theory

In this section, we develop a perturbation treatment on the exponential growth of the atomic population into the stimulated momentum modes from Eq. (5.5). Here we transfer the operators for atoms and photons into a rotating frame with $a_{\mathbf{k}} \to a_{\mathbf{k}} e^{i\epsilon_{\mathbf{k}} t/\hbar}$ and $b \to b e^{i\omega t}$, and ignore the fast varying terms, the Hamiltonian becomes

$$H_{int} = \sum_{\mathbf{k_1},\mathbf{k_2},\Delta\mathbf{k}} (A a^\dagger_{\mathbf{k}_1+\Delta\mathbf{k}} a^\dagger_{\mathbf{k}_2-\Delta\mathbf{k}} a_{\mathbf{k}_1} a_{\mathbf{k}_2} b e^{-i\delta t} + h.c.), \tag{5.11}$$

with $\delta = (\epsilon_{\mathbf{k}_1+\Delta\mathbf{k}} + \epsilon_{\mathbf{k}_2+\Delta\mathbf{k}} - \epsilon_{\mathbf{k}_1} - \epsilon_{\mathbf{k}_2} - \hbar\omega)/\hbar$. When $\delta = 0$, the corresponding term in the Hamiltonian is on resonance satisfying energy conservation.

For simplicity, we treat the operators b and $b^\dagger$ for RF photons as C-numbers and assume the condensate is far from depletion (Bogoliubov approximation). By only considering the resonant interaction terms, we simplify the Hamiltonian to

$$H_{int} = \hbar\nu \sum_{\mathbf{k}_1,\mathbf{k}_2,\Delta\mathbf{k}} (a^\dagger_{\mathbf{k}_1+\Delta\mathbf{k}} a^\dagger_{\mathbf{k}_2-\Delta\mathbf{k}} a_{\mathbf{k}_1} a_{\mathbf{k}_2} + h.c.), \tag{5.12}$$

with $\nu = \frac{2\pi\hbar a_{ac}}{mV}$. We inspect the equation of motion for $a_{\mathbf{k}_1+\Delta\mathbf{k}}$,

$$i\dot{a}_{\mathbf{k}_1+\Delta\mathbf{k}} = \nu \sum_{\mathbf{k}_2,\Delta\mathbf{k}} a^\dagger_{\mathbf{k}_2-\Delta\mathbf{k}} a_{\mathbf{k}_1} a_{\mathbf{k}_2}, \tag{5.13}$$

where all the energy-and-momentum conserved collisions contribute to the the population growth of mode $\mathbf{k}_1 + \Delta\mathbf{k}$. However, these collisions do not contribute equally. Collision processes are more dominant when they involve more macroscopically occupied modes. Here we study the terms that describe dominant collision processes corresponding to our identified

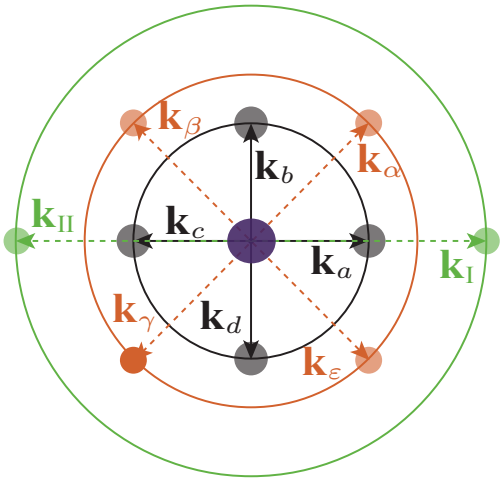

Figure 5.5: **Dominant momentum modes after primary and secondary collisions.** Here momentum modes $\mathbf{k}_a$, $\mathbf{k}_b$, $\mathbf{k}_c$, and $\mathbf{k}_d$ in ring 1 are from the primary collisions. Modes $\mathbf{k}_\alpha$, $\mathbf{k}_\beta$, $\mathbf{k}_\gamma$ and $\mathbf{k}_\epsilon$ in ring 2, and modes $\mathbf{k}_I$ and $\mathbf{k}_{II}$ in ring 4 are from secondary collisions

pattern Φ (Fig. 5.5).

First of all, we consider the primary collisions, the two modes $\mathbf{k}_a$ and $\mathbf{k}_c$ are simultaneously occupied due to stimulated inelastic scattering. The primary interaction terms in Hamiltonian is given by

$$H_P = \hbar\nu a_a^\dagger a_c^\dagger a_0 a_0 + h.c.. \tag{5.14}$$

As a result, the corresponding equations of motion are

$$i\dot{a}_{\mathbf{k}_a} = \nu a_{\mathbf{k}_c}^\dagger a_{\mathbf{k}_0} a_{\mathbf{k}_0}, \tag{5.15}$$

$$i\dot{a}_{\mathbf{k}_c} = \nu a_{\mathbf{k}_a}^\dagger a_{\mathbf{k}_0} a_{\mathbf{k}_0}. \tag{5.16}$$

We solve these equations analytically and obtain

$$a_a(t) = a_a(0)\cosh(\gamma\tau) - ia_c^\dagger(0)\sinh(\gamma\tau), \tag{5.17}$$

$$a_c^\dagger(\tau) = a_c^\dagger(0)\cosh(\gamma\tau) + ia_a(0)\sinh(\gamma\tau). \tag{5.18}$$

where we have applied the Bogoliubov approximation $a_0 \approx a_0^\dagger \approx \sqrt{N_0}$ and define $\gamma = \nu N_0$ with N_0 the total number of atoms in the condensate. Thus the population in ring 1 grows as

$$\langle a_a^\dagger(\tau) a_a(\tau)\rangle = \langle a_c^\dagger(\tau) a_c(\tau)\rangle = \sinh^2(\gamma\tau), \tag{5.19}$$

assuming that the initial population is zero. Similar solutions also apply to modes $\mathbf{k}_b$ and $\mathbf{k}_d$ although they are not correlated to modes $\mathbf{k}_a$ and $\mathbf{k}_c$.

We then proceed to the secondary collisions which involves atoms generated from primary collisions. For ring 2, the dominant interaction terms in the Hamiltonian involving all the eight modes in ring 1 and 2 (Fig. 5.5) are given by

$$\begin{aligned} H_{S1} &= \hbar\nu(a_\alpha^\dagger a_d^\dagger a_a a_0 + a_\epsilon^\dagger a_b^\dagger a_a a_0 + a_\beta^\dagger a_a^\dagger a_b a_0 + a_\alpha^\dagger a_c^\dagger a_a a_0 \\ &\quad + a_\gamma^\dagger a_b^\dagger a_c a_0 + a_\beta^\dagger a_d^\dagger a_c a_0 + a_\epsilon^\dagger a_c^\dagger a_d a_0 + a_\gamma^\dagger a_a^\dagger a_d a_0 + h.c.). \end{aligned} \tag{5.20}$$

For convenience, we first check the equation of motion for a_α, which gives

$$i\dot{a}_\alpha = \nu(a_d^\dagger a_a\sqrt{N_0} + a_c^\dagger a_b\sqrt{N_0}) \tag{5.21}$$

under Bogoliubov approximation. Assuming that a_a, a_b, a_c and a_d are unaffected by the secondary collisions, we insert Eq. 5.17 and 5.18 into 5.21, and get the perturbative solution for population in ring 2,

$$\langle a_\alpha^\dagger(\tau) a_\alpha(\tau)\rangle = \langle a_\beta^\dagger(\tau) a_\beta(\tau)\rangle = \langle a_\gamma^\dagger(\tau) a_\gamma(\tau)\rangle = \langle a_\epsilon^\dagger(\tau) a_\epsilon(\tau)\rangle = \frac{1}{2N_0}\sinh^4(\gamma\tau). \tag{5.22}$$

For the generation of population in ring 4, the relevant interaction terms in the Hamiltonian are given by

$$H_{S2} = \hbar\nu(a_I^\dagger a_0^\dagger a_a a_a + a_{II}^\dagger a_0^\dagger a_c a_c + h.c.). \tag{5.23}$$

Following the same procedure, we get the equation of motion for a_I,

$$i\dot{a}_I = \nu a_0^\dagger a_a^2 = \nu\sqrt{N_0}a_a^2. \tag{5.24}$$

Based on the same approach, we obtain

$$\langle a_I^\dagger a_I\rangle = \langle a_{II}^\dagger a_{II}\rangle = \frac{1}{8N_0}[\sinh(2\gamma\tau) - 2\gamma\tau]^2. \tag{5.25}$$

It is easy to find $N_2 \propto N_1^2$ from Eqs. (5.19) and (5.22), where N_1 is the total population in ring 1 coming from modes like $\mathbf{k}_a$, $\mathbf{k}_b$, $\mathbf{k}_c$ and $\mathbf{k}_d$, and N_2 is the total population in ring 2 resulting from modes like $\mathbf{k}_\alpha$, $\mathbf{k}_\beta$, $\mathbf{k}_\gamma$ and $\mathbf{k}_\epsilon$. When the driving time τ is long compared to $1/\gamma$, we can see that

$$\lim_{\tau\to\infty}\langle a_\alpha^\dagger(\tau)a_\alpha(\tau)\rangle = \lim_{\tau\to\infty}\langle a_I^\dagger(\tau)a_I(\tau)\rangle = \frac{1}{32N_0}e^{4\gamma\tau}. \tag{5.26}$$

This indicates $N_4 \approx N_2 \propto N_1^2$ which is consistent with our experimental observations shown in Fig. 2**B**, where N_4 is the total population in ring 4 coming from modes like $\mathbf{k}_I$ and $\mathbf{k}_{II}$.

There are also weaker secondary collisions beside the dominant processes described above. One example is the generation of ring 3 where two atoms from ring 1 in the same angular mode collide. The collision process scatter one atom to ring 3 with momentum $\hbar\sqrt{3}k_f$ and another back to ring 1 at angles of 30° and -60° relative to the initial momentum mode respectively. Due to limited signal level in the population of ring 3, we do not perform quantitative study in this work. Finally, as modes involved in secondary collisions become macroscopically occupied, we anticipate occurrence of tertiary collisions which shall enable generation of even higher harmonics.

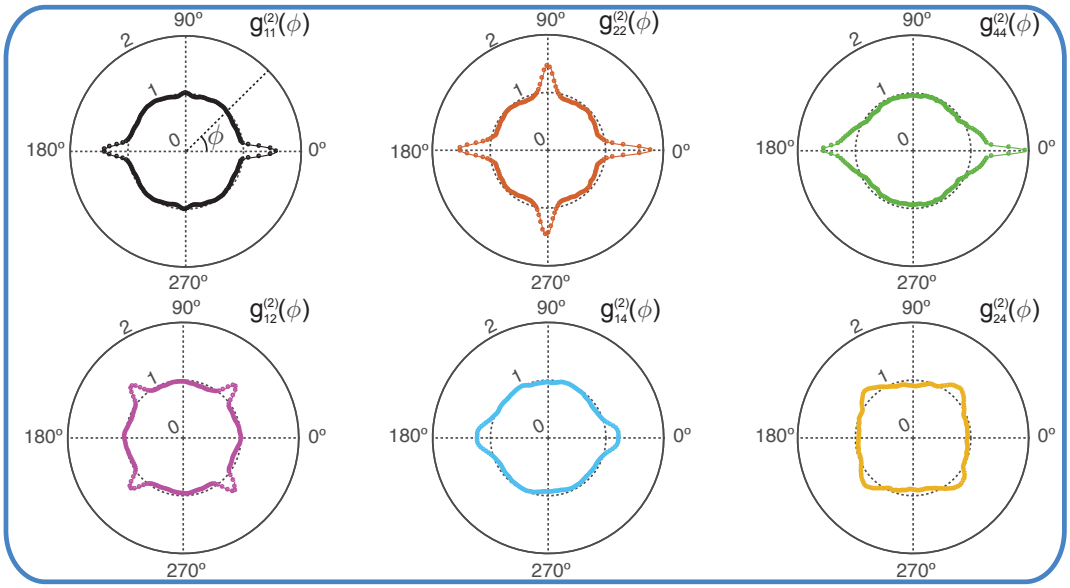

Figure 5.6: **Second-order correlations of emitted matter-wave jets.** The second-order correlation functions $g^{(2)}_{ij}(\phi)$ within and between rings with $i(j)$ =1, 2 or 4.

5.6 Density-density correlation

In our experiment, we measure the density distribution in the momentum space and calculate mth-order density correlation between m different momentum modes defined as

$$g^{(m)}_{j_1,j_2,...,j_m}(\phi_{12},...,\phi_{1m}) = \frac{\langle n_{j_1}(\theta)\prod_{k=2}^{m} n_{j_k}(\theta+\phi_{1k})\rangle}{\langle n_{j_1}(\theta)\rangle\prod_{k=2}^{m}\langle n_{j_k}(\theta+\phi_{1k})\rangle}, \tag{5.27}$$

where $j_k = 1$, 2 or 4 is the ring number for the k-th mode and ϕ_{1k} is the relative angle between 1st mode and k-th mode. Here the $\langle . \rangle$ represents angular averaging over θ, followed by ensemble averaging over images. When $g^{(m)} > 1$, the m modes $\{n_{j_k}(\theta+\phi_{1k})\}$ are correlated.

This density-density correlation can also serve as a further support to the dominant microscopic collision processes implied by the pattern Φ. First we calculate the second-order

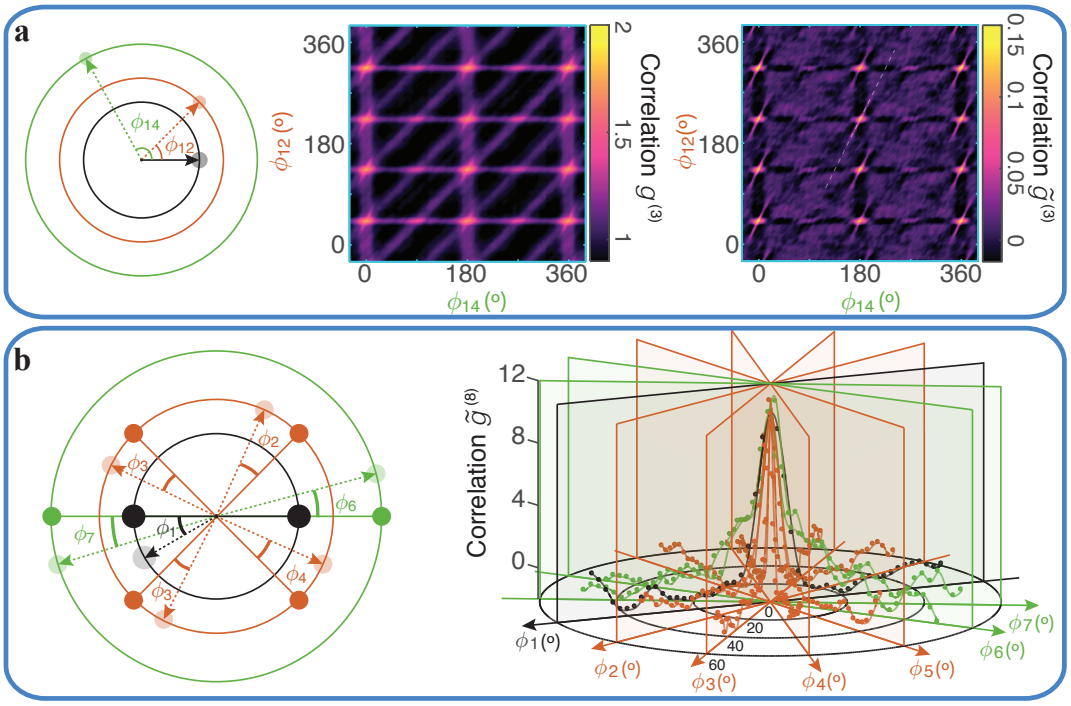

Figure 5.7: **Third- and eighth-order correlations of emitted matter-wave jets. a** shows the third-order correlations $g^{(3)}_{124}(\phi_{12}, \phi_{14})$ and the connected part $\tilde{g}^{(3)}_{124}(\phi_{12}, \phi_{14})$. Here ϕ_{12} (ϕ_{14}) are the relative angles between atoms in ring 1 and 2 (4), shown in the left figure. The extended weak correlations across the peaks in $\tilde{g}^{(3)}_{124}(\phi_{12}, \phi_{14})$ indicate a relation between small angular deviations $\delta\phi_{12} = 2\delta\phi_{14}$ (see white-dashed line as an example). **b** shows the eighth-order connected correlation function $\tilde{g}^{(8)}(\phi_1, ..., \phi_7)$. We choose a primary jet direction in ring 1 as the reference and show the connected correlation as a function of seven angles relative to the locations of seven bright spots in pattern Φ: one in ring 1 (at 180°, black), four in ring 2 (at 45°, 135°, 225° and 315°, orange), and two in ring 4 (at 0° and 180°, green). The correlation is shown on seven vertical planes. Within each plane, only one of the seven angles is varied. The connected $\tilde{g}^{(8)}$ reaches 12 and decays rapidly to zero as the angles increase, suggesting a peak in the 7-dimensional space. Here solid lines are spline fits to guide the eye.

correlation function $g_{ij}^{(2)}(\phi)$ between momentum modes in ring i and ring j, namely,

$$g_{ij}^{(2)}(\phi) = \frac{\langle n_i(\theta)[n_j(\theta+\phi) - \delta_{ij}\delta(\phi)]\rangle}{\langle n_i(\theta)\rangle\langle n_j(\theta+\phi)\rangle}, \tag{5.28}$$

where $n_i(\theta)$ is the angular density in ring i at angle θ, δ_{ij} is the Kronecker delta, and $\delta(\phi)$ is the Dirac delta function. The angle brackets correspond to angular averaging over θ, followed by ensemble averaging over raw images.

All of the second-order correlations involving momenta on the dominant rings display multiple peaks (Fig. 5.6). The results are in full consistency with the spots in the pattern Φ and the collisional processes that we identify. In particular, we can associate all the peaks in $g_{22}^{(2)}$ and $g_{12}^{(2)}$ with the process shown in Fig. 5.3**e**, where jets in ring 2 are created at $\pm 45^\circ$ relative to the primary jets. The peaks in $g_{44}^{(2)}$ and $g_{14}^{(2)}$ are associated with the process in Fig. 5.3**f**, where jets are created along the direction of the primary jets.

We also find four peaks in the cross-correlation between rings 2 and 4. To the best of our knowledge, these correlations cannot come directly from a single secondary collision process. Instead, they could result from the concurrence of two secondary collision processes. Such correlation develops since both processes involve the same macroscopically-occupied modes in ring 1 and the condensate.

We further investigate such indirect correlation by calculating the high-order correlation function. Simple density-density high-order correlation, however, may not offer more information about how different modes are correlated with each other than the lower-order correlations. For example, let's see the third-order correlation function $g_{124}^{(3)}(\phi_{12}, \phi_{14})$. Assuming that $n_2(\theta+\phi_{12})$ and $n_4(\theta+\phi_{14})$ are correlated but neither of them is correlated to $n_1(\theta)$, we have

$$\langle n_1(\theta) n_2(\theta+\phi_{12}) n_4(\theta+\phi_{14})\rangle = \langle n_1(\theta)\rangle\langle n_2(\theta+\phi_{12}) n_4(\theta+\phi_{14})\rangle. \tag{5.29}$$

Consequently, the third-order correlation reduces to the second-order correlation,

$$\begin{aligned} g^{(3)}_{124}(\phi_{12},\phi_{14}) &= \frac{\langle n_1(\theta)\rangle\langle n_2(\theta+\phi_{12})n_4(\theta+\phi_{14})\rangle}{\langle n_1(\theta)\rangle\langle n_2(\theta+\phi_{12})\rangle\langle n_4(\theta+\phi_{14})\rangle} \\ &= \frac{\langle n_2(\theta+\phi_{12})n_4(\theta+\phi_{14})\rangle}{\langle n_2(\theta+\phi_{12})\rangle\langle n_4(\theta+\phi_{14})\rangle} \\ &= g^{(2)}_{24}(\phi_{12}-\phi_{14}). \end{aligned} \tag{5.30}$$

In order to obtain how genuinely m modes are correlated to each other, we extract the connected correlation function $\tilde{g}^{(m)}$ by subtracting the contributions from all the lower-order correlations [96],

$$\tilde{g}^{(m)} = g^{(m)} - g^{(m)}_{dis}, \tag{5.31}$$

where $g^{(m)}_{dis}$ is the disconnected contains redundant information from all lower-order correlations. According to *(24, 38)*, g^{m}_{dis} is given by

$$g^{(m)}_{dis} = \frac{1}{\prod_{k=1}\langle n_{j_k}(\theta+\phi_{1k})\rangle}\sum_{\Lambda}\left[(N_\Lambda-1)!(-1)^{N_\Lambda-1}\prod_{B\in\Lambda}\langle\prod_{k\in B} n_{j_k}(\theta+\phi_{1k})\rangle\right]. \tag{5.32}$$

Here the sum $\sum_\Lambda$ runs over all possible partitions Λ of $\{1,2,\ldots,m\}$ with the number of blocks B larger than 1, the first product in the square brackets runs over all blocks of the partition and the second product runs over all elements k in the block; N_Λ is the number of blocks in the partition. We have absorbed $n_{j_1}(\theta)$ into the product with $\phi_{11}=0$.

As a result, we can obtain the connected third-order correlation function. The distinct peaks in the connected third-order correlation reveals genuine bunching of the population fluctuations at specific angles in all three rings. In addition, we observe extended weak correlations along lines across the peaks, which relate the angular deviations $\delta\phi_{12}\approx 2\delta\phi_{14}$ (see Fig.5.7**a**). We attribute such weak correlations to a Raman-like collision process that couples these three momentum modes by absorbing two energy quanta from the modulation field (see Sec. 5.7).

Beyond third-order correlations, high harmonic generation can induce even higher order correlations. An example shown in Fig. 5.7**b** is the connected eighth-order correlation. Plotted in the seven-dimensional space spanned by the angular deviations, a prominent peak appears when the angles match the bright spots in our pattern Φ.

Our experiment shows that bosonic stimulation in a driven system can connect different momentum modes in a strongly correlated manner. While other ways exist to generate high harmonics of matter waves, such as atom-photon superradiance [59, 94] or strong Bragg scattering [12], our system is unique in the formation of symmetry-breaking correlations between harmonics by stimulated scattering of matterwaves. This observation suggests a novel way to prepare highly correlated systems for applications in quantum simulation and quantum information. In addition, the implementation of the pattern recognition can inspire further applications of machine learning to understand complex dynamics of quantum systems.

5.7 Effective three-body collision revealed by correlation function

In this section, we inspect the connected third-order correlation function $\tilde{g}^{(3)}_{124}$ in detail and find weak correlations along lines across the peaks in Fig. 5.7**a**. We found that these lines are mainly due to effective three-body collisions where the atoms interact with the modulation field twice through an intermediate state, similar to the Raman transitions in quantum optics. To see this, we derive the effective Hamiltonian that describes this process.

We follow the derivation from the Hamiltonian with five-wave mixing and start with

$$H_{int}(t) = \hbar\nu \sum (a^\dagger_{\mathbf{k}_1+\Delta k} a^\dagger_{\mathbf{k}_2-\Delta k} a_{\mathbf{k}_1} a_{\mathbf{k}_2} e^{-i\delta t} + h.c.). \tag{5.33}$$

When $\delta \neq 0$, the corresponding term in the Hamiltonian is off resonant and such direct collision is not allowed. However, two such off-resonant terms can potentially cancel the detuning together to yield a resonant coupling in a time averaged Hamiltonian.

To perform this time averaging, we first look at the time evolution operator $U(t)$ that satisfies

$$i\hbar\frac{\partial U(t)}{\partial t} = H(t)U(t). \tag{5.34}$$

When $H(t)$ is changing rapidly in time, we can average the overall evolution operator and get rid of the rapid oscillating terms to gain physics at slow time scale under adiabatic elimination. Thus we define a time average function $F(t)$ with peaks at $t = 0$ and $\int dtF(t) = 1$ that spans over a short period of time. The detail form of $F(t)$ is not important. Therefore the average evolution operator $\overline{U(t)}$ is $\overline{U(t)} = \int dt' F(t-t')U(t')$ (Schrieffer-Wolff transformation) and the equation of motion becomes

$$i\hbar\frac{\partial}{\partial t}\overline{U(t)} = \overline{H(t)U(t)}. \tag{5.35}$$

Effectively, we expect the equation of motion to be $i\hbar\frac{\partial}{\partial t}\overline{U(t)} = H_{eff}(t)\overline{U(t)}$. As a result, the general form of the effective Hamiltonian after time averaging is

$$H_{eff}(t) = \overline{H(t)U(t)}\left[\overline{U(t)}\right]^{-1}. \tag{5.36}$$

By expanding this effective Hamiltonian only to the first order, we have the result of

$$H_{eff}(t) = \overline{H(t)} + \frac{1}{2}\left(\overline{[H(t), U_1(t)]} - \left[\overline{H(t)}, \overline{U_1(t)}\right]\right), \tag{5.37}$$

with $U_1(t) = \frac{1}{i\hbar}\int_0^t dt' H(t')$.

As an particular example shown in Fig. 5.8, we are interested in the line across the peak at $(\phi_{14}, \phi_{12}) = (0°, 135°)$. Here the angle deviations from the peak position are defined as $\delta\phi_{14}$ and $\delta\phi_{12}$ respectively. The line gives $\delta\phi_{12} \approx 2\delta\phi_{14}$ that is universally true close to every peak. The two responsible secondary collisions are shown in Fig.5.8**b**. When both of the collisions are on single-photon resonance, they can happen simutaneously and directly

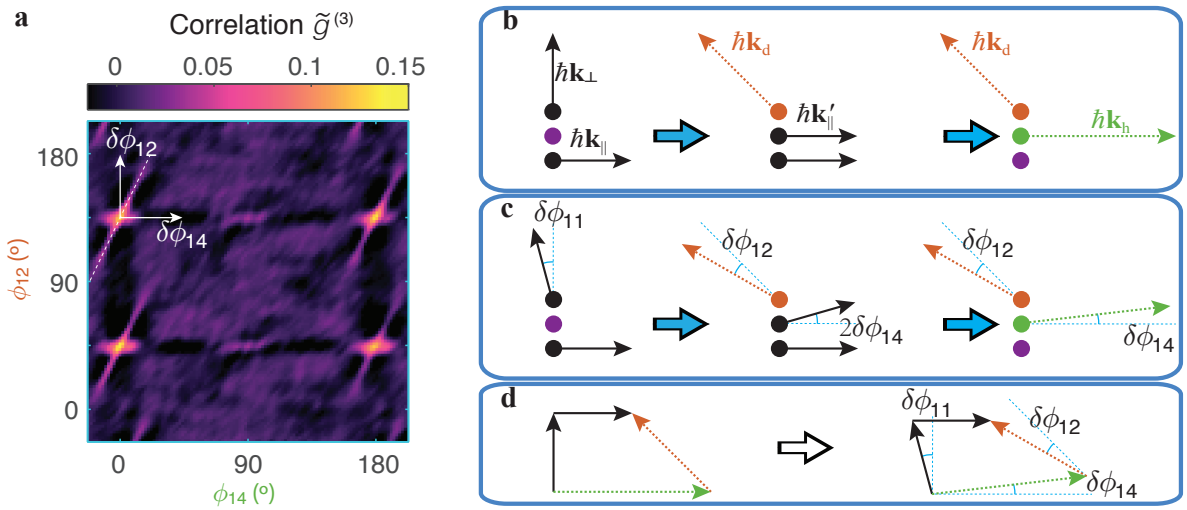

Figure 5.8: **Thin correlation lines in third-order correlations $\tilde{g}^{(3)}_{124}$. a** shows thin lines across the peaks in the connected third-order correlation $\tilde{g}^{(3)}_{124}$ from our measurement. One example is illustrated with white dashed line across the peak position $(\phi_{14}, \phi_{12}) = (0°, 135°)$. The angle deviations are defined as $\delta\phi_{14}$ and $\delta\phi_{12}$, respectively. **b** illustrates an exemplary two-step collision process that generates a pair of atoms in ring 2 and 4 from two atoms in ring 2 in single-photon resonant way. Here $|\mathbf{k}_\perp| = |\mathbf{k}_\parallel| = |\mathbf{k}'_\parallel| = k_f$, $|\mathbf{k}_d| = \sqrt{2}k_f$ and $|\mathbf{k}_h| = 2k_f$. Each step conserves energy and momentum. **c** presents the Raman process responsible for the thin line, where each step is slightly off resonant but the whole process conserves energy. Here each step still satisfies momentum conservation and $\delta\phi_{11}$ is the angle deviation of $\mathbf{k}_\perp$ from its resonant orientation. **d** shows the phase-matching condition for the effective three-body collision.

contribute to the peak. When individual collision is off-resonant, they have to happen in a sequential manner to form resonant Raman coupling shown in Fig.5.8**c**.

Following the primary collisions, the Hamiltonian involving these momentum modes is written as

$$H_{int} = \hbar\nu(e^{-i\delta t}a^{\dagger}_{\mathbf{k}_d}a^{\dagger}_{\mathbf{k}'_{\parallel}}a_{\mathbf{k}_\perp}a_0 + e^{i\delta t}a^{\dagger}_{\mathbf{k}_h}a^{\dagger}_0 a_{\mathbf{k}_\parallel}a_{\mathbf{k}'_{\parallel}} + h.c). \tag{5.38}$$

Plugging this in to Eq. 5.37, we get the effective Hamiltonian,

$$H_{eff} = -\hbar\frac{\nu^2}{\delta}(a^{\dagger}_{\mathbf{k}_h}a^{\dagger}_{\mathbf{k}_d}a^{\dagger}_0 a_0 a_{\mathbf{k}_\perp}a_{\mathbf{k}_\parallel} + h.c). \tag{5.39}$$

which shows an effective three-body interaction. To explain in detail in Fig.5.8**d**, we can assume small perturbations so that $|\mathbf{k}_\perp| = (1-\varepsilon)k_f$ with angle deviation of $\delta\phi_{11}$, $\mathbf{k}_d$ deviate from its original angle by $\delta\phi_{12}$ with the length of the vector unperturbed, and $\mathbf{k}_h$ deviate from its original angle by $\delta\phi_{14}$. For simplicity, we also assume that the intermediate $|\mathbf{k}'_{\parallel}| = k_f$, therefore $\mathbf{k}'_{\parallel}$ deviates from the horizontal direction by $2\delta\phi_{14}$ and $|\mathbf{k}_h| = 2\cos(\delta\phi_{14})k_f$ as a result of momentum conservation in the second step. Due to total energy conservation for the two-step process, the detuning for the first step $\delta_f = \frac{\hbar^2 k_f^2}{2m}[1-(1-\varepsilon)^2]$ should cancel the detuning for the second step $\delta_s = -\frac{2\hbar^2 k_f^2}{m}[1-\cos^2(\delta\phi_{14})]$. Thus we have

$$\cos(2\delta\phi_{14}) = \frac{1}{2}[1+(1-\varepsilon)^2]. \tag{5.40}$$

Further considering the momentum conservation in the first step, we obtain two equations from horizontal and vertical component respectively,

$$-(1-\varepsilon)\sin(\delta\phi_{11}) = \sqrt{2}\cos(135^\circ+\delta\phi_{12}) + \cos(2\delta\phi_{14}) \tag{5.41}$$

$$(1-\varepsilon)\cos(\delta\phi_{11}) = \sqrt{2}\sin(135^\circ+\delta\phi_{12}) + \sin(2\delta\phi_{14}). \tag{5.42}$$

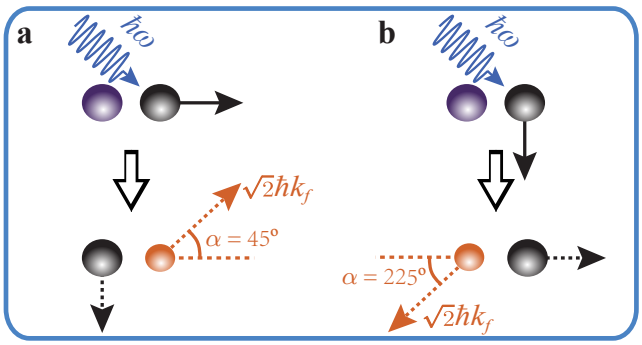

Figure 5.9: **Secondary collision process promoting atoms to ring 2.** **a** and **b** show two equally stimulated processes that promote atoms to ring 2 while merely change atomic distribution in ring 1 when combined.

Based on Eqs. (5.40), (5.41) and (5.42), we have

$$\delta\phi_{12} = 2\delta\phi_{14} + \arcsin[\frac{2-\cos(2\delta\phi_{14})}{\sqrt{2}}] - 45^{\circ}. \tag{5.43}$$

For small angle deviations $\delta\phi_{12} \approx 2\delta\phi_{14}$ agrees with the line in the third-order correlation function in Fig. 5.7**a**.

5.8 Further discussion

According to our theory, the dominant stimulated process for generating such weak peaks is illustrated in Fig. 5.8**e**, with the stimulation rate $\propto \sqrt{N_0}N_1$. We emphasize this process in Fig. 5.9**a**. Here one forward-going atom in ring 1 collides with one condensate atom, and such a collision promotes one atom 45 degree off axis to ring 2 and puts another atoms back to ring 1 at -90 degree. Following a direct intuition based on only this process, since we populate 4 modes in ring 2 while simultaneously populating only 2 mode in ring 1, one would expect the peak at 90 and -90 degrees in ring 1 to be twice as high as that in ring 2.

However, there is another equally stimulated process that depopulates the mode at 90 and -90 degrees in ring 1 simultaneously, which is shown in Fig. 5.9. Here the collision takes an atom going along -90 degrees in ring 1 and a condensate atoms and promotes one of them

to ring 2 at 225 degree while putting the other back to ring 1 at 0 degree. This process is equally strongly stimulated with stimulation rate $\propto \sqrt{N_0}N_1$ and consumes the atoms at -90 degree in ring 1. Therefore, on average the population in the momentum modes at -90 and 0 degrees should not be changed in the end. Based on this reasoning, one would not expect to see any peak at all. We still see a very weak peak in the pattern at 90 degrees because our algorithm aligns the four most largely populated modes in ring 2. These most largely populated modes have to require more population at 90 and -90 degrees than the average in ring 1 in order to most strongly stimulate the corresponding scattering processes.

CHAPTER 6

DENSITY WAVES AND JET EMISSION ASYMMETRY IN BOSE FIREWORKS

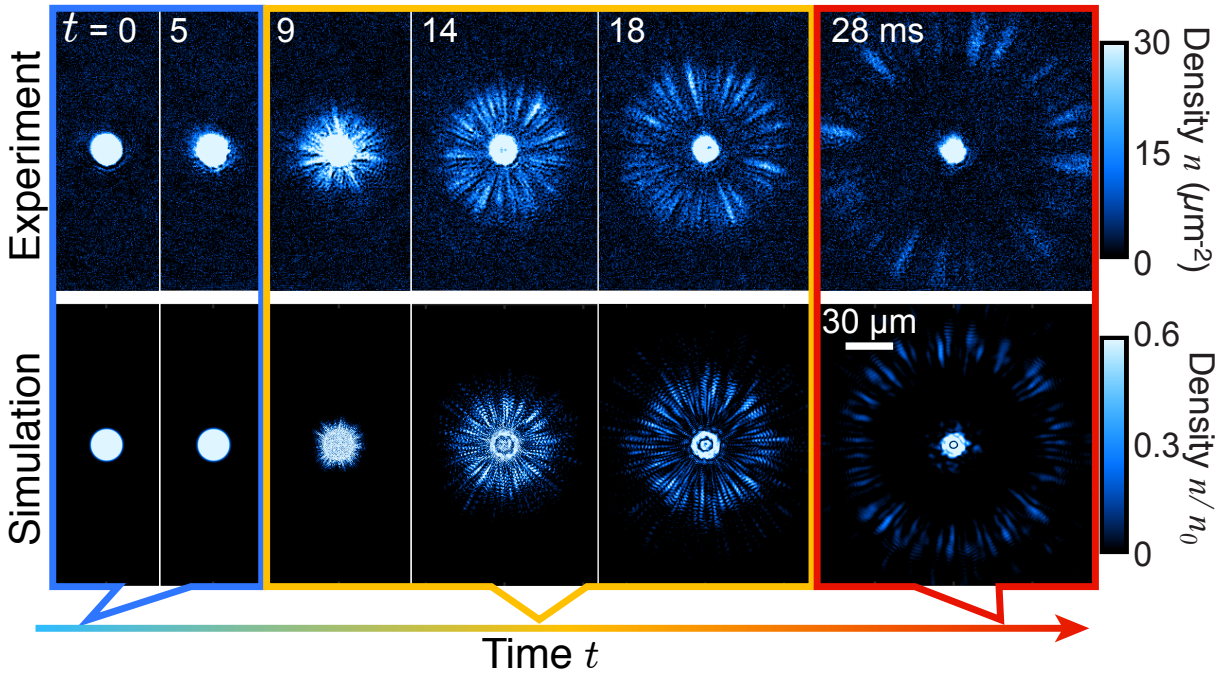

Figure 6.1: **The real space density distribution $n(\mathbf{r})$ as a comparison between experimental data and simulations.** In both, the modulation frequency $\omega/2\pi$ is 2 kHz, the DC and AC interaction energies respectively are $U_0 n_0 \approx h\times 40$ Hz, and $U_1 n_0 \approx h\times 480$ Hz, where h is Planck's constant (see the main text for detailed definitions). As a function of modulation time t, the system exhibits three phases: density waves in a confined condensate (blue box), near-field emission (orange box) and far-field emission (red box).

In the present chapter we study the full dynamics throughout the emission of matter-wave jets starting from its initial generation within the condensates in both from experiment and theory. In experiment, we implement a low frequency driving such that features of density wave at the length scale $\lambda \sim 1/k_f$ become visible given the imaging resolution. In theory use the time-dependent Gross-Pitaevskii (GP) equation to study the evolution of the modulated BEC and the emission of jets. We shall show that the simulations agree well the "Bose fireworks" dynamics seen in experiments. In combination with a new set of experiments, we

identify a previously unobserved early stage of the time evolution. Particularly, immediately after the onset of modulation, we observe that density waves emerge and grow rapidly within the condensate. The density waves display a high degree of disorder, reflecting quantum fluctuations which we model with a very small random noise term.

This feature of density modulation connects Bose fireworks to the general category of parametric resonances [71, 67, 18], where the density waves set up an effective, self consistently produced "grating" which, through feed-back effects, resonantly amplifies their pattern [59]. This process proceeds until pairs of jets (having wavenumber determined by [25, 37] the modulation frequency ω.)are ejected in opposite directions.

In addition to the new observation of density modulation prior to jet emission, we further address the pair-wise correlations. Within these pair-wise correlations, there remains a quantitative asymmetry that has attracted attentions in condensed matter [108] and high-energy physics [7]. We shall see that it can be explained by jet interference in near or far field in the following sections.

In all, we shall focus on two important results: first, we show that the density wave pattern underlies the jet-emission process, and second, we provide a quantitative understanding of the puzzling asymmetry in the emission pattern. Figure 6.1 summarizes the full evolution of the system and shows good agreement between our simulations and experiment. Three distinct regimes of the Bose fireworks can be identified: the early density wave (DW) regime, the initial emergence of jets (called the "near-field emission") and the well established jet emission regime (called the "far-field emission"). In the near field stage the excited modes begin to leave the condensate while still substantially overlapping with each other. After a sufficiently long time, the matter-wave jets become well separated in the far field and the observed density profiles primarily reflect the populations in momentum-space.

6.1 Observation of density wave at early stage

We begin with the investigation of the early-stage density waves. Figure 6.6 presents the experimental observation of the emergence of density waves along with the numerical simulation. The experiments begin with a Bose condensate of 4×10^4 cesium atoms prepared in a uniform disk-shaped trap with a radius of $13\,\mu$m (see Ch. 5 for experimental details). The trap has a potential barrier of height $h \times 200$ Hz in the horizontal direction (h is the Planck constant) and is harmonic vertically with a frequency of 220 Hz. By modulating the magnetic field near a Feshbach resonance, we make the scattering length oscillate as $a(t) = a_{\rm dc} + a_{\rm ac}\sin(\omega t)$ with a small offset $a_{\rm dc} = 4a_0$ and large amplitude $a_{\rm ac} = 40a_0$ at frequency $\omega/2\pi = 620$ Hz that gives a detectable length scale of $\lambda = 2\pi/k_f = 2\pi/\sqrt{m\omega/\hbar} \approx 2.2\ \mu m$ within our imaging resolution.

After modulating the interaction for time t, we perform *in situ* imaging and observe density waves forming within the condensate prior to jet emission. Figure 6.2 and 6.3 shows snapshots of the condensate density distribution $n(\mathbf{r})$. This density wave quickly emerges and oscillates with time as the modulation of interaction turned on at $t = 0\ ms$. To see this dynamics more clearly, we perform the Fourier transform of the condensate density $\tilde{n}(\mathbf{k}) = (2\pi)^{-1}\int d\mathbf{r} e^{-i\mathbf{k}\cdot\mathbf{r}} n(\mathbf{r})$, shown in Fig. 6.4 and Fig. 6.5. To be more quantitative, we extract the density wave amplitude $A_{k_f} = n_0^{-1}\int_{|\mathbf{k}|=k_f} d\mathbf{k}\,|\tilde{n}(\mathbf{k})|$ from the Fourier transform $\tilde{n}(\mathbf{k})$, see Fig. 6.6**b**. Here $k_f = \sqrt{m\omega/\hbar}$ is the wavenumber of the density wave determined by the parametric resonance condition; n_0 is the average density of the static condensate prior to interaction oscillations; m is the boson mass; and $\hbar$ is the reduced Planck constant. Interestingly, this density wave amplitude exhibits fast oscillation under a slowly growing envelope.

We note that this density wave pattern is reminiscent of Faraday waves in classical fluids [77, 110] and related to that predicted for driven atomic gases [98, 62, 84, 8] as well as observed in a one-dimensional condensate [34]. In contrast to classical Faraday waves our system does not spontaneously exhibit three-fold or higher symmetries since it is well captured by the

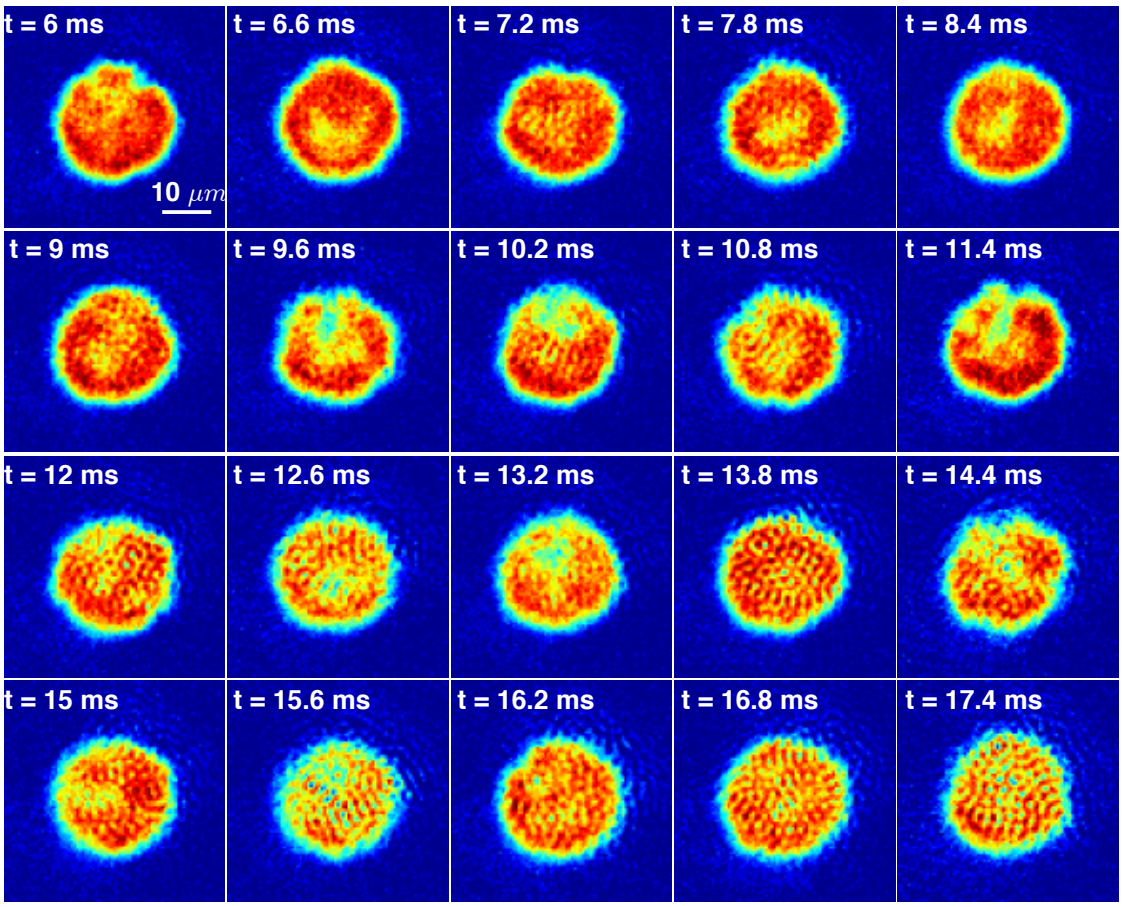

Figure 6.2: **Emergence of density wave (DW) at early-stage with $|k| = k_f$-Part I.**

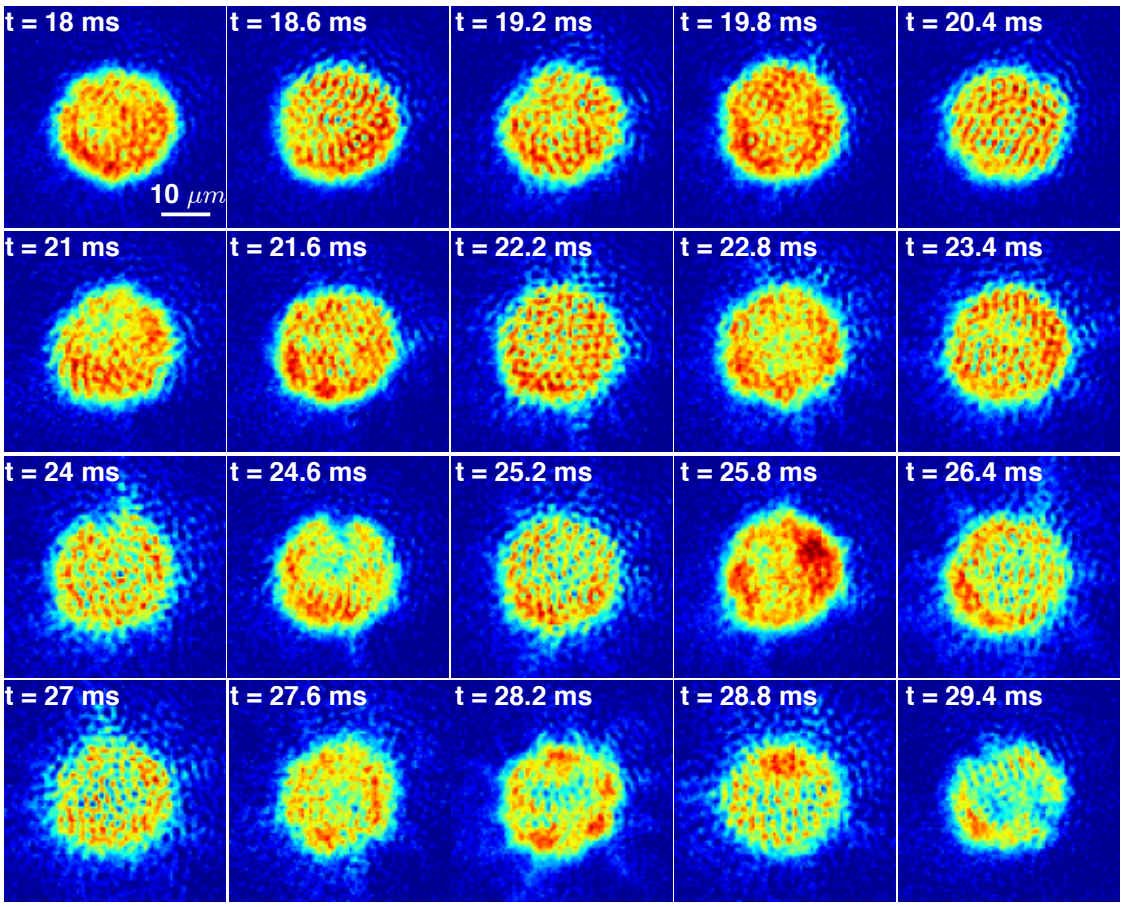

Figure 6.3: **Emergence of density wave at early-stage with $|k| = k_f$-Part II.**

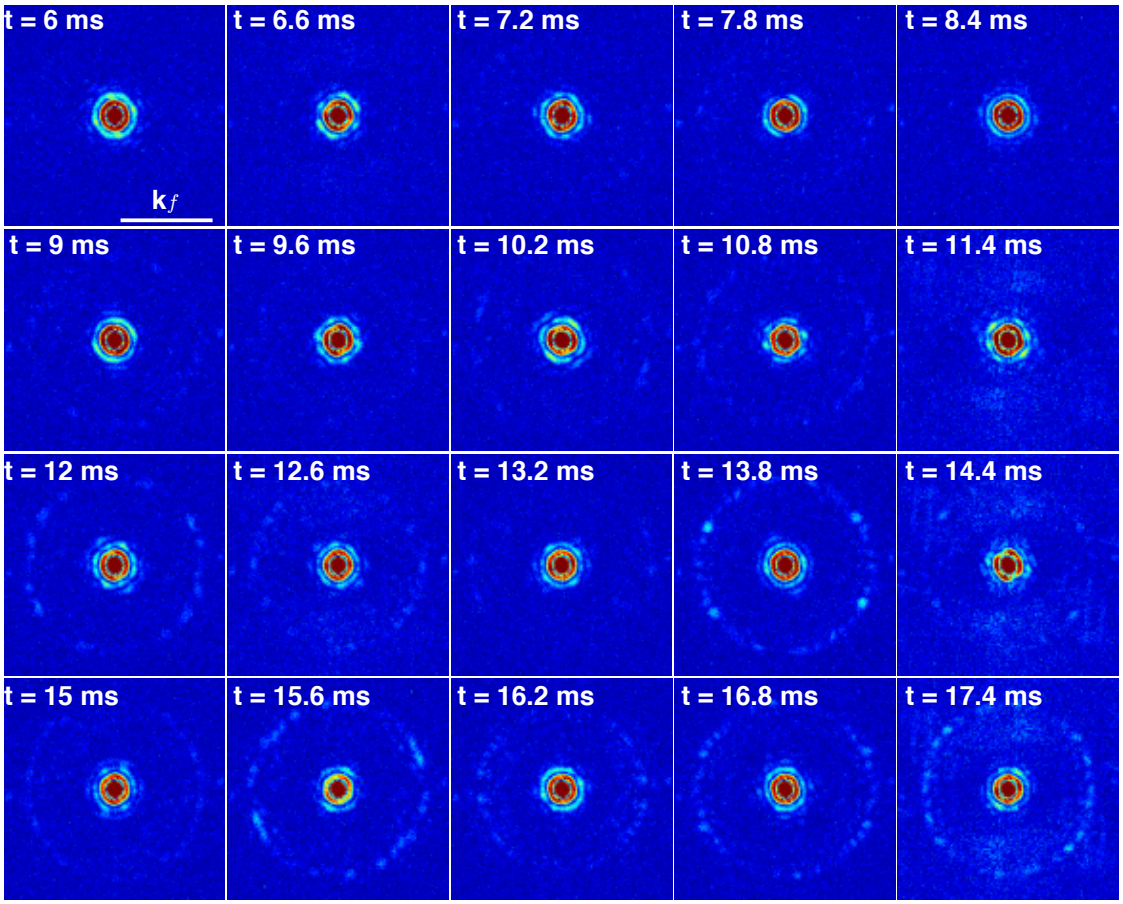

Figure 6.4: **Fourier spectrum of the density modulation-Part I.** The Fourier spectrum of the density wave is extracted directly from the Fig. 6.2 with fast Fourier transform.

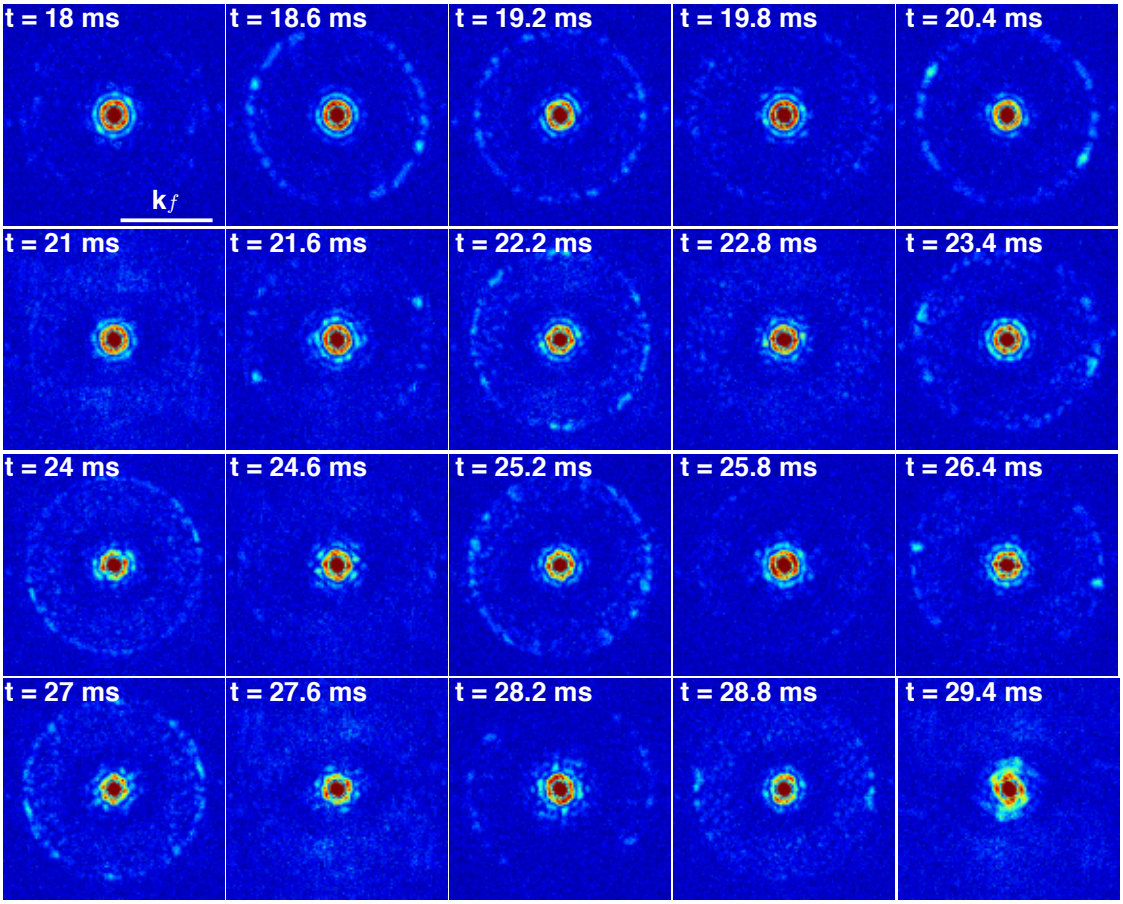

Figure 6.5: **Fourier spectrum of the density modulation-Part II.** The Fourier spectrum of the density wave is extracted directly from the Fig. 6.3 with fast Fourier transform.

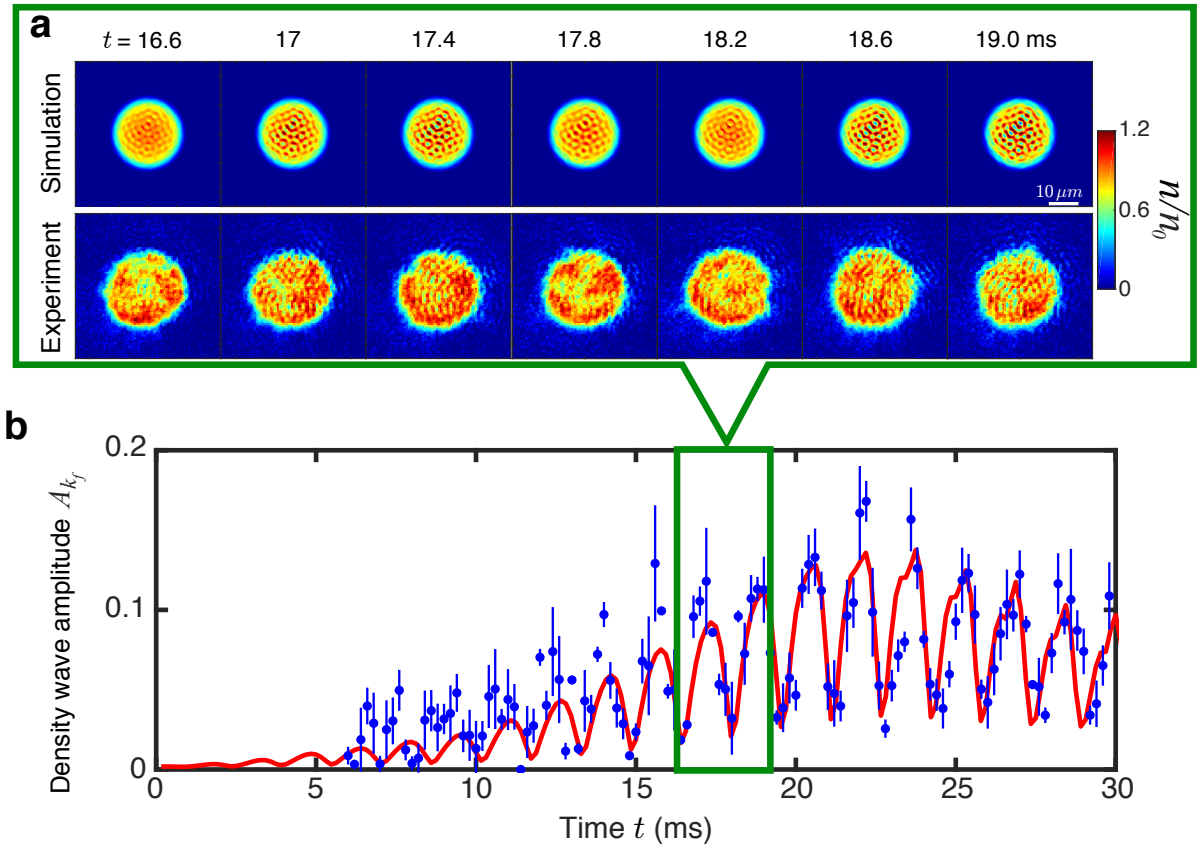

Figure 6.6: **Experiment and simulation comparison for early-stage density waves (DW) with $|k| = k_f$. a** The real-space DW oscillations inside the condensate. Theory (top) and experiment (bottom) show good qualitative agreement. The experiment exhibits additional static, long-wavelength density modulations due to trap imperfections. The experimental details are provided in the main text. **b** The amplitude of the density waves in the primary mode comparing simulations (red solid line) and experiments (blue dots with error bars). In addition to fast oscillations, both results show consistent observation of an exponential growth of the envelope until the matter-wave jets are emitted from the condensate.

GP equation (see Sec. 6.2). These symmetries are expected to arise from nonlinear kinetic terms in the hydrodynamic equations of motion [77, 110], which are not present in the GP equation.

6.2 Time-dependent Gross-Pitaevskii (GP) simulation

Our theoretical approach is based on a dynamical GP equation:

$$\begin{aligned} i\hbar\frac{\partial\psi}{\partial t} = &\left[-\frac{\hbar^2}{2m}\nabla^2 + V(\mathbf{r}) + U_0|\psi|^2 - \mu\right]\psi \\ &+ U_1\sin(\omega t)|\psi|^2\psi, \end{aligned} \tag{6.1}$$

where ψ is the wavefunction, $\mu = U_0 n_0$ is the chemical potential of the static condensate, $V(\mathbf{r})$ is the external trap potential, and $\mathbf{r} = (x, y)$ is a two-dimensional (2D) spatial coordinate (with origin at the trap center). In addition, $U_0 = 4\pi\hbar^2 a_{\rm dc}/m$ and $U_1 = 4\pi\hbar^2 a_{\rm ac}/m$ are the DC and AC interaction strengths, respectively. At short times, the condensate is weakly excited and the wavefunction can be linearized [98, 62]

$$\psi = \psi_0\left[1 + \nu(\mathbf{r}, t)\right], \tag{6.2}$$

where $\psi_0 = \sqrt{n_0}\exp\left[iU_1 n_0\cos(\omega t)/\hbar\omega\right]$ is the wavefunction of a uniform BEC, and U_0 has been absorbed through the parametrization in Eq. (6.1). Since the characteristic DW length scales are much smaller than the trap size, we ignore trap effects in our analytical approach. In the plane wave basis we write $\nu(\mathbf{r}, t) = [\xi(t) + i\zeta(t)]\cos(\mathbf{k}\cdot\mathbf{r} + \varphi)$ with both $\xi(t)$ and $\zeta(t)$ real and φ a random phase. Since $|\nu| \ll 1$, ξ satisfies the Mathieu equation for parametric resonances:

$$\frac{\partial^2\xi}{\partial t^2} + \Omega^2\left[1 + \alpha\sin(\omega t)\right]\xi = 0, \tag{6.3}$$

and ζ satisfies the same equation with an extra term $-\alpha\omega\cos(\omega t)\frac{\partial\zeta}{\partial t}$ on the left hand side. Here we keep only leading terms in α; $\Omega^2 = \hbar^2 k^4/4m^2 + U_0 n_0 k^2/m$, and $\alpha = U_1 n_0 k^2/m\Omega^2$.

The solution of Eq. (6.3) is $\xi(t) \approx A_+ \cos(\omega t/2+\vartheta_+)\exp(\lambda_+ t)+A_- \sin(\omega t/2+\vartheta_-)\exp(\lambda_- t)$. Here $A_\pm$ are numerical coefficients, and the exponents are

$$\lambda_\pm = \pm\sqrt{\frac{\alpha^2\Omega^2}{16} - \left(\Omega - \frac{\omega}{2}\right)^2}. \tag{6.4}$$

The solution exhibits both subharmonic oscillations with half the driving frequency ω and an exponential envelope growth (via λ_+). For $U_0 \approx 0$ as in experiments, the resonance with maximal λ_+ occurs at $k = k_f$. At this point, $\vartheta_\pm \approx 0$, and $\zeta(t) \approx -A_+ \sin(\omega t/2)\exp(\lambda_+ t) + A_- \cos(\omega t/2)\exp(\lambda_- t)$.

The interference between the uniform background and the excitations then gives the density $n(\mathbf{r}) = n_0|1+\nu(\mathbf{r},t)|^2 \approx n_0\,[1+2\xi(t)\cos(\mathbf{k}\cdot\mathbf{r}+\varphi)]$, leading to the density waves of exponentially growing envelope that we report here. To provide the full dynamical evolution and to include trap effects, we next appeal to the more complete numerical simulations of the GP equation.

Our simulations are 2D and incorporate a ring trap with inner and outer radii $R_{\rm in}$ and $R_{\rm out}$, respectively. We choose $V(\mathbf{r}) = V_0$ for $R_{\rm in} < r < R_{\rm out}$ and zero elsewhere. V_0 is taken to be compatible with experiment, $R_{\rm in}$ is taken to be the condensate radius, and, as in experiment [25], $R_{\rm out} \approx 1.5R_{\rm in}$. We use a CUDA-based GP equation solver [93, 2], implemented on graphic processing units, based on a split-step algorithm. At $t > 0$ we introduce a periodic oscillation of the two-body interaction term. Given the same experimental parameters, the corresponding results from GP simulation agree very well with emergence of density wave in our experiment shown in Fig. 6.7. This great agreement proves that our method can faithfully captures the dynamics of the driven condensates. With more comprehensive information about the dynamics from the simulation, we can gain further intuitive physical understandings.

It should be noted that the exponents in Eq. (6.4) coincide with those derived in Ch. 5 for the matter-wave jets. This suggests that the two forms of excitations are manifestations

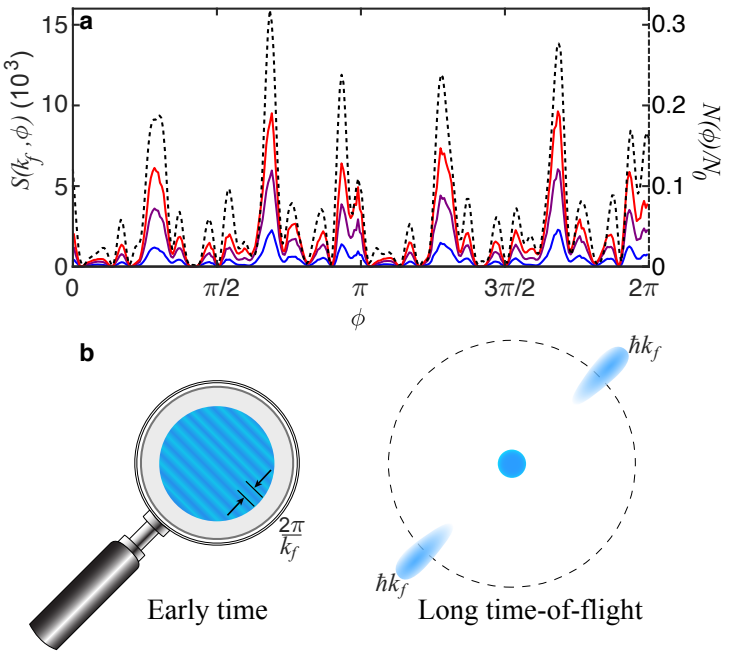

Figure 6.7: **Connection between density waves before jet emission and the subsequent matter-wave jet pattern.** **a** shows the azimuthal density structure factor $S(k_f)$ from a single iteration of the GP simulations at resonant wavenumber k_f at $t = 10$ (blue), 13 (purple), 15 (red) ms prior to jet emission. At each time we observe the same shape with growing amplitude, consistent with the expected amplification process of density waves. The dashed black curve is the real-space azimuthal population distribution of jets $N(\phi)$ at $t = 45$ ms. The scaling factor N_0 is the total number of atoms in the system. The alignment of all maxima and minima between $S(k_f, \phi)$ and $N(\phi)$ shows the equivalence between density waves and jets. **b** schematically shows that the early-time density waves with wavenumber k_f leads to the emission of counter-propagating jets with the same wavenumber k_f at long time.

of the same physics. This can be seen from Fig. 6.7 which contains results from our full GP simulations. Figure 6.7 provides strong simulation evidence that the density waves are necessary precursors to the jets and that they establish the template for the subsequent jet emission pattern. In particular, we find that the structure factor with fixed extrema (established by the DW pattern at the onset of shaking) is precisely equivalent to the real-space emitted jet population $N(\phi)$ observed after a long propagation time.

The structure factor is defined by $S(k_f, \phi) = N_0^{-1} \int k dk |\tilde{n}(\mathbf{k})|^2$, where the magnitude and phase of the wavevector are $|\mathbf{k}| = k \approx k_f$ and $\phi = \arctan(k_x/k_y)$. Note from Fig. 6.7**a** that the structure factor contains random peaks and valleys as determined by the initial random seed which emulates the fluctuations of real experiments. These patterns are established at the onset of shaking, and the only change with increasing time is an exponential growth of the peak amplitudes.

The dashed black line plotted in Fig. 6.7**a** is the real-space azimuthal distribution for the jet population $N(\phi) = \int_{\mathbf{r}=(\hbar t/m)\mathbf{k}} r dr\, n(\mathbf{r})$, at long times. Importantly, the angular distribution shows the equivalence between $S(k_f, \phi)$ and $N(\phi)$. This underlies our claim that density waves and jets are deterministically correlated. These results are summarized in Fig. 6.7**b**. This presents a schematic plot linking the momentum space spectrum of the DW and the population of jets with the same wavevector $\pm\mathbf{k}$ after long time of flight.

6.3 Asymmetry of jet emission

Having established the equivalence between the far-field jets and the initial density waves, one might naturally expect that the same azimuthal distribution would appear in the near-field regime, when jets are first emitted from the condensate. However, the numerical simulations show that this is not the case. Fig. 6.8 presents the density distribution in real and momentum space in **a** and **b**, respectively. The left column corresponds to early times where the jets are just emerging while the right column is for long times. In momentum space a primary ring (and weak secondary rings) are visible and one sees very little time dependence; this is

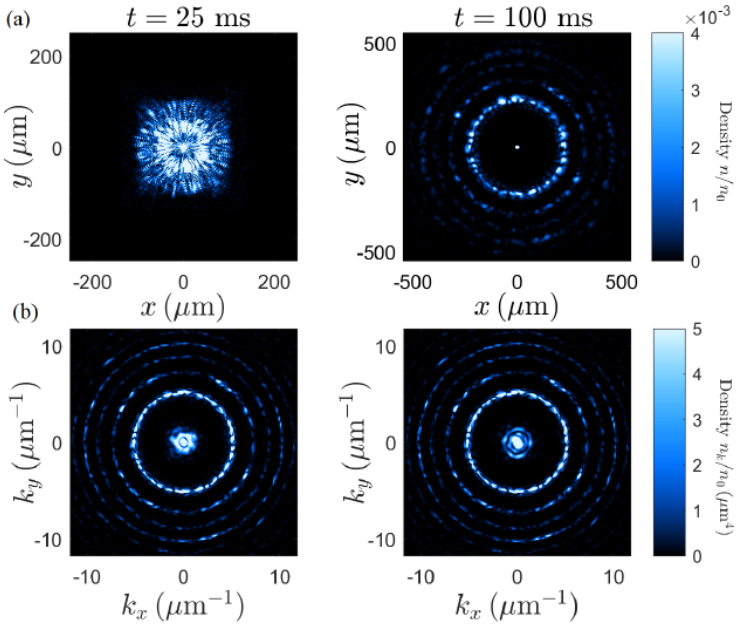

Figure 6.8: **Density distributions at early and late times. a** Real-space distribution $n(\mathbf{r})$ (denoted by n). The TOF distribution changes substantially with growing time and approximately reproduces the k-space results at large t. **b** Momentum-space distribution $n(\mathbf{k})$ (denoted by n_k). A primary ring (along with weak secondary rings representing higher harmonics) shows little variation with time. The left column shows the early-time behavior ($t = 25$ ms) when jets have just emerged. The right column indicates the late-time distribution ($t = 100$ ms) when jets are far away from the trap.

in contrast to the real-space plots. Nevertheless at longer times it seems that the real-space time of flight (TOF) appears to reproduce the k-space distribution of particles.

To gain further insight, in Fig. 6.9 we plot the momentum- (left column) and real-space (right column) azimuthal number distributions. These correspond, respectively to $N_{k_f}(\phi)$ and $N(\phi)$, where $N_{k_f}(\phi) = \int_{\mathbf{k}'=\mathbf{k}} k dk\, n(\mathbf{k}')$ and $\mathbf{k} = k_f(\cos\phi, \sin\phi)$. Plotted as solid lines in each row are distributions for the same 4 indicated times. The dashed lines correspond to the same plot with each angle shifted by π. This corresponds to the shifted distribution $N'_{k_f}(\phi) = N_{k_f}(\phi + \pi)$ and $N'(\phi) = N(\phi + \pi)$, respectively.

In the momentum-space plot of Fig. 6.9 one can see an essentially exact coincidence of the solid and dashed curves showing the full symmetry between excitations with opposite momentum. This occurs for all times and is a manifestation of momentum conservation throughout. This behavior should be contrasted with plots of the real-space distribution in Fig. 6.9 where one can see quite generally, that the peaks of $N(\phi)$ and in the shifted distribution $N'(\phi) = N(\phi + \pi)$ are misaligned. Importantly, only at the latest times (in the far field) is there a complete overlap of the curves which translates into a $(0, \pi)$ symmetry for the correlation function $g^{(2)}(\phi)$. As a result, a clear modification of the distribution shape with varying time is seen and is accompanied by an "inversion symmetry breaking" (in the near field), see in Fig. 6.10 **a** and Fig. 6.10 **b**. This is associated with the previous observation in Ch. 5 of an asymmetric two-particle correlation function $g^{(2)}(\phi)$ of the jet emission pattern, i.e., $g^{(2)}(\pi) \neq g^{(2)}(0)$.

To quantify this inversion asymmetry, we introduce a parameter

$$\eta_r = \frac{\left\langle [N(\theta) - N(\theta + \pi)]^2 \right\rangle}{2 \langle N(\theta) \rangle^2} = g^{(2)}(0) - g^{(2)}(\pi) \tag{6.5}$$

for real space and its analogue, η_k in momentum space, where $\langle \ldots \rangle$ corresponds to averaging over angles θ and ensembles. Here the two-particle correlation function $g^{(2)}$ in

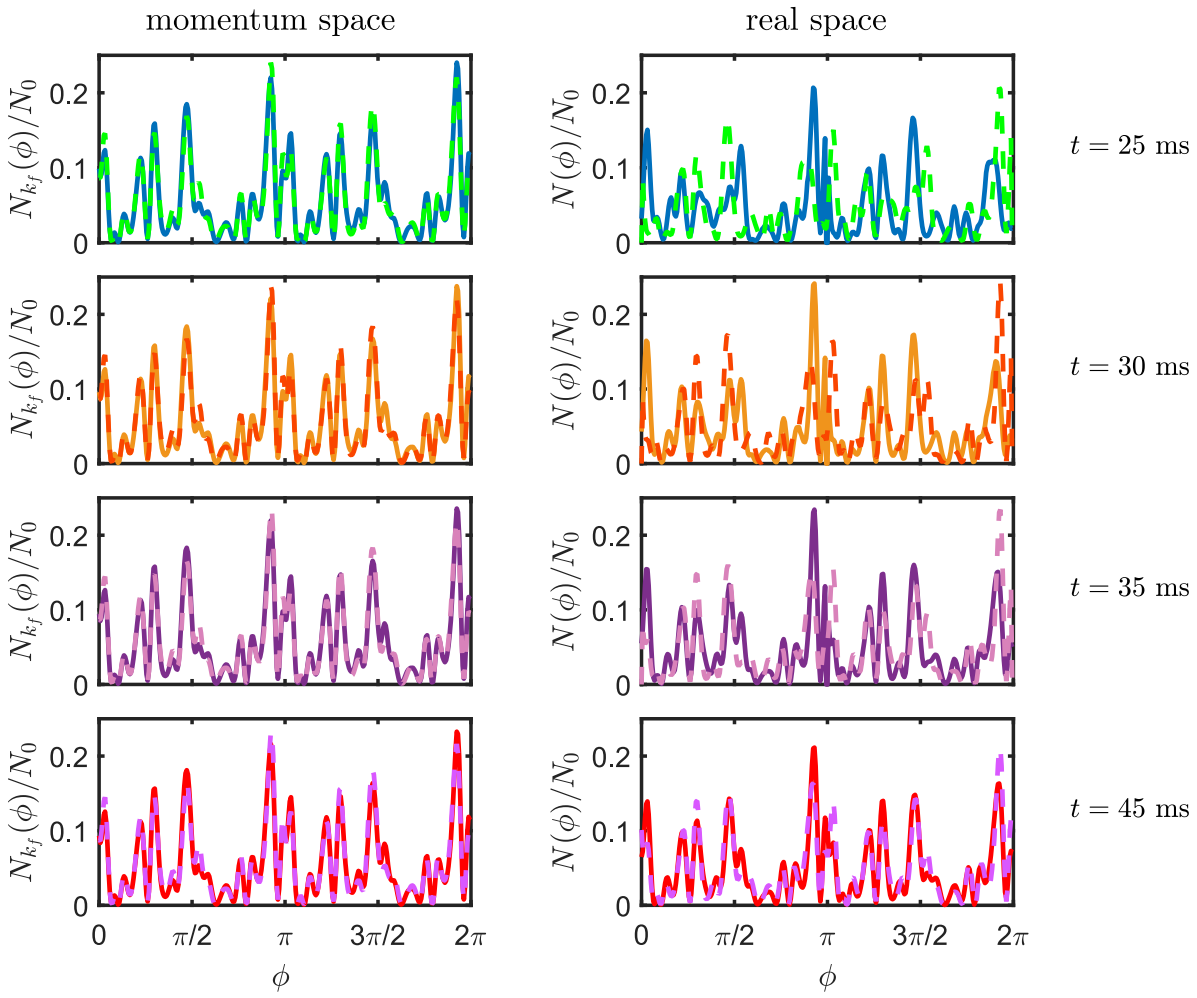

Figure 6.9: **Momentum- and real-space π-shifted plots.** Each panel shows the real-space azimuthal number distribution $N(\phi)$ (solid line) superposed with its π-shifted curve (dashed line) $N'(\phi) = N(\phi + \pi)$. Different colors correspond to different times: $t = 25$ ms (blue), $t = 30$ ms (yellow), $t = 35$ ms (purple), and $t = 45$ ms (red). Peaks of $N(\phi)$ and $N'(\phi)$ are misaligned at small t and well aligned at large t.

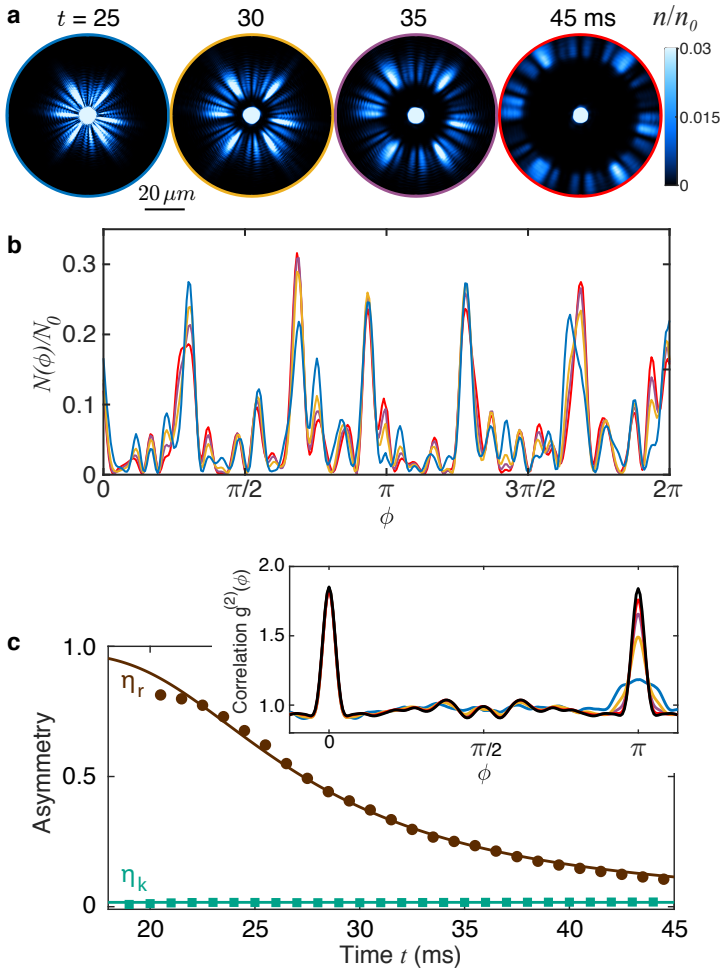

Figure 6.10: **Time evolution and correlations of the emitted jets.** **a** shows the calculated jet emission pattern evolving from the near- to far-field regimes. The calculation is based on identical initial noise seeding. **b** shows the real space azimuthal population of the four images in **a**, identified by the same color. Note that the $t = 45$ ms far-field curve is equivalent to that shown dashed in Fig. 6.7**a**. Here unlike in Fig. 6.7, the peaks and valleys are slightly displaced with time. Panel **c** probes the emission asymmetry in real space $\eta_r = g^{(2)}(\pi) - g^{(2)}(0)$ (brown circles) and the momentum-space analogue η_k (green squares). The main figure shows that the $(0, \pi)$ asymmetry is always absent in momentum space (η_k is strictly zero within numerical precision) so that momentum is conserved. In real space, using Panel (b) we find that this $(0, \pi)$ asymmetry decreases with increasing time. The inset indicates the correlation function $g^{(2)}(\phi)$ at the same 4 times as in **a**, along with an early time momentum correlation function at $t = 20$ ms (black curve). Again, inversion 0-π symmetry is broken at short times, but recovers after long time-of-flight, and is fully preserved in momentum space. The solid line (brown) in **c** is an analytical fit to η_r.

real/momentum space as

$$g^{(2)}(\phi) = \frac{\langle n(\theta)\, n(\theta+\phi)\rangle}{\langle n(\theta)\rangle^{\,2}}, \tag{6.6}$$

where $n(\theta)$ is the particle population at azimuthal angle θ. In real space, this corresponds to density $n(\mathbf{r})$ at the position $\mathbf{r} = r(\cos\theta, \sin\theta)$. We can also define the momentum-space analogue of $g^{(2)}(\phi)$, where $n(\theta)$ refers to $n(\mathbf{k})$ at $\mathbf{k} = k_f(\cos\theta, \sin\theta)$. Here $r = v_f t$ and $v_f = \hbar k_f/m$ is the jet velocity. $n(\mathbf{r}) = |\psi(\mathbf{r})|^2$, $n(\mathbf{k}) = |\psi(\mathbf{k})|^2$, and $\psi(\mathbf{k}) = (2\pi)^{-1}\int d\mathbf{r} e^{-i\mathbf{k}\cdot\mathbf{r}}\psi(\mathbf{r})$ is the Fourier transform of the wave function $\psi(\mathbf{r})$. $\langle \ldots \rangle$ refers to an average over different angles θ and ensembles.

Figure 6.10 **c** plots the asymmetry functions, $\eta_{r,k}$, in real- and momentum-space, together with the corresponding correlation function $g^{(2)}(\phi)$ shown in the inset. The spatial asymmetry η_r decreases from a finite value to zero when going from the near to far field. This indicates that the inversion symmetry is recovered at large times. The momentum-space asymmetry η_k, interestingly, remains zero independent of time, showing clearly that momentum conservation is obeyed at all times.

We attribute this asymmetry to the fact that, in the near field, excitations of different wavevectors substantially overlap with each other. The resulting pattern is derived from interference between these overlapping modes, which have uncorrelated random phases. Thus, when measuring the population at angles θ and $\theta + \pi$, the symmetry between the relevant counter-propagating pair $\pm\mathbf{k}$ ($\tan\theta = k_y/k_x$) is masked by interference from other uncorrelated modes. By contrast, in the far field, different modes are well separated so that each jet now represents a single mode. Here momentum conservation is more apparent and inversion symmetry in real space is recovered.

We further develop a simple analytic model based on this intuitive physical picture. This model builds on our understanding that the phase remains correlated only within the same excitation mode. We shall demonstrate this later in Ch. 6.4.

As shown in Fig. 6.11, in both the near-field and far-field situations, the only perfectly correlated pair of modes is the counter-propagating one going through the center of the

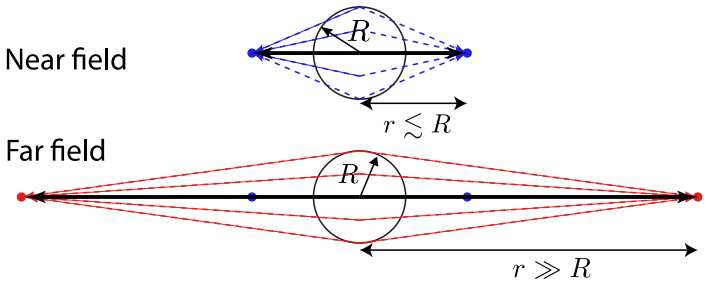

Figure 6.11: **Schematic of near- and far-field TOF.** In both near and far fields, the only correlated modes are the counter-propagating pair. In the far field where the distance between jets and trap center (called r) is much bigger than trap size R, fewer modes appear to overlap as seen from the measurement point.

condensate (marked as thick black lines with arrow heads). As a result, the wave function at $\mathbf{r}$ and $-\mathbf{r}$ can be approximated as

$$\begin{aligned} \psi(\mathbf{r}) &= \sqrt{n_1}e^{i\varphi_1} + \sum_{j=2}^{m} \sqrt{n_j}e^{i\varphi_j} \\ \psi(-\mathbf{r}) &= \sqrt{n_1}e^{-i\varphi_1} + \sum_{j=2}^{m} \sqrt{n'_j}e^{-i\varphi'_j}, \end{aligned} \tag{6.7}$$

where n_1 is the occupation of the perfectly correlated modes while n_j and n'_j are the occupations of modes propagating in different directions. Note φ_i and φ'_j are uncorrelated.

We now want to count the number of overlapping modes M at the measurement point $r = v_f t$ forming the jet. Entering into the count is $\Delta\phi/\delta\theta = \arctan(R/r)/\delta\theta = \arctan(R/v_f t)/\delta\theta$ with $\delta\theta \sim 1/k_f R$ representing the angular half width of the jets. This provides a reasonable estimate of M in the near field. However, this is inadequate in the far field because it approaches zero, rather than the expected 1. Thus a more appropriate, phenomenological estimate would be to add the near- and far-field estimates in quadrature

$$M = \sqrt{1 + \left(\frac{\Delta\phi}{\delta\theta}\right)^2}. \tag{6.8}$$

Using Eq.(6.7), the correlation function can then be written as

$$
\begin{aligned}
g^{(2)}(0) &= \frac{\langle \psi^*(\mathbf{r})\psi(\mathbf{r})\psi^*(\mathbf{r})\psi(\mathbf{r})\rangle}{\langle \psi^*(\mathbf{r})\psi(\mathbf{r})\rangle \langle \psi^*(\mathbf{r})\psi(\mathbf{r})\rangle} \\
g^{(2)}(\pi) &= \frac{\langle \psi^*(\mathbf{r})\psi(\mathbf{r})\psi^*(-\mathbf{r})\psi(-\mathbf{r})\rangle}{\langle \psi^*(\mathbf{r})\psi(\mathbf{r})\rangle \langle \psi^*(-\mathbf{r})\psi(-\mathbf{r})\rangle}.
\end{aligned}
\tag{6.9}
$$

And we have

$$
\langle \psi^*(\mathbf{r})\psi(\mathbf{r})\rangle = \langle \psi^*(-\mathbf{r})\psi(-\mathbf{r})\rangle \tag{6.10}
$$

$$
= \sum_{j=1}^{m} \langle n_j \rangle + \left\langle \sum_{i\neq j} \sqrt{n_i n_j}\cos(\varphi_i - \varphi_j) \right\rangle \tag{6.11}
$$

$$
= M \langle n \rangle , \tag{6.12}
$$

where $\langle n \rangle$ is the average density associated with a jet. The same-site correlation function is

$$
\begin{aligned}
&\langle \psi^*(\mathbf{r})\psi(\mathbf{r})\psi^*(\mathbf{r})\psi(\mathbf{r})\rangle \\
=&\sum_{i,j} \langle n_i n_j \rangle + 2\sum_{i\neq j} \left\langle n_i n_j \cos^2(\varphi_i - \varphi_j) \right\rangle \\
=& M \left\langle n^2 \right\rangle + 2M(M-1)\langle n \rangle^2 \\
=& 2M^2 \langle n \rangle^2 ,
\end{aligned}
$$

where $\left\langle n^2 \right\rangle = 2\langle n \rangle^2$ for the parametrically driven jet emission [25], see Ch. 5.

We compare this with the correlation between forward and backward modes which is

given by

$$\begin{aligned}
&\langle\psi^*(\mathbf{r})\psi(\mathbf{r})\psi^*(-\mathbf{r})\psi(-\mathbf{r})\rangle = \left\langle n_1^2 \right\rangle + \sum_{i,j=2}^{M} \left\langle n_i n_j' \right\rangle \\
&+ \sum_{j=2}^{M} \langle n_1 n_j \rangle + \sum_{j=2}^{M} \left\langle n_1 n_j' \right\rangle \\
&= \left\langle n^2 \right\rangle + (M-1)^2 \langle n \rangle^2 + 2(M-1) \langle n \rangle^2 \\
&= (M^2+1) \langle n \rangle^2 .
\end{aligned}$$

We can then write for the real-space correlation functions

$$\begin{aligned}
g^{(2)}(0) &= 2 \\
g^{(2)}(\pi) &= 1 + \frac{1}{M^2} = 1 + \frac{1}{1 + \arctan(R/vt)^2/\delta\theta^2}.
\end{aligned} \tag{6.13}$$

In very near field, $M \gg 1$, $g_2(\pi) \approx 1$, indicating a nearly full suppression of the π peak or equivalently very strong asymmetry. In the far-field limit ($m \sim 1$) we have $g^{(2)}(\pi) = g^{(2)}(0) \approx 2$, so that perfect symmetry is restored.

As a result we can derive the asymmetry between peaks at $\phi = 0$ and $\phi = \pi$ in real space, which is given by

$$\begin{aligned}
\eta_r &= \frac{\left\langle [N(\theta) - N(\theta+\pi)]^2 \right\rangle}{2 \langle N(\theta) \rangle^2} \\
&= \frac{\left\langle [n(\theta) - n(\theta+\pi)]^2 \right\rangle}{2 \langle n(\theta) \rangle^2} \\
&= g^{(2)}(0) - g^{(2)}(\pi) \\
&= 1 - \frac{1}{1 + \arctan(R/vt)^2/\delta\theta^2}.
\end{aligned} \tag{6.14}$$

For momentum space, we similarly define the analogous function η_k using the same expression as for η_r but with the real-space population $N(\theta)$ replaced by the momentum-space occupation $N_{k_f}(\theta)$. A fit of the asymmetry function η_r by Eq. (6.14) is given by the solid

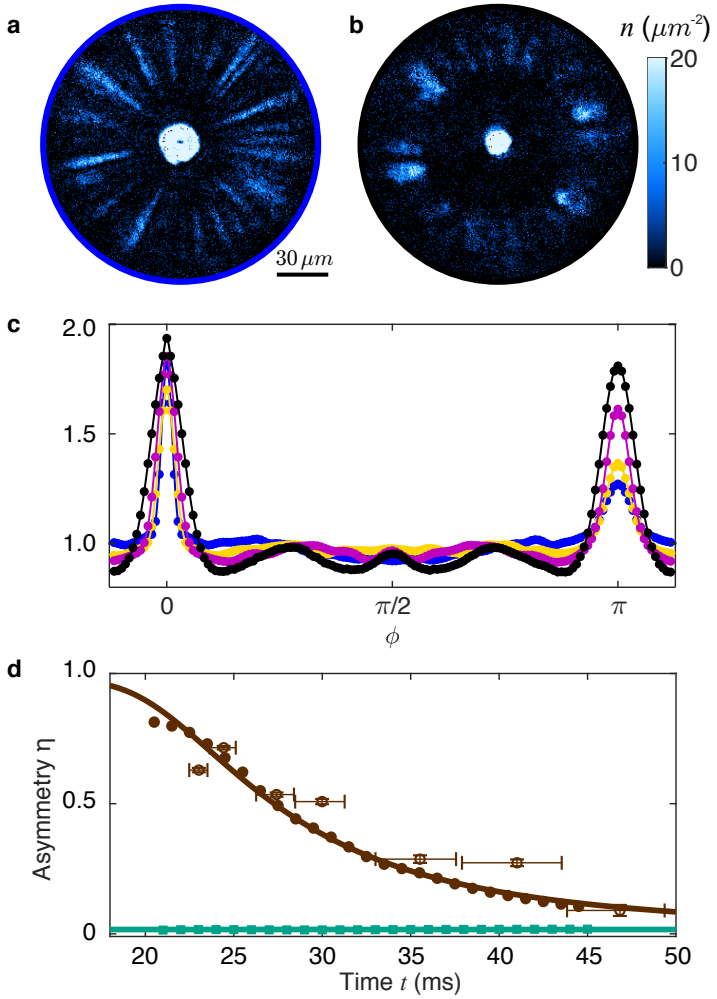

Figure 6.12: **Experimental probes of the $(0,\pi)$ asymmetry: measured correlations of emitted jets for different condensate sizes.** Examples of jet emission of radii R =12.4 μm and 5.9 μm are shown in **a** and **b** respectively. **c** Correlation functions $g^{(2)}(\phi)$ for traps of radii R =5.9 μm (black), 7.6 μm (purple), 9.3 μm (yellow), and 12.4 μm (blue); these are measured at roughly similar distances from the condensates r=52.3 μm (black), 55.4 μm (purple), 52.0 μm (yellow), and 61.7 μm (blue), respectively. The mode number $M \approx 1.23 k_f R^2/r$ in the relevant parameter range is 4.3 (black), 6.5 (purple), 10.5 (yellow), and 15.7 (blue). Note that the symmetry gradually recovers as M decreases. **d** Asymmetry function $\eta(t')$ from both simulations and experiments. In addition to results present in Fig. 6.10, the scaled experimental data for the real-space asymmetry function $\eta_r(t')$ are shown, as denoted by square symbols with error bars (brown). To compare with previous results of the condensate of radius 6.5 μm, the conversion is done where the effective time t' is obtained by equating $\arctan(R_0/v_f t')R_0 = \arctan(R/r)R$, where R_0 is the reference trap radius 6.5 μm. Note that the experimental data are reasonably consistent with simulations and the analytical fit.

line (brown) in Fig. 6.10**c**, where the agreement is quite satisfactory.

From Eq. (6.8), one can also see that varying the trap size for a similar observation point is equivalent to changing the point from the near- to far-field regimes. In this regard, we present further experimental data for different condensate radii. In Fig. 6.12**a**, a symmetry of the two-particle correlation function at $\phi = 0$ and π, similar to the one in Fig. 6.12**c**, is recovered, where the mode number m is decreased mainly via decreasing the trap size. To be more quantitative, we plot the real-space asymmetry function $\eta_r(t')$ from the experimental data in Fig. 6.12**b**. For the sake of comparison, all data are scaled to a condensate of size $6.5\,\mu$m, as simulated in Fig. 6.10. The effective observation time t' for such a condensate is obtained by equating the mode number M in the real experiments and that for the reference trap at t'. From Eq. 6.8, one can see that this leads to $\arctan(R_0/v_f t')R_0 = \arctan(R/r)R$, where R_0 is $6.5\,\mu$m, R is the real condensate size, $r = v_f t$ is the actual imaging distance from the trap with t being the real measurement time. The scaled experimental $\eta_r(t')$ is reasonably consistent with simulations and the analytical fit, which corroborates our theory.

6.4 Phase coherence of jet emission

We finally look at Fig. 6.13 which addresses the phase coherence of the different modes. This serves to motivate the analytical model in Eq. 6.7. Plotted in this figure is the phase of the full GP wavefunction in the far-field configuration, as a function of position. This is overlaid with a momentum distribution plot (yellow line) which indicates the real space configuration of the jets in the far field. "Phase slips" are evident with varying azimuthal position. Dashed lines have been inserted to mark these phase discontinuities; one can see that the phase slips occur somewhere in the empty space between the jets (which each represent a single mode in the far field). Importantly there is phase coherence within a jet while different modes have uncorrelated phases. All of this is consistent with the analytical model discussed above and serves as a validation. In addition, we shall further see in Ch. 7 that the phase between forward and backward jets are correlated.

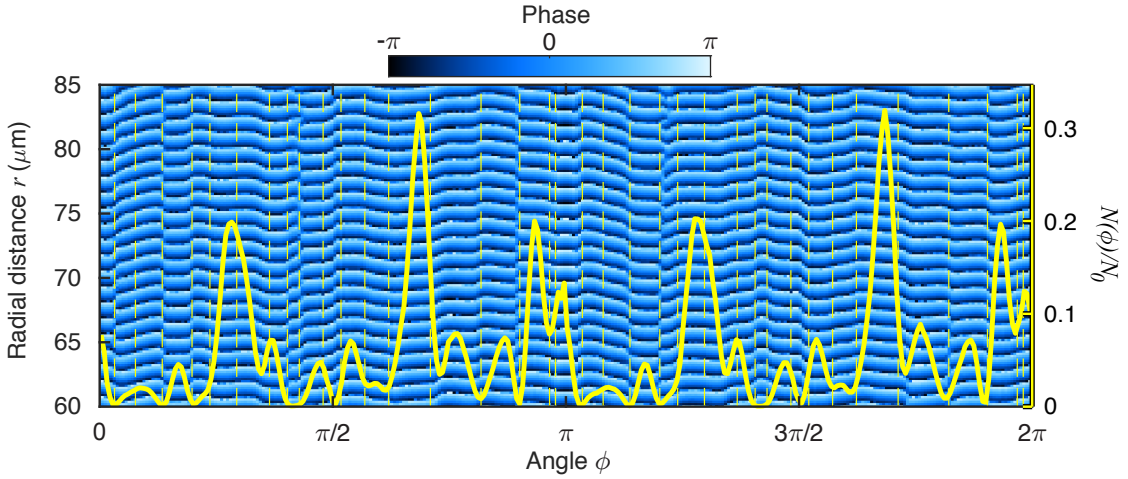

Figure 6.13: **Intra-jet phase coherence in far field.** Comparison of GP wave-function phase and momentum distribution of jets as a function of the azimuthal angle ϕ for the relevant radial range where the jets are located. Dashed lines have been inserted to mark phase discontinuities. The yellow curve is the momentum distribution which represents the far field spatial configuration of the jets. Within each jet there is phase coherence. However, coherence typically ends at the boundary between different jets (modes) where a "phase slip" can be seen. It should be noted that the applicability of the "edge finding" algorithm used here leads to occasional errors when the phase slips are found to be particularly small.

CHAPTER 7

QUANTUM SIMULATION OF UNRUH RADIATION

In this chapter, we investigate comprehensively into the mode population distribution the stimulated emission of jets in strongly driven condensates. We find that the mode population exhibits a thermal-like distribution in Sec. 7.1. This thermal-like distribution is generated from a two-mode squeezing process (see Sec. 7.2), which further connects to the famous Unruh radiation [103] in a constant accelerating frame. Although the population distribution is thermal-like, the matter-wave jets from pair-generation are still coherent, which is examined in two experiments in Sec. 7.4. By applying two pulses of driving with different frequencies in sequence, we are able to show the phase coherence between jets generated in pairs. Meanwhile, by inverting the driving phase, we are able to reverse the process and demote atoms back to the condensates. At last, we propose a general type of quantum simulation frame transformation with non-equilibrium quantum gases.

7.1 Observation of thermal-like atomic number distribution

Previously, we have shown the Bose fireworks due to stimulated emission of matterwave in strongly driven condensates. The emission manifests as a number of jets flying out of the condensate after modulating the interaction for short amount of time. We have studied variously interesting properties of the emitted jets, including their kinetic energy, angular width, and density-density correlations. Besides, we also notice that atomic population along different angular directions are not homogeneous, see Fig. 7.1 as an example. Along some of the angular directions we see more atoms in the jets as opposed to the others. In a statistic view, we see that the probability $P(n)$ of finding n particles in a slice is exponential-like at large n limit, which resemble that from a thermal radiation where the probability $P(n)$ $\beta e^{-\beta n}$ with $\beta = E_k/k_{\mathrm{B}}T$, where T is defined as an effective temperature and $E_{k_f} = \hbar\omega/2$ is the kinetic energy of each atom. We shall that this exponential-like distribution is another

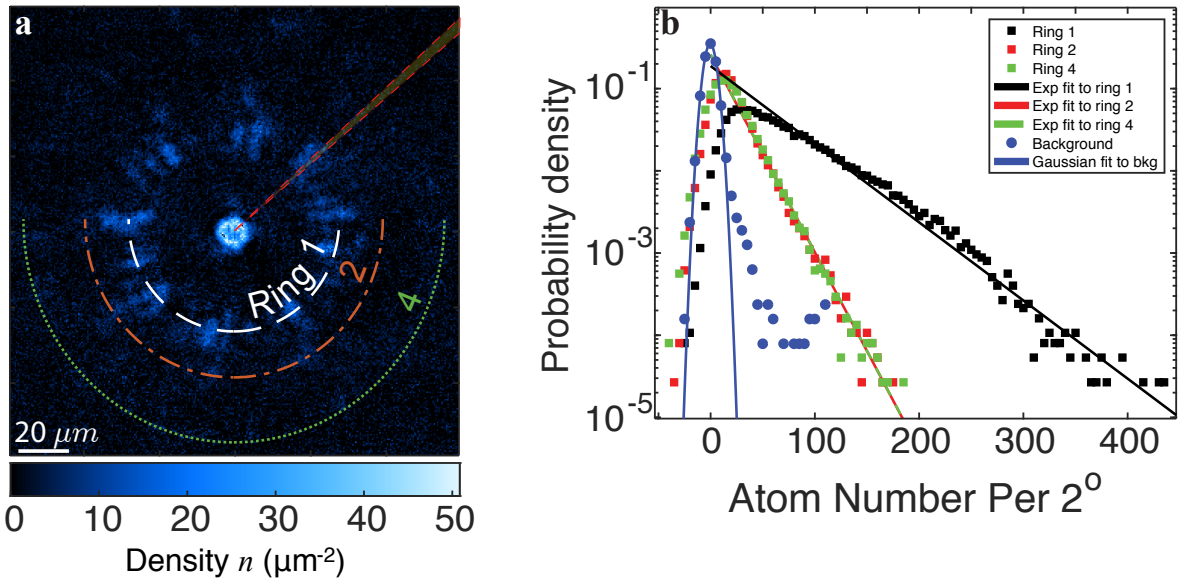

Figure 7.1: **Atomic population distribution.** **a** shows three rings (illustrated by the white, orange and green circles) in a single shot image at a larger modulation amplitude $a_{ac} = 45\ a_0$ and modulation frequency of $\omega = 2\pi\times 2$ kHz, which is under the same condition as that of Fig. 5.1**d**. We divide the image into 2° slices and count the atom number for each slice within separate rings. **b** shows the probability density of finding N atoms within a 2° slice in ring 1, 2 and 4 (black, red and green square). The corresponding solid lines are exponential fits at large atom number limit. The blue square shows the background fluctuations from imaging without atoms and the blue solid line is a Gaussian fit.

manifestation of quantum nature of the jet emission.

For simplicity, we perform our experiment with conditions that suppress generation of high-order harmonics and only focuses on the population distribution from primary collisions. Following a similar procedure to that which is described in chapter 5, this experiment starts with a Bose-Einstein condensate of 6×10^4 atoms confined in a disk-shaped trap with a radius of 13 μm. By modulating the magnetic field at frequency $\omega = 2\pi\times 2.1$ kHz near a Feshbach resonance [20, 82], we oscillate the scattering length with an amplitude of $a_{ac} = 50a_0$ around a small offset $a_{dc} = 3a_0$. A few millisecond after the modulation, a single ring of jets of atoms with momentum $k_f = \sqrt{m\omega/\hbar}$ flies out of the condensates. Such emission forms a fluctuating bosonic field and is a result of bosonic stimulation.

Experimentally we slice our emission patterns into 180 slices and count the atom number

in each slice. Based on the histogram of atom counting from the measurements, we build the probability distribution function $P(n)$. Based on this particular distribution, we can achieve a separate calibration of the mode width of the jets beside that from the density-density correlation function. We further calculate $\langle n\rangle = \int nP(n)dn$ and $\Delta n^2 = \langle n^2\rangle - \langle n\rangle^2 - \Delta n^2_{noise}$. Here Δn^2_{noise} is the variance contributed from the detection noise which is statistically independent from the signal from atom counting, as shown in Fig. 7.1**b**. We find a linear dependence between the mean square of atom number and the variance from the experiment as (see Fig. 7.2)

$$\langle n\rangle^2 = \xi\Delta n^2. \tag{7.1}$$

Here $\xi = \Delta\theta_S/\Delta\theta_J = 1.49(7)$ is determined from the fitting, characterizing the mode width $\Delta\theta_J$ with each slice's width $\Delta\theta_S = 2^\circ$. Therefore, $\Delta\theta_J$ equals to 1.33°. We also calculate $\Delta\theta_J$ from another independent way. Using the formula $\Delta\theta_J = 1.62/(Rk_f)$ in Ref. [25] which comes from the half width at half maximum of the peak at $\phi = 0$ in the $g^{(2)}$ function, we obtain a consistent result of $\Delta\theta_J = 1.3^\circ$. It worth mentioning a special case that when we choose the slice to be the width of a jet with $\xi = 2$ we have $\langle n_M\rangle^2 = \xi\Delta n^2_M$, given by the correlation function.

We notice that a angular slice could include several different modes. Based on this probability distribution that is built up from angular slices, we want to test and verify that the emitted atom number in each mode follows a thermal distribution. We derive a more general formula for the probability distribution $p(n,\xi)$ in a slice with any width $\Delta\theta_S = \xi\Delta\theta_J$. Because the mean population per mode $\langle n_M\rangle$ is always larger than 1 in our measurements, we treat the distribution $p(n,\xi)$ as a continuous function where the summation $\sum_{n=0}^{\infty} p(n,\xi) = 1$ is replaced by an integral $\int_0^\infty dnp(n,\xi) = 1$.

We shall start by listing a few properties of the function $p(n,\xi)$. First, $p(n,\xi)$ must equal to 0 when n is a negative number. Second, if the angular slice only contains one momentum mode (*i.e.* $\xi = 1$), $p(n,1)$ should be a thermal distribution, where $p(n,1)$ equals $\beta e^{-\beta n}$ with $\beta = E_{k_f}/k_{\mathrm{B}}T$. Third, $p(n,\xi)$ has to satisfy the addition rule that combining two slices of ξ_1

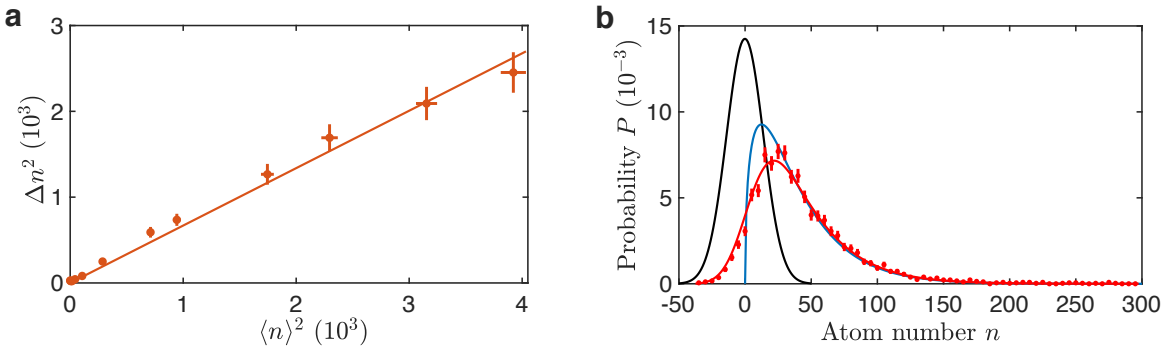

Figure 7.2: **Determination of the mode width and the fitting of the measured probability distribution P(n).** **a** shows the linear dependence of mean square $\langle n \rangle^2$ and variance Δn^2 of atom number distribution in the slice with an angular width $\Delta\theta_S = 2°$, from which we have subtracted the contribution from the detection noise. **b** shows the background atom number distribution $G(n, 1.5)$ (black line), ideal emitted atom number distribution $p(n, 1.5)$ (blue line) and the convolution between both of them $P(n, 1.5)$ (red line) which fits the measured probability distribution $P(n)$ (red circles) at the modulation time $\tau = 4.8$ ms.

and ξ_2 will create a new slice of $\xi_1 + \xi_2$. We can write the third requirement more explicitly as a mathematical equation

$$p(n, \xi_1 + \xi_2) = \int_{-\infty}^{\infty} p(n', \xi_1) p(n - n', \xi_2) dn'. \tag{7.2}$$

From all the above conditions, we solve the probability distribution $p(n, \xi)$ analytically as

$$p(n, \xi) = \begin{cases} \beta^{\xi} n^{\xi - 1} e^{-\beta n} / \Gamma(\xi) & n \geq 0 \\ 0 & n < 0, \end{cases} \tag{7.3}$$

where $\Gamma(\xi)$ is the gamma function.

In addition to the signals from the atoms, the detection noise contributes to the measured probability distribution of the atom number. Experimentally we characterize this noise distribution $G(n, \xi)$ by inspecting the images without any radiations. Once we get $G(n, \xi)$,

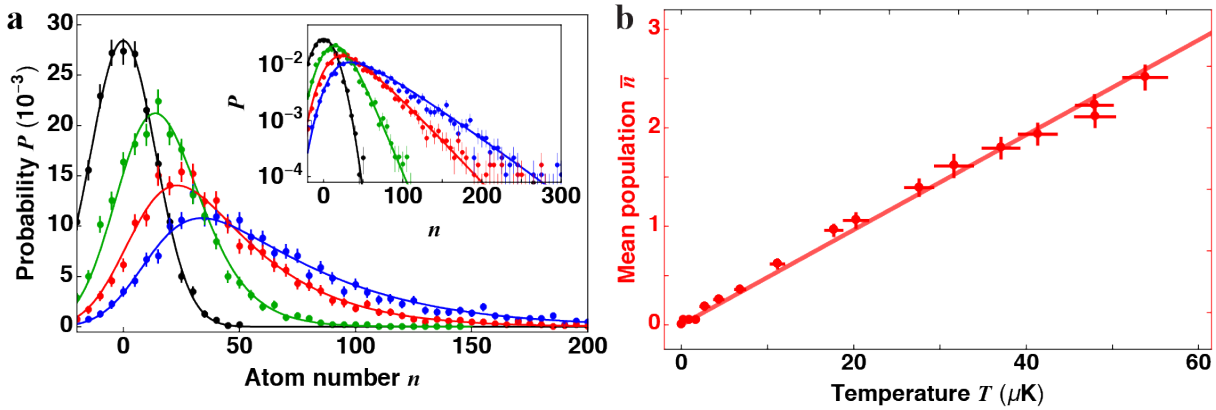

Figure 7.3: **Thermal-like behavior of the matter-wave emission.** **a** shows the measured probability distribution $P(n)$ within a 2° slice of the emission pattern after modulation time $\tau =$ 0, 3.36, 4.8 and 6.24 ms (black, green, red and blue circles). The solid lines are fits based on a thermal model. The inset shows the data in the log scale. **b** shows the effective temperature T (red circles). The red solid line is a linear fit. All error bars correspond to one standard deviation of the mean values.

we convolve it with $p(n, \xi)$ to get a full distribution function

$$P(n, \xi) = \int_{-\infty}^{\infty} dn' p(n', \xi) G(n - n', \xi). \tag{7.4}$$

Then we use this function to fit our data extracting out the effective temperature T under the condition of $\xi = 1.49$ (see Fig. 7.2**b**).

We later study this thermal-like distribution after different amount of time after modulation, see Fig. 7.2**a**. At very early time, few atoms are excited into jets, the distribution is simply dominated by imaging noise. As the modulation time further increases, the distribution extends much more to the right while the average excited atom number increase exponentially as a function of modulation time. By fitting the experimental data with the convoluted distribution function, Eq. (7.4), we can extract the effective temperature. The effective temperature is plotted together with the mean atomic population within a single jets $\bar{n}$, see Fig. 7.2**b**. It very interesting to notice that the effective temperature linearly depends on the mean atomic population, which can be seen from the calculation based on

two-mode squeezing in Sec. 7.2.

7.2 Effective temperature and entropy

We start with Hamiltonian in a rotating-wave frame and under Bogoliubov approximations, see Eq. (5.12),

$$H = i\hbar\nu \sum_{|\mathbf{k}|=k_f} (a_k^\dagger a_{-k}^\dagger - a_k a_{-k}), \tag{7.5}$$

where $\nu = \pi\hbar N_0 a_{ac}/mV$ and $k_f = \sqrt{m\omega/\hbar}$. This Hamiltonian is essentially a combination of a series of two-mode squeezing terms [106] in the view of quantum optics.

Previously, we looked at the time evolution of the creation and annihilation operators; we shall now try to obtain the evolution of the wavefunction instead. Since the two counter-propagating modes with momentum k and $-k$ are generated simultaneously, we have to consider both of them. By grouping k and $-k$ modes together, we decompose the Hamiltonian into $H = \sum h_k$, where $h_k = i\hbar\nu(a_k^\dagger a_{-k}^\dagger - a_k a_{-k})$. We thus only need to consider the evolution of the wavefunction under each h_k. To simplify the notation without loss of the generality, we use h to replace h_k. Therefore, the evolution of the wave function can be written as [106]

$$|\psi(\tau)\rangle = e^{-ih\tau/\hbar}|0\rangle = \frac{1}{\cosh(\nu\tau)} \sum_{n=0}^{\infty} \tanh^n(\nu\tau)|n,n\rangle. \tag{7.6}$$

Based on this wavefunction, we are able to get the density matrix for the system $\rho_{k,-k} = |\psi(\tau)\rangle_I \langle\psi(\tau)|_I$. Therefore the density matrix of one single mode such as k is determined by tracing out the other mode $-k$, *i.e.*

$$\hat{\rho}_k(\tau) = \mathrm{Tr}_{-k}|\psi(\tau)\rangle_I \langle\psi(\tau)|_I = \sum_{n=0}^{\infty} p_n |n\rangle_k \langle n|_k \tag{7.7}$$

where $p_n = \tanh^{2n}(g\tau)/\cosh^2(g\tau)$.

7.2.1 Effective temperature

By comparing with a thermal distribution of an ideal Bose gas

$$\tilde{p}(T) = e^{-\frac{n\hbar\omega}{2k_{\mathrm{B}}T}}(1 - e^{-\frac{\hbar\omega}{2k_{\mathrm{B}}T}}), \tag{7.8}$$

we can build a direct mapping between the effective temperature with the time τ or the mean population $\bar{n}$ as

$$T = \frac{E_{k_f}}{2k_{\mathrm{B}} \ln \coth(\nu\tau)} \tag{7.9}$$

$$= \frac{E_{k_f}}{k_{\mathrm{B}} \ln(1 + 1/\bar{n})} \xrightarrow[\bar{n}\gg 1]{} \frac{E_{k_f}}{k_{\mathrm{B}}}\bar{n}. \tag{7.10}$$

where the mean population

$$\bar{n} = \sum_{n=0}^{\infty} n p_n = \frac{1}{e^{E_{k_f}/k_{\mathrm{B}}T} - 1} \tag{7.11}$$

follows the Bose-Einstein statistics. The linear dependence of the effective temperature on mean atom number agrees very well with our experimental observation in Fig. 7.3.

7.2.2 Entropy

We first evaluate the entropy per momentum mode based on our experiment data. In experiment, we build probability distribution based on angular slices. We define the entropy in one slice with the width of $\xi\Delta\theta_J$ as $S(\xi)$. First we use the probability distribution $p(n, \xi)$ from Eq. (7.1) to evaluate $S(\xi)$, which gives

$$S(\xi)/k_{\mathrm{B}} = -\int_{-\infty}^{\infty} dn p(n, \xi) \ln p(n, \xi) = -\ln\beta + \xi + \ln\Gamma(\xi) - (\xi - 1)\Gamma'(\xi)/\Gamma(\xi). \tag{7.12}$$

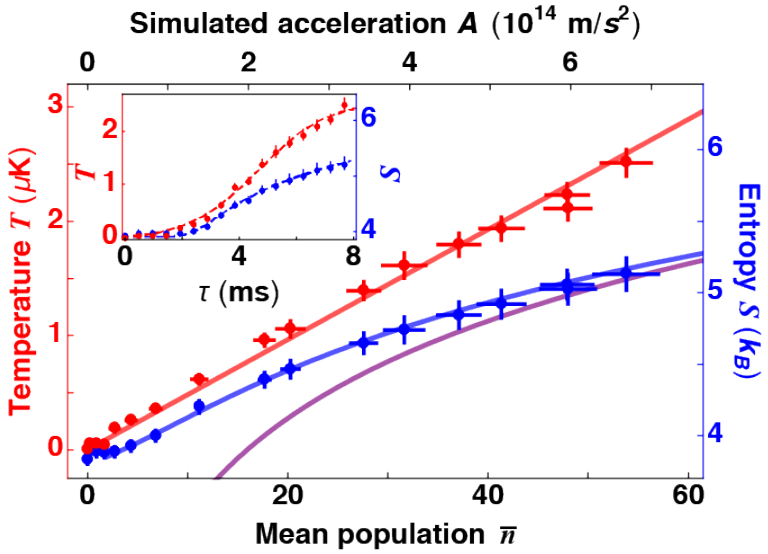

Figure 7.4: **Effective temperature and entropy.** Here we show the effective temperature T (red circles) and entropy per mode S (blue circles) versus the mean population per mode. The derived acceleration A is shown on the top. The red solid line is a fit of $T = \kappa A/c$. The blue solid line is the prediction that includes the detection noise while the purple line is the prediction excluding the noise. The inset shows the evolution of T and S. The dashed lines are guides to the eye.

Thus the entropy for single mode is $S(1) = S(\xi) - S_0(\xi)$, where S_0 only depends on the size of angular slice, $S_0(\xi) = k_{\rm B}\left[\xi - 1 + \ln\Gamma(\xi) - (\xi-1)\Gamma'(\xi)/\Gamma(\xi)\right]$. During data analysis, we have chosen $\xi \approx 1.5$ and $S_0(\xi = 1.5) = 0.37 k_{\rm B}$; as a result, the corresponding entropy is given by experimental distribution $P(n)$,

$$S(1.5) = -k_{\rm B}\sum_n P(n)\ln P(n). \tag{7.13}$$

Thus the entropy for a single mode $S(1)$ can obtained by subtracting the S_0,

$$S(1) = S(1.5) - S_0(1.5) = -k_{\rm B}\sum_n P(n)\ln P(n) - S_0(1.5). \tag{7.14}$$

For short modulation time $\tau < 3$ ms, the measured entropy is dominated by the detection noise $S_{\rm b} = 3.8\ k_{\rm B}$. For long modulation duration τ, the measured S faithfully reflects the entropy of the matter-wave radiation, see Fig. 7.4.

Based on two-mode squeezing, the von Neumann entropy of the thermal distribution is

$$\begin{aligned} S =& -k_{\mathrm{B}}\mathrm{Tr}\left(\hat{\rho}_k \ln \hat{\rho}_k\right) \\ =& k_{\mathrm{B}}[\ln(\bar{n}+1) + \bar{n}\ln(1+1/\bar{n})], \end{aligned} \tag{7.15}$$

which is the solid purple line (theory without detection noise) plotted in Fig. 7.4. The deviation of the data from our theory is due to the detection noise. We calibrate the detection noise per mode $G(n,1)$ accordingly, as shown in Fig. 7.1, and then derive the theoretical distribution by convolving $G(n,1)$ with $p(n,1)$ as

$$\tilde{P}(n,1) = \int_{-\infty}^{\infty} dn' p(n',1) G(n-n',1). \tag{7.16}$$

Thus theoretically the observed entropy is given by

$$S = -k_{\mathrm{B}} \int dn \tilde{P}(n,1) \ln \tilde{P}(n,1), \tag{7.17}$$

which matches our experimental data very well (see the blue solid line in Fig. 7.4).

7.2.3 Connection to thermal dynamics of ideal gas

We start by looking at the mean atom number as a function of temperature T is $\bar{n} = 1/(e^{E_{k_f}/k_{\mathrm{B}}T} - 1)$. We insert it into Eq. (7.15) and get the relation between entropy S and effective temperature T, which is given by

$$S = -k_{\mathrm{B}} \left[\ln\left(e^{E_{k_f}/k_{\mathrm{B}}T} - 1\right) - \frac{E_{k_f}/k_{\mathrm{B}}T}{(1 - e^{-E_{k_f}/k_{\mathrm{B}}T})} \right]. \tag{7.18}$$

When $\bar{n} \gg 1$, the entropy is approximated as $S = k_{\mathrm{B}} \ln(e\bar{n})$, where $e = 2.718\ldots$. Using Eq. (7.10), we obtain the entropy S dependence on T in the large $\bar{n}$ limit as

$$S = k_{\mathrm{B}} \ln\left(\frac{ek_{\mathrm{B}}T}{E_{k_f}}\right), \tag{7.19}$$

in which S increases logarithmically with T. We shall see this dependence is identical to that of a grand cononical ensemble of idea gas.

Consider a system of free atoms in contact with a reservoir at temperature T and chemical potential μ, each atom can only occupy the momentum state with energy $E_{k_f} = \hbar\omega/2$. The probability distribution for the system to contain N particles is,

$$p(N) = e^{-\beta N(E_{k_f}-\mu)}/Z(T,\mu) \tag{7.20}$$

where $\beta = 1/k_{\mathrm{B}}T$ and the normalization factor is the grand partition function,

$$\begin{aligned} Z(T,\mu) &= \sum_{N=0}^{\infty} e^{-\beta N(E_{k_f}-\mu)} \\ &= \frac{1}{1-e^{-\beta(E_{k_f}-\mu)}}. \end{aligned} \tag{7.21}$$

Based on the probability distribution, we can evaluate the mean particle number in the system, which is

$$\begin{aligned} \langle N\rangle &= \sum_{N=0}^{\infty} N e^{-\beta N(E_{k_f}-\mu)}/Z(T,\mu) \\ &= \frac{\partial}{\partial(\beta\mu)} \ln Z(T,\mu) \\ &= \frac{1}{e^{\beta(E_{k_f}-\mu)}-1}. \end{aligned} \tag{7.22}$$

When chemical potential $\mu = 0$, (7.22) gives us exactly the same form of relation between

temperature and mean particle number as that in (7.10), where

$$T = \frac{E_{k_f}}{k_B \ln(1 + \frac{1}{\langle N \rangle})}. \tag{7.23}$$

Beside that the effective temperature of the jet emission has similar form as that of idea gas, we further that entropy behaves similarly. Starting with he grand potential given by the partition function,

$$G(T, \mu) = -k_B T \ln Z(T, \mu) = k_B T \ln(1 - e^{-\beta(E_{k_f} - \mu)}), \tag{7.24}$$

and

$$dG(T, \mu) = d(E(S, N) - TS - \mu N) = -SdT - Nd\mu. \tag{7.25}$$

We can derive the entropy which can be simply given by

$$S = -\left.\frac{\partial G}{\partial T}\right|_{\mu} = -k_B \ln(e^{\beta(E_{k_f} - \mu)} - 1) + \frac{k_B \beta(E_{k_f} - \mu)}{1 - e^{-\beta(E_{k_f} - \mu)}}. \tag{7.26}$$

Again in the case of $\mu = 0$, we obtain exactly the same form for entropy as the entanglement entropy per jet as in (7.18),

$$S/k_B = -\ln(e^{E_{k_f}/k_B T} - 1) + \frac{E_{k_f}/k_B T}{1 - e^{-E_{k_f}/k_B T}}. \tag{7.27}$$

Particularly when $k_B T / E_{k_f} \gg 1$,

$$S/k_B = \ln\left(\frac{e k_B T}{E_{k_f}}\right) \tag{7.28}$$

Thus the thermodynamical behaviors of the emitted matter-wave jets coincides with that of the idea gas of free atoms with chemical potential $\mu = 0$ while occupying single energy state

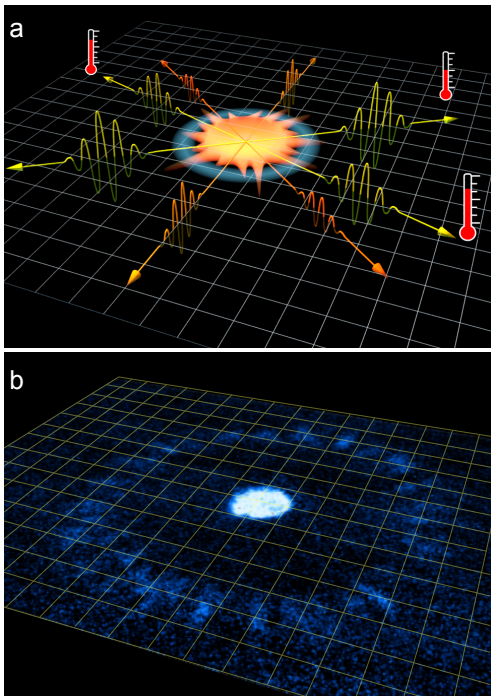

Figure 7.5: **Illustration of quantum simulation of Unruh radiation. a**, To an accelerating observer, a vacuum state in the inertial frame appears identical to a thermal state. **b**, We simulate the Unruh effect by a pair-creation process in a driven condensate, whose evolution is equivalent to a coordinate transformation to an accelerating frame. The matter-wave field shares the same characteristics as the Unruh radiation: it is locally indistinguishable from a Boltzmann distribution, but is long-range coherent and temporally reversible.

E_{k_f} at temperature T.

7.3 Connection to Unruh radiation

Among quantum physics in curved spacetime, Unruh radiation is one of the most studied and intriguing phenomena [103], see Fig. 7.5. Unruh predicts that vacuum state of a quantum field in the Minkowski space can appear as a thermal state in an accelerating frame. The thermal field is characterized by the Unruh temperaature T_{U}, which depends on the acceleration A as

$$T_{\mathrm{U}} = \frac{\hbar A}{2\pi c k_{\mathrm{B}}}. \tag{7.29}$$

where c is the speed of light. Because of the equivalence of inertial and gravitational acceleration, this surprising phenomenon shares the same root as the Hawking radiation [50] near the black hole horizon. Experimentally, it is, however, extremely challenging to observe Unruh effect; an enormous acceleration of $A = 2.5 \times 10^{14}$ m/s^2 is required to create the Unruh radiation of $T_{\rm U} = 1$ μK.

A quantum state can be boosted into accelerating frame thought the Rindler transformation R_A [105, 101],

$$\begin{bmatrix} \hat{b}_k^R \\ \hat{b}_k^{\dagger L} \end{bmatrix} = \begin{bmatrix} \cosh(r_k) & \sinh(r_k) \\ \sinh(r_k) & \cosh(r_k) \end{bmatrix} \begin{bmatrix} \hat{c}_k \\ \hat{d}_k^{\dagger} \end{bmatrix}, \tag{7.30}$$

where $\hat{b}_k^R$ and $\hat{b}_k^L$ are the annihilation operators of "Rindler modes" with energy E_k in the accelerating frame, L and R correspond to two Rindler wedges propagating along two different directions, $(\hat{c}_k, \hat{d}_k)$ are the annihilation operators of Unruh modes whose vacuum is the Minkovski vacuum in the inertial frame. The parameter r_k satisfies the equation of $\tanh r_k = e^{-\pi E_k c/A}$.

Meanwhile, when we look at the time evolution of the bosonic creation and annihilation operators in our system, which is given by

$$\begin{bmatrix} a_k(\tau) \\ a_{-k}^{\dagger}(\tau) \end{bmatrix} = \begin{bmatrix} \cosh(\nu\tau) & \sinh(\nu\tau) \\ \sinh(\nu\tau) & \cosh(\nu\tau) \end{bmatrix} \begin{bmatrix} a_k(0) \\ a_{-k}^{\dagger}(0) \end{bmatrix}. \tag{7.31}$$

By comparing Eq. (7.31) with Eq. (7.30), we find the mathematical form of the frame transformation and the time evolution are very similar to each other. We thus can draw an equivalence by treating the operators at time τ as the Rindler operators in a non-inertial frame, namely $\hat{b}_k^R \to a_k(\tau)$, $\hat{b}_k^L \to a_{-k}(\tau)$,$\hat{c}_k \to a_k(0)$, and $\hat{d}_k \to a_{-k}(0)$, which leads to

$\tanh(\nu\tau) = r_{\omega/2}$. Thus, we obtain the corresponding acceleration A,

$$A = \frac{\pi\omega c}{2\ln\coth(g\tau)}. \tag{7.32}$$

. Thus, we can use the time evolution of a two-mode squeezing Hamiltonian to achieve a quantum simulation of Unruh radiation that is expected to be observed in a non-inertial frame with large constant acceleration.

This simulated acceleration also linearly depend on the mean population in a single mode. The mean population per mode increases as $\bar{n} = \langle a_k^\dagger(\tau)a_k(\tau)\rangle = \sinh^2(g\tau)$. A thus can be rewritten using $\bar{n}$ as

$$A = \frac{2\pi c E_{k_f}}{\hbar\ln(1+1/\bar{n})} \xrightarrow[\bar{n}\gg 1]{} \frac{2\pi c E_{k_f}}{\hbar}\bar{n}, \tag{7.33}$$

where $E_{k_f} = \hbar\omega/2$ is the kinetic energy of each atom.

Intrigued by this simple connection,we can further propose a new type of quantum simulation to investigate quantum physics in an non-inertial frame, which, according to the equivalence principle, is equivalent systems in a curved space-time. We can simulate the transformation $\hat{R}$ from an inertial to a non-inertial frame by a controlled time evolution of the system with a prescribed Hamiltonian $\hat{\mathcal{H}}$. For a given quantum state Ψ_0, this method is equivalent to evolve the system according to

$$\hat{U}(\tau)\Psi_0 = \hat{R}\Psi_0, \tag{7.34}$$

where $\hat{U}(\tau) = \exp(-i\mathcal{H}\tau/\hbar)$ is the evolution operator in quantum mechanics, and the time τ serves as a parameter to match the desired frame transformation $\hat{R}$.

7.4 Coherence in jet emission

While local measurements in our system seem to reveal a thermal distribution, however, unlike incoherent black-body radiation, Unruh radiation should exhibit both spatial and

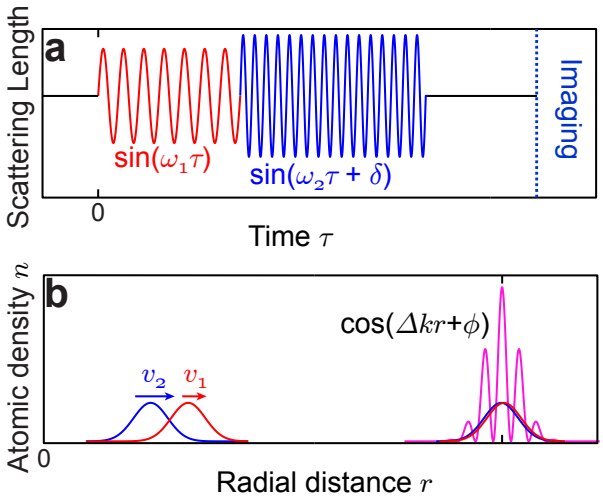

Figure 7.6: **Double-pulse sequence for jet interference. a** illustrates the application of two pulses of scattering length modulation with frequencies $\omega_1/2\pi = 3$ and $\omega_2/2\pi = 5.63$ kHz, and modulation amplitudes $a_{ac} = 56$ and $72a_0$. The relative phase of the pulses is δ. **b**. The matter-wave jet created by the latter pulse propagates at a greater speed $v_2 > v_1$ and interferes with atoms from the first pulse when they overlap. Here the matter-wave speeds are $v_i = \sqrt{\hbar\omega_i/m}$ for the $i-$th pulse. The interference is characterized by the wavenumber difference $\Delta k = k_2 - k_1$, and the phase ϕ.

temporal coherence, reflecting its quantum origin. In the following we investigate the coherence properties of the matter-wave radiation.

7.4.1 Spatial phase coherence from interference experiment

We first show the spatial coherence of the matter-wave field by probing the phase correlation between jets. For this, we perform a matter-wave interference experiment by applying two independent pulses of modulation on the scattering length. The first pulse has a lower frequency of $\omega_1 = 2\pi\times3$ kHz compared to the second one of $\omega_2 = 2\pi\times5.63$ kHz (see Fig. 7.6**a**). The amplitudes for the two pulses of modulation are $a_{ac}^{(1)} = 56a_0$ and $a_{ac}^{(2)} = 72a_0$. The two frequencies are incommensurate to avoid influence from high-harmonic generations [37]. The pulses are arranged such that the atoms created by the second pulse leave the condensate later, but with a greater velocity than the atoms from the first pulse. When the two emitted waves overlap, they interfere and produce fringes (see Fig. 7.6**b** for illustration). We can

directly image such interference fringes in real space atomic density with *in situ* imaging and the examples of experimental data are show in Fig. 7.7.

We extract the phases of the interference fringes along different angular direction based on its Fourier transformation, see Fig. 7.8. The phase of the fringes ϕ is given by the relative phase of the interfering matterwaves, and is random among different the emission angles θ. However, it is very interesting to see that the phase of the fringes along counter-propagating directions are correlated. In Fig. 7.8**c**, we present the occurrence distribution of the fringe phases in opposite directions, namely, ϕ_θ and $\phi_{\theta+\pi}$. The two phases correlate as $\phi_\theta + \phi_{\theta+\pi} = \phi_s$ (see Fig. 7.8**d**) with $\phi_s = 0.79(3)$ depending on the phase of the pulses and dynamical phase during propagation in our experiment.

To be more quantitative, we evaluate the phase correlation function $g_\pm(\varphi)$ for all angular span φ [70], defined as (see Fig. 7.8**e**)

$$g_\pm(\varphi) = |\langle e^{i\phi_\theta \pm i\phi_{\theta+\varphi}}\rangle|. \tag{7.35}$$

Here the angle brackets correspond to angular averaging over θ and ensemble averaging. The peak of g_+ at $\varphi = \pi$ confirms that fringe phases are only anti-correlated in the opposite directions. The lone peak of g_- at $\varphi = 0$ shows the phase coherence within a single jet. Since jets with different energy are generated independently, the correlations of the fringes indicate the phase correlations of counter-propagating jets with the same momentum. Such phase correlation results from the coherent generation of atom pairs which are phase locked to the modulation; the correlation is also expected for the Unruh radiation [105], and resembles the phase coherence in the parametric down-conversion process in quantum optics [55].

Theoretically, we can calculate the phase correlations between interference fringes, which directly relate to that between emitted jets. We consider two sets of independent jets which are generated by two pulses of scattering length modulation with certain phase. In the interaction picture, the wave function can be written as $|\psi\rangle_I = |\psi^{(1)}\rangle_I \otimes |\psi^{(2)}\rangle_I$. Each

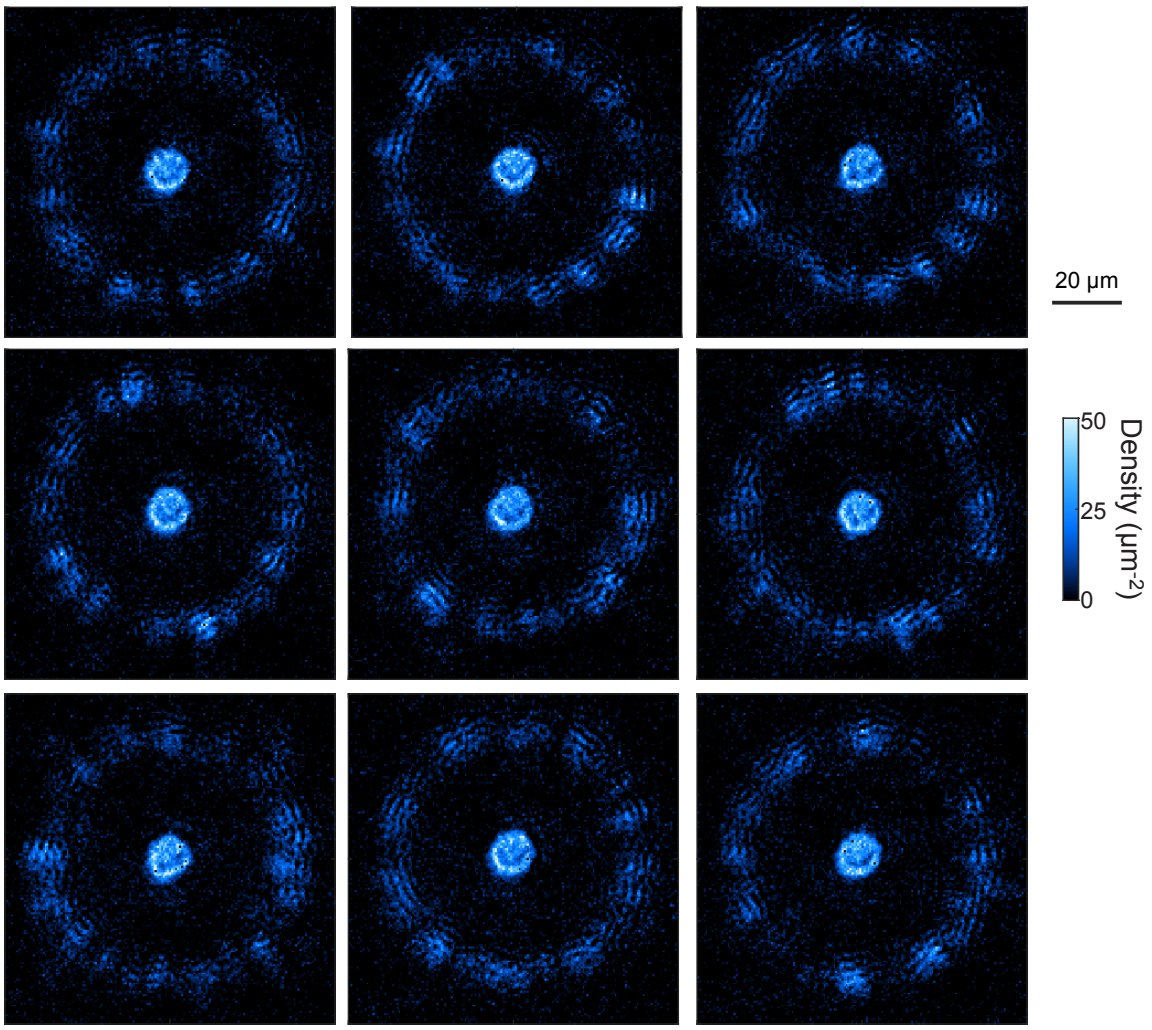

Figure 7.7: **Gallery of jet interference.** Here we show several example images of the interference between jets generated by the two pulses of scattering length modulation with frequencies $\omega_1/2\pi = 3$ and $\omega_2/2\pi = 5.63$ kHz, and modulation amplitudes $a_{ac} = 56$ and $72a_0$.

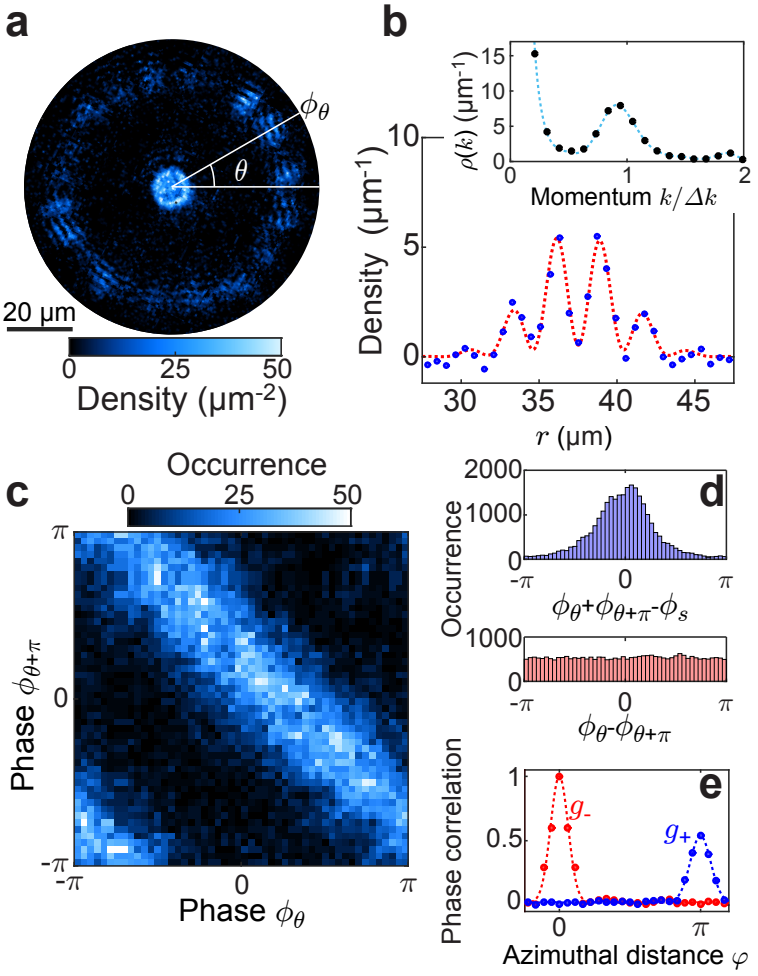

Figure 7.8: **Phase correlation of matter-wave radiation.** **a** shows an example interference pattern of the two radiation fields. The phase of the interference fringes ϕ_θ is recorded as a function of the emission angle θ. **b** shows the radial cut of the interference pattern, from which we determine the phase of the fringes based on Fourier transformation (See Methods). Dotted lines show guides to the eye. **c** and **d** show the concurrence of the extracted phases in the opposite directions, ϕ_θ and $\phi_{\theta+\pi}$ for all emission angle θ from a collection of 200 images. A strong correlation of the two phases is described by $\phi_\theta + \phi_{\theta+\pi} = \phi_s$, where $\phi_s = 0.79(3)$ is obtained from fitting the data; $\phi_\theta - \phi_{\theta+\pi}$ appears to be random. **e** shows phase correlations g_+ (blue) and g_- (red) between fringes separated by an angular distance φ. Dots represent experimental data while dashed curves are guides to the eye.

$|\psi^{(j)}\rangle_I$ follows

$$|\psi^{(j)}\rangle_I = \frac{1}{\cosh(\gamma_j)} \sum_{n=0}^{\infty} \left[e^{i(\phi_{M_j} - \pi/2)} \tanh(\gamma_j) \right]^n |n,n\rangle_{k_j,-k_j} \tag{7.36}$$

under the Hamiltonian

$$H_I^{(i)} = \nu_j e^{i\phi_{M_j}} a_{k_j}^\dagger a_{-k_j}^\dagger + \nu_j e^{-i\phi_{M_j}} a_{k_j} a_{-k_j} \tag{7.37}$$

where ϕ_{M_j} is given by the phase of external driving field, $\gamma_j = \nu_j \tau_j$ and τ_i is the modulation duration of the pulse.

To take the dynamical phase into account, we convert the wave function back to Schrödinger's picture, and the wave function is written as

$$|\psi\rangle_S = |\psi^{(1)}\rangle_S \otimes |\psi^{(2)}\rangle_S, \tag{7.38}$$

where $|\psi^{(j)}\rangle_S$ is given by

$$\begin{aligned} |\psi^{(j)}\rangle_S &= e^{-iH_0^{(j)} t/\hbar} |\psi^{(j)}\rangle_I \\ &= \frac{1}{\cosh(\gamma_j)} \sum_{n=0}^{\infty} \left[e^{i(\phi_{M_j} - \omega_j t - \pi/2)} \tanh(\gamma_j) \right]^n |n,n\rangle_{k_j,-k_j}. \end{aligned} \tag{7.39}$$

Here $H_0^{(i)} = \hbar\omega_i (a_{\mathbf{k}_j}^\dagger a_{\mathbf{k}_j} + a_{-\mathbf{k}_j}^\dagger a_{-\mathbf{k}_j})/2$ is energy term which was previously eliminated in the interaction picture.

The interference operators between the two sets of jets are $\hat{I}_f = a_{\mathbf{k}_1} a_{\mathbf{k}_2}^\dagger$ and $\hat{I}_b = a_{-\mathbf{k}_1} a_{-\mathbf{k}_2}^\dagger$ which correspond to the forward and backward directions. We introduce four more interference operators as $\hat{I}_{j+} = a_{\mathbf{k}_j} a_{-\mathbf{k}_j}$ and $\hat{I}_{j-} = a_{\mathbf{k}_j} a_{-\mathbf{k}_j}^\dagger$ with $j = 1$ or 2. The

mean value for the interference operator $\hat{I}_{i\pm}$ is evaluated as

$$\begin{aligned}
\langle \hat{I}_{j+} \rangle &= \langle \psi^{(j)}|_S \left(a_{\mathbf{k}_j} a_{-\mathbf{k}_j} \right) |\psi^{(j)}\rangle_S \\
&= \sqrt{\langle n_j \rangle (\langle n_j \rangle + 1)} e^{i(\phi_{M_j} - \omega_j t - \pi/2)} \qquad (7.40) \\
\langle \hat{I}_{j-} \rangle &= \langle \psi^{(j)}|_S \left(a_{\mathbf{k}_j} a^{\dagger}_{-\mathbf{k}_j} \right) |\psi^{(j)}\rangle_S \\
&= 0, \qquad (7.41)
\end{aligned}$$

where $\langle n_j \rangle$ is the mean atom number in each set of jets.

Phase correlation between interference fringes can be directly decomposed into the interference operators in each set of jets. The phase correlation $g_+(\theta = \pi)$ is proportional to the correlation between $\hat{I}_f$ and $\hat{I}_b$, together with Eq. (7.40) we get

$$\begin{aligned}
\langle e^{i(\phi_\theta + \phi_{\theta+\pi})} \rangle \propto \langle \hat{I}_f \hat{I}_b \rangle &= \langle \psi^{(1)}|_S \otimes \langle \psi^{(2)}|_S \left(a_{\mathbf{k}_1} a^{\dagger}_{\mathbf{k}_2} a_{-\mathbf{k}_1} a^{\dagger}_{-\mathbf{k}_2} \right) |\psi^{(1)}\rangle_S \otimes |\psi^{(2)}\rangle_S \\
&= \langle \psi^{(1)}|_S \left(a_{\mathbf{k}_1} a_{-\mathbf{k}_1} \right) |\psi^{(1)}\rangle_S \langle \psi|^{(2)}_S \left(a^{\dagger}_{\mathbf{k}_2} a^{\dagger}_{-\mathbf{k}_2} \right) |\psi\rangle^{(2)}_S \\
&= \langle \hat{I}_{1+} \rangle \langle \hat{I}^{\dagger}_{2+} \rangle \\
&= \sqrt{\langle n_1 \rangle (\langle n_1 \rangle + 1)} \sqrt{\langle n_2 \rangle (\langle n_2 \rangle + 1)} e^{i\left[(\phi_{M_1} - \phi_{M_2}) - (\omega_1 - \omega_2) t \right]} \qquad (7.42)
\end{aligned}$$

Therefore, the sum of the phases of the forward and backward interference fringes only depends on the phase of the driving and the dynamical phase. Thus we have the phase constant $\phi_s = \phi_\theta + \phi_{\theta+\pi} = (\phi_{M_1} - \phi_{M_2}) - (\omega_1 - \omega_2)t$ and $g_+(\pi) = 1$.

Meanwhile, phase correlation $g_-(\theta = \pi)$ is proportional to the mean value of $\hat{I}_f \hat{I}^{\dagger}_b$, together with Eq. (7.41) we have

$$\begin{aligned}
\langle e^{i\phi_\theta - \phi_{\theta+\pi}} \rangle \propto \langle \hat{I}_f \hat{I}^{\dagger}_b \rangle &= \langle \psi^{(1)}|_S \otimes \langle \psi^{(2)}|_S \left(a_{\mathbf{k}_1} a^{\dagger}_{\mathbf{k}_2} a^{\dagger}_{-\mathbf{k}_1} a_{-\mathbf{k}_2} \right) |\psi^{(1)}\rangle_S \otimes |\psi^{(2)}\rangle_S \\
&= \langle \psi^{(1)}|_S \left(a_{\mathbf{k}_1} a^{\dagger}_{-\mathbf{k}_1} \right) |\psi^{(1)}\rangle_S \langle \psi^{(2)}|_S \left(a^{\dagger}_{\mathbf{k}_2} a_{-\mathbf{k}_2} \right) |\psi^{(2)}\rangle_S \\
&= \langle \hat{I}_{1-} \rangle \langle \hat{I}^{\dagger}_{2-} \rangle \\
&= 0 \qquad (7.43)
\end{aligned}$$

therefore we have $g_{-}(\pi) = 0$, indicating that phases in each pair of jets are totally random although their sum is fixed. The results from Eqs. (7.42, 7.43) are consistent with our measurement shown in Fig. 3**g**.

We also derive a more general analytic formula for $g_{+}(\theta)$ and $g_{-}(\theta)$ between two arbitrary angular directions in addition to that between the counter-propagating directions in Eqs. (7.42, 7.43) as follows,

$$g_{+}(\theta) = \left| \frac{\langle a_{\mathbf{k}_1} a^{\dagger}_{\mathbf{k}_2} a_{\mathbf{k}'_1} a^{\dagger}_{\mathbf{k}'_2} \rangle}{\langle a^{\dagger}_{\mathbf{k}_1} a_{\mathbf{k}_1} \rangle \left\langle a^{\dagger}_{\mathbf{k}_2} a_{\mathbf{k}_2} \right\rangle} \right| = \left| \frac{\langle a_{\mathbf{k}_1} a_{\mathbf{k}'_1} \rangle \langle a^{\dagger}_{\mathbf{k}_2} a^{\dagger}_{\mathbf{k}'_2} \rangle}{\langle a^{\dagger}_{\mathbf{k}_1} a_{\mathbf{k}_1} \rangle \left\langle a^{\dagger}_{\mathbf{k}_2} a_{\mathbf{k}_2} \right\rangle} \right|, \tag{7.44}$$

$$g_{-}(\theta) = \left| \frac{\langle a_{\mathbf{k}_1} a^{\dagger}_{\mathbf{k}_2} a^{\dagger}_{\mathbf{k}'_1} a_{\mathbf{k}'_2} \rangle}{\langle a^{\dagger}_{\mathbf{k}_1} a_{\mathbf{k}_1} \rangle \left\langle a^{\dagger}_{\mathbf{k}_2} a_{\mathbf{k}_2} \right\rangle} \right| = \left| \frac{\langle a_{\mathbf{k}_1} a^{\dagger}_{\mathbf{k}'_1} \rangle \langle a^{\dagger}_{\mathbf{k}_2} a_{\mathbf{k}'_2} \rangle}{\langle a^{\dagger}_{\mathbf{k}_1} a_{\mathbf{k}_1} \rangle \left\langle a^{\dagger}_{\mathbf{k}_2} a_{\mathbf{k}_2} \right\rangle} \right|. \tag{7.45}$$

Here the symbol $\mathbf{k}_1$ and $\mathbf{k}_2$ indicate two jets of different kinetic energy but propagating along the same direction, while $\mathbf{k}'_1$ and $\mathbf{k}'_2$ represent another pair of such co-propagating jets along a direction with a relative angle of θ to that of $\mathbf{k}_1$ and $\mathbf{k}_2$. Following the same spirit as that in Ref. [25] and by taking the finite size of the condensate into consideration, we obtain

$$\left\langle a_{\mathbf{k}_j} a_{\mathbf{k}'_j} \right\rangle = e^{i(\phi_{M_j} - \omega_j t - \pi/2)} \frac{\tilde{\rho}(\mathbf{k}_j + \mathbf{k}'_j)}{2\pi} \cosh(\gamma_j) \sinh(\gamma_j), \tag{7.46}$$

$$\left\langle a^{\dagger}_{\mathbf{k}_j} a_{\mathbf{k}'_j} \right\rangle = \frac{\tilde{\rho}(\mathbf{k}_j - \mathbf{k}'_j)}{2\pi} \sinh^2(\gamma_j), \tag{7.47}$$

where $\tilde{\rho}(\mathbf{k})$ is defined as the Fourier transformation of a uniform disk-shape density $\rho(\mathbf{r})$,

$$\rho(\mathbf{r}) = \frac{1}{2\pi} \int d^2\mathbf{k} e^{i\mathbf{k}\cdot\mathbf{r}} \tilde{\rho}(\mathbf{k}). \tag{7.48}$$

And $\rho(\mathbf{r})$ is the density distribution function of the condensate as

$$\rho(\mathbf{r}) = \begin{cases} 1 & |\mathbf{r}| \leq R \\ 0 & |\mathbf{r}| > R \end{cases} \tag{7.49}$$

with R is the radius. Therefore, the analytic formulas for $g_{\pm}(\theta)$ when $\gamma_j \gg 1$ and $|\mathbf{k}_i|R \gg 1$ are

$$\begin{aligned} g_{+}(\theta) &= \left|\frac{4\tilde{\rho}(\mathbf{k}_1+\mathbf{k}_1')\tilde{\rho}^{*}(\mathbf{k}_2+\mathbf{k}_2')}{\tilde{R}^4}\right| \\ &= \left|\frac{4J_1(|\mathbf{k}_1|R(\theta-\pi))J_1(|\mathbf{k}_2|R(\theta-\pi))}{|\mathbf{k}_1||\mathbf{k}_2|R^2(\theta-\pi)^2}\right|, \end{aligned} \tag{7.50}$$

and

$$\begin{aligned} g_{-}(\theta) &= \left|\frac{4\tilde{\rho}(\mathbf{k}_1-\mathbf{k}_1')\tilde{\rho}^{*}(\mathbf{k}_2-\mathbf{k}_2')}{\tilde{R}^4}\right| \\ &= \left|\frac{4J_1(|\mathbf{k}_1|R\theta)J_1(|\mathbf{k}_2|R\theta)}{|\mathbf{k}_1||\mathbf{k}_2|R^2\theta^2}\right|, \end{aligned} \tag{7.51}$$

where $J_1(x)$ is the first order Bessel function of the first kind.

It worth mentioning in more detail that to experimentally extract the interference fringe phase ϕ_θ at a particular emission direction θ, we average over an angular span from $\theta - 0.12$ to $\theta + 0.12$ to obtain the radial density distribution $\rho(r,\theta)$ in order to achieve the best signal to noise ratio (see Fig. 7.8**b**). We then perform Fourier transformation on the radial density to get the complex density amplitude of the interference fringes in momentum space $\rho(k,\theta)$. The phase ϕ_θ at k_f is then evaluated from this complex amplitude. Although our jet width is small, that is 2° for $\omega/2\pi = 3$ kHz and 1.5° for $\omega/2\pi = 5.63$ kHz, this average results in a significantly broadened phase correlation shown in Fig. 7.8**e**. To experimentally extract the phase constant ϕ_s, we fit the histogram of $\phi_\theta + \phi_{\theta+\pi}$ to get the peak position. We also calculate the expected phase shift based on our experimental sequence with a time of 18.5 ms from the start of the modulation to the start of imaging. The first sinusoidal modulation pulse lasts for 6 periods while the second lasts for 17 periods. Meanwhile we take into account the time delay of the modulation pulse of 0.041 ms due to system response. Therefore the phase constant estimated from our experimental sequence is 0.9(2) where the uncertainty arises from the duration of our 20 μs imaging pulse.

7.4.2 Temporal coherence from inversion of time-evolution

Next we show the temporal coherence of the matter-waves radiation by reversing the time evolution. Similar experiments to reverse parametric amplification are realized based on photonic and atomic fields with two well-defined outgoing modes and low atom numbers [112, 74, 73], whereas the condensate in our system simultaneously couples to about 300 momentum modes, and involves about 10^5 atoms.

We perform the experiment as follows: after modulating the scattering length, we jump the phase of the modulation by α (see Fig 7.9**a**). Here a single frequency modulation of $\omega/2\pi = 2.1$ kHz with amplitude $a_{ac} = 50a_0$ is applied. We monitor the evolution of the radiation patterns, from which we determine the total emitted atom number N (Fig. 7.9**b**). Without phase jump, the atoms excited into jets increase exponentially as a function of modulation time. As soon as we change the driving phase, a clear suppression of atom number is shown for large phase jump. Figure 7.9**c** shows a comparison between two cases with phase shift $\alpha = 0$ and $\alpha = \pi$ with example average images of the emission pattern. To be more quantitative, we evaluate the suppression ratio $\eta(\alpha) = N_\alpha(\tau_c)/N_0(\tau_c)$ at time $\tau_c = 5.76$ ms when the maximal reversal occurs (see Fig. 7.9**b**). In particular when α equals to π, the total excited atom number N reduces by as much as 51(3)% of that without the phase jump ($\alpha = 0$). At $\alpha = \pi$, a reversal of 26(3)% (or 2,200 atoms) of the matter-wave excitations back to the original condensate is observed.

We further evaluate the entropy S and effective temperature T from the distribution of emitted atom number, which remains thermal before and after the phase jump, see Fig. 7.10. Here we compare them for the two cases with phase jump $\alpha = 0$ and π. In the case of $\alpha = 0$, S and T continuously increase while in the latter case, both of them decrease first but eventually increase again. The reversal of these quantities suggests that the radiation originates from a unitary evolution. The limited amount of reversal we can achieve is due to off-resonant coupling to the finite momentum modes close to $|\vec{k}| = k_f$, which can be seen from our numerical calculation based GP equation in Sec. 7.5.

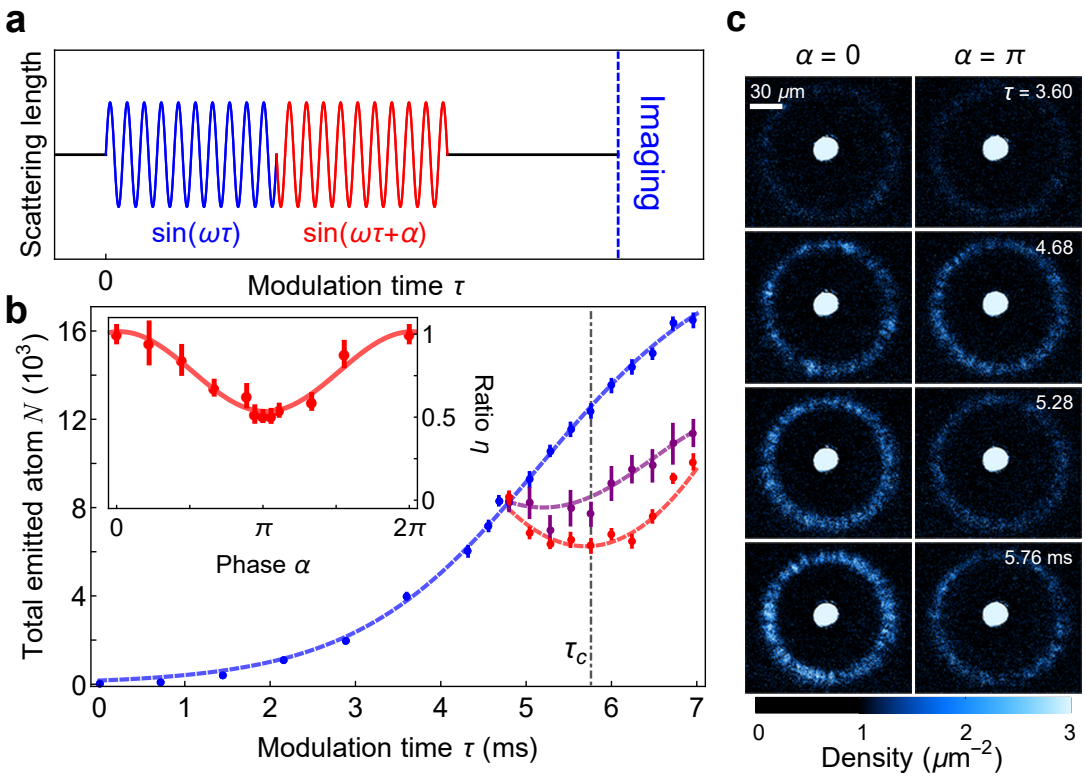

Figure 7.9: **Time reversal of the matter-wave radiation field.** **a** shows that the scattering length is modulated at frequency $\omega/2\pi = 2.1$ kHz with amplitude $a_{ac} = 50\ a_0$ for 4.75 ms before a phase jump α is introduced to the modulation. **b** shows the total emitted atom number N versus total modulation time τ. The blue, purple and red data correspond to the phase jumps of $\alpha = 0$, $2\pi/3$ and π, respectively. The dashed lines are guides to the eye. The inset shows the suppression ratio η versus α evaluated at $\tau = \tau_c$. A sinusoidal fit gives the maximum reversal at $\alpha = 0.98(3)\pi$, where η reaches 51(3)%. **c** shows the average of 15 images of the matter-wave radiation at different times with phase jump $\alpha = 0$ or π. Here the condensates are confined in a disk-shaped trap with radius 13 μm. All error bars correspond to one standard deviation of the mean value.

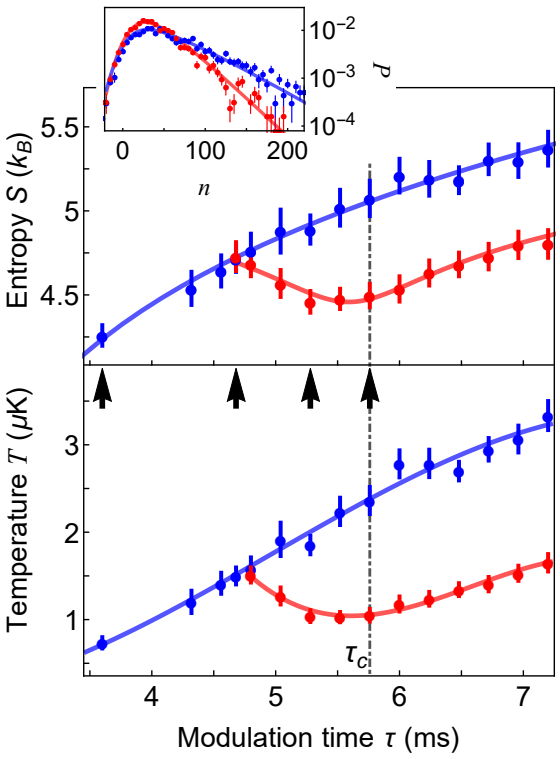

Figure 7.10: **Effective temperature and entropy of the matter-wave radiation field.** Here we shows the entropy S and temperature T without ($\alpha = 0$, blue circles) and with the phase jump ($\alpha = \pi$, red circles). The lines here are guides to the eye. The inset compares the population distributions $P(n)$ at τ_c with $\alpha = 0$ (blue) and π (red). The arrows in panel indicate the corresponding time when the average images of matter-wave emission are shown in Fig. 7.9**c**.

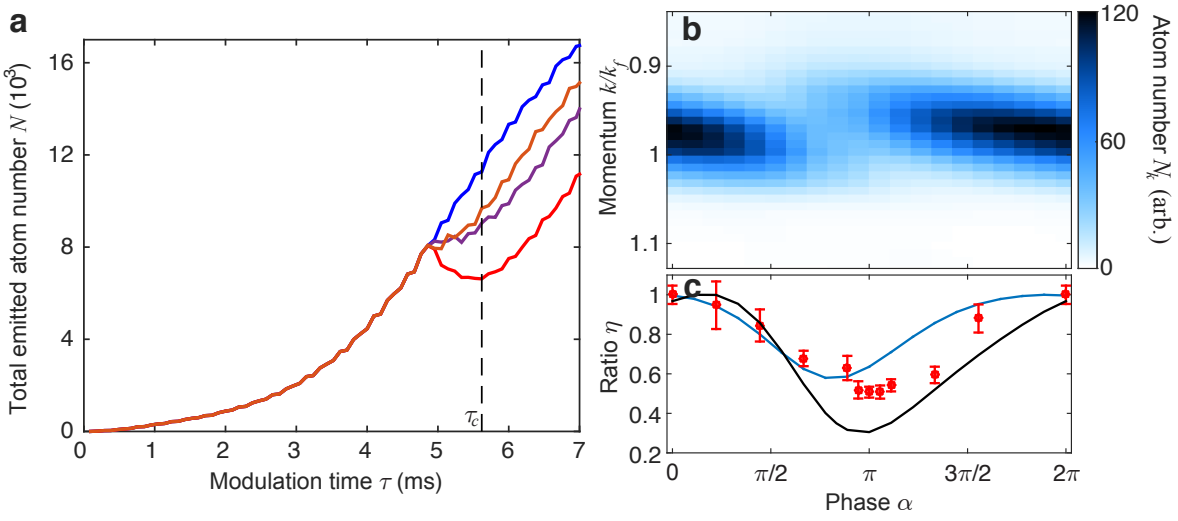

Figure 7.11: **Numerical simulation on reversal of matter-wave radiation.** **a** shows the time evolution of the total emitted atom number N for different phase jump $\alpha = 0$ (blue), 0.44π (purple), 0.89π (red), and 1.33π (orange). Here the phase jump happens at $\tau = 4.76$ ms while optimal suppression is achieved at $\tau_c = 5.62$ ms. **b** shows the emitted atom number at different momentum modes $N_k(\alpha)$ as a function of phase jump α at τ_c. **c** compares the overall suppression ratio η from simulation (blue curve), suppression ratio for a particular momentum mode k_f (black curve), and experiment (dots).

7.5 Numerical simulation of time reversal experiment

In this section, we use numerical simulation based a dynamical Gross-Pitaevskii equation to investigate the partial reversal of radiating matter-wave fields. We find that this imperfect reversal results mostly from the off-resonant coupling to finite momentum modes close to $|\mathbf{k}| = k_f$.

Here we start with the same Gross-Pitaevskii equation, see Eq. (6.1),

$$i\hbar\frac{\partial\psi}{\partial t} = \left[-\frac{\hbar^2}{2m}\nabla^2 + V(\mathbf{r}) + U_{dc}|\psi|^2 - \mu\right]\psi + U_{ac}f(t)|\psi|^2\psi, \tag{7.52}$$

where ψ is the wavefunction and $\mu = 2\pi\hbar \times 19$ Hz is the static chemical potential of the condensate, $V(r)$ is the disk-shaped trapping potential as a function of radius r with $V(r) = 2\pi\hbar \times 300$ Hz for 13.6 μm$\geq r \geq$ 13 μm and $V(r) = 0$ for the rest, $U_{dc} = 4\pi\hbar^2 a_{dc}/m$

and $U_{ac} = 4\pi\hbar^2 a_{ac}/m$ are the DC and AC interaction strengths with $a_{dc} = 3a_0$ and $a_{ac} = 50a_0$. In addition, we have $f(t) = \sin(\omega t)$ when $t \leq 4.76$ ms and $f(t) = \sin(\omega t + \alpha)$ for $t > 4.76$ ms. These parameters are chosen according to our experimental conditions.

The results from simulation using a CUDA-based solver [23] shows great agreement with the experiment. First of all, the total emitted atom number is suppressed after the phase jump α close to π (see Fig.7.11**a**). The suppression sensitively depends on the phase of the second pulse α. Similarly to the analysis of our experimental data, we then look at the suppression ratio as a function of phase α at $\tau_c = 5.62$ ms when the optimal suppression appears (see Fig.7.11**c**). The suppression ratio varies as a function of α in the same way as in our experiment and the best suppression can be achieved is $\eta = 0.57$ comparable to the experimental result.

The reason for this partial suppression is the off-resonant coupling to finite momentum modes close to $|\mathbf{k}| = k_f$. We examine more carefully the emitted atoms in different momentum modes (see Fig. 7.11**b**), not all atoms are excited with a particular well-defined momentum. Instead, atoms spread across a range of momentum modes due to uncertainty principle since the atoms are confined within a finite radius of 13 μm. These momentum modes are then off-resonantly coupled to the external modulation without perfect phase matching. Therefore population in these off-resonantly excited modes are maximally reversed at different phase jumps. For one particular momentum mode, the population can be reduced by as much as 70%, while the overall population is only suppressed to about 50%, consistent with our measurement.

Beside this off-resonant coupling, we anticipate the reversal can be limited by other effects such as the fast counter-rotating terms and the motion of the emitted atoms as well. The counter-rotating terms lead to quick population oscillations seen in Fig. 7.11**a**; they also accumulate phase and eventually limit the reversal. Furthermore, when atoms move out of the condensate, they can not be transferred back to the condensate anymore. These effects are included in the simulation but their contributions to the limited reversal are hard to

separate in our numerical model.

7.6 Conclusion

In conclusion, we have investigated more deeply into the properties of the emitted jets and showed that the mode population exhibits a thermal-like distribution. This thermal-like distribution is generated from a two-mode squeezing process connecting to the famous Unruh radiation in a constant accelerating frame. Thus we consider this experiment as a demonstration of a new type of quantum simulation to investigate quantum phenomena in a non-inertial frame. Albeit thermal from local measurements [63], such matter-wave radiation possesses long-range spatial and temporal coherence, which distinguish it from classical thermal radiation. Quantum simulation of frame transformation can pave an alternate way to study the intriguing topics at the interface of quantum and relativistic physics [41, 95, 54, 11, 99, 89, 35] such as the quantization of field in a curved spacetime.

CHAPTER 8

OUTLOOK TO FUTURE RESEARCH

Beside the results presented in the previous chapters, we have come across various interesting observations that have not been studied in comparable depth. This chapter is dedicated to these interesting results that we have explored in both experiment and numerical simulations that have not yet been well studied. I hope this serve as a lead to future investigation of the interesting noneqiulibrium physics in driven condensates.

8.1 Lattice shaking

8.1.1 Domain structure engineering

Periodic shaking of an optical lattice is a very effective way of Floquet engineering the single particle dispersion. We have demonstrated the quantum simulation of a paramagnetic to ferromagnetic phase transition by dramatically modify the ground band structure with strong driving. We also learned that quantum noise plays a important role in the formation of domains during the coherent inflation process in chapter 4. We hence tried to use phase imprinting to seed fluctuations at particular length scale to measure the inflation rate of a particular inflaton mode.

We realized that this phase imprinting can be implemented a engineering technique to form specific domain structures in a deterministic manner. Here we perform a seeded quench experiment similar to that in section 4.4. The condensates are quenched from shaking amplitude $s_c = 13.1$ nm to $s = 25$ nm. Right before the quench of the shaking amplitude, we perform a fast phase imprinting by quickly pulsing the DMD laser with a typical duration of 20 μs. We can perform such phase imprinting with different seeding momentum, see Fig. 4.4. After the quench of shaking amplitude, we reconstruct the spin density image after the domain fully forms. Figure 8.1 shows two examples of the engineered domain structure with seeded momentum $q' = 0.084\ q_L$ (**a**) and $0.13\ q_L$ (**b**). The resulting domain size is

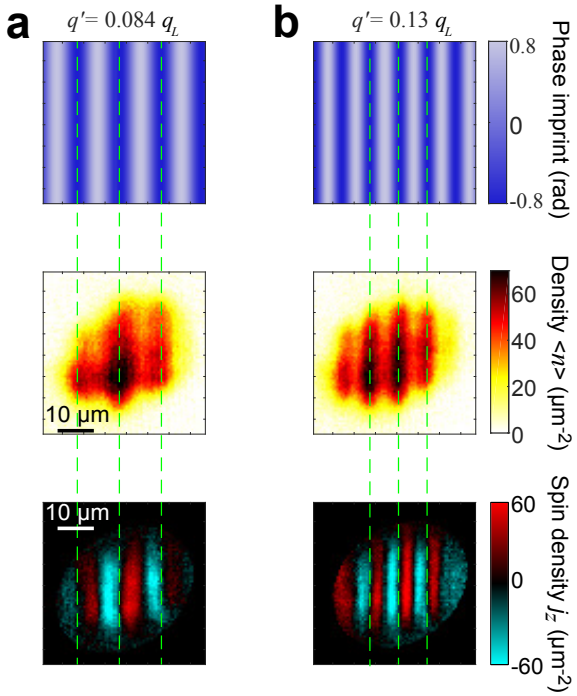

Figure 8.1: **Density wave and domain structure with phase imprinting**. The condensates are quenched from shaking amplitude $s_c = 13.1$ nm to $s = 25$ nm after phase imprinting with the seeding momentum $q' = 0.084\ q_L$ (**a**) and $0.13\ q_L$ (**b**). The phase pattern is illustrated in the top row. The middle row shows the density wave at time $t = 12$ ms (**a**) and 8 ms (**b**). The bottom row shows the corresponding domain structure at time $t = 16$ ms (**a**) and 14 ms (**b**), which remains stationary.

simply given by the seeded momentum $d = 2\pi\hbar/q'$ since the imprinted phase is a sinusoidal in real space, $\delta\phi \sin(q'x/\hbar)$.

This bring opportunities to further study the dynamics of domain walls. Normally, system forms intricate structures of domains when driven across the phase transition non-adiabatically. These domains are far from thermal equilibrium but topologically stable for long time compared to the critical/inflation dynamics. Due to the varying intricacy from shot to shot, it hard to learn about how these domains approach further equilibrium after they form. In many systems the domains tend to gradually grow over time and this process is called coarsening [16, 107]. The theory of universality expects that the coarsening process to satisfy the dynamic scaling hypothesis. According to this hypothesis, the domain structures at later times should look identical to those at early times except for an increase in the domain size. With the capability of staring from a deterministic regular domain structure, it is possible to study such coarsening process. We can initialize the system in the ferromagnetic phase with the finest phase imprinting to have smallest possible domains, thus the domains dynamics will not be affected by the edges before the size becomes comparable to the size of the gas. It is also interesting to test how long it takes to scramble the initial distribution during the coarsening process starting from different domain configurations.

8.1.2 Interesting dynamics from double quench dynamics

In another interesting experiment further investigating the coherent dynamics, we suddenly quench off the lattice shaking after the system evolved sometime in the ferromagnetic phase. In a regular seeded experiment, we observe the damped oscillation of the density wave as we keep shaking. We next suddenly turn off the lattice shaking at various times when the amplitude of the density reaches a minimum (see Fig. 8.2). We observe a large revival of the density wave oscillation after the lattice shaking being turned off. This later density wave oscillation reflects the amount of energy being deposited to the condensate because of shaking and serve a probe to the energy transfer between the lattice and atoms. Another

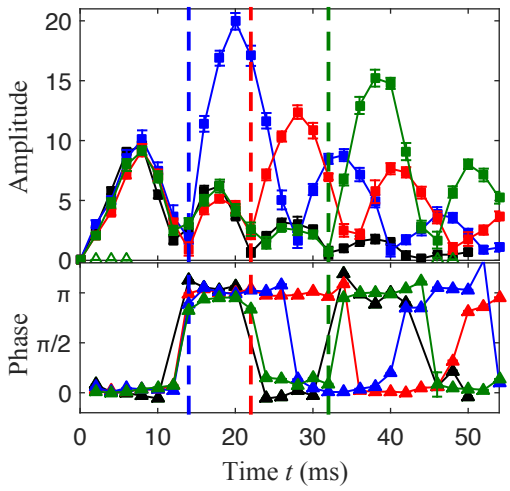

Figure 8.2: **Density wave oscillation in double quench seeded experiment** The condensates are seeded at momentum $q' = 0.13\ q_L$ and quenched from shaking amplitude $s_c = 13.1$ nm to $s = 25\ nm$. Amplitude (top panel) and phase (bottom panel) of the density wave are compared between cases when shaking amplitude is quenched back to zero at $t = 14$ (blue), 22 (red), and 32 ms (green). The data without the second quench is shown in black. The error bars indicate 1σ standard error.

interesting aspect is that the revived the density waves after quench-off signals the positions of the domain walls.

We also perform a similar quench-off experiment in the unseeded ramp experiment (see Fig. 8.3). Here we linearly ramp the shaking amplitude with a ramp rate $\dot{s} = 0.64$ nm/ms across the critical point at $t = 0$. After passing the critical point, the lattice shaking is suddenly turned off at $t = 38.6$ ms. As the system transitions to the ferromagnetic phase, we observe the initial formation of the density wave facilitating the formation of domains at the later time. This density wave quickly relaxes as domain forms. After the lattice shaking is quenched off, we observe a huge revival signal of the density wave whose peaks and troughs mark the position of the domain walls. This signal can serve as a probe of domain walls in studying coarsening dynamics without domain reconstruction imaging.

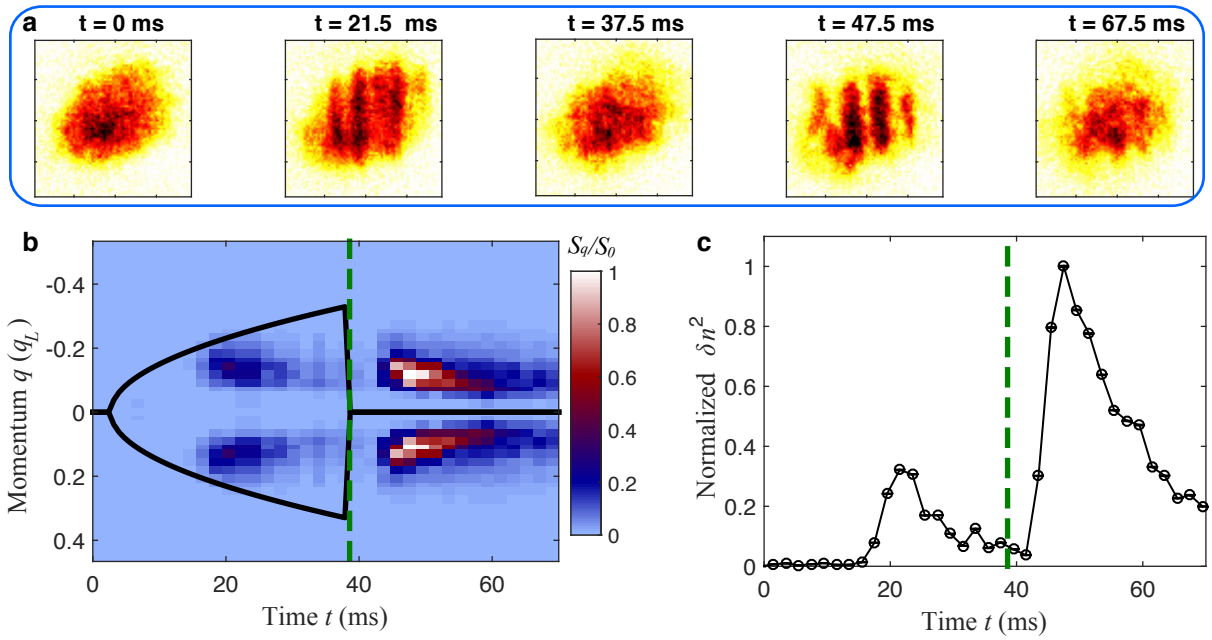

Figure 8.3: **Density wave oscillation in double quench unseeded experiment.** Here we linearly ramp up the shaking amplitude s with a ramp rate $\dot{s} = 0.64$ nm/ms across the critical point $s_c = 13.1$ nm at time $t = 0$. The shaking amplitude is suddenly turned to zero at $t = 38.6$ ms. **a**, Examples of density density waves emerged during inflation and after quench off the lattice shaking. **b**, The density structure factor S_q normalized to its maximum value after the quench back. Peaks appear at $\pm q_d = \pm 0.14\ q_L$. **c**, The density variance δn^2 from integrating the structure factor S_q and again normalized to its maximum value after quenching off the lattice shaking. The error bars indicate 1σ standard error.

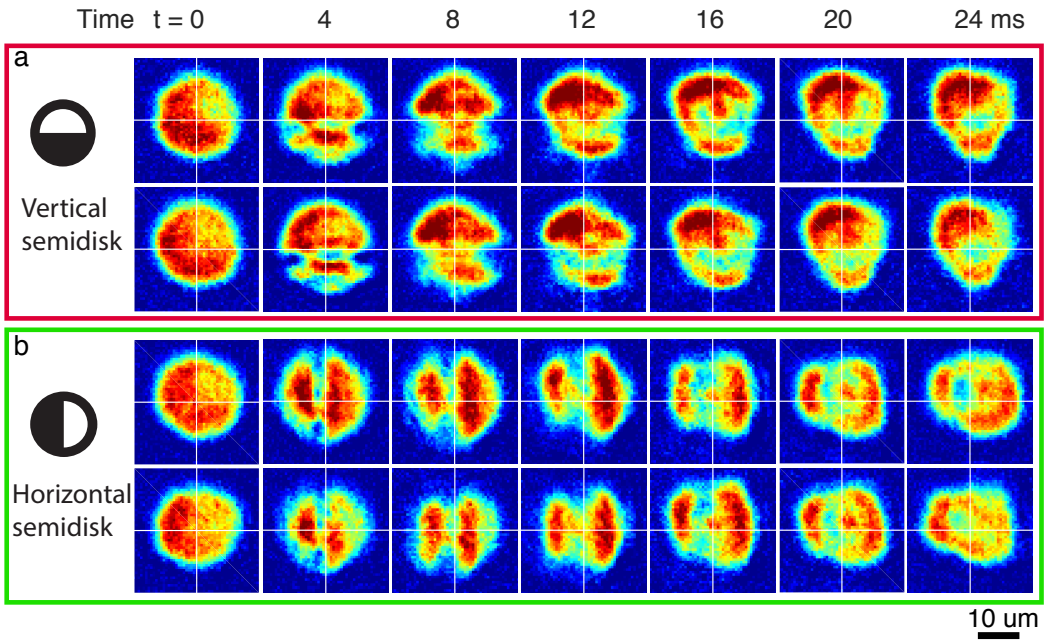

Figure 8.4: **Time evolution of dark soliton-like excitation in BEC.** Here we use a ring trap with a radius of $R = 10\ \mu m$ from DMD and the DC scattering length is kept at $a_{dc} = 5a_0$. **a** and **b** show the time evolution of the condensates after phase imprinting pulse with a duration of 0.8 ms with a vertical and horizontal semidisk DMD pattern (the black region indicate the mirrors that are turned on).

8.2 Oscillating interaction

8.2.1 Jet emission with excited condensates

We are always fascinated by the quantum origin of the jets in our Bose firework. These jets are amplified quantum fluctuations using the oscillating interaction as an example of parametric amplification. Toward the application of our Bose fireworks, one naturally would come up with the interesting idea of amplifying other weak excitation in condensates which are normally hard to detect. Such idea of comprehensive tomography of the momentum space spectrum using parametric amplification would require modulation of interaction at various frequencies in order to amplify population in different momentum mode. On the other hand, since the jets drain particles from a ground state (BEC or vacuum in the regular Bose fireworks case), we think if the emission pattern from a single frequency modulation

would carry enough information of the particular ground state. Here we first tried to look at the matter-wave emission when the condensates host a dark soliton-like excitation.

We introduce such excitation by phase imprinting using DMD. Here we want to achieve a large phase shift up to π far beyond the perturbation regime in the inflation case. There are several difficulties in terms of such phase imprinting. First of all, since we use the DMD to project horizontal box potential at the same time, we can only use pattern switching to flash on and off the phase imprinting pattern. Because the fastest switching rate for the DMD (DLP300) is only 4 kHz, the shortest pulse time is limited to 0.2 ms. Since the coating of the DMD window is not designed for the 788 nm laser that we are use for projection, we can only deliver $\sim 10\%$ of laser power to the atoms and thus the amount of phase shift will be limited. In addition, the projection resolution will also limit the phase imprinting. In the ideal case, the imprinted phase should go from zero to finite value ϕ as a step function in space but finite resolution will smooth this step function causing intermediate phase shift across the transition region. Despite the difficulties we managed to try this experiment using the existing DMD setup.

We first just look at the evolution of the condensates after a phase imprinting DMD pulse, see Fig. 8.4. Here we start with condensates ($\sim$35,000 atoms) trapped in a ring trap with a radius of $R = 10\ \mu m$ from DMD and the DC scattering length is set to $a_{dc} = 5a_0$. In this experiment, we quickly flash on either the horizontal or vertical semi-disk potential for $T_{pulse} = 0.8$ ms. We later take *in situ* images at time t after the start of the pulse. The density evolution from *in situ* imaging suggests a dark soliton-like excitation is created by the phase imprinting pulse and the region within which the density was maximally depleted stays at the same position as a function of time. A 1D GPE simulation shows that this kind of phase imprint will also create some phonon excitations and their reflection from the trap wall is probably responsible for later time evolution where the density profile becomes donut-like.

Right after the phase imprinting pulse, we start to modulate the interaction as $a(t) =$

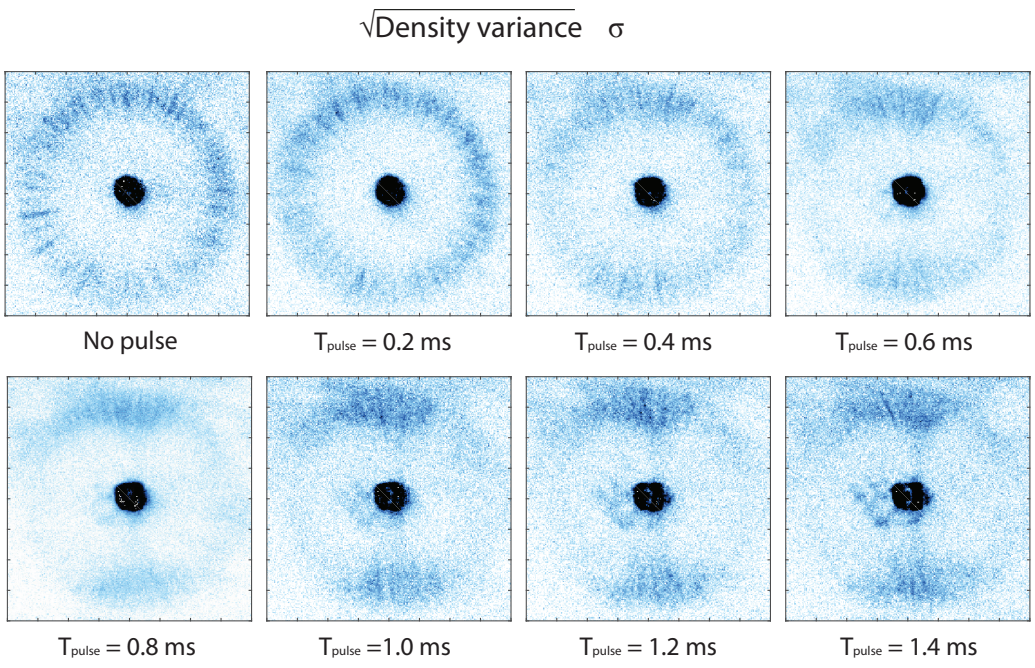

Figure 8.5: **Density variance from jet emission with vertical phase imprinting.** Here we apply a vertically oriented semi-disk potential using DMD for various pulse duration of T_{pulse}. As pulse duration gets longer, the emission in the vertical direction become more suppressed. For even longer pulse duration, there are extra atoms being excited out the condensate beside emitted jets.

$a_{dc} + a_{ac}\sin(2\pi ft)$ with frequency $f = 3.5$ kHz with the DC scattering length $a_{dc} = 5a_0$ and the AC scattering length $a_{ac} = 62.5a_0$. In order to see the effect of the semi-disk potential pulse on the jet emission more clearly, we show the square root of density variance $\sigma = \sqrt{\langle n^2\rangle - \langle n\rangle^2}$ instead of the mean density $\langle n\rangle$. This observable is particularly good for seeing small shot-to-shot varying signals on top of a large static background. Since the density of the condensates we use here is low giving weaker jets compared to that in the previous chapters, the static imaging background is more problematic. By looking at the variance of density, we will eliminate the static background while the signal from random jet emission pattern are preserved. Here we only look into the case for the vertical semi-disk potential by pulsing it on for a different amount of time T_{pulse}, see Fig.8.5. In the case without the pulse, jets emit in all directions symmetrically. As we increase the pulse time, the effect becomes visible, where the jet emission along the horizontal direction (along which, we have a phase jump in the middle at $x = 0$) is suppressed. In principle, this effect should reach a maximum when we have π phase jump and then diminishes when the jet emission become symmetric again (2π phase jump). However, it induces some other effects and the jets become messy because the pulse time is too long and comparable to other time scales in the condensates.

We later test the suppression effect for different orientations of the semi-disk potential. Previously we already showed the effect from a vertically orientated semi-disk in Fig.8.5, this time we rotate it 90 degrees so it becomes horizontally oriented. Applying this pulse will now suppress the emission in the vertical direction and indeed observed in the experiment shown, see Fig.8.6. On might argue that this effect can just come from the fact that the dark soliton divides the gas into two semi-disks, which changes the geometry, and jets now only like to emit in the direction where they can find the longest path across the condensates instead of destructive interference. One way to argue against this statement is to see how well a semi-disk trap can suppress the jet emission along its short axis as compared to that in the phase imprinting case. An example of this test with atoms in a horizontally oriented

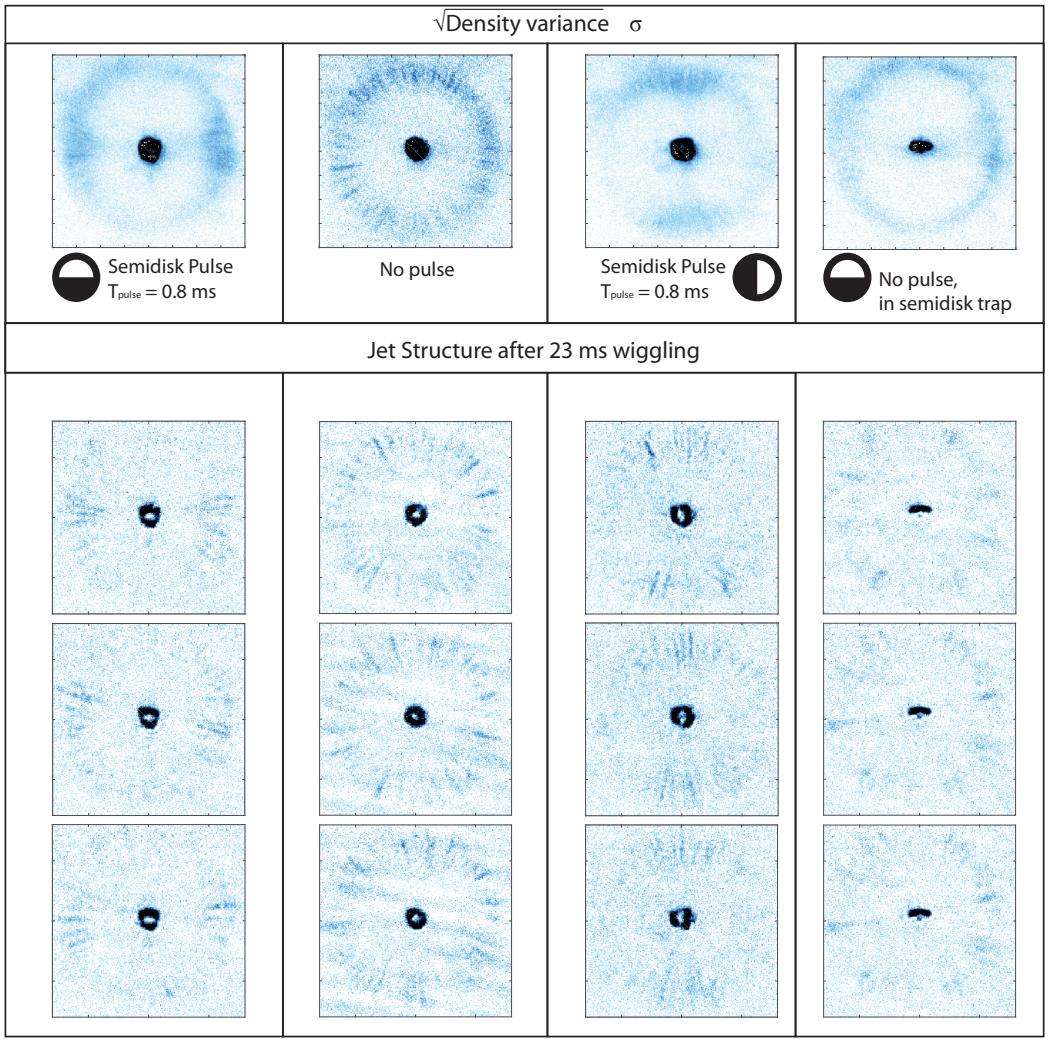

Figure 8.6: **Jet emission suppression along different directions.** Here we compare the emission pattern after phase imprinting with a vertical and horizontal semi-disk potential with pulse duration of $T_{pulse} = 0.8$ ms. For vertical (horizontal) semi-disk potential, the jet emission is suppressed along the vertical (horizontal) direction. And this suppressed jet emission pattern is different from that of jets emitted from condensates initially in a semi-disk trap.

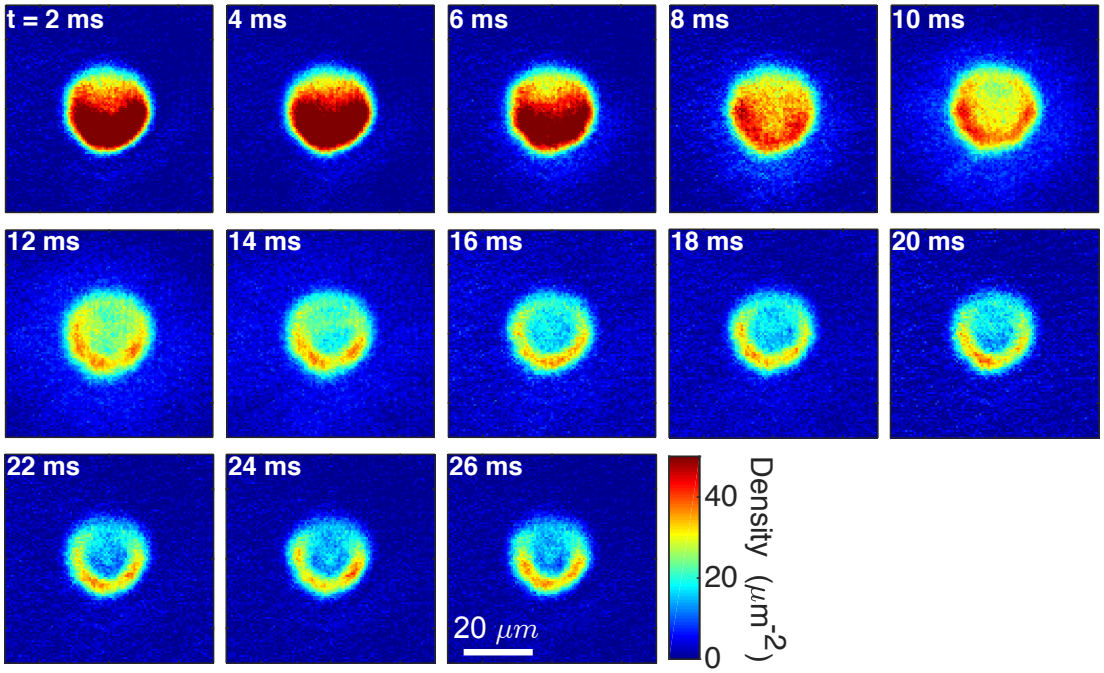

Figure 8.7: **Excitation in remnant BEC.** The remnant atoms in the BEC are captured in the high-intensity imaging after modulation for time t. After the jets are emitted, the remnant atoms form a nice looking donut. Although emission pattern of jets is random from shot to shot, the structure of the remnant BEC does not vary much. Here the modulation has a frequency of $f = 3.5$ kHz and an amplitude of $a_{ac} = 52a_0$. The BEC has 30,000 atoms and a radius of $R = 13.7\mu m$.

semi-disk trap is shown in Fig.8.6. We see the semi-disk does not suppress the jet emission as much as the phase imprinting does, which is a clear indication that destructive interference plays a critical role in jet suppression.

Although these experimental results are still preliminary, it is showing very different behavior compared to the regular emission of matter-wave jets. We can clearly see that the information of the initial condensates is imprinted to the jet structure. Thus a careful backtracking analysis on the emission structure from an arbitrary initial state might help to understand its properties.

8.2.2 Excitation in remnant BEC

So far in this thesis, we study the jet emission in Ch. 7 and Ch. 5, and density waves that predate the emission in Ch. 6. What is left within the condensates after the fireworks? This is also a very interesting question. Previously in Ch. 7 and Ch. 5, we use low-intensity imaging to boost our signal-to-noise ratio for detecting low-density atomic jets. As a result, the high-density center part of the BEC turns out to be highly saturated in the absorption image and does not faithfully show the structure of the remnant atoms.

In this experiment, we focus on the BEC after the emission of the jets with high-intensity imaging (see Fig. 8.7). In this case, the jets become faint background but the structure of the remnant BEC become clear. Here the modulation has a frequency of $f = 3.5$ kHz and an amplitude of $a_{ac} = 52a_0$. The BEC has 30,000 atoms and a radius of $R = 13.7\mu m$. Although the emission pattern of jets is completely random from shot to shot, the structure of the remnant BEC does not vary very much. After averaging for 15 images at each time t, the density wave at the early time is smeared out ($t < 6$ ms); the emitted jets are averaged to a weak background ($t > 8$ ms and $t < 16$ ms); the remnant BEC shows the same donut-shaped structure from shot to shot ($t > 12$ ms). Numerical simulations also show similar behavior and the "donut" even oscillates at much longer time scale than the jet emission. This observation indicates that such remnant excitation is relatively low-energy and potentially relates to the interesting collective excitation in the hydrodynamic limit [52, 100].

LIST OF PUBLICATIONS

1. **Lei Feng**, Jiazhong Hu, Logan W. Clark, and Cheng Chin, Correlation in high-harmonic generation of matter-wave jets revealed by pattern recognition, *Science*, 363, 521 (2019)

2. Han Fu, **Lei Feng**, Brandon M. Anderson, Logan W. Clark, Cheng Chin, and Kathryn Levin, Density waves and jet emission asymmetry in Bose Fireworks, *Phys. Rev. Lett.*, 121, 243001 (2018)

3. Logan W. Clark , Brandon M. Anderson, **Lei Feng**, Kathy Levin, and Cheng Chin, Observation of density-dependent gauge fields in a Bose-Einstein condensate based on micromotion control in a shaken two-dimensional lattice, *Phys. Rev. Lett.*, 121, 030402 (2018)

4. **Lei Feng**, Logan W. Clark, Anita, Gaj, and Cheng Chin, Coherent inflationary dynamics for Bose-Einstein condensates crossing a quantum critical point, *Nature Physics*, 14, 269 (2018)

5. Logan Clark, Anita Gaj, **Lei Feng**, and Cheng Chin, Collective emission of mater-wave jets from driven Bose-Einstein condensates, *Nature*, 551, 356 (2017)

6. Brandon M. Anderson, Logan W. Clark, Jennifer Crawford, Andreas Glatz, Igor S. Aranson, Peter Scherpelz, **Lei Feng**, Cheng Chin, and K. Levin, Direct lattice shaking of Bose condensates: finite momentum superfluids, *Phys. Rev. Lett.*, 118, 220401 (2017)

7. Logan W. Clark, **Lei Feng**, and Cheng Chin, Universal space-time scaling symmetry in the dynamics of bosons across a quantum phase transition, *Science*, 354, 606 (2016)

8. Jiazhong Hu, **Lei Feng**, Zhendong Zhang, and Cheng Chin, Quantum simulation of coherent Unruh Radiation, *arXiv*: 1807.07504 (2018)

REFERENCES

[1] B. P. Anderson and M. A. Kasevich. Macroscopic quantum interference from atomic tunnel arrays. *Science*, 282(5394):1686–1689, 1998.

[2] Brandon M. Anderson, Logan W. Clark, Jennifer Crawford, Andreas Glatz, Igor S. Aranson, Peter Scherpelz, Lei Feng, Cheng Chin, and K. Levin. Direct lattice shaking of bose condensates: Finite momentum superfluids. *Phys. Rev. Lett.*, 118:220401, 2017.

[3] M. H. Anderson, J. R. Ensher, M. R. Matthews, C. E. Wieman, and E. A. Cornell. Observation of bose-einstein condensation in a dilute atomic vapor. *Science*, 269(5221):198–201, 1995.

[4] P. W. Anderson. More is different. *Science*, 177(4047):393–396, 1972.

[5] M. R. Andrews, C. G. Townsend, H.-J. Miesner, D. S. Durfee, D. M. Kurn, and W. Ketterle. Observation of interference between two bose condensates. *Science*, 275(5300):637–641, 1997.

[6] M. Anquez, B. A. Robbins, H. M Bharath, M. Boguslawski, T. M. Hoang, and M. S. Chapman. Quantum kibble-zurek mechanism in a spin-1 bose-einstein condensate. *Phys. Rev. Lett.*, 116:155301, 2016.

[7] Miguel Arratia. On the jets emitted by driven bose–einstein condensates. *Journal of Physics B: Atomic, Molecular and Optical Physics*, 52(5):055301, 2019.

[8] Antun Balaž, Remus Paun, Alexandru I. Nicolin, Sudharsan Balasubramanian, and Radha Ramaswamy. Faraday waves in collisionally inhomogeneous bose-einstein condensates. *Phys. Rev. A*, 89:023609, 2014.

[9] Ryan Barnett, Anatoli Polkovnikov, and Mukund Vengalattore. Prethermalization in quenched spinor condensates. *Phys. Rev. A*, 84:023606, 2011.

[10] K. Baumann, R. Mottl, F. Brennecke, and T. Esslinger. Exploring symmetry breaking at the dicke quantum phase transition. *Phys. Rev. Lett.*, 107:140402, 2011.

[11] Rivka Bekenstein, Ran Schley, Maor Mutzafi, Carmel Rotschild, and Mordechai Segev. Optical simulations of gravitational effects in the newton–schrödinger system. *Nature Physics*, 11:872, 2015.

[12] Stefan Bernet, Markus K. Oberthaler, Roland Abfalterer, Jörg Schmiedmayer, and Anton Zeilinger. Coherent frequency shift of atomic matter waves. *Phys. Rev. Lett.*, 77:5160–5163, 1996.

[13] Immanuel Bloch, Jean Dalibard, and Wilhelm Zwerger. Many-body physics with ultracold gases. *Rev. Mod. Phys.*, 80:885–964, 2008.

[14] Immanuel Bloch, Theodor W. Hänsch, and Tilman Esslinger. Atom laser with a cw output coupler. *Phys. Rev. Lett.*, 82:3008–3011, 1999.

[15] R. W. Boyd. *Nonlinear Optics*. Academic Press, 3 edition, 2008.

[16] A.J. Bray. Theory of phase-ordering kinetics. *Advances in Physics*, 43(3):357–459, 1994.

[17] Robert Bücker, Julian Grond, Stephanie Manz, Tarik Berrada, Thomas Betz, Christian Koller, Ulrich Hohenester, Thorsten Schumm, Aurélien Perrin, and Jörg Schmiedmayer. Twin-atom beams. *Nature Physics*, 7:608, 2011.

[18] Gretchen K. Campbell, Jongchul Mun, Micah Boyd, Erik W. Streed, Wolfgang Ketterle, and David E. Pritchard. Parametric amplification of scattered atom pairs. *Phys. Rev. Lett.*, 96:020406, 2006.

[19] Zenghu Chang, Andy Rundquist, Haiwen Wang, Margaret M. Murnane, and Henry C. Kapteyn. Generation of coherent soft x rays at 2.7 nm using high harmonics. *Phys. Rev. Lett.*, 79:2967–2970, 1997.

[20] Cheng Chin, Rudolf Grimm, Paul Julienne, and Eite Tiesinga. Feshbach resonances in ultracold gases. *Rev. Mod. Phys.*, 82:1225–1286, 2010.

[21] Soonwon Choi, Joonhee Choi, Renate Landig, Georg Kucsko, Hengyun Zhou, Junichi Isoya, Fedor Jelezko, Shinobu Onoda, Hitoshi Sumiya, Vedika Khemani, Curt von Keyserlingk, Norman Y. Yao, Eugene Demler, and Mikhail D. Lukin. Observation of discrete time-crystalline order in a disordered dipolar many-body system. *Nature*, 543:221, 2017.

[22] L. W. Clark. *Quantum many-body dynamics with driven Bose condensates: Kibble-Zurek mechanism and Bose fireworks*. PhD thesis, The University of Chicago, 2017.

[23] Logan W. Clark, Brandon M. Anderson, Lei Feng, Anita Gaj, K. Levin, and Cheng Chin. Observation of density-dependent gauge fields in a bose-einstein condensate based on micromotion control in a shaken two-dimensional lattice. *Phys. Rev. Lett.*, 121:030402, 2018.

[24] Logan W. Clark, Lei Feng, and Cheng Chin. Universal space-time scaling symmetry in the dynamics of bosons across a quantum phase transition. *Science*, 354(6312):606–610, 2016.

[25] Logan W. Clark, Anita Gaj, Lei Feng, and Cheng Chin. Collective emission of matter-wave jets from driven bose–einstein condensates. *Nature*, 551:356, 2017.

[26] Alexander D. Cronin, Jörg Schmiedmayer, and David E. Pritchard. Optics and interferometry with atoms and molecules. *Rev. Mod. Phys.*, 81:1051–1129, 2009.

[27] R. G. Dall, A. G. Manning, S. S. Hodgman, Wu RuGway, K. V. Kheruntsyan, and A. G. Truscott. Ideal n-body correlations with massive particles. *Nature Physics*, 9:341, 2013.

[28] K. B. Davis, M. O. Mewes, M. R. Andrews, N. J. van Druten, D. S. Durfee, D. M. Kurn, and W. Ketterle. Bose-einstein condensation in a gas of sodium atoms. *Phys. Rev. Lett.*, 75:3969–3973, 1995.

[29] Adolfo del Campo and Wojciech H. Zurek. Universality of phase transition dynamics: Topological defects from symmetry breaking. *International Journal of Modern Physics A*, 29(08):1430018, 2014.

[30] L. Deng, E. W. Hagley, J. Wen, M. Trippenbach, Y. Band, P. S. Julienne, J. E. Simsarian, K. Helmerson, S. L. Rolston, and W. D. Phillips. Four-wave mixing with matter waves. *Nature*, 398(6724):218–220, 1999.

[31] Markus Drescher, Michael Hentschel, Reinhard Kienberger, Gabriel Tempea, Christian Spielmann, Georg A. Reider, Paul B. Corkum, and Ferenc Krausz. X-ray pulses approaching the attosecond frontier. *Science*, 291(5510):1923–1927, 2001.

[32] Jacek Dziarmaga. Dynamics of a quantum phase transition and relaxation to a steady state. *Advances in Physics*, 59(6):1063–1189, 2010.

[33] André Eckardt. Colloquium: Atomic quantum gases in periodically driven optical lattices. *Rev. Mod. Phys.*, 89:011004, 2017.

[34] P. Engels, C. Atherton, and M. A. Hoefer. Observation of faraday waves in a bose-einstein condensate. *Phys. Rev. Lett.*, 98:095301, 2007.

[35] Petr O. Fedichev and Uwe R. Fischer. Gibbons-hawking effect in the sonic de sitter space-time of an expanding bose-einstein-condensed gas. *Phys. Rev. Lett.*, 91:240407, 2003.

[36] Lei Feng, Logan W. Clark, Anita Gaj, and Cheng Chin. Coherent inflationary dynamics for bose–einstein condensates crossing a quantum critical point. *Nature Physics*, 14(3):269–272, 2018.

[37] Lei Feng, Jiazhong Hu, Logan W. Clark, and Cheng Chin. Correlations in high-harmonic generation of matter-wave jets revealed by pattern recognition. *Science*, 363(6426):521–524, 2019.

[38] Lei Feng, Pengxiong Li, Liang Jiang, Jianming Wen, and Yanhong Xiao. Coherence-assisted resonance with sub-transit-limited linewidth. *Phys. Rev. Lett.*, 109:233006, 2012.

[39] Lei Feng, Pengxiong Li, Mengzhen Zhang, Tun Wang, and Yanhong Xiao. Transition linewidth of cross correlations in random intensity fluctuations in electromagnetically induced transparency. *Phys. Rev. A*, 89:013815, 2014.

[40] Jan Flusser and Tomás Suk. Pattern recognition by affine moment invariants. *Pattern Recognition*, 26(1):167 – 174, 1993.

[41] L. J. Garay, J. R. Anglin, J. I. Cirac, and P. Zoller. Sonic analog of gravitational black holes in bose-einstein condensates. *Phys. Rev. Lett.*, 85:4643–4647, 2000.

[42] Christoph Gohle, Thomas Udem, Maximilian Herrmann, Jens Rauschenberger, Ronald Holzwarth, Hans A. Schuessler, Ferenc Krausz, and Theodor W. Hänsch. A frequency comb in the extreme ultraviolet. *Nature*, 436(7048):234–237, 2005.

[43] C. Gross, T. Zibold, E. Nicklas, J. Estève, and M. K. Oberthaler. Nonlinear atom interferometer surpasses classical precision limit. *Nature*, 464:1165, 2010.

[44] Vera Guarrera, Peter Würtz, Arne Ewerbeck, Andreas Vogler, Giovanni Barontini, and Herwig Ott. Observation of local temporal correlations in trapped quantum gases. *Phys. Rev. Lett.*, 107:160403, 2011.

[45] A. H. Guth. Inflationary universe: A possible solution to the horizon and flatness problems. *Physical Review D*, 23:347–356, 1981.

[46] Li-Chung Ha. *Bose-Einstein condensates in a shaken optical lattice*. PhD thesis, The University of Chicago, 2016.

[47] Li-Chung Ha, Logan W. Clark, Colin V. Parker, Brandon M. Anderson, and Cheng Chin. Roton-maxon excitation spectrum of bose condensates in a shaken optical lattice. *Phys. Rev. Lett.*, 114:055301, 2015.

[48] E. W. Hagley, L. Deng, M. Kozuma, J. Wen, K. Helmerson, S. L. Rolston, and W. D. Phillips. A well-collimated quasi-continuous atom laser. *Science*, 283(5408):1706–1709, 1999.

[49] D. S. Hall, M. R. Matthews, C. E. Wieman, and E. A. Cornell. Measurements of relative phase in two-component bose-einstein condensates. *Phys. Rev. Lett.*, 81:1543–1546, 1998.

[50] S. W. Hawking. Particle creation by black holes. *Communications in Mathematical Physics*, 43(3):199–220, 1975.

[51] M. Hentschel, R. Kienberger, Ch. Spielmann, G. A. Reider, N. Milosevic, T. Brabec, P. Corkum, U. Heinzmann, M. Drescher, and F. Krausz. Attosecond metrology. *Nature*, 414(6863):509–513, 2001.

[52] Tin-Lun Ho and Michael Ma. Quasi 1 and 2d dilute bose gas in magnetic traps: Existence of off-diagonal order and anomalous quantum fluctuations. *Journal of Low Temperature Physics*, 115(1):61–70, 1999.

[53] Martin Holthaus. Floquet engineering with quasienergy bands of periodically driven optical lattices. *Journal of Physics B: Atomic, Molecular and Optical Physics*, 49(1):013001, 2015.

[54] B. Horstmann, B. Reznik, S. Fagnocchi, and J. I. Cirac. Hawking radiation from an acoustic black hole on an ion ring. *Phys. Rev. Lett.*, 104:250403, 2010.

[55] John C. Howell, Ryan S. Bennink, Sean J. Bentley, and R. W. Boyd. Realization of the einstein-podolsky-rosen paradox using momentum- and position-entangled photons from spontaneous parametric down conversion. *Phys. Rev. Lett.*, 92:210403, 2004.

[56] Chen-Lung Hung. *In situ probing of two-dimensional quantum gases*. PhD thesis, The University of Chicago, 2011.

[57] Chen-Lung Hung, Victor Gurarie, and Cheng Chin. From cosmology to cold atoms: Observation of sakharov oscillations in a quenched atomic superfluid. *Science*, 341(6151):1213–1215, 2013.

[58] Chen-Lung Hung, Xibo Zhang, Li-Chung Ha, Shih-Kuang Tung, Nathan Gemelke, and Cheng Chin. Extracting density-density correlations from in situ images of atomic quantum gases. *New Journal of Physics*, 13(7):075019, 2011.

[59] S. Inouye, A. P. Chikkatur, D. M. Stamper-Kurn, J. Stenger, D. E. Pritchard, and W. Ketterle. Superradiant rayleigh scattering from a bose-einstein condensate. *Science*, 285(5427):571–574, 1999.

[60] J.-C. Jaskula, G. B. Partridge, M. Bonneau, R. Lopes, J. Ruaudel, D. Boiron, and C. I. Westbrook. Acoustic analog to the dynamical casimir effect in a bose-einstein condensate. *Phys. Rev. Lett.*, 109:220401, 2012.

[61] R. Jason Jones, Kevin D. Moll, Michael J. Thorpe, and Jun Ye. Phase-coherent frequency combs in the vacuum ultraviolet via high-harmonic generation inside a femtosecond enhancement cavity. *Phys. Rev. Lett.*, 94:193201, 2005.

[62] Yu. Kagan and L.A. Manakova. Condensation of phonons in an ultracold bose gas. *Physics Letters A*, 361(4):401 – 405, 2007.

[63] Adam M. Kaufman, M. Eric Tai, Alexander Lukin, Matthew Rispoli, Robert Schittko,

Philipp M. Preiss, and Markus Greiner. Quantum thermalization through entanglement in an isolated many-body system. *Science*, 353(6301):794–800, 2016.

[64] T. W. B. Kibble. Topology of cosmic domains and strings. *J. Phys. A: Math. Gen.*, 9:387–1398, 1976.

[65] T. W. B. Kibble. Some implications of a cosmological phase transition. *PHYSICS REPORTS (Review Section of Physics Letters)*, 67:183–199, 1980.

[66] Jens Klinder, Hans Keßler, Matthias Wolke, Ludwig Mathey, and Andreas Hemmerich. Dynamical phase transition in the open dicke model. *Proceedings of the National Academy of Sciences*, 112(11):3290–3295, 2015.

[67] M. Krämer, C. Tozzo, and F. Dalfovo. Parametric excitation of a bose-einstein condensate in a one-dimensional optical lattice. *Phys. Rev. A*, 71:061602, 2005.

[68] Giacomo Lamporesi, Simone Donadello, Simone Serafini, Franco Dalfovo, and Gabriele Ferrari. Spontaneous creation of kibble–zurek solitons in a bose–einstein condensate. *Nature Physics*, 9:656, 2013.

[69] L. D. Landau and E. M. Lafshitz. *Statistical Physics, Part 2*. Oxford, 3 edition, 2008.

[70] T. Langen, R. Geiger, M. Kuhnert, B. Rauer, and J. Schmiedmayer. Local emergence of thermal correlations in an isolated quantum many-body system. *Nature Physics*, 9:640, 2013.

[71] S. Lellouch, M. Bukov, E. Demler, and N. Goldman. Parametric instability rates in periodically driven band systems. *Phys. Rev. X*, 7:021015, 2017.

[72] Pengxiong Li, Lei Feng, and Yanhong Xiao. Resolving multiple peaks using a sub-transit-linewidth cross-correlation resonance. *Phys. Rev. A*, 89:043835, 2014.

[73] D Linnemann, J Schulz, W Muessel, P Kunkel, M Prüfer, A Frölian, H Strobel, and M K Oberthaler. Active SU(1,1) atom interferometry. *Quantum Science and Technology*, 2(4):044009, 2017.

[74] D. Linnemann, H. Strobel, W. Muessel, J. Schulz, R. J. Lewis-Swan, K. V. Kheruntsyan, and M. K. Oberthaler. Quantum-enhanced sensing based on time reversal of nonlinear dynamics. *Phys. Rev. Lett.*, 117:013001, 2016.

[75] Carolyn Meldgin, Ushnish Ray, Philip Russ, David Chen, David M. Ceperley, and Brian DeMarco. Probing the bose glass–superfluid transition using quantum quenches of disorder. *Nature Physics*, 12:646, 2016.

[76] M.-O. Mewes, M. R. Andrews, D. M. Kurn, D. S. Durfee, C. G. Townsend, and W. Ketterle. Output coupler for bose-einstein condensed atoms. *Phys. Rev. Lett.*, 78:582–585, 1997.

[77] S. T. Milner. Square patterns and secondary instabilities in driven capillary waves. *Journal of Fluid Mechanics*, 225:81—100, 1991.

[78] M. G. Moore and P. Meystre. Theory of superradiant scattering of laser light from bose-einstein condensates. *Phys. Rev. Lett.*, 83:5202–5205, 1999.

[79] Masahiro Morikawa. Cosmological inflation as a quantum phase transition. *Progress of Theoretical Physics*, 93(4):685–709, 1995.

[80] Nasser M. Nasrabadi. Pattern recognition and machine learning. *Journal of Electronic Imaging*, 16(4), 2007.

[81] Nir Navon, Alexander L. Gaunt, Robert P. Smith, and Zoran Hadzibabic. Critical dynamics of spontaneous symmetry breaking in a homogeneous bose gas. *Science*, 347(6218):167–170, 2015.

[82] J. H. V. Nguyen, M. C. Tsatsos, D. Luo, A. U. J. Lode, G. D. Telles, V. S. Bagnato, and R. G. Hulet. Parametric excitation of a bose-einstein condensate: From faraday waves to granulation. *Phys. Rev. X*, 9:011052, 2019.

[83] E. Nicklas, M. Karl, M. Höfer, A. Johnson, W. Muessel, H. Strobel, J. Tomkovič, T. Gasenzer, and M. K. Oberthaler. Observation of scaling in the dynamics of a strongly quenched quantum gas. *Phys. Rev. Lett.*, 115:245301, 2015.

[84] Alexandru I. Nicolin, R. Carretero-González, and P. G. Kevrekidis. Faraday waves in bose-einstein condensates. *Phys. Rev. A*, 76:063609, 2007.

[85] Colin V. Parker, Li-Chung Ha, and Cheng Chin. Direct observation of effective ferromagnetic domains of cold atoms in a shaken optical lattice. *Nature Physics*, 9:769, 2013.

[86] C. J. Pethick and H. Smith. *Bose-Einstein Condensation in Dilute Gases*. Cambridge University Press, 2 edition, 2008.

[87] Anatoli Polkovnikov, Krishnendu Sengupta, Alessandro Silva, and Mukund Vengalattore. Colloquium: Nonequilibrium dynamics of closed interacting quantum systems. *Rev. Mod. Phys.*, 83:863–883, 2011.

[88] Max F. Riedel, Pascal Böhi, Yun Li, Theodor W. Hänsch, Alice Sinatra, and Philipp Treutlein. Atom-chip-based generation of entanglement for quantum metrology. *Nature*, 464:1170, 2010.

[89] Javier Rodríguez-Laguna, Leticia Tarruell, Maciej Lewenstein, and Alessio Celi. Synthetic unruh effect in cold atoms. *Phys. Rev. A*, 95:013627, 2017.

[90] S. L. Rolston and W. D. Phillips. Nonlinear and quantum atom optics. *Nature*, 416(6877):219–224, 2002.

[91] Subir Sachdev. *Quantum Phase Transitions*. Cambridge University Press, 1 edition, 2011.

[92] L. E. Sadler, J. M. Higbie, S. R. Leslie, M. Vengalattore, and D. M. Stamper-Kurn. Spontaneous symmetry breaking in a quenched ferromagnetic spinor bose–einstein condensate. *Nature*, 443(7109):312–315, 2006.

[93] Peter Scherpelz, Karmela Padavić, Adam Rançon, Andreas Glatz, Igor S. Aranson, and K. Levin. Phase imprinting in equilibrating fermi gases: The transience of vortex rings and other defects. *Phys. Rev. Lett.*, 113:125301, 2014.

[94] Dominik Schneble, Yoshio Torii, Micah Boyd, Erik W. Streed, David E. Pritchard, and Wolfgang Ketterle. The onset of matter-wave amplification in a superradiant bose-einstein condensate. *Science*, 300(5618):475–478, 2003.

[95] Ralf Schützhold and William G. Unruh. Hawking radiation in an electromagnetic waveguide? *Phys. Rev. Lett.*, 95:031301, 2005.

[96] Thomas Schweigler, Valentin Kasper, Sebastian Erne, Igor Mazets, Bernhard Rauer, Federica Cataldini, Tim Langen, Thomas Gasenzer, Jürgen Berges, and Jörg Schmiedmayer. Experimental characterization of a quantum many-body system via higher-order correlations. *Nature*, 545:323, 2017.

[97] I. Shvarchuck, Ch. Buggle, D. S. Petrov, K. Dieckmann, M. Zielonkowski, M. Kemmann, T. G. Tiecke, W. von Klitzing, G. V. Shlyapnikov, and J. T. M. Walraven. Bose-einstein condensation into nonequilibrium states studied by condensate focusing. *Phys. Rev. Lett.*, 89:270404, 2002.

[98] Kestutis Staliunas, Stefano Longhi, and Germán J. de Valcárcel. Faraday patterns in bose-einstein condensates. *Phys. Rev. Lett.*, 89:210406, 2002.

[99] Jeff Steinhauer. Observation of quantum hawking radiation and its entanglement in an analogue black hole. *Nature Physics*, 12:959, 2016.

[100] S. Stringari. Dynamics of bose-einstein condensed gases in highly deformed traps. *Phys. Rev. A*, 58:2385–2388, 1998.

[101] Daiqin Su, C T Marco Ho, Robert B Mann, and Timothy C Ralph. Quantum circuit model for non-inertial objects: a uniformly accelerated mirror. *New Journal of Physics*, 19(6):063017, 2017.

[102] Marek Trippenbach, Y. B. Band, and P. S. Julienne. Theory of four-wave mixing of matter waves from a bose-einstein condensate. *Phys. Rev. A*, 62:023608, 2000.

[103] W. G. Unruh. Notes on black-hole evaporation. *Phys. Rev. D*, 14:870–892, 1976.

[104] Thomas Vojta. Phases and phase transitions in disordered quantum systems. *AIP Conference Proceedings*, 1550(1):188–247, 2013.

[105] R. M. Wald. *Quantum Field Theory in Curved Spacetime and Black Hole Ther- modynamics*. The University of Chicago Press, 1994.

[106] Xiang-Bin Wang, Tohya Hiroshima, Akihisa Tomita, and Masahito Hayashi. Quantum information with gaussian states. *Physics Reports*, 448(1):1 – 111, 2007.

[107] Lewis A. Williamson and P. B. Blakie. Universal coarsening dynamics of a quenched ferromagnetic spin-1 condensate. *Phys. Rev. Lett.*, 116:025301, 2016.

[108] Zhigang Wu and Zhai Hui. Density correlations in matter wave jet emission of a driven condensate. *arXiv*, page 1801.05515, 2018.

[109] J. Zhang, P. W. Hess, A. Kyprianidis, P. Becker, A. Lee, J. Smith, G. Pagano, I. D. Potirniche, A. C. Potter, A. Vishwanath, N. Y. Yao, and C. Monroe. Observation of a discrete time crystal. *Nature*, 543:217, 2017.

[110] Wenbin Zhang and Jorge Vinals. Pattern formation in weakly damped parametric surface waves. *Journal of Fluid Mechanics*, 336:301–330, 1997.

[111] Xibo Zhang. *Observation of quantum criticality with ultracold atoms in optical lattices*. PhD thesis, The University of Chicago, 2012.

[112] Yuanlin Zheng, Huaijin Ren, Wenjie Wan, and Xianfeng Chen. Time-reversed wave mixing in nonlinear optics. *Scientific Reports*, 3:3245, 2013.

[113] W. H. Zurek. Cosmological experiments in superfluid helium? *Nature*, 317(6037):505–508, 1985.